THE SURFACE CHEMISTRY OF CHALCOPYRITE DURING ELECTROCHEMICAL DISSOLUTION

by

Ahmad Ghahremaninezhad

M.Sc., Sharif University of Technology, 2007

B.Sc., Sharif University of Technology, 2005

A THESIS SUBMITTED IN PARTIAL FULFILLMENT OF

THE REQUIREMENTS FOR THE DEGREE OF

DOCTOR OF PHILOSOPHY

in

The Faculty of Graduate Studies

(Materials Engineering)

THE UNIVERSITY OF BRITISH COLUMBIA

(Vancouver)

July 2012

Abstract

Hydrometallurgy may be an alternative to the currently practiced smelting process for copper extraction from chalcopyrite ($CuFeS_2$). However, the low temperature hydrometallurgical processes for chalcopyrite continue to face challenges, mostly relating to their slow dissolution rates or high sulfuric acid production. The slow dissolution rate of the mineral is strongly linked to the formation of the passive film on its surface. However, despite 40 years of research on this topic, there is still not a complete agreement between researchers about the composition and stability of chalcopyrite's passive film in sulfuric acid solutions. In this work, the nature of chalcopyrite's passive film and its stability were studied by application of a variety of electrochemical techniques. Additionally, the electrochemical results of the chalcopyrite study were compared to those obtained for a pyrrhotite electrode ($Fe_{1-x}S$), as pyrrhotite electrochemistry represents a simplified case of the chalcopyrite system. X-ray photoelectron spectroscopy (XPS) was used to analyze the composition of the product layers formed on the surface.

It is shown that the chalcopyrite electrode is passive for potentials up to 0.90 V_{SHE}. Above this potential, transpassive dissolution occurs. Results of XPS studies have suggested that a metal-deficient sulfide film ($Cu_{1-x}Fe_{1-y}S_{2-z}$) is the most plausible copper and iron containing sulfide phase which passivates the surface of chalcopyrite. In addition, an outer layer of iron oxyhydroxide (FeOOH) forms on the passive film. FeOOH forms via oxidation of the passive film's ferrous sulfide phases. The thickness of the sulfide passive film was calculated to be approximately 6.7 nm. It is demonstrated that the transpassive dissolution of chalcopyrite is significantly linked to oxidation of sulfur (from sulfide in the passive film to elemental sulfur and maybe sulfur species with higher oxidation states, e.g. thiosulfate). No elemental sulfur or polysulfide species were detected on the surface for potentials below 0.90 V_{SHE}.

Preface

A version of chapter 5 has been published: Ghahremaninezhad, A., Asselin, E., Dixon, D.G., 2010, Journal of Electrochemical Society, 157, C248–C257. Chapter 6 has also been published: Ghahremaninezhad, A., Asselin, E., Dixon, D.G., 2010, Electrochimica Acta, 55, 5041–5056. I have conducted all the testing and written both of the manuscripts. Chapter 9 has been accepted for publication: Ghahremaninezhad, A., Dixon, D.G., Asselin, E., 2012, Hydrometallurgy, 125–126, 42–49.

I have conducted all of the experiments for these publications. I also wrote the manuscripts.

Table of Contents

List of Tables

List of Figures

Acknowledgements

Dedication

This thesis is dedicated to the memory of my late brother Mahmoud Ghahremaninezhad, who passed away on 14 June 2010.

میان آتش و آبم تو رفته ای انگار
به پیش چشم خیالم نشسته ای انگار

گذشتن از تو برایم به تلخی مرگ ست
ز مرز بودن با من گذشته ای انگار

مثال سایه روانم به جان تو پیوست
ز سایه هم به کنارم گسسته ای انگار

تمام دلخوشیم دیدن سرور تو بود
عذاب بیدلی ام دل شکسته ای انگار

خجل شدم چو بدیدم مرام ناب تو را
نه از تبار بشر خود فرشته ای انگار

مرا تو مونس جانی که جان فدایت باد
اگر چه دست خود از من تو شسته ای انگار

میان خواب خوشی در سحر گمان کردم
هنوز بار سفر را نبسته ای انگار

Mahmoud Ghahremaninezhad

1980-2010

I never imagined you'd ever be so far away!

1 Introduction

The major copper producing countries include USA, Canada and Mexico; Chile, Peru and Brazil in South America; Zaire, Zambia, Zimbabwe, South Africa and Namibia in Africa; Papua New Guinea and Australia in Oceania; Russia, Kazakhstan, Japan, Uzbekistan, Philippines, Indonesia, India, Iran and Turkey in Asia; and Poland, Spain, Norway, Sweden and Finland in Europe [Habashi F., 1997]. According to the database of the Australian Bureau of Agricultural and Resource Economics (ABARE), world copper production has shown a progressive increase in the period 1984 to 2008 from 9Mt to 18.5Mt per annum (data for 2009 to 2011 was not available). Above 20% of world copper production is via hydrometallurgy [Watling, 2006]. The market for copper has increased each year while the quantity produced is hardly sufficient to allow all countries to reach developed world levels of usage [Gordon et al., 2006].

There are more than 200 copper-containing minerals whereas only about 20 of them are potentially relevant to copper extraction processes [Habashi F., 1997]. Since copper is a chalcophilic element, i.e. an element that would rather react with sulfur than oxygen, most of its minerals occur as sulfides. Some examples of the most significant copper bearing minerals are chalcopyrite ($CuFeS_2$), bornite (Cu_5FeS_4) and chalcocite (Cu_2S). Chalcopyrite is the world's most abundant copper bearing mineral [Dutrizac, 1978]. Industry standard practice is to treat this mineral via smelting to extract the copper. However, gas emissions from smelters result in soil and air pollution. As an example, a study by Aznar et al. [Aznar et al., 2008] has shown that metal pollution is 5.8 times higher in the vicinity of a smelter than in the 'background' sites. Using Lichens to evaluate the metal pollution in a forest ecosystem around the Murdochville smelter, Canada, Aznar et al. [Aznar et al., 2008] have shown that the forest contamination was detectable up to 30 km from the smelter. The observed enrichment of pollutants was reported to be 2 times higher for 3 metals (i.e. Cu, Cd and Pb) and the highest measured As, Ba, Cd, Cu, and Pb concentrations in lichens were 4, 112, 1, 23, 50 and 952 mg/kg respectively. Elsewhere, Hedberg et al [Hedberg et al., 2005] have shown that the fine particles originating from smelters (Quillota and Linares, two rural sites in vicinity of two smelters in Central Chile) account for more than 72% of the arsenic levels in the vicinity of the smelters. Due to environmental concerns such as these and the

high capital cost of building a smelter, the construction of new smelters in Canada is unlikely. Canada currently operates only a single primary copper smelter (The Horne, Rouyn-Noranda, PQ) which is known to treat mostly custom feed. This represents a strategic problem for a developed country such as Canada that relies heavily on natural resources for economic development. Since smelters are unlikely to be built in Canada, there is a significant opportunity for a hydrometallurgical process implementation in this country.

Hydrometallurgical copper extraction is more attractive from many perspectives such as its ability to deal with a large spectrum of impurities, its applicability to low grade materials, its capability of low capacity operation and, very importantly, low CO_2 and fine particle emissions. Considering the current state of the technology of hydrometallurgical treatment of copper sulfide concentrates, there exist a large number of quite different technologies of which today only very few have commercially been implemented for particular applications. Most of the proposed processes cannot attain sustained commercial production due to facing one or more of the following problems [Dreisinger, 2006]: (1) low copper recovery in the primary leach step; (2) copper co-precipitation with iron hydrolysis products resulting in copper loss; (3) incomplete recovery of precious metals; (4) issues with electrowinning; (5) high acid production due to unsuccessful elemental sulfur recovery; (6) corrosion problems especially in chloride circuits; (7) incomplete fixation of toxic by-products; (8) high energy demand for mixing and oxygen dispersion and finally (9) low quality copper production which requires further processing (electrorefining). Some of the leading technologies for concentrate leaching involve high temperature and pressure leaching steps which suffer from high cost and excess sulfuric acid production. The main problem associated with atmospheric leaching processes is the slow dissolution rate of chalcopyrite due to its passivation (failure to react) [Dutrizac, 1978]. The term "passivation" is widely used for chalcopyrite dissolution in different literature [Viramontes-Gamboa *et al.*, 2007; Velásquez *et al.*, 2005; Mikhlin *et al.*, 2004; Abed and Dreisinger, 2003; Warren *et al.*, 1982; Hackl *et al.*, 1995]. The passive state is defined in Shreir's "Corrosion" book [2000] as:

> *"Passivity is a state of low corrosion rate brought about under a high anodic driving force, or potential, by the presence of an interfacial solid film, usually an oxide. The typical passivating oxide film on many metals is only some*

1-10 nm in thickness, and is produced by oxidation of the surface to a depth measured in monolayers of atoms."

Such passive films (ultra–thin films) would normally be directly detectable by the sensitive surface analysis methods such as X-ray photoelectron spectroscopy (XPS/ESCA), Auger electron microscopy (AES), or secondary ion mass spectroscopy (SIMS) [Marcus and Mansfeld, 2006]. Generally, different in-situ electrochemical techniques (i.e. cyclic voltammetry, potentiodynamic and potentiostatic polarization, chronoamperometry) and ex-situ spectroscopic methods (i.e. XPS, AES, Raman spectroscopy) have been applied to understand the dissolution mechanism of chalcopyrite and furthermore to characterize their surface layers. However, there remain uncertainties about the dissolution process. The trouble with most of the DC electrochemical techniques used so far is that only circumstantial evidence is derivable to help with the elucidation of possible reaction mechanisms. The ex-situ analytical methods are controversial for the case of sulfide minerals due to the possible evaporation of elemental sulfur under experimental conditions [Buckley and Woods, 1994]. Thus, the precise nature of the passive layers is not yet understood. In particular, there are some fundamental questions that should be answered as to the nature of the passive layers and sulfur film that form during leaching.

In the present study we will concentrate on the electrochemical dissolution of chalcopyrite in simple sulfuric acid solution. The ultimate goal of any electrochemical study pertaining to the dissolution of chalcopyrite is to overcome its slow dissolution rate. Clearly, the path to this goal runs through obtaining a comprehensive knowledge on the surface chemistry of chalcopyrite in the desired dissolution environment. Thus, the present work seeks to understand the exact nature of the surface layers (mainly the passive layers) which form at low anodic potential (< 1 V vs. SHE) through their careful characterization to obtain their composition. In order to characterize the surface properties of chalcopyrite electrodes at different anodic potentials and understand the growth sequence of surface layers, we will apply different electrochemical and analytical methods.

In the following chapter (chapter 2) the literature pertaining to this study will be discussed. Chapter 3 will present the objectives of this study. The experimental procedures for the electrochemical and analytical methods will be provided in chapter 4. Chapter 5 discusses the results of electrochemical tests on a pyrrhotite ($Fe_{1-x}S$) electrode, which is a

simplified case of chalcopyrite (CuFeS$_2$) electrochemistry. Chapter 6 presents the results of an electrochemical impedance spectroscopy study on chalcopyrite. The results of XPS and cyclic voltammetry studies on a chalcopyrite electrode will be presented in chapters 7 and 8, respectively. Chapter 9 discusses the kinetics of the ferric/ferrous couple on a passivated chalcopyrite electrode. In chapter 10, a dissolution model for chalcopyrite in 0.5 M sulfuric acid solution is proposed. Finally, chapter 11 presents the conclusions and recommendations for future work in this area.

2 Literature review

2.1 General aspects

2.1.1 Chalcopyrite crystal structure

The crystal structure of chalcopyrite was determined by Burdick and Ellis in 1917 [Burdick and Ellis, 1917]. Chalcopyrite's structure was the first determined crystal structure in USA and in addition, its structure was the first structure of a complex sulfide material to be determined in the World [Donnay et al., 1958]. The crystal structure of chalcopyrite is derived from the zincblende (sphalerite, β–ZnS) structure, in which the two zinc atoms are replaced by copper and iron [Habashi, 1978; Hiskey, 1993]. Figure 2-1 shows the crystal structure of chalcopyrite. Each metal atom is surrounded by sulfur and each sulfur atom by metal in tetrahedral interstices. In this structure, each sulfur atom has bonds with two copper atoms and two iron atoms. The copper and iron atoms have opposite magnetic moments and hence chalcopyrite shows antiferromagnetic property at room temperature [Donnay et al., 1958]. From neutron diffraction studies, the moments of iron and copper in the chalcopyrite structure were found to be 3.85 and 0±0.2 μ_B respectively. The moment of iron atoms, 3.85 μ_B, is lower than that of a typical trivalent iron, 5 μ_B [Greenwood and Whitfield, 1968]. It is worth mentioning that iron atoms in the pyrite structure (FeS_2) have no magnetic moment [Hamajima et al., 1981]. Hence the iron atom in chalcopyrite can be considered neither as Fe^{3+} nor Fe^{2+} and the bonding of Fe atoms is undoubtedly complex. Donnay et al., [Donnay et al., 1958] have suggested that the complex behavior of iron atoms can be explained by postulating further participation of the 3d level electrons of trivalent iron atoms in the covalent bonding. By this, one would expect a decrease in the iron moment (i.e. from 5 to 3.85 μ_B) and at the same time a stronger bond between sulfur atoms and trivalent iron atom.

Considering the above discussion, from the two probable ionic states for chalcopyrite, $Cu^+Fe^{3+}S_2^{2-}$ and $Cu^{2+}Fe^{2+}S_2^{2-}$, the first is the most appropriate. Indeed, the Mossbauer spectra study by Greenwood and Whitfield [Greenwood and Whitfield, 1968] has further confirmed that the best chemical formula for chalcopyrite is $Cu^+Fe^{3+}S_2^{2-}$. In fact, most of the recent workers have considered this structure in their studies [Mikhlin *et al.*, 2004; Boekema

et al., 2004; Córdoba *et al.*, 2008]. The average bond distances for S–S, Fe–S and Cu–S are 0.368, 0.225 and 0.235 nm, respectively [Robie *et al.*, 1967; Hall and Stewart, 1973]. Lattice constants for the unit cell are $a = 5.2988 \pm 0.0010$ and $c = 10.4340 \pm 0.0050$ angstroms [Robie *et al.*, 1967].
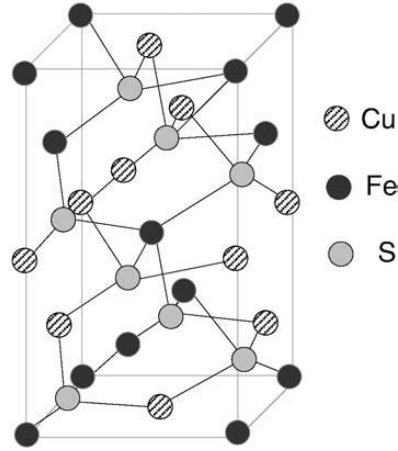
Figure 2-1: Unit-cell crystal structure of CuFeS$_2$ [Córdoba et al., 2008].

2.1.2 Semiconductive properties of chalcopyrite

Results from infra–red studies show an energy gap (E$_g$) of 0.53 eV for natural chalcopyrite specimens [Austin *et al.*, 1956]. For a thin film of evaporated chalcopyrite the band gap energy was determined to be 0.60 eV [Teranishi, 1974]. Due to the antiferromagnetic property of chalcopyrite and its crystal structure, it is very difficult to precisely compute the energy bands for chalcopyrite. However, studies on Fe-doped CuAlS$_2$ and CuGaS$_2$ materials provided evidence that the valence band edge is made up of Cu 3d and S 3p orbits and the conduction band is mainly Fe 3d in character [Shuey, 1975]. Figure 2-2 shows the schematic energy band diagram for an n-type chalcopyrite sample.
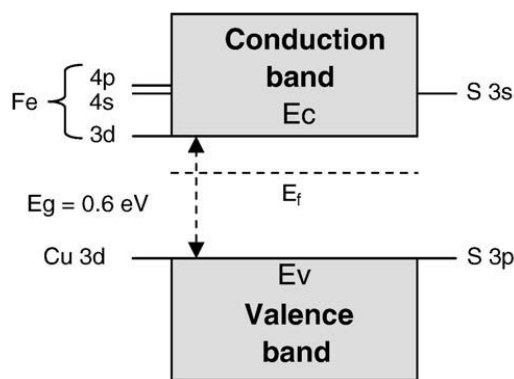
Figure 2-2: Schematic energy band diagram for chalcopyrite CuFeS$_2$ [Córdoba et al., 2008].

Conduction of semiconductor materials is related to the movement of mobile charge carriers; namely, free electrons of the normally empty conduction band or holes of the normally full valence band. Charge carriers in solid materials may be derived from: (a) non–stoichiometry; (b) impurity defects; (c) thermal excitation [Rockett, 2008]. The main donor in chalcopyrite is a metal interstitial. The conduction band carrier density for large natural single crystal chalcopyrite specimen at room temperature is calculated to be 10^{25} m^{-3} [Teranishi, 1961]. For a polycrystalline sample it is shown that the charge carrier density is around 4×10^{25} m^{-3} [Donovan and Reichenbaum, 1958]. Some of the material properties of chalcopyrite, extracted from Hiskey's work [Hiskey, 1993] are summarized in Table 2-1. Electrical studies show that chalcopyrite clearly has properties of a good semiconductor material and, with only a few exceptions chalcopyrite demonstrates an n–type semiconductor behavior. Note that the general semiconductor type on chalcopyrite strongly depends on the impurities of the mineral. Electrons show less mobility rather than holes in natural chalcopyrite samples [Tell *et al.*, 1972]. Since chalcopyrite is a semiconductor material, it is worth having a brief discussion of the dissolution of semiconductor materials.

2.2 Dissolution of semiconductor materials

In order to understand the properties of semiconductor electrodes, and their differences from those of metallic electrodes, one should understand the electronic structures of semiconductors and be familiar with the concept of energy bands in solids. Figure 2-3 shows the generation of a band model in solids from atomic orbitals of isolated atoms [Bard and Faulkner, 2001].

Table 2-1: Materials properties of CuFeS$_2$ at room temperature [Hiskey, 1993].

Structure	Tetragonal
Ionic structure	$Cu^+Fe^{3+}S_2^{2-}$
Density (g cm^{-3})	4.0878
Hardness, Moh	3.5 – 4
Cleavage surface	(011)
C_p^o (J mol^{-1} K^{-1}) 298 – 830 K	$88.71 + 5.19 \times 10^{-2}T - 7.45 \times 10^5 T^{-2}$
ΔG_f^o (kJ mol^{-1})	-173.4
ΔH_f^o (kJ mol^{-1})	-173.3
α-CuFeS$_2$ (tetragonal) → β-CuFeS$_2$ (cubic)	550 °C
Energy gap at room temperature (eV)	0.60
Thermo electric power (μVK^{-1})	480
Resistivity (Ωm)	$2 \times 10^{-4} - 3 \times 10^{-1}$
Carrier density (m^{-3})	$10^{25} - 4 \times 10^{25}$
Electron mobility (cm^{2}V^{-1}s^{-1})	18
Hole mobility (cm^{2}V^{-1}s^{-1})	21
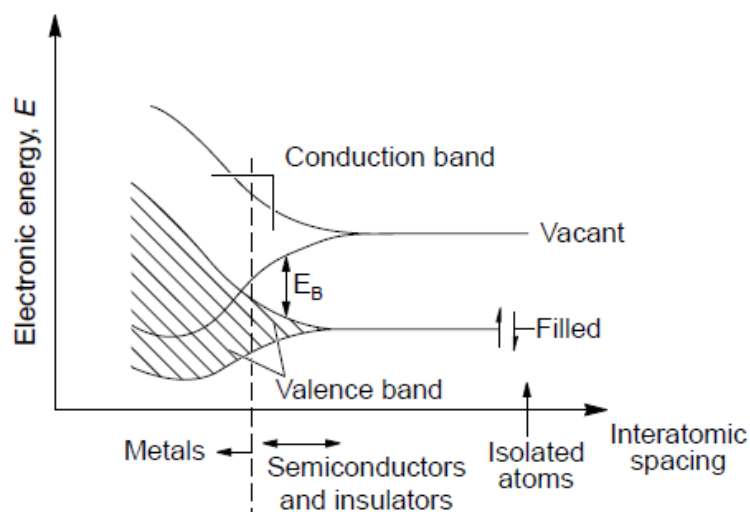
Figure 2-3: Band model in solids [Bard and Faulkner, 2001].

The highest and lowest energy levels of a band are referred to as the band edges. The energy bands of interest are the highest occupied (called the valence band) and the lowest unoccupied (called the conduction) bands (Figure 2-3). It is the energy gap (the band gap) between these bands (i.e., the difference in energy between the upper edge of the valence band and the lower edge of the conduction band, E_B) that determines the properties of the material [Yacobi, 2004]. A solid state material is considered as an electrically conductive material if the electrons occupy partially filled orbitals. In other words, for conductivity, electrons should occupy the conduction band (lowest unoccupied band). For metals, the conduction and valence bands overlap, and so, the conduction band can be readily occupied (Figure 2-3). For insulators, the band gap is sufficiently large that electrons cannot be promoted from the valence band to the conduction band (typically above 4 eV). However, for semiconductors, the band gap is not as large (below 4 eV), and electrons can be moved into the conduction band. The promotion of electrons from valence band to the conduction band leaves positively charged vacancies in the valence band, which is referred to as a hole. This is shown in the schematic of Figure 2-4. In this figure, the dark dots represent electrons while holes are represented by the plus sign. These holes can be moved through space by the transfer of an electron to the vacancy; therefore, holes are considered to be mobile [Yacobi, 2004; Rockett, 2008].
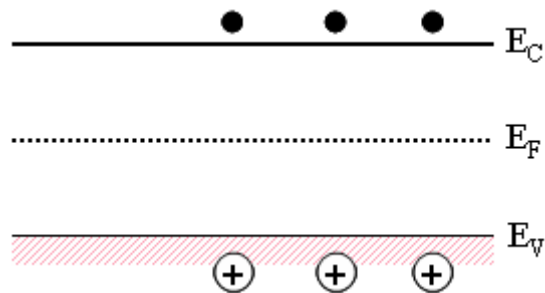
Figure 2-4: Schematic diagram of the energy levels of a semiconductor.

The promotion of electrons from the valence band to the conduction band is possible either thermally or photochemically; however, there is another method for generating charge carriers (i.e., electrons or holes) within a semiconductor, referred to as doping. Doping is the addition of a different element(s) into the semiconductor. The simplest example of this process involves the doping of a group V element (e.g., P) or a group III element (e.g., Al)

into a group IV element (e.g., Si), as presented in Figure 2-5. For instance, the doping of phosphorous (P) into Si semiconductors introduces occupied energy levels into the band gap close to the lower edge of the conduction band, thereby allowing facile promotion of electrons from the valance band into the conduction band. Thus the addition of aluminum (Al) into Si introduces vacant energy levels into the band gap close to the upper edge of the valence band, which allows facile promotion of electrons from the valence band by formation of holes in the valence band. Doped semiconductors in which the dominant (or majority) charge carriers are electrons are referred to as *n-type* semiconductors, whereas those in which holes are the majority charge carriers are referred to as *p-type* semiconductors. Un-doped semiconductors are referred to as intrinsic semiconductors [Yacobi, 2004; Rockett, 2008].
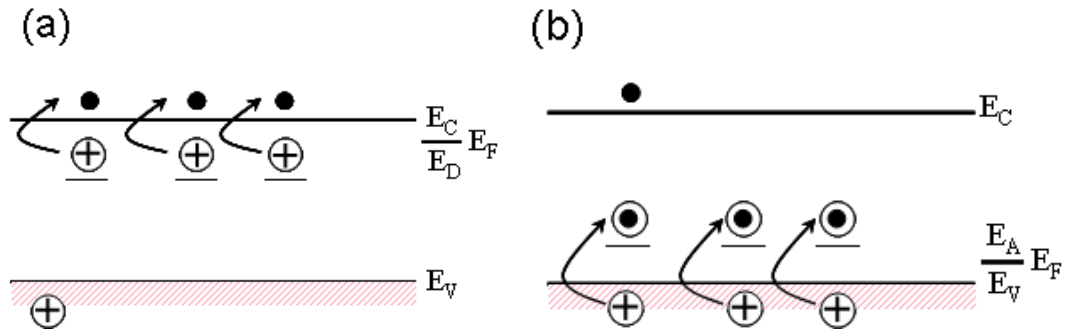
Figure 2-5: Schematic diagram of the energy levels of (a) an *n-type* semiconductor and (b) a *p-type* semiconductor.

An important concept in the study of solid state materials is the Fermi level. The Fermi level is the level of energy which is occupied by an electron with a probability of 0.5. For example, as shown in Figure 2-4, for an intrinsic (un-doped) semiconductor the Fermi level lies at the mid-point of the band gap. Doping changes the distribution of electrons within the solid, and hence changes the Fermi level. For instance, in an *n-type* semiconductor the Fermi level lies closer to the conduction band (Figure 2-5a), whereas for *p-type* semiconductors it lies closer to the valence band (Figure 2-5b). It should be mentioned that the Fermi level of a semiconductor electrode changes with applied potential, just as it does in metal electrodes; for example, moving to more negative potentials will raise the Fermi level [Morrison, 1980].

2.2.1 Semiconductor-electrolyte interface

Generally, in electrochemical science, the understanding of reactions and phenomena at the interface between electrode and electrolyte is important. In order for the two separate phases to be thermodynamically in equilibrium, their electrochemical potential must be the same. The electrochemical potential of the solution is determined by the redox potential of the electrolyte solution, and the electrochemical potential of the semiconductor is determined by the Fermi level. If the redox potential of the solution and the Fermi level do not lie at the same energy, then charges will be exchanged between the semiconductor and the solution in order to equilibrate the two phases [Memming, 2001]. In contrast to metals, the carrier density in a semiconductor is much smaller. Therefore, in a semiconductor electrode the charge in the solid is distributed over a certain distance below the electrode surface. This region, with a thickness of 100-10,000 Å, is called the "space charge region", and has an associated electrical field. The resulting potential and charge distribution is shown in Figure 2-6 (considering an electrolyte with a high ion concentration so that the diffuse layer on the solution side is neglected). Hence, in the case of semiconductors, there are two double layers to consider: the interfacial (electrode/electrolyte) double layer and the space charge layer [Morrison, 1980; Memming, 2001].
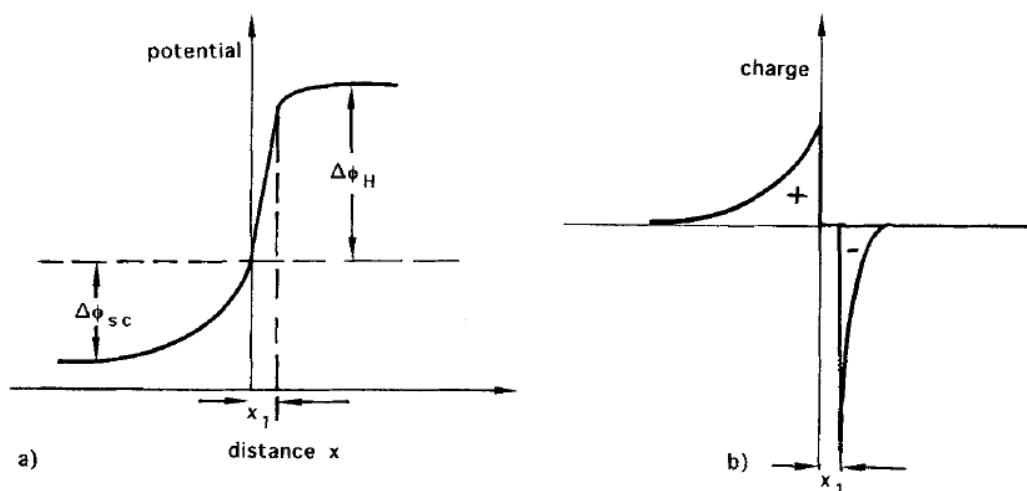
Figure 2-6: Potential (a) and charge (b) distribution at the semiconductor(left side)/electrolyte(right side) interface. Note that a high ion concentration for solution is assumed hence the diffuse layer on the solution side is neglected [Memming, 2001].

Considering the contact between an *n-type* semiconductor electrode and an electrolyte at open circuit, the Fermi level (electrochemical potential of the semiconductor) is typically higher than the redox potential of the electrolyte, and hence electrons will be transferred from the semiconductor electrode into the solution. Therefore, the space charge region will have positive charge and the band edge will be bent upward. Since the majority charge carrier of the semiconductor has been removed from the space charge region, this region is also referred to as a "depletion layer". In the case of a *p-type* semiconductor, the Fermi layer is generally lower than the redox potential. Hence, in order to have equilibrium at the interface, electrons must transfer from the solution to the electrode. This generates a negative charge in the space charge region, which causes a downward bending in the band edges. Since the holes in the space charge region are removed by this process, this region is again a depletion layer [Morrison, 1980; Memming, 2001].

As for metallic electrodes, the Fermi level of a semiconductor is a function of the applied potential. The band edges in the interior of the semiconductor (i.e., away from the depletion region) also vary with the applied potential in the same way as the Fermi level. However, the energies of the band edges at the interface are not affected by changes in the applied potential. Therefore, going from the interior of the semiconductor to the interface, the energies of the band edges varies with the applied potential. There are three different scenarios to be considered [Morrison, 1980; Memming, 2001]:

(a) The Fermi energy level of the semiconductor lies at an energy equal to the solution redox potential. In this case, there is no net transfer of charge, and hence there is no band bending. This potential is therefore referred to as the "flat band potential", E_{fb}.

(b) Depletion regions arise at potentials positive of the flat band potential for an *n-type* semiconductor and at potentials negative of the flat band potential for a *p-type* semiconductor.

(c) In the case of an *n-type* semiconductor at potentials negative of the flat band potential there is an excess of the electrons (majority charge carrier) in this space charge region, and so the region is referred to as an "accumulation" region. For *p-type* semiconductors an accumulation region arises at potentials more positive than the flat band potential.

It is important to note that having an accumulation layer or a depletion layer determines the charge transfer ability of a semiconductor electrode. If there is an

accumulation layer, the semiconductor electrode will behave similarly to a metallic electrode, since there is an excess of the majority charge carrier available for charge transfer. In contrast, if there is a depletion layer, then there are few available charge carriers, and electron transfer reactions will occur slowly.

2.2.2 Mott-Schottky equation

There are a few different experiments for measuring the various parameters of semiconductors. As an example, by applying different radiation intensity to a semiconductor electrode and measuring the photo-potential, it is possible to determine the flat band potential of the semiconductor. The simplest method is to measure the open-circuit potential (photo-potential) of the electrochemical cell as a function of irradiation intensity. Another important method for studying semiconductors is measuring the apparent capacitance of the surface of the semiconductor as a function of potential under depletion conditions and this approach is based on the Mott-Schottky relationship [Morrison, 1980; Memming, 2001]. The potential and charge distribution within the space charge region is quantitatively described by the Poisson equation as given by:

$$\frac{d^2 \Delta \phi_{SC}}{dx^2} = \frac{-1}{\varepsilon \varepsilon_0} \rho(x) \qquad \qquad \text{2-1}$$

in which the charge density is given by

$$\rho(x) = e[N_d - N_a - n(x) + p(x)] \qquad \qquad \text{2-2}$$

here, x is the distance from the surface and N_d and N_a, are the fixed ionized donor and acceptor densities, respectively, which are given by the doping of the semiconductor. The ε is the dielectric constant of the medium and ε_o is the permittivity of free space. The electron and hole densities, $n(x)$ and $p(x)$, vary with the distance x according to:

$$n(x) = n_o \exp\left(-\frac{e\Delta\phi_{SC}(x)}{kT}\right) \qquad \qquad \text{2-3}$$

$$p(x) = p_o \exp\left(\frac{e\Delta\phi_{SC}(x)}{kT}\right) \qquad \qquad \text{2-4}$$

Considering the charge neutrality in the bulk of the semiconductor material, then we have,

$$N_d - N_a = n_o - p_o$$ 2-5

Inserting of Eqs. 2-2, 2-3, 2-4 and 2.5 into the Eq. 2-1 then one can obtain:

$$\frac{d^2 \Delta \phi_{SC}}{dx^2} = \frac{e}{\varepsilon \varepsilon_o} \left[n_o - p_o - n_o \exp\left(-\frac{e \Delta \phi_{SC}(x)}{kT} \right) + p_o \exp\left(\frac{e \Delta \phi_{SC}(x)}{kT} \right) \right]$$ 2-6

After integration of Eq. 2-6 the electric field at the surface (E_s) can be derived as given by

$$E_s = \frac{d \Delta \phi_{SC}}{dx}\Big|_{x=0} = \left(\frac{kT}{e L_D} \right)^2 \left\{ \frac{P_o}{n_i} \left[\exp\left(\frac{e \Delta \phi_{SC}}{kT} \right) - 1 \right] + \frac{n_o}{n_i} \left[-\exp\left(\frac{e \Delta \phi_{SC}}{kT} - 1 \right) \right] \right\}$$ 2-7

where, n_i is the intrinsic carrier density which is determined by the equilibrium equation, $n_o p_o = n_i^2$. The term L_D is the so-called *Debye length* as given by,

$$L_D = \left(\frac{\varepsilon \varepsilon_o kT}{2 n_i e^2} \right)^{1/2}$$ 2-8

Furthermore, it is possible to determine the required space charge for producing the field E_s by Gauss' law,

$$Q_{SC} = \varepsilon \varepsilon_o E_S$$ 2-9

The differential capacity of the space charge layer is defined by

$$C_{SC} = \frac{dQ_{SC}}{d(\Delta \phi_{SC})}$$ 2-10

Inserting Eqs. 2-7 and 2-8 into 2-10 and differentiation, then we will have,

$$C_{SC} = \frac{\varepsilon \varepsilon_o}{L_D} \cosh\left(\frac{e \Delta Q_{SC}}{kT} \right)$$ 2-11

This equation shows the strong relationship between the space charge capacity (C_{SC}) and potential across the space charge layer. Rearranging the equation we will have the famous Mott-Schottky relationship [Memming, 2001],

$$\frac{1}{C_{SC}^2} = \left(\frac{2L_{D.eff}}{\varepsilon\varepsilon_o}\right)^2 \left(\frac{e\Delta\phi_{SC}}{kT} - 1\right)$$ 2-12

where,

$$L_{D.eff} = \left(\frac{\varepsilon\varepsilon_o kT}{2n_i e^2}\right)^{\frac{1}{2}}$$; C_{sc} is the capacitance of the space charge region, ε is the dielectric

constant of the semiconductor and ε_o is the permittivity of free space. In equation 12-2, $\Delta\phi_{SC} = E - E_{fb}$ and in here E represents applied potential and E_{fb} presents flat band potential. Making the equation simpler, then we will have [Morrison, 1980],

$$\frac{1}{C_{SC}^2} = \frac{2}{e\varepsilon\varepsilon_o n_o}\left(E - E_{fb} - \frac{kT}{e}\right)$$ 2-13

Equation 2-13 predicts a linear relation between $1/C^2$ and applied potential (E) in the depletion region. A classical example of a Mott-Schottky experiment on an *n-type* and a *p-type* silicon electrode has been presented by Schmuki et al. [Schmuki *et al.*, 1995]. The donor density can be calculated from the slope of the Mott-Schottky plots ($1/C^2$ *vs. E*), and the flat band potential can be determined by extrapolation to $C = 0$. The capacitance values are calculated from electrochemical impedance spectroscopy (EIS) measurements. In the case of a semiconductor electrode, there are two capacitances to be considered, that of the space charge region and that of the double layer. These two capacitances are in series and as a result, the total capacitance is the sum of their reciprocal. The capacitance for the space charge region is much smaller than that of the double layer (2-3 orders of magnitude) such that the double layer capacitance can be practically neglected in calculations. Therefore, the measured capacitance value is equal to the space charge capacitance. Through EIS experiments the capacitance can then be calculated from the imaginary component of the impedance (Z") using the relationship $Z'' = 1/2\pi fC$.

2.2.3 Current-potential curves for semiconductors

The application of a potential between a semiconductor electrode and a counter electrode in an electrolyte leads to a current flux between the two electrodes. Since the charge transfer across a semiconductor/electrolyte interface can only occur via the

conduction or valence band, the processes in the two bands have to be treated separately. In general anodic and cathodic currents are given by equations similar to those for metallic electrodes, but with some corrections (using boundary conditions which are specific for semiconductors) in the generation of the relationships [Memming, 2001]. For an *n-type* semiconductor in the accumulation region, electrons accumulate at the surface and a cathodic current can flow. At high anodic potentials, holes accumulate in the surface region and an anodic current can flow. For a *p-type* semiconductor in the accumulation region an anodic current is observed. In the depletion region current cannot flow, and in the degeneration region a cathodic current can flow [Plieth, 2008]. This is shown in the schematic current–potential curve in Figure 2-7.
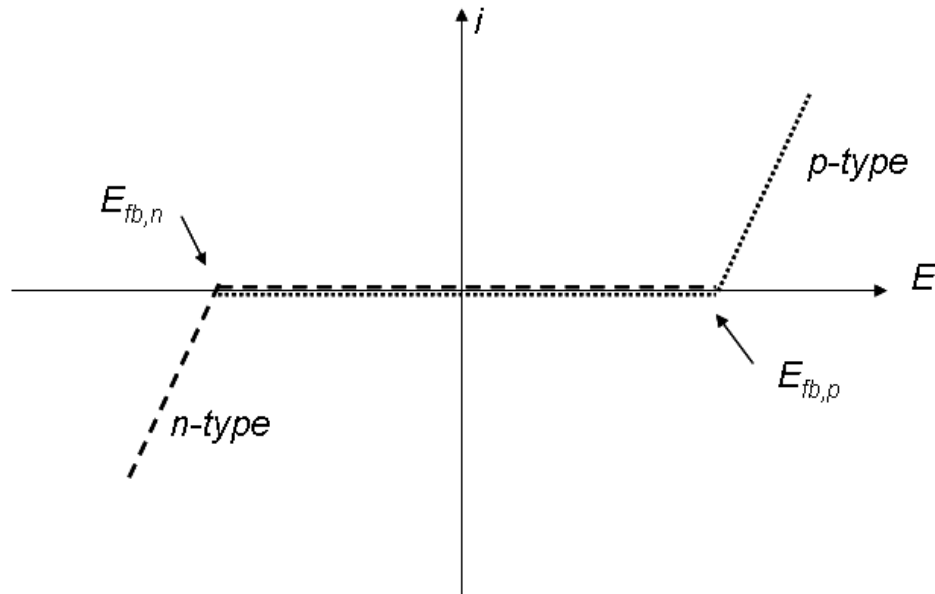
Figure 2-7: Schematic current–potential curve for *n-type* and *p-type* semiconductors.

The charge transfer on a metallic electrode depends on the overlap between occupied and unoccupied energy levels in the metal and electrolyte. This can be found around the Fermi level. However, in the case of a semiconductor electrode in contact with electrolyte, the redox system can overlap with both conduction and valence bands. Depending on the redox system and electrode potential, charge transfer is possible between the conduction band and redox system and between the valence band and redox system [Memming, 2001; Plieth, 2008]. If the density of electrons in the conduction band on the surface of the

semiconductor electrode is n_s and the density of unoccupied energy levels in the electrolyte is D_{ox}, then the partial current density of conduction band reduction is

$$j_{c,c} = k_{c,c} \int_{-\infty}^{+\infty} n_S D_{ox} dE \qquad\qquad 2\text{-}14$$

Otherwise, the anodic conduction band current is proportional to the density of occupied states in the electrolyte D_{red} times the density of states in the conduction band;

$$j_{c,a} = k_{c,a} \int_{-\infty}^{+\infty} N_C D_{red} dE \qquad\qquad 2\text{-}15$$

Similarly, it is possible to formulate the anodic valence band process with p_s denoting the surface density of holes in the valence band

$$j_{v,a} = k_{v,a} \int_{-\infty}^{+\infty} D_{red} p_s dE \qquad\qquad 2\text{-}16$$

For the cathodic valence band process also, with N_{vb}, the density of energy levels in the valence band, we have

$$j_{v,c} = k_{v,c} \int_{-\infty}^{+\infty} D_{ox} N_v dE \qquad\qquad 2\text{-}17$$

In a first approximation D_{red}, D_{ox}, N_c, and N_v are independent of the potential. The surface density of electrons in the conduction band and the surface density of holes in the valence band, n_s and p_s, depend exponentially on the potential. The current density at the flat band potential can be used as a reference point. In this approximation one obtains [Plieth, 2008],

$$i_{c,c} = i_{c,o} \exp\left(-\frac{F}{RT}\left(E - E_{fb}\right)\right), \qquad \text{and} \qquad i_{c,a} = const \qquad\qquad 2\text{-}18$$

and

$$i_{v,a} = i_{v,o} \exp\left(+\frac{F}{RT}\left(E - E_{fb}\right)\right), \qquad \text{and} \qquad i_{v,c} = const \qquad\qquad 2\text{-}19$$

This behavior is schematically represented in Figure 2-7. The slope of the rise of the current in the accumulation region in Figure 2-7, often differs from the 59 mV expected according to Eqs. 2.18 and 2.19. Otherwise, in the accumulation region the semiconductor

electrodes approach metal-like properties and the classical theory of electron transfer must be applied [Plieth, 2008].

2.3 Chalcopyrite dissolution and electrochemistry

Electrochemical investigations can build valuable insight about the characterization of leaching mechanisms and rate–determining steps for chalcopyrite. Generally the anodic dissolution of chalcopyrite reveals two distinct regions, namely, low potential processes (up to 0.8 V vs. SHE), and high potential processes (1.0 to 1.2 V vs. SHE). The low potential region is characterized by "passive" behavior which shows progressively thickening surface films. Since this potential region is the typical oxidation potential range employed in hydrometallurgy, the reactions in this potential region are very important. In the high potential region (1.0 to 1.2 V vs. SHE) substantial oxidation of chalcopyrite occurs [Hiskey, 1993]. The Pourbaix diagram for the $CuFeS_2$-H_2O system [Garrels and Christ, 1965] suggests that the acidic dissolution (25 ºC and 1 atm of total pressure) of chalcopyrite is thermodynamically possible at pH values lower than 6 and oxidation potentials higher than 0.2 V vs. SHE [Garrels and Christ, 1965]. Additionally, the Pourbaix diagram of chalcopyrite suggests that the dissolution process of chalcopyrite occurs through a solid transformation in different intermediate sulfides (Cu_5FeS_4, CuS, Cu_2S), increasingly richer in copper content [Biswas and Davenport, 1976]. In order to study the electrochemical behavior of chalcopyrite in different solutions, various electrochemical techniques have been used previously. In the next section, we will discuss the electrochemical dissolution of chalcopyrite based on the applied electrochemical technique.

2.3.1 Polarization studies

Potentiodynamic polarization studies on natural chalcopyrite samples in 1M H_2SO_4 indicate passive–like behavior during anodic polarization. Figure 2-8 shows the anodic polarization curves for $CuFeS_2$ from 6 different mines in 1 M H_2SO_4 [Warren *et al.*, 1982]. As presented in this figure, the corrosion potential, passive current density and transpassive potential of chalcopyrite depends on the origin of the mineral, i.e. the chemical composition of mineral. It has been suggested by these workers that the impurities present in the mineral play a significant role in the dissolution behavior of the electrode. From potentiodynamic

studies, Warren et al [Warren *et al.*, 1982] have suggested that during the anodic polarization two distinct intermediate layers form on the surface. Additionally, it was concluded that the second surface film forms by decomposition of the first film. In this study, it was suggested that the first surface layer might be bornite (Cu_5FeS_4), which forms due to selective dissolution of iron atoms from chalcopyrite structure, and the second layer was suggested to be covellite (CuS). Thermodynamic predictions from the system's Pourbaix diagram were the origin for these phase choices. [Warren *et al.*, 1982].
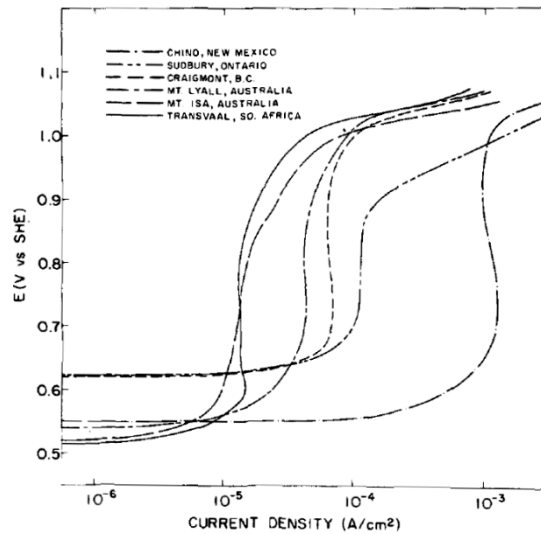
Figure 2-8: Anodic polarization curves for CuFeS$_2$ from 6 different locations in 1 M H$_2$SO$_4$, 30 mV min^{-1}, 25°C [Warren *et al.*, 1982].

Studies by Viramontes-Gamboa et al. [2006] have demonstrated that many of the uncertainties associated with potentiodynamic anodic polarizations of chalcopyrite samples are due to the fast scanning rates of the tests and that these will disappear if the potentiostatic method, effectively a very slow scan rate, is applied. Thus the scan rate should be slow enough to detect the effects of the passive layer [Viramontes-Gamboa *et al.*, 2006]. Potentiostatic anodic polarization studies from the same group relating to the oxidation of bulk chalcopyrite electrodes in H_2O–H_2SO_4–$Fe_2(SO_4)_3$–$FeSO_4$ media (the acid concentration varies from 2 to 100 gL^{-1} and temperature from 25 to 80°C) have demonstrated that chalcopyrite oxidation displays the classic active–passive behavior of passivating metals [Viramontes-Gamboa *et al.*, 2007]. As shown in Figure 2-9, the passivation potential is a function of temperature. These workers have claimed that increasing temperature increases

the transpassive potential of chalcopyrite. It has also been stated that the time required for passivation of chalcopyrite ranges roughly from 4 to 24 h, which means that the formation of the passive layer is a very slow process at chalcopyrite electrodes.
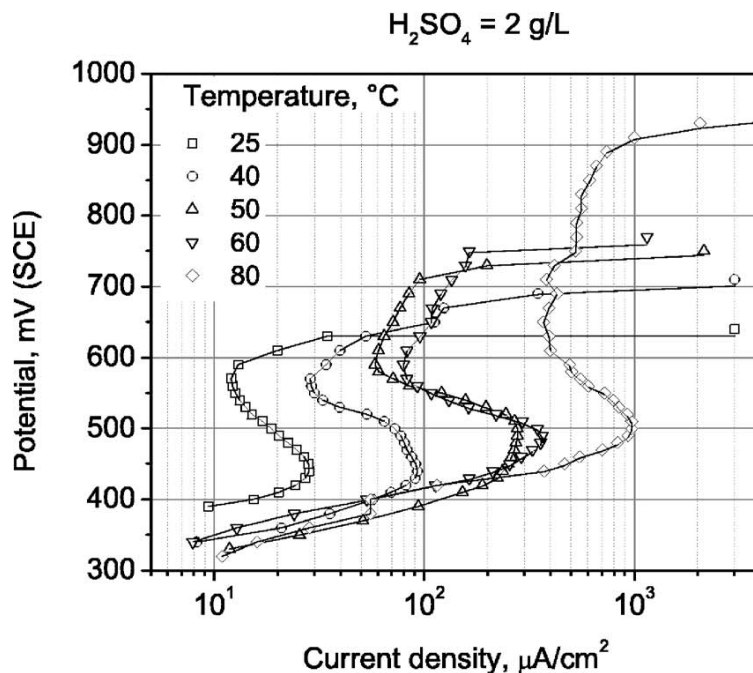
Figure 2-9: Potentiostatic anodic polarizations of chalcopyrite, 10 mV hr^{-1} [Viramontes-Gamboa *et al.*, 2007].

In a very recent study [Vasquez *et al.*, 2012] on the electrochemical response of chalcopyrite microelectrodes in 90 g/l sulfuric acid solution, it has been shown that the transpassive potential of chalcopyrite decreases with increased temperature. This apparent discrepancy with previous findings [Viramontes-Gamboa *et al.*, 2006] has been attributed to the use of micro-particles (ranging between 20 – 100 μm) instead of bulk chalcopyrite (Figure 2-10).
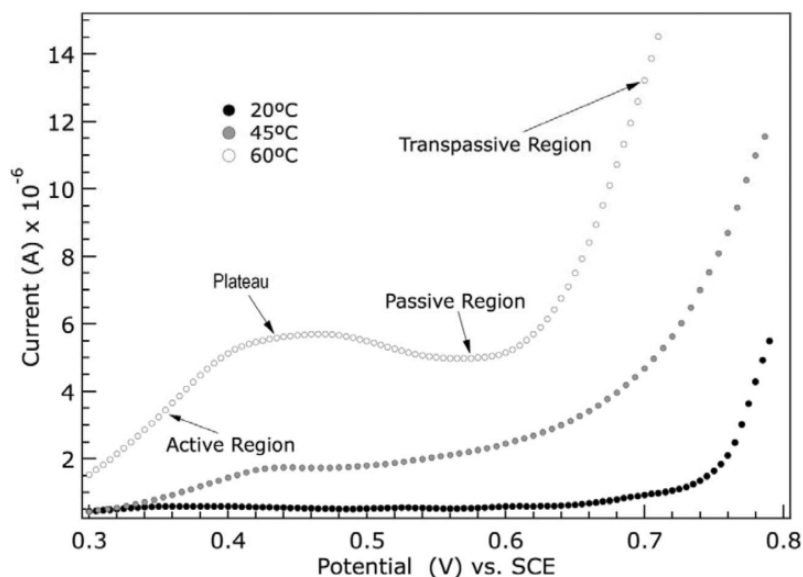
Figure 2-10: Anodic oxidative behavior of chalcopyrite microparticles at 20, 45 and 60°C and 90 g/L of H₂SO₄ [Vasquez *et al.*, 2012].

Generally, all of the polarization work by different researchers has demonstrated active–passive behavior for chalcopyrite in acidic media during the dissolution process.

2.3.2 Chronoamperometry studies

Current *vs.* time behavior of chalcopyrite at a constant anodic potential has been studied by several researchers. Studies by Biegler and Swift [1979] showed critical potentials of 1.01 V and 1.13 V *vs.* SHE for the dissolution of chalcopyrite in 1 M H_2SO_4 and 1 M HCl solutions, respectively, below which potentials the current always decays with time and above which, a minimum current value is registered (Figure 2-11). By increasing the dissolution potential the minimum current value appears after a shorter time. Biegler and Swift considered that the dissolution of the chalcopyrite occurs at localized sites, and the number of sites varies with potential. Also, the potentiostatic current–time curves were interpreted in terms of the kinetics of nucleation of dissolution centers, their 3D growth, and finally overlapping of the dissolution centers. Raising the potential increased the number of corrosion sites dramatically. In the case of the hemispherical growth of pits, the current should increase with t^2, which is seen in Figure 2-11b. The dissolution potentiostatic current transient is more complex in Figure 2-11a. The presence of the second minimum is related to the overlapping of separate growth centers in a surface process [Biegler and Swift, 1979].
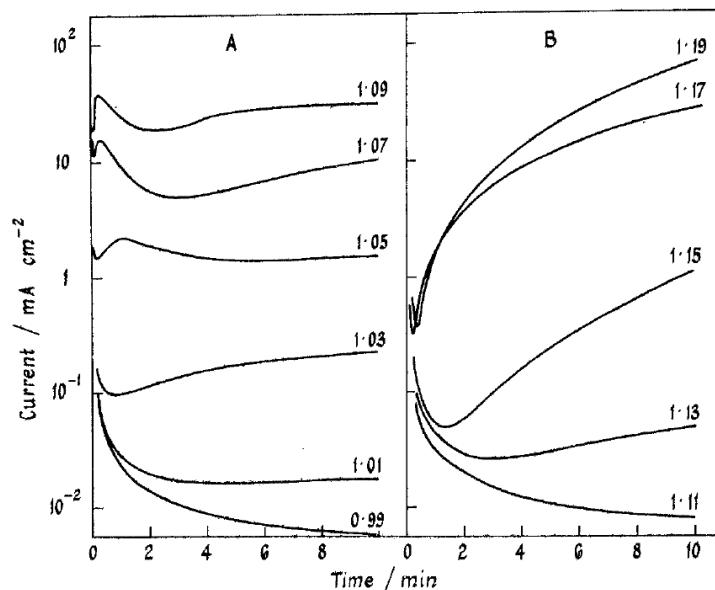
Figure 2-11: Current-time curves for a chalcopyrite electrode at the potentials (*vs.* SHE) indicated in (a) 1 M H_2SO_4, (b) 1 M HCl [Biegler and Swift, 1979].

Another study considers the current-time transient behavior of a freshly polished chalcopyrite electrode in 0.3 M HCl and 0.3 M H_2SO_4 solutions over the temperature range of 25 to 90°C [McMillan et al., 1982]. Results show an initial capacitance charging current followed by a faradaic reaction for which the current decays with time for an overpotential range of 20 to 600 mV *vs.* SHE. For the current transient at potentials higher than 600 mV (less than 1 V) there is no longer a decay of current by time. These results are similar to those obtained by Biegler and Swift [1979]. McMillan *et al.* [1982] have also suggested the formation of an iron deficient copper sulfide species (similar to the surface layer proposed by Warren *et al.* [1982]) on the surface which acts as an interphase between the electrode and the electrolyte; this layer has characteristics of a solid electrolyte which is electronically insulating but can transfer the ionic species from the chalcopyrite to the electrolyte [McMillan *et al.*, 1982]. In another study, the current decay measurements for a chalcopyrite electrode at constant potential in 1 M H_2SO_4 solution adhered to the Sato-Cohen (logarithmic) model for solid film formation [Warren *et al.*, 1982]. In the low potential passive region (approximately < 0.79 V *vs.* SHE) current and mass balance measurements support the formation of two intermediate sulfide phases in the sequence $CuFeS_2 \rightarrow S_1 \rightarrow S_2$. At higher potentials (> 1.0 V), in the transpassive region, the observed increase in current is

compatible with the decomposition of water to form chemisorbed oxygen which releases copper and forms sulfate ions [Warren *et al.*, 1982].

Previously, results of a study on the anodic oxidation of galena in acidic electrolyte showed that "surface relaxation" occurs on the metal–deficient products of the surface, with lead diffusing from the bulk of the mineral to the metal–deficient surface [Buckley and Woods, 1996]. The same process has been detected with carbon paste chalcopyrite electrodes in 1 M H_2SO_4 electrolyte. The chalcopyrite electrode has been oxidized at 800 mV *vs.* SHE for 120 s and then allowed to rest at its open circuit potential for different time durations, and afterward, the 800 mV reapplied. As shown in Figure 2-12, the resulting current transients reveal the dependence of the current on the rest time of the electrode. This behavior provides further evidence that the passive layer of chalcopyrite is a metal-deficient surface layer and not elemental sulfur. A longer rest time results in more copper and iron diffusion from the bulk electrode to the surface, and thus, the re–oxidation process of chalcopyrite occurs at a much more rapid rate [Lu *et al.*, 2000].
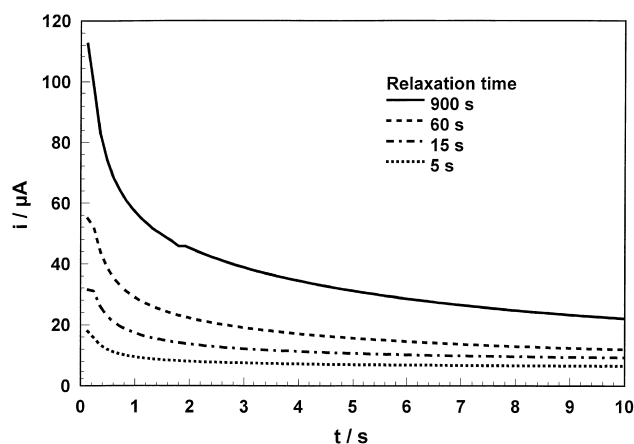
Figure 2-12: Current–time curves representing the re-oxidation of chalcopyrite at 800 mV *vs.* SHE [Lu *et al.*, 2000].

2.3.3 Electrochemical impedance spectroscopy (EIS) studies

The electrochemical impedance spectroscopy (EIS) method provides a kinetic model in the form of an equivalent circuit. One can attribute a clear physical meaning to each of the parameters (circuit elements) of the model. Moreover, EIS is a powerful technique for surface layer studies that can be used to study the layers formed on the surface of a chalcopyrite electrode. EIS has almost been disregarded for chalcopyrite studies despite the

fact that it presents a powerful way of analyzing surface processes. The number of published papers in reputable journals which have studied the anodic dissolution of chalcopyrite electrodes by EIS is fewer than ten. This is partially due to the complexity of the EIS responses of chalcopyrite electrodes which make the analysis and modeling of the electrode processes difficult. Velasquez *et al.* [1998] were the first group to have studied chalcopyrite dissolution by EIS. Their studies focused on the dissolution of natural chalcopyrite samples from the "El Teniente" mine, Chile, in an alkaline solution (pH 9.2) for different oxidation potentials. They concluded that for potentials lower than 0.4 V *vs.* SCE (0.642 *vs.* SHE) a Randles equivalent circuit can be used and for potentials higher than 0.4 V *vs.* SCE (0.642 *vs.* SHE) a layer model had to be applied. The Randles equivalent circuit is a circuit that consists of an active electrolyte resistance (R_S) in series with the parallel combination of the double-layer capacitance (C_{dl}) and an impedance of a faradaic reaction. The detected layers in the high potential region, $E > 0.642$ *vs.* SHE, are suggested to be an inner layer of CuO and outer layer of Fe_2O_3 [Velasquez *et al.*, 1998].

Another EIS study has been done by Hiroyoshi *et al.* [2004] on the effect of cupric and ferrous on the active-passive behavior of natural chalcopyrite in 0.1 M H_2SO_4 solution (with or without cupric and/or ferrous ions). The results indicated that the coexistence of cupric and ferrous ions promote the anodic dissolution current at low anodic potentials (< 0.65 V *vs.* SHE). It has also been shown that the coexistence of cupric and ferrous ions causes the formation of a product layer on the electrode surface which inhibits the growth of a high resistance passive layer – typically a high resistance passive layer forms on the surface in the case of simple sulfuric acid solutions without cupric and ferrous ions. Figure 2-13a shows the impedance plots for a chalcopyrite electrode with or without the ferrous and the cupric ion (not coexistence of cupric and ferrous ions) and Figure 2-13b shows the effect of the coexistence of cupric and ferrous [Hiroyoshi *et al.*, 2004].
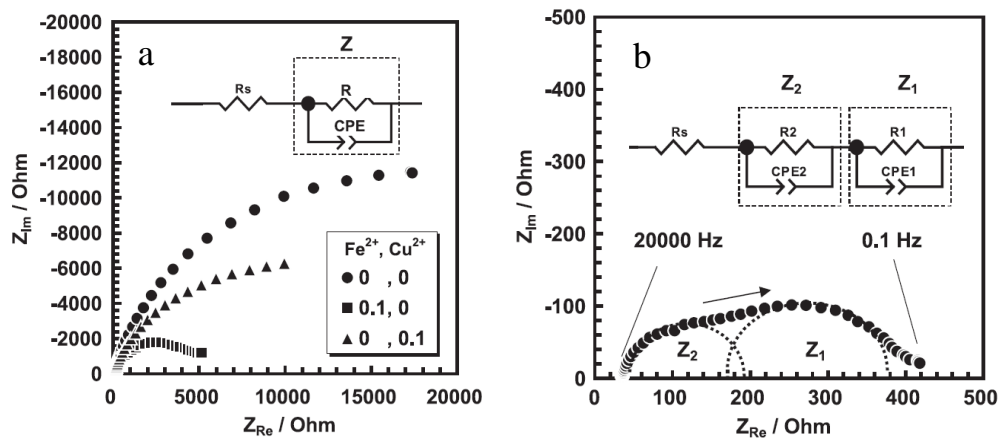
Figure 2-13: Impedance plots for the chalcopyrite electrode; (a) with or without the ferrous and the cupric ion, (b) coexisting of ferrous and the cupric ion, at 0.65 V *vs.* SHE [Hiroyoshi *et al.*, 2004].

From the analysis of the EIS results Hiroyoshi *et al.* have proposed that in the case of the coexistence of cupric and ferrous ions in solution, a chalcocite film (Cu_2S) might form on the surface of the electrode which inhibits the formation of a typical passive film on the surface. The model proposed by these workers has the following reaction scheme [Hiroyoshi *et al.*, 2004]:

$$CuFeS_2 + 2Cu^{2+} + 3Fe^{2+} = 2Cu_2S + 4Fe^{3+} \qquad \text{2-20}$$

$$Cu_2S + 4Fe^{3+} = 2Cu^{2+} + S + 4Fe^{2+} \qquad \text{2-21}$$

$$Cu_2S + 4H^+ + 2O_2 = 2Cu^{2+} + S + 2H_2O \qquad \text{2-22}$$

It must be mentioned that the formation of elemental sulfur and its passivating effect via reactions 2-21 and 2-22 have not been verified in this study. Additionally, the most well known dissolution path for chalcocite is through formation of covellite (CuS) by the following reactions [Dutrizac and MacDonald 1974]:

$$Cu_2S = Cu_{2-x}S + xCu^{2+} + 2xe^- \qquad \text{2-23}$$

$$CuS = S + Cu^{2+} + 2e^- \qquad \text{2-24}$$

Reaction 2-23 is reportedly a fast reaction while the second step of dissolution (reaction 2-24) is a slow reaction that controls the rate of chalcocite dissolution. In the study by Hiroyoshi *et al.* [2004], the reason for considering a direct dissolution path for chalcocite to copper ions via reactions 2-21 and 2-22, without formation of covellite intermediate, has not been explained.

Another published EIS study on the dissolution of chalcopyrite electrodes is by Velasquez *et al.* [2005] which followed from their previous study [Velasquez *et al.*, 1998] in a pH 9.2 solution. Figure 2-14 shows the experimentally obtained and simulated Nyquist plots at different potentials and the applied electrical circuit models are presented in Figure 2-15. The circuit for the potential of – 0.150 V *vs.* SCE (0.092 *vs.* SHE) appears to be related to three relaxation processes (Figure 2-15a): R_e is the ohmic resistance; R_{ct} is the charge transfer resistance; Q_c corresponds to the capacitance of a surface layer (which forms spontaneously during the polishing of the electrode). R_p is the pore resistance of this film, Q_{dl} is the double-layer capacitance, and R_{sl}–Q_{sl} refers to the adsorbed species (e.g. iron species). Q_c, Q_{sl}, and Q_{dl} were modeled by a CPE; CPE behaves as a capacitance, which varies with the frequency. For the potential of 0.20 V *vs.* SCE (0.442 *vs.* SHE), the equivalent circuit is shown in Figure 2-15b. This circuit has been proposed to be related to two Faradaic relaxation processes. The change in the equivalent circuit is associated with a decrease of Q_c and R_{ct} values together and with an important increase in the R_p value, which shows that the kinetics of the electrochemical process and the thickness and porosity of the film on the electrode surface are increased. For potentials of 0.45 and 0.60 V *vs.* SCE (0.692 and 0.842 *vs.* SHE, respectively), considerable changes were observed in the Nyquist plots, showing two loops: one at high frequency which is associated with a capacitive loop, and one at low frequencies which is a pseudo–inductive loop. The equivalent circuit for both potentials was considered to be composed of two sub–circuits, as shown in Figure 2-15c: one forms from the association parallel to a CPE, with Q_{dl}/R_{ct} pair representing the double-layer capacitance and the resistance of the electron transfer of the electrochemical process, and the other R_{sl}/L pair, corresponds to the resistance associated to the accumulation of superficial species, and an inductive element. The element L may be due to the transfer of ions across the double layer or an increase of the area of the electrode by the partial dissolution of the surface film. Partial dissolution of the film will result in the formation of islands that partially cover the electrode surface [Velasquez *et al.*, 2005].
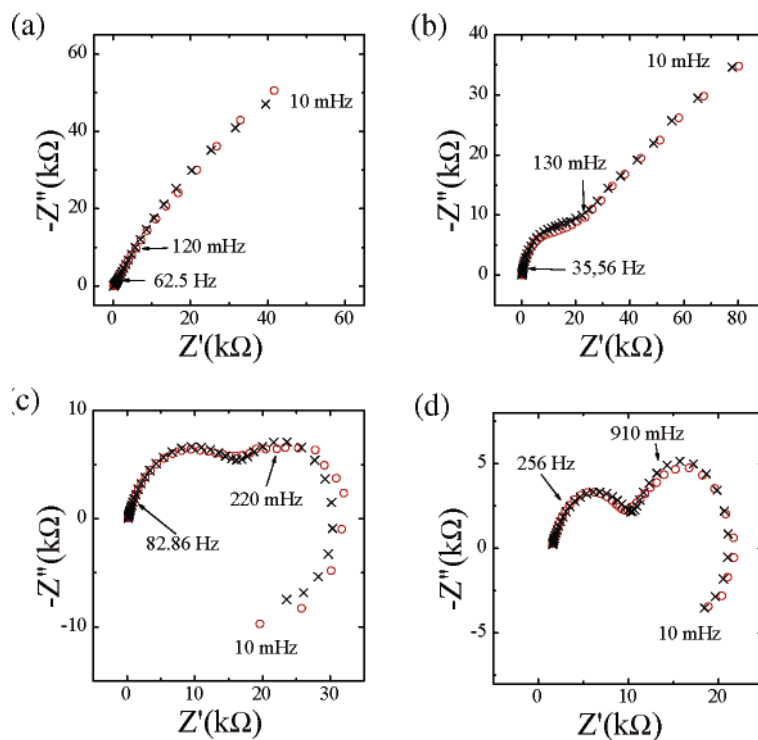
Figure 2-14: Measured and simulated Nyquist plots at; (a) – 0.15 V, (b) 0.2 V, (c) 0.45 V and (d) 0.6 V *vs.* SCE [Velasquez *et al.*, 2005].
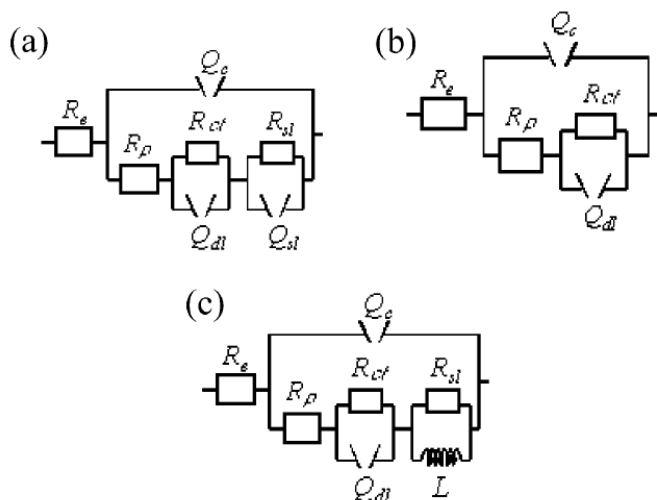
Figure 2-15: Equivalent circuits for; (a) – 0.15 V, (b) 0.2 V, (c) 0.45 V and 0.6 V *vs.* SCE [Velasquez *et al.*, 2005].

2.3.4 Cyclic voltammetry (CV) studies

Without a doubt, the most popular electrochemical technique to study chalcopyrite dissolution has been cyclic voltammetry. Since CV is a very powerful electrochemical

technique for identifying reactions, almost all researchers who have studied chalcopyrite electrochemistry have availed themselves of this method. The pioneers in this area are Biegler and Swift [1979], who published a study on the anodic behavior of natural chalcopyrite in 1 M H_2SO_4 and 1 M HC1 by linear sweep voltammetry. The obtained voltammograms with a fresh electrode surface showed a small prewave, attributed to a surface oxidation process, followed by a region of active dissolution characterized by a steeply rising anodic current (Figure 2-16). The current in Figure 2-16 has been drawn on a logarithmic scale to show features over a broad range. From the OC potential (around 0.4 V *vs.* SHE) to 0.85 V there was a wide prewave in which the current passed through a peak. If the electrode potential was cycled, this prewave was absent from the second and subsequent scans. Hence, the prewave related to a surface oxidation process which involved a thin layer of chalcopyrite. The oxidation process consumes a charge of around 1 mC cm^{-2} and it has been suggested that this surface reaction involves the selective dissolution of iron [Biegler and Swift, 1979]. With the same approach, Parker *et al.* [1981] showed that the surface film in the prewave region (in 1 M H_2SO_4) is a metal deficient polysulfide, with semiconductive behavior, and forms on chalcopyrite during oxidation. Also, the film is thermally unstable (higher temperatures will decompose the film and faster oxidation of chalcopyrite will be achieved). This latter finding is inconsistent with the results of Viramontes-Gamboa et al. [2006] where they detected higher stability for the passive film as temperature was increased (refer to Figure 2-9). Moreover, Parker *et al.* [1981] have shown that the metal deficient polysulfide surface film slows transport of ions, slows electron transfer to oxidants and slows the supply of holes to the solid-solution interface. Furthermore, it has been mentioned by Parker *et al.* [1981] that the sulfur film which forms on corroded chalcopyrite does not account for the electrochemical or kinetic aspects of chalcopyrite leaching. The same results regarding the sulfur film were obtained by McMillan *et al.* [1982].
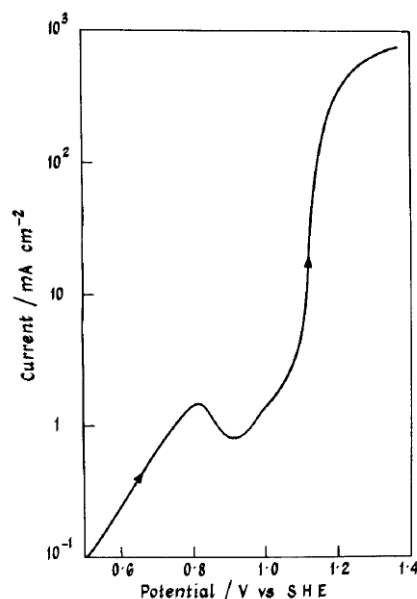
Figure 2-16: First positive going current–voltage sweep on a freshly polished chalcopyrite surface [Biegler and Swift, 1979].

Under nitrogen sparged conditions, Biegler and Horne [1985] suggested that the prewave peak is not a consequence of atmospheric oxidation during surface preparation. Also, it has been shown that the accumulation of the products of the initial voltammetry cycle causes diminishing decrease in the size of the prewave current at more cycles [Biegler and Horne 1985]. The passed charge for the initial formation of the film is measured to be 2 mC cm^{-2}, while previously, in the former study of Biegler and Swift [1979], it was reported to be 1 mC cm^{-2}. Also these researchers showed that the surface film is stable at 25 °C for long periods at open circuit and the film is not stable at high temperatures (> 80 °C). Through study of the relative charge passed during film formation, the electrochemical reduction of the surface film and the presence of dissolved copper in solution, Biegler and Swift [1979] came to the following suggested stoichiometry for the prewave reaction:

$$CuFeS_2 \rightarrow 0.75CuS + 0.2Cu^{2+} + Fe^{2+} + 1.25S + 2.5e^{-} \hspace{1cm} \text{2-25}$$
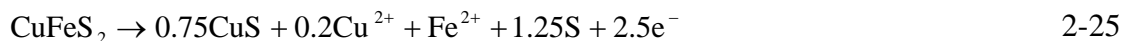
where, the product layer of elemental sulfur and the CuS is about 3 nm thick.

Results of rotating ring disk electrode (RRDE) studies showed that the prewave reaction caused a partial dissolution of the chalcopyrite with iron being more readily dissolved in solution than copper. The ratio of the Fe^{2+} to Cu^{2+} released by oxidation was roughly 5:1 [Holliday and Richmond, 1990], while the rotating disk electrode (RDE) studies

previously had showed it to be 4:1 [Biegler and Horne, 1985]. The overall oxidation reaction in the prewave region resulting from RRDE studies is suggested to be:

$$CuFeS_2 \rightarrow Cu_xS_2 + yCu^{2+} + Fe^{2+} + 2(2-x)e^-$$ 2-26
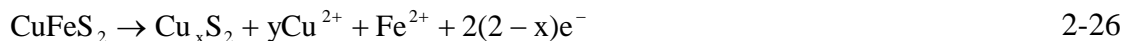
where x, the portion of oxidized Cu^{2+} is 0.8 and y, the solvated copper is 0.2 [Holliday and Richmond, 1990]. The proposed reaction is to some extent similar to that suggested by Biegler and Horne [1985].

Parker *et al.* [1981] and Biegler and Horne [1985] were of the opinion that the prewave peak was not a consequence of atmospheric oxidation during surface preparation. The prewave peak reaction was considered to be associated with the reaction of a clean chalcopyrite surface rather than reaction with atmospheric oxygen prior to voltammetry. However, the atmospheric oxidation studies of chalcopyrite by Yin *et al.* [1995] showed the opposite. In their study on a natural chalcopyrite electrode in 0.1 M HCl solution, it was shown that exposing a chalcopyrite electrode to the atmosphere will oxidize the surface and a passive film will form which diminishes the extent of the subsequent electrochemical oxidation in the prewave region. Calculations elucidated that after 64 h of exposure to the atmosphere, a passive film of approximately 4 nm forms on the surface. To form such a film, about seven monolayers of chalcopyrite must be oxidized. Also the effect of immersion of the electrode in hydrochloric acid on the prewave reaction has been studied by the same researchers [Yin *et al.*, 1995]. Immersing the electrode for 18 hr in 1 M HCl solution saturated with oxygen-free nitrogen causes a larger prewave rather than immersing in the same solution for less than 1 min. However, immersing the electrode in HCl solution saturated with air for 43 hr will diminish the prewave current. Therefore, it was concluded that oxygen is the cause for passivation of the chalcopyrite surface, whereas, hydrochloric acid can activate the surface oxidation [Yin *et al.*, 1995]. These same authors also studied the relationship between the solution pH and the prewave. The relationship was reported to be quite complex where, in acidic (pH < 2) and basic (pH > 9) electrolytes the prewave is easily distinguishable from the main anodic peak of higher current (and higher potential), and at pH between 2 to 9 the prewave is difficult to differentiate from the main anodic peak [Yin *et al.*, 1995].

In addition to the previous study, the general surface oxidation behavior of natural chalcopyrite in basic solutions (pH 9.2 and 12.7) has been studied by Yin *et al.* [2000]. Their

results showed that the oxidation process consists of three potential and pH dependent stages. By increasing the electrode potential from – 0.6 to 0.0 V *vs.* SCE (– 0.358 to 0.242 *vs.* SHE) the iron in the top layer of the chalcopyrite surface was oxidized. However, the copper and sulfur atoms remained unoxidized and the surface of the electrode was covered by a metastable CuS_2* phase. CuS_2*, together with the oxidized iron layer formed a passivating layer on the electrode. As the potential increased further, deeper layers were involved in the oxidation, which caused a thickening of the passivating film. At this stage, the oxidation process was under solid-state mass transport control. A further increase of the potential – > 0.4 V *vs.* SCE (> 0.642 *vs.* SHE) – decomposed the passive film and the dissolution rate was accelerated. It is also mentioned that higher concentrations of OH^- enhance the dissolution rate [Yin *et al.*, 2000].

The effect of chloride ion and temperature has been studied in 1 M H_2SO_4 solution by CV on carbon paste-chalcopyrite electrodes [Lu *et al.*, 2000]. From this work, it has been shown that the presence of the chloride ion and higher temperature significantly enhance the oxidation rate of chalcopyrite. The observed higher dissolution rate of chalcopyrite in the presence of chloride is thought to be related to the aggressive nature of halides in corrosion processes [Lu *et al.*, 2000].

Through a ring–disk electrode study on a natural chalcopyrite electrode in 0.1 M H_2SO_4 solution at 60 °C, Lazaro and Nicol [2006] proposed the formation of soluble sulfur species such as thiosulfate. In order to investigate the effect of potential on the dissolution process, different potentials within the non–oxidative and oxidative region (0.45–0.65 V *vs.* SHE) were applied on the chalcopyrite disk for 1 hr and anodic stripping curves for the platinum ring (held at –0.06 V) were obtained (Figure 2-17). In addition to the peak for the stripping of copper metal (peak A1 in Figure 2-17), the appearance of peaks (A2 and A3) is noteworthy. Some interesting features of these peaks are that A2 appears at all potentials and the magnitude of A2 does not seem to be dependent on potential during the prior potentiostatic period while the magnitude of peaks A1 and A3 do vary with this potential. These additional peaks (A2 and A3) are observed in a potential region similar to those which are known to be associated with the oxidation of the copper sulfides. Since different copper sulfides can be oxidized in this potential region it is not easy to assign these peaks to a particular copper sulfide (e.g. CuS, Cu_2S and Cu_xS). As a result, if these peaks are

representative of the oxidation of copper sulfides, then in addition to copper ions, soluble sulfur species such as thiosulfate ($S_2O_3^{2-}$) and/or hydrogen sulfide (H_2S) could be formed in the dissolution reaction at the disk [Lazaro and Nicol, 2006]:

$$CuFeS_2 + 3H_2O = Cu^{2+} + Fe^{2+} + S_2O_3^{2-} + 6H^+ + 8e^-$$ 2-27

Recently the interaction between water molecules and the (001) plane of chalcopyrite has been studied by means of density functional modeling [Ferreira de Lima *et al.,* 2011]. This work has suggested that hydrogen sulfide gas is evolved at anodic potentials. These authors show that in a highly acidic solution, protons adsorb to the surface of the disulfides (S_2^{2-} species) and this will cause elongation of the S–S bond and formation of H_2S. Indeed, it has been acknowledged in the literature that the sulfur dimers (S_2^{2-} species) are the precursor for polysulfide formation and that polysulfide, with time, will transform to elemental sulfur [Acres *et al.*, 2011; Hackl *et al.,* 1995]. In the study by Ferreira de Lima *et al.,* [2011] it has been concluded that adsorption of positively charged protons to the sulfur dimers inhibits the initiation of the polysulfide formation, and in return H_2S forms.
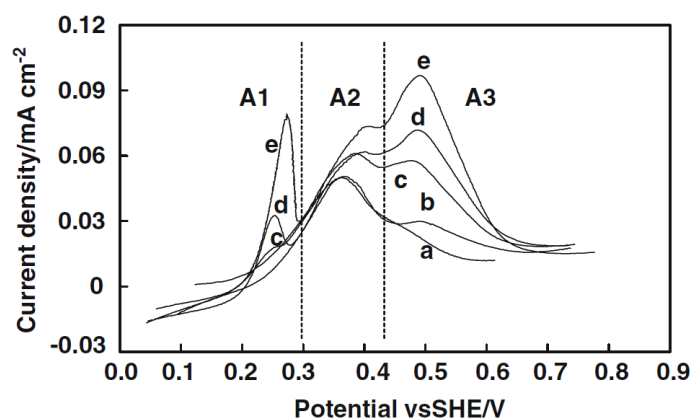
Figure 2-17: Anodic stripping curves for a platinum ring held at – 0.06 V after dissolution of a CuFeS₂ disk which was held at potentials of (a) 0.45, (b) 0.49, (c) 0.54, (d) 0.59 and (e) 0.65 V *vs*. SHE for 1 h at 200 rpm [Lazaro and Nicol, 2006].

Nava *et al.* [2006; 2008] have done an extended electrochemical study (mostly by CV technique) on the characterization of the chemical species that form during the electrochemical anodic and cathodic dissolution of carbon paste chalcopyrite electrodes in 1.7 M H_2SO_4 solution. They detected dissolved copper ions using a mercury film electrode (MFE) and anodic stripping voltammetry of the carbon disk. Also they analyzed the surface

of the chalcopyrite electrode before and after the dissolution by cyclic voltammetry. Their results demonstrated different electrode behavior that had not been previously reported. They suggest that there are at least two types of non-stoichiometric sulfides: the first one forms at $E \leq 1.015$ V *vs.* SHE with passive behavior ($Cu_{1-r}Fe_{1-s}S_{2-t}$), whereas the second one forms at $1.015 < E \leq 1.085$ V with an active character ($Cu_{1-x}Fe_{1-y}S_{2-z}$); the formation of only one non-stoichiometric sulfide was recognized previously [Hackl *et al.*, 1995; Parker *et al.*, 1981; Elsherief, 2002]. Consequently, Nava and Gonzalez [2006] suggest that in the higher potential region ($1.015 < E \leq 1.085$ V) partial oxidation of chalcopyrite occurs through the dissolution of porous layers of non-stoichiometric polysulfide ($Cu_{1-x}Fe_{1-y}S_{2-z}$).

2.4 Surface analysis of chalcopyrite

The term "passivation" is widely used for chalcopyrite dissolution in different literature [Viramontes-Gamboa *et al.*, 2007; Velásquez *et al.*, 2005; Mikhlin *et al.*, 2004; Abed and Dreisinger, 2003; Warren *et al.*, 1982; Hackl *et al.*, 1995]. The passive state is defined in Shreir's "Corrosion" book [2000] as a state of low corrosion rate usually due to the presence of an (oxide) film on the surface. The typical thickness for a passive film is about a few nanometers. Such passive films (ultra thin films) would normally be directly detectable by sensitive surface analysis methods such as X-ray photoelectron spectroscopy (XPS/ESCA), Auger electron microscopy (AES), or secondary ion mass spectroscopy (SIMS) [Marcus and Mansfeld, 2006]. Generally, different in-situ electrochemical techniques (e.g. cyclic voltammetry, potentiodynamic and potentiostatic polarization, electrochemical impedance spectroscopy, and chronoamperometry) and ex-situ spectroscopic methods (e.g. X-ray photoelectron spectroscopy, auger electron spectroscopy, Raman spectroscopy) have been applied to understand the dissolution mechanism of chalcopyrite and furthermore to characterize the surface layers on electrodes, but there remains uncertainty about the dissolution process. The trouble with most of the DC electrochemical techniques used so far is that only circumstantial evidence is derivable to help with the elucidation of possible reaction mechanisms. The ex-situ analytical methods are plagued with controversy associated with the possible evaporation of elemental sulfur under experimental conditions [Buckley and Woods, 1994]. Nevertheless, Klauber *et al.* [Klauber *et al.,* 2001] have pointed out that there is a significant difference between the loss of multiple layers of elemental

sulfur and the loss of a monolayer of elemental sulfur. In other words, the adsorption energy of sulfur atoms interacting with a sulfur mono(or multi) layer is expected to be less that the adsorption energy of adsorbed sulfur to the surface of chalcopyrite or another leached mineral. In order to justify this reasoning, Klauber *et al.* [Klauber *et al.,* 2001] have compared the situation with that of the adsorbed water to the surface of a material; adsorbed water molecules are easily detectable with XPS (considering the point that water has a much higher vapor pressure than sulfur). In this section we will consider some of the previous analytical work on the surface chemistry of chalcopyrite.

Hackl *et al.* [1995] provided a brief introduction to XPS studies of chalcopyrite from 1977 to 1995. Generally, the studies supported the electrochemical studies with regards to the formation of copper-rich sulfide layer(s) during the dissolution of chalcopyrite. Hackl *et al.* [1995] provided narrow scan Cu 2p, Fe 2p, and S 2p XPS spectra for the unleached chalcopyrite as well as leached chalcopyrite at 110 °C and 1.38 MPa oxygen for 3 hr. The results demonstrated that the unleached sample does not have any detectable oxidized copper and the leached sample is free of Cu^{2+} species. In the case of iron, even exposing the sample for a very short time in air caused formation of significant quantity of iron oxide (possible species are Fe_2O_3, Fe_3O_4 and FeOOH) on the surface. On the other hand, the analysis on the surface of the leached sample illustrated that the leaching causes dissolution of the iron oxide species. Analyzing the S 2p spectra, Hackl *et al.* [1995] detected monosulfide (S^{2-}) referring to unaltered $CuFeS_2$, disulfide (S_2^{2-}) which was thought to be an iron deficient sulfide with the composition of $Cu_{1-x}Fe_{1-y}S_2$ (*y»x* and *x+y ≈1*) and polysulfide (S_n^{2-}) which was assumed to be CuS_n (*n > 2*). The precise value of *n* was not defined in the study [Hackl et al., 1995].

Yin *et al.* [1995] identified the oxidation products of natural chalcopyrite on a freshly cleaved surface as well as after electrochemical dissolution in the potential region of > 0.5 V *vs.* SCE in 1 M $HClO_4$ solution. The Cu 2p spectra are almost identical in binding energy. It is proposed by the authors that the CuO, Cu_2O and Cu_2S cannot be formed by oxidation of chalcopyrite in $HClO_4$ solution, and they suggested the formation of CuS and S or CuS_2* [Yin *et al.*, 1995]. Their study also confirms the results of Hackl *et al.* [1995] on the dissolution of iron species during oxidation. In addition to their study in $HClO_4$ solution, Yin *et al.* [2000] also studied the formation of species on the surface of a natural chalcopyrite electrode in alkaline solutions of 0.1 M borax (pH 9.2) and 0.05 M NaOH (pH 12.7). In the

case of the borax solution, they have observed more oxidized iron at higher anodic potential of 0.4 V *vs.* SCE (0.642 *vs.* SHE) rather than at 0.15 V (0.392 *vs.* SHE). Also the formation of $Fe(OH)_3$ and Fe_2O_3 species have been suggested. Furthermore, it has been mentioned that argon ion bombardment may cause the formation of FeO species during the XPS test. Yin *et al.* [2000] have proposed that CuO is the only oxidized form of copper and that the identical peak of Cu_2O originates from the reduction of CuO to Cu_2O by argon ion bombardment in the XPS chamber. So, According to Yin *et al.* [2000], the existence of the Cu_2O species is related to the reduction of CuO during the XPS analysis and not to the oxidation of copper during the electrochemical dissolution process. Moreover, $CuFe_{1-x}S_2$ and CuS_2* were identified and both had a distorted chalcopyrite structure. In other words, these species form by dissolution of iron atoms from the chalcopyrite crystal structure. The induced distortion in the chalcopyrite crystal structure is due to the vacancies introduced in the iron atom positions during the dissolution process. In NaOH solution (pH 12.7), in addition to the above-mentioned species, the formation of CuO and $CuSO_4$ was reported at 0.8 V *vs.* SCE (1.042 *vs.* SHE). The results of this work by Yin et al. at pH 9.2 are in agreement with the work of others [Velásquez *et al.*, 1998; Velásquez *et al.*, 2005].

Farquhar *et al.* [2003] have studied the electrochemical dissolution of natural chalcopyrite samples in 0.1 M $NaNO_3$ solution (pH 4). Their results are very close to those of the previous studies. However, it was mentioned that after dissolution at 0.5 V *vs.* Ag/AgCl (0.697 *vs.* SHE) the sulfide or natural sulfur concentrations gradually increase with depth below the surface and at approximately 40 Å all the sulfur is present as sulfide or elemental sulfur. Parker *et al.* [2003] have studied species on the surface of chalcopyrite after leaching in four different sulfuric acid solutions (starting pH values of 1.3 to 1.9) in the presence of: (1) ferric, (2) ferrous, (3) ferric plus silver and (4) microbes. Table 2-2 summarizes the XPS results that highlight the different species found in each case. According to Table 2-2, the species formed in the presence of ferric and ferrous are almost the same while in the case of Ag^+ addition, quite different surface compositions are produced. In the silver containing solution the only forms of sulfur are sulfide (S^{2-}) and sulfate (SO_4^{2-}). Chalcopyrite demonstrated a very high reactivity toward weak silver concentrations (down to 0.0002 M) whether or not ferric was present. The reaction accelerated at the lower pH of 1.9 and

produced a silver dominated surface phase of Ag_2S with several thousand Å's thickness in less than 30 min [Parker *et al.*, 2003].

Table 2-2: Various sulfur, copper, and iron species on the surface of the chalcopyrite after oxidative dissolution; between 50 to 80 °C [Parker *et al.*, 2003].

Speciation	Fe(III)	Fe(II)	Fe(III)–Ag$^+$	Bioleach
Sulphide—S^{2-}	●		●	●
Disulphide—S_2^{2-}	●	●	–	●
Polysulphide—S_n^{2-}	–	–	–	–
Sulphur—S^0	●	●	–	●
Sulphate—SO_4^{2-}	●	●	●	●
Cupric—Cu^{2+}	–	–	–	–
Cuprous—Cu^+	●	●	–	●
Oxidic—Fe^{3+}	●	●	●	●
Sulphate—Fe^{3+}	●	●	–	●

Present (●) and not detected (–).

The atomic percentage of sulfur species on the top layer of natural chalcopyrite (extracted from XPS results) as a function of dissolution time in 1 M $HClO_4$ (pH 1) and 85 °C was studied by Harmer *et al.* [2006]. From this study (summarized in Table 2-3), the total concentration of sulfur species increases from 25.3% to 39.3% during the first two hours of leaching. The SO_4^{2-} species which was present on the unleached sample was removed from the surface by leaching. The concentrations of both S_2^{2-} and S_n^{2-} species was increased by leaching. The total surface concentration of S was 21.7% after 24 h of leaching and was increased dramatically to 77.3% after 144 h of leaching. Also, within this extended leaching period, a significant increase in leaching rate was reported. The S 2p XPS spectrum of the sample leached for 144 h showed a combination of S^{2-}, S_2^{2-}, S_n^{2-}, and S^0 species on the surface, wherein, the concentration of S^{2-} species increased from 5.9% at 24 h to 17.7% at 144 h (an almost threefold increase). The S concentration and speciation on the surfaces after 144 and 313 h of leaching were reported to be very similar. Because the concentration of S increased on the surface during the leach and because the leaching rate increased during this same period, it was concluded by Harmer *et al.* [2006] that neither the formation of S^0 or S_n^{2-} is passivating.

Table 2-3: Atomic percentage of different sulfur species on the surface of chalcopyrite before and after leaching [Harmer *et al.*, 2006].

Species	S $2p_{3/2}$ binding energy (eV)	Unleached	2 h	24 h	144 h	313 h
S^{2-}	161.4	12.6	5.8	5.9	17.7	11.0
S_2^{2-}	162.4	5.2	15.3	8.3	13.7	9.2
S_n^{2-}	163.0–163.9	2.3	18.2	7.5	38.2	49.8
S^0	164.1	0.0	0.0	0.0	7.7	8.3
SO_4^{2-}	168.5	5.2	0.0	0.0	0.0	0.0
Total S %		25.3	39.3	21.7	77.3	78.3

2.5 Electrochemical (and chemical) dissolution reactions

During the dissolution process, increasing the potential of chalcopyrite in the anodic direction will cause the formation of surface layers which hinder the dissolution rate of the mineral [Warren *et al.*, 1982]. As mentioned in previous sections, the precise composition of the layer(s) is still in dispute. Previous studies have concluded that these layers could be sulfur [Dutrizac, 1978; Munoz *et al.*, 1979], precipitated iron compounds [Dutrizac, 1978], a solid electrolyte interphase (SEI) [McMillan, *et al.*, 1982], a metal deficient sulfide [Linge, 1976], or polysulfidic in nature [Parker, *et al.*, 1981; Hackl, *et al.*, 1995]. Studies by Biegler [1977] show nucleation and growth of a thin two-dimensional sulfide phase on the surface of chalcopyrite during the exposure of a polished sample in H_2SO_4 solution or air. More studies by Biegler and Swift [1979] have shown evidence for nucleation and growth of a 3-dimensional phase at low anodic potentials (around +200 mV vs. OCP). The current-time behavior of the dissolution process in this potential area has the characteristics of expansion and overlap of localized dissolution centers. Anodic dissolution (around +200 mV vs. OCP) of the chalcopyrite is considered to be a bulk dissolution process which is a distinct mechanism from the surface oxidation process at lower potentials (anodic potentials close to OCP) [Biegler and Horne, 1985]. It was mentioned earlier that the surface oxidation process is detectable as a "prewave" in cyclic voltammetry tests. Technically, the prewave represents the initial stage of the dissolution of chalcopyrite and furthermore, determines the surface properties of the mineral during the rest of the dissolution process. Many publications on chalcopyrite have concentrated on the dissolution behavior in the prewave region [Biegler, 1977; Biegler and Swift, 1979; Biegler and Horne, 1985]. Studies by Lazaro and Nicol [2006] on the dissolution of chalcopyrite in dilute sulfuric acid solutions have produced some

37

evidence for the formation of Cu^{2+}, Fe^{2+}, and soluble sulfur species at the initial stages of dissolution at 60 °C. More kinetic studies on the prewave reaction by Holliday and Richmond [1990] have demonstrated a sequential mechanism for the surface oxidation which consists of an initial rate determining step for the production of adsorbed Cu^{2+} followed by the production of Fe^{2+} ions. These reactions are responsible for making a passive surface layer on the mineral and hindering the dissolution rate. These results are along the same lines as those presented by Biegler and Horne [Biegler and Horne, 1985]. Calculations by Biegler [1977] have shown that the thickness of the layer formed during the prewave reaction in sulfuric acid solution is around 2 nm and in another reference [Biegler and Horne, 1985] this layer is reported to be a CuS and S compound with thickness of about 3 nm. Studies by Yin *et al.* [1995] indicate that exposing polished chalcopyrite to air causes the formation of a passive layer with a thickness of 4 nm. Moreover, it has been shown that the anodic prewave disappears if the sample is exposed to air due to the formation of the passive layer on the surface. For a 1 M HCl solution the prewave peak appears at around 0.52 V vs. SHE and at higher potentials (around 0.8 V vs. SHE) the second anodic peak appears. The main anodic reactions proposed by these researchers in 1 M HCl solution are [Yin, *et al.*, 1995]:

$$CuFeS_2 \longleftrightarrow Cu^{2+} + Fe^{3+} + 2S + 5e^- \qquad\qquad 2\text{-}28$$

and

$$CuFeS_2 + 8H_2O \longleftrightarrow Cu^{2+} + Fe^{3+} + 2SO_4^{2-} + 16H^+ + 17e^- \qquad 2\text{-}29$$
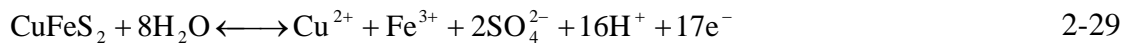
Nava *et al.* [2006; 2008] have studied the dissolution of a carbon paste/chalcopyrite electrode in sulfuric acid solution. It was indicated that the dissolution of chalcopyrite starts at low anodic potentials ($0.615 \leq E < 1.015$ V vs. SHE) and results in the formation of a non-stoichiometric polysulfide layer of composition $Cu_{1-x}Fe_{1-y}S_{2-z}$ according to the following reaction:

$$CuFeS_2 + 4zH_2O \longleftrightarrow Cu_{1-x}Fe_{1-y}S_{2-z} + xCu^{2+} + yFe^{3+}$$
$$+ zSO_4^{2-} + 8zH^+ + (2x + 3y + 6z)e^- \qquad 2\text{-}30$$
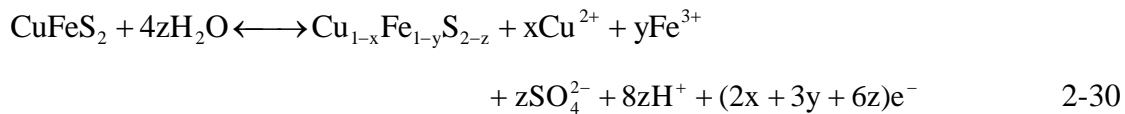
In this potential region the concentration of the dissolved copper ion is very low and the anodic stripping voltammetry (ASV), which is known to have a very good detection limit, was not able to detect the copper ion in solution [Nava and Gonzalez, 2006]. Consequently, these authors have concluded that $Cu_{1-x}Fe_{1-y}S_{2-z}$ is a passive film which slows down the

dissolution rate of chalcopyrite and keeps the concentration of copper ion in solution to a very low value. At higher potentials ($1.015 \leq E < 1.085$ V vs. SHE), a small amount of copper ion was detected in solution which confirmed the partial dissolution of the polysulfide layer. The reaction for chalcopyrite dissolution in this higher potential range was proposed to be:

$$CuFeS_2 + 4pH_2O \longleftrightarrow Cu_{1-m}Fe_{1-n}S_{2-p} + mCu^{2+} + nFe^{3+}$$

$$+ pSO_4^{2-} + 8pH^+ + (2m + 3n + 6p)e^- \qquad 2\text{-}31$$
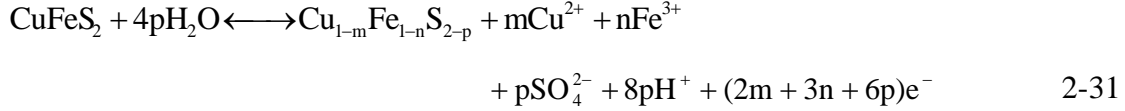
While reactions 2-30 and 2-31 are similar, it was concluded by Nava and Gonzalez [Nava and Gonzalez, 2006] that the sulfide product in reaction 2-31, i.e. $Cu_{1-m}Fe_{1-n}S_{2-p}$, is active as opposed to the passive layer formed in reaction 2-30, i.e. $Cu_{1-x}Fe_{1-y}S_{2-z}$. The dissolution rate of chalcopyrite was found to be a function of the decomposition rate of the layer obtained through reaction 2-31. Increasing the potential into the range of $1.085 \leq E < 1.165$ V *vs.* SHE caused the complete release of iron from the lattice of chalcopyrite into the solution and the formation of a CuS layer on the surface of the electrode according to reaction 2-32:

$$2CuFeS_2 + 13H_2O \longleftrightarrow 0.75CuS + 1.25Cu^{2+} + Fe_2(SO_4)_3$$

$$+ 0.25SO_4^{2-} + 26H^+ + 28e^- \qquad 2\text{-}32$$
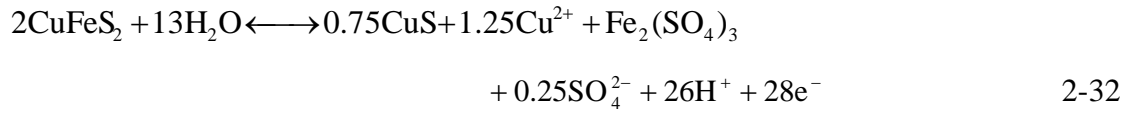
The CuS layer is not stable at potentials higher than 1.165 V vs. SHE and so the complete dissolution of chalcopyrite will occur by further increasing the potential, according to reactions 2-33 and 2-34:

$$CuS + 4H_2O \longleftrightarrow Cu^{2+} + SO_4^{2-} + 8H^+ + 8e^- \qquad 2\text{-}33$$

$$2CuFeS_2 + 16H_2O \longleftrightarrow 2Cu^{2+} + Fe_2(SO_4)_3 + SO_4^{2-} + 32H^+ + 34e^- \qquad 2\text{-}34$$
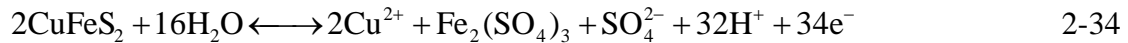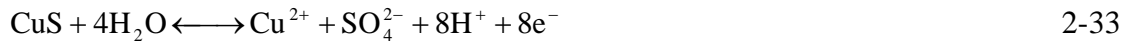
At high potentials, the formation of jarosite on the surface of chalcopyrite was found to decrease the dissolution rate of the electrode. In fact, the products of reaction 2-34 result in the formation of jarosite on the electrode surface [Nava and Gonzalez, 2006; Nava, *et al.*, 2008]. This dissolution model is similar to that of Hackl et al. [1995].

In alkaline solutions, researchers [Yin, *et al.*, 2000; Vaughan, *et al.*, 1997] have observed three different stages of oxidation. The prewave occurs at low potentials (around 0.26 V *vs.* SHE) which they considered to be the top atomic layer oxidation of iron to a monolayer of $Fe(OH)_3$ and Fe_2O_3, while the Cu and S of the chalcopyrite structure remained

unchanged as CuS_2*. The layer consisting of oxidized iron and CuS_2* acted as a passive layer which inhibits further oxidation of chalcopyrite. At higher potentials (around 0.64 V *vs.* SHE) the same reactions were found to occur and iron atoms located deeper within the electrode surface were found to take part in the oxidation reaction. At this potential the passive film was stable and thickened with time. The electrochemical reactions under these conditions were considered to be solid-state mass transport-controlled. For higher potentials (> 0.64 V vs. SHE) the CuS_2* layer oxidized to CuO, and SO_4^{2-} which accelerated the rate of the total electrode dissolution. Studies by Velasquez *et al.* [2005] confirm these results except that they were not able to detect the formation of elemental sulfur due to possible evaporation of this element under the experimental conditions of XPS. Studies by electrochemical impedance spectroscopy (EIS) have shown the formation of islands of passive layers on the surface of chalcopyrite electrodes [Velásquez *et al.*, 2005]. Another EIS study has demonstrated the active-passive behavior of chalcopyrite but did not point out the passive islands on the surface of electrode [Viramontes-Gamboa *et al.*, 2006; Hiroyoshi *et al.*, 2004; Velasquez *et al.*, 1998].

2.6 What is missing?

As one can see from the literature, a fully accepted mechanism for the dissolution of chalcopyrite is missing and the passive layer(s) which form on the surface of this mineral result in a very slow dissolution and thus a practical engineering challenge for the hydrometallurgist. Furthermore, from literature, the properties of the chalcopyrite passive film are not clear. It is not known whether mass transport through the passive film (i.e. a diffusion process), dissolution of the passive film itself (i.e. reaction) or electron transfer through the passive film is controlling the chalcopyrite dissolution rate in the leaching solution.

In this study, the semiconductor, electrochemical and chemical properties of chalcopyrite's passive film will be studied. Additionally, the electronic and ionic conductivity of chalcopyrite's passive film is a crucial missing point. Indeed, to interpret many of the phenomena currently being observed in chalcopyrite leaching studies, it is important to understand the extent to which chalcopyrite's passive film conducts electrons or ions. For example, during development of leaching processes, the answer to this question

will help us to decide if the electron transfer rate of the electrochemical reactions should be increased or the rate of ion transfer through the passive film should be promoted.

3 Objectives

The ultimate goal of any electrochemical study pertaining to the dissolution of chalcopyrite is to overcome its slow dissolution rate. Clearly, the path to this goal runs through obtaining comprehensive knowledge of the surface chemistry of chalcopyrite in the desired dissolution environment. Thus, the proposed research seeks the following objectives:

- To investigate the electrochemical dissolution mechanism of pyrrhotite ($Fe_{1-x}S$). Pyrrhotite electrochemistry may be considered to represent a simplified case of chalcopyrite electrochemistry; as pyrrhotite is a Fe-S binary system (metal to sulfur ratio of *c.a.* 1) while chalcopyrite is the more complex ternary system of Cu-Fe-S (metal to sulfur ratio of 1). Hence, the results obtained regarding the dissolution mechanism of pyrrhotite may be applicable to chalcopyrite dissolution. Additionally, it must be mentioned that the dissolution mechanism of both pyrrhotite and chalcopyrite minerals are very similar as they both passivate in acidic solutions by formation of a metal-deficient sulfide film (this will be further proven in the next few chapters). However, other Fe-S minerals (e.g. pyrite, FeS_2) dissolve through different mechanisms. For instance, pyrite leaching proceeds by simultaneous dissolution of Fe and S and no passive film forms on the surface. Hence, we believe that the electrochemical dissolution of pyrrhotite is similar to that of chalcopyrite.

- To understand the nature of the surface layers (mainly the passive layers) which form at low anodic potential (< 1 V *vs.* SHE) on the surface of chalcopyrite through careful characterization of said layers to obtain their composition.

- To offer a comprehensive dissolution reaction scheme for chalcopyrite in sulfuric acid solutions which takes into account all of the observed critical characteristics of chalcopyrite dissolution.

- To investigate the physical properties of the chalcopyrite passive film. The semiconducting properties of the passive film and its electrical conductivity will be studied.

4 Experimental

4.1 Minerals used

High quality natural polycrystalline pyrrhotite ($Fe_{1-x}S$) and chalcopyrite ($CuFeS_2$) samples originating from the Creighton Mine (Sudbury, Ontario) were used for electrode fabrication. In some parts of the study, other iron sulfide and copper sulfide minerals (i.e. pyrite, pyrrhotite, chalcocite and covellite) were used for comparison purposes. The composition of the minerals, obtained by Rietveld method and X-ray powder diffraction, and associated reference number to each mineral (which will be used during the course of study), are presented in Table 4-1.

Table 4-1: Composition of the as received sulfide minerals used in this research.

Mineral	# of mineral				
	1 (chalcopyrite)	2 (pyrite)	3 (pyrrhotite)	4 (chalcocite)	5 (covellite)
Chalcopyrite ($CuFeS_2$)	98.1	-	-	-	-
Pyrite (FeS_2)	-	97.6	-	-	-
Pyrrhotite ($Fe_{1-x}S$)	-	-	93.7	-	-
Chalcocite (Cu_2S)	-	-	-	73.7	-
Djurleite ($Cu_{31}S_{16}$)	-	-	-	26.3	-
Covellite (CuS)	-	-	-	-	98.3
Digenite (Cu_9S_5)	-	-	-	-	1.7
Magnetite (Fe_3O_4)	-	-	6.3	-	-
Siderite ($FeCO_3$)	1.9	-	-	-	-
Quartz (SiO_2)	-	0.6	-	-	-
Anhydrite ($CaSO_4$)	-	1.8	-	-	-

4.2 Electrode preparation

Massive electrodes were prepared by cutting the minerals into approximately cubic shapes with areas of 1 cm^2 exposed to the solution. In order to have a uniform current distribution on the samples, a thin layer of copper was electrodeposited on the back of the electrodes (the side to which the electrical connection was attached). Copper was electrodeposited from a copper sulfate solution with low current density of 4 mA cm^{-2}. An electrical contact with copper wires was made in the back of the samples with silver-loaded epoxy resin (Mg Chemicals). The electrode contacts were protected from the solution by

mounting the whole assembly in epoxy resin (LECO), leaving only one face of the electrode exposed to the solution. Prior to each electrochemical experiment the electrodes were checked to ensure that there was no evidence of crevice corrosion in the electrode. This was possible due to the transparent epoxy resin mounts. Before each test, the exposed face of the electrode was polished with brand new carbide papers, starting from no. 300 paper up to no. 1200, to begin each experiment with a fresh surface. Afterwards, the surface of the electrodes was checked with optical microscope in order to make sure that the morphology of the electrodes was similar. The electrodes were then washed with DI water, sonicated in DI water, rinsed with DI water, and then finally dried in a stream of air.

4.3 Solution preparation

The goal of this study was to understand the fundamentals of chalcopyrite and pyrrhotite electrochemical dissolution. Thus, the electrolytes for electrochemical experiments were prepared by addition of only acids into deionized (DI) water. Solutions were prepared by dissolving reagent grade hydrochloric acid (HCl, Fisher Scientific) or sulfuric acid (H_2SO_4, Fisher Scientific) in DI water. The solution used for all of the experiments pertaining to pyrrhotite was 1 M HCl (pH within 0.2 – 0.3) and for chalcopyrite study it was 0.5 M sulfuric acid (pH ~ 0.3). In all of the experiments the oxygen content of the solution was controlled. In some of the experiments the oxygen in solution was removed to less than 10 ppb by sparging pure argon gas through the solution. In these experiments, the argon gas was sparged for 30 min prior to the experiment and sparging was continued during the test. When the experiment was performed in quiescent conditions the argon sparging was stopped during the experiment. All other experiments were performed in aerated solution by sparging filtered air into the cell. The volume of solution for all of the electrochemical experiments was 800 mL of fresh electrolyte.

4.4 Electrochemical experiments

All electrochemical experiments were performed at 25 ºC (this temperature was selected because most of the available data in literature are extracted from experiments at 25 ºC) using a VersaSTAT 4 potentiostat/galvanostat controlled by VersaStudio software (version 1.51, Princeton Applied Research). Some of the electrochemical data were obtained

using of a PAR 273 potentiostat-galvanostat connected to a PAR 1025 frequency response detector controlled by PowerCorr, PowerStep, and PowerSine software (Princeton Applied Research). The ZSimpWin 3.20 (2004) software was used for fitting the impedance data.

A conventional three-electrode electrolytic cell was used for electrochemical analysis. The test cell was jacketed and a silicon fluid was circulated through the jacket to maintain the desired test temperature of 25 ºC. The working electrode was always the prepared mineral electrode (electrodes are presented in Table 4-1). Opposite to the working electrode, a graphite electrode (99.999%, Alfa Aesar) was used as counter electrode. Three different reference electrodes, based on availability in the laboratory, were used. The first one was a glass body mercury/mercurous sulfate electrode (MSE, 0.600V vs. SHE at 25 ºC) filled with saturated K_2SO_4 electrolyte (Princeton Applied Research). The second electrode was a glass body Ag/AgCl reference electrode filled with 4 M KCl electrolyte saturated with AgCl (Accumet 13-620-523), 199 mV vs SHE at 25 ºC. Lastly, a glass body saturated calomel reference electrode (Accumet 13-620-525), 242 mV vs SHE at 25 ºC. The reference electrode was connected to a Luggin capillary to minimize IR drop. The electrolyte inside the reference electrodes was refreshed after each 20 hours of use and the electrodes were tested against a lab-standard Ag/AgCl electrode before each experiment.

The electrode potential was allowed to stabilize for 6 hours before starting the measurements and, in order to ensure reproducibility, tests were begun only after reaching the same OCP within ±5 mV. The potentiodynamic polarization experiments were conducted at potential sweep rates between 0.05 to 50 mV s^{-1}. The potentiostatic polarization experiments were performed by application of a constant potential and the current flow through the sample was registered. In addition to the above DC tests, cyclic voltammetry was applied to study the electrodissolution behavior of chalcopyrite. The sweep rate was 50 mV/s for all CV experiments, as the essential features were evident at these rates. Electrochemical impedance spectroscopy tests were conducted at different potentials and in the frequency range of 10^{-2}–10^5 Hz with peak-to-peak amplitude of 10 mV. Capacitance measurements were carried out at frequencies of 1, 10, and 50 kHz with potential amplitude of 10 mV peak to peak. Each electrochemical experiment was repeated at least twice to insure the reproducibility of results.

4.5 X-ray photoelectron experiments

In order to investigate the chemical composition of the surface films, the chalcopyrite electrodes were polarized at different constant potentials of 450, 650, 700, 870, 900, 950 and 1000 mV (*vs.* SHE) and then analyzed using X-ray photoelectron spectroscopy. For the sake of comparison, the surface composition of a polished sample of chalcopyrite with no exposure to solution and that of a sample immersed in the electrolyte for 6 hours were also analyzed. In order to minimize surface modifications after polarization, the chalcopyrite electrodes were rinsed with distilled water to remove residual acid and then transferred immediately to an evacuated desiccator and stored before transfer into the XPS vacuum. XPS was conducted with an Axis Ultra DLD spectrometer (Kratos Analytical) with a monochromatic Al excitation (1486.7 eV) operating at 108W. For reference, the binding energy of the Au 4f7/2 line was found to be 83.88 eV with the FWHM of 1.4 eV. Binding energy calibration was based on C 1s at 284.6 eV.

In addition to all of the above XPS experiments, in order to remove the passive film, only a few XPS experiments were performed after etching of the mineral with an Ar^+ ion beam (1 keV beam energy). The results of these experiments were used as reference for the peak position of different species in chalcopyrite. However, a consequence of the ion beam etching might be alteration of the surface species. In order to eliminate the acquisition of invalid results, the peak positions obtained were compared with those in the literature. One parameter of particular concern for the alteration of surface species is the argon ion beam energy and this parameter should be selected carefully. Ar^+ ion etching with energies higher than 1.5 keV at long durations (more than 20 min) can result in species alteration and enrichment of the metals on the surface [Otte *et al.,* 2000; Glatzel *et al.*, 2002]. Therefore, a beam energy of 1 keV and short etching times were applied. Additionally, in order to limit the creation of etch pits, the ion beam was rastered on the surface of chalcopyrite to etch a large surface area in comparison to the area that was used to collect the spectra. XPSPeak 4.1 software was used to fit the XPS peaks.

4.6 Scanning electron microscope study

In order to characterize the surface morphology of the minerals and the surface layers which were formed after dissolution, a scanning electron microscope with light element EDX (Hitachi S-3000N) was used.

5 Electrochemical dissolution of pyrrhotite in hydrochloric acid solution[1]

5.1 Introduction

Minerals of pyrrhotite ($Fe_{1-x}S$ and Fe_7S_8) are among the major minerals found in ores of the Sudbury basin (Ontario, Canada). These minerals are usually separated from the other desired metal sulfides through ore beneficiation and as a result, a large amount of pyrrhotite tails are available in the area as waste material. The paymetal content of the disposed tailings make them an interesting mineral resource for further processing and extraction of nickel [Droppert and Shang, 1995; Ke and Li, 2006; Wang, 2008], and gold [Wang, 2008; Lehmann *et al.*, 2000; Ellisa and Senanayake, 2004]. Therefore, studies aimed at understanding the dissolution behavior of pyrrhotite in acidic electrolytes are essential. However, the most interesting aspect of the electrodissolution study of pyrrhotite is its compositional similarity to chalcopyrite. In fact, pyrrhotite electrochemistry may be considered to represent a simplified case of chalcopyrite electrochemistry; as pyrrhotite is a Fe-S binary system (metal to sulfur ratio of *c.a.* 1) while chalcopyrite is the more complex ternary system of Cu-Fe-S (metal to sulfur ratio of 1). Hence, the results obtained regarding the dissolution mechanism of pyrrhotite would be applicable to chalcopyrite dissolution. Additionally, it must be mentioned that the dissolution mechanism of both pyrrhotite and chalcopyrite minerals are very similar as they both passivate in acidic solutions by formation of a metal deficient sulfide film (this will be further proven in the next few chapters). However, other Fe-S minerals (e.g. pyrite, FeS_2) dissolve through different mechanisms. For instance, pyrite leaching proceeds by simultaneous dissolution of Fe and S and no passive film forms on the surface. Hence, we believe that the electrochemical dissolution of pyrrhotite is most like that of chalcopyrite. Moreover, it should be mentioned that electrochemical impedance spectroscopy (EIS) is the major technique applied in this thesis. Although EIS is a powerful method for such studies, due to the complexity of the layers which form when complex minerals are dissolved and due to the intricacy of EIS, this technique has been disregarded in

---

[1] A version of this chapter has been published: "Ghahremaninezhad, A., Asselin, E., Dixon, D.G., 2010, Journal of Electrochemical Society, 157, C248–C257".

mineral electrochemistry. Thus application of this technique on a simpler system (i.e. Fe-S) before the more complex chalcopyrite system seemed essential.

Thermodynamic data (via E-pH diagrams) indicate that pyrrhotite will dissolve at pH less than 2 [Hamilton and Woods, 1981; Biernat and Robins, 1972]. Several workers have suggested that main issue in the acidic dissolution of pyrrhotite is the formation of an impermeable layer of elemental sulfur around the pyrrhotite particles which hinders their dissolution [Filippou et al., 1997; Beolchini and Veglio, 1999]. In order to increase the leaching kinetics of pyrrhotite, characterization of the layers formed during dissolution is essential and electrochemistry is a powerful method to this end. Cyclic voltammetry studies on pyrrhotite carbon paste electrodes by Almeida and Giannetti [2003] in acetic acid/sodium acetate solution (pH 4.5) show three anodic peaks above the open circuit potential (E_{OC}). These results are similar to those of Hamilton and Woods [1981] and Mikhlin [2000]. The first anodic peak is considered to be the formation of elemental sulfur:

$$Fe_{1-x}S \longrightarrow (1-x)\,Fe^{2+} + S + 2\,(1-x)\,e^- \qquad\qquad 5\text{-}1$$

In this step, ferrous ions dissolve and elemental sulfur accumulates on the surface of the electrode [Hamilton and Woods, 1981]. As more sulfur mounts up on the surface, it becomes more difficult for Fe^{2+} ions to diffuse and a high concentration of ferrous ions remains between the mineral surface and sulfur layer. Further increase in potential will result in the second peak which represents the oxidization of a portion of the trapped Fe^{2+} to Fe^{3+} [Almeida and Giannetti, 2003]. However, according to Paul et al. [1978], the accumulation of Fe^{2+} can reduce the proton concentration near the electrode which favors the formation of thiosulfate [Almeida and Giannetti, 2003]. While their study focused on the dissolution behavior of galena, their reaction mechanism may be extended to pyrrhotite yielding the following reactions [Almeida and Giannetti, 2003]:

$$2\,S + 3\,H_2O \longrightarrow S_2O_3^{2-} + 6\,H^+ + 4\,e^- \qquad\qquad 5\text{-}2$$

$$2FeS + 3H_2O \longrightarrow S_2O_3^{2-} + 2Fe^{2+} + 6H^+ + 8e^- \qquad\qquad 5\text{-}3$$
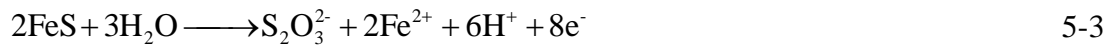
According to Biernat and Robins [1972] these reactions are thermodynamically feasible; however these reactions may not be possible in very low pH solutions with high proton acitivity such as in the case of the test solution used in the present study. A further increase in potential shows the third peak in a cyclic voltammogram which is possibly

associated with the oxidation of reaction-formed intermediates and/or sulfate formation [Almeida and Giannetti, 2003]:

$$S_2O_3^{2-} + 5\,H_2O \longrightarrow 2\,SO_4^{2-} + 10H^+ + 8e^- \qquad\qquad 5\text{-}4$$

Various studies show that, in addition to the species mentioned, the formation of different sulfur species during the electrochemical dissolution of sulfide minerals is possible [Bevilaqua *et al.*, 2004; Viramontes-Gamboa *et al.*, 2007; Abraitis *et al.*, 2004; Mikhlin *et al.*, 2004; Harmer *et al.*, 2006]. There is not complete agreement between researchers on the reaction mechanisms and reaction products, but the final product of pyrrhotite dissolution is considered to be some ferric compounds, elemental sulfur, and sulfate according to the following overall reaction [Mikhlin 2000]:

$$Fe_{1-x}S + 4yH_2O \longrightarrow (1\text{-}x)Fe^{3+} + y\,SO_4^{2-} + (1\text{-}y)\,S + 8yH^+ + 3(1\text{-}x+2y)e^- \qquad 5\text{-}5$$
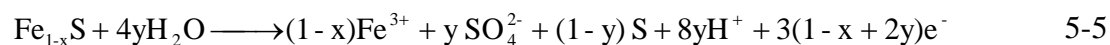
The evolution of surface layers during the dissolution of sulfide minerals has been studied with different electrochemical and analytical methods and there is some controversy associated with the application of some ex-situ methods such as X-ray photoelectron spectroscopy [Bevilaqua *et al.*, 2004; Mikhlin *et al.*, 2004; Buckley and Woods, 1994]. Hence, in-situ analytical techniques are among the major methods of interest for studies related to dissolution processes. Most of the sulfide minerals are considered to be semiconductor materials and therefore applying proper analytical methods for semiconductors would be very useful. Mott-Schottky analysis is a powerful in-situ electrochemical technique which can characterize the semiconducting behavior of surface layers formed during the dissolution of minerals. Applying this method makes it possible to understand the semiconducting behavior of the surface layers at different potentials [Morrison 1980; Memming 2001].

In this chapter, which is concerned with the electrochemical dissolution of pyrrhotite, the nature of the surface layers and their semiconducting properties at different potentials will be discussed. EIS is applied to understand the growth sequence of different surface layers. In-situ AC impedance is used to extract Mott-Schottky plots and characterize the electrolyte/semiconductor interface. Using the EIS and chronoamperometry results, a model is generated for the dissolution sequence of pyrrhotite at different potential intervals.

5.2 Results and discussion

5.2.1 Open circuit potential study

Figure 5-1 presents five open circuit potential (OCP) *vs.* time curves for three different pyrrhotite electrodes. Two of the curves are repeat OCP measurements of the same sample after polishing with carbide paper. There is a slight increase during the first 20 minutes of the test before reaching steady state. The maximum potential variation at initial immersion and after 20 min immersion is $\pm$ 35 mV and $\pm$ 5 mV, respectively. All electrodes used in this study displayed a zero immersion time OC potential of 350 ± 35 mV.
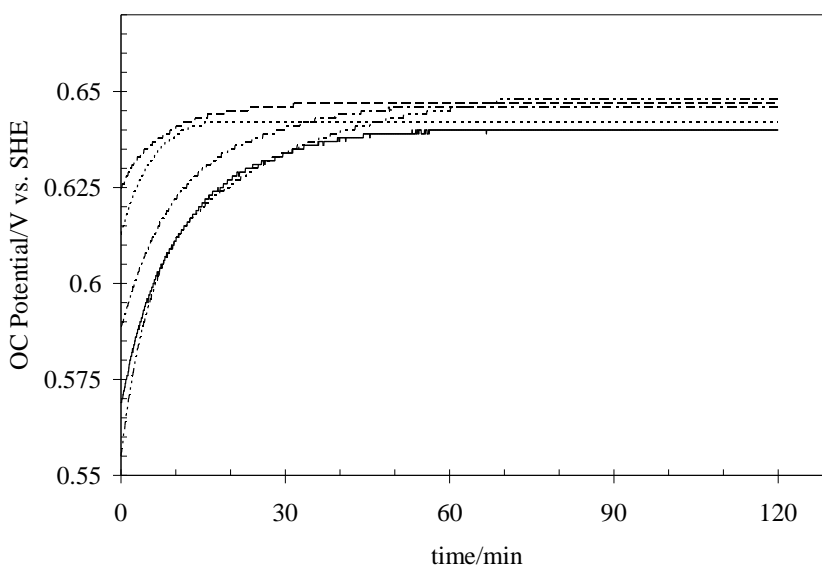
Figure 5-1: Open circuit potential (OCP) of the three different pyrrhotite electrodes *vs.* time; two of the curves show the OCP of same samples after polishing with carbide paper.

5.2.2 Potentiodynamic study

Figure 5-2 shows the potentiodynamic curves for the electrode in the dark and under irradiation at scan rates of 0.5 and 5 mV s^{-1}. Potentiodynamic polarization curves (a) and (b) are very similar, and both demonstrate a change in slope around 470 mV, indicating increasing resistance to dissolution. Afterward, a rapid increase in the dissolution rate begins in the potential range of 630 to 700 mV. Curve (c) of Figure 5-2 presents the polarization at a lower scan rate of 0.5 mV s^{-1}. Generally, applying a lower scan rate will reveal a closer approximation of steady state electrode behavior. Through comparison of curves (a) and (b)

51

in Figure 5-2, it is clear that the increased slope of the *E–i* curve in the potential range of 470 to 600 mV is not associated with the formation of a true passive film on the surface. This will be discussed further in the next section. On the other hand, the slower scan rate plot lends support to the idea that a passive layer is formed at potentials above 700 mV. Therefore, the potentiodynamic polarization curves at different scan rates reveal the existence of two distinct regions during pyrrhotite polarization: a quasi-passive region at low potentials (470 to 600 mV) and a passive region at potentials higher than 700 mV. The nature of these layers will be discussed in more detail in the next section.
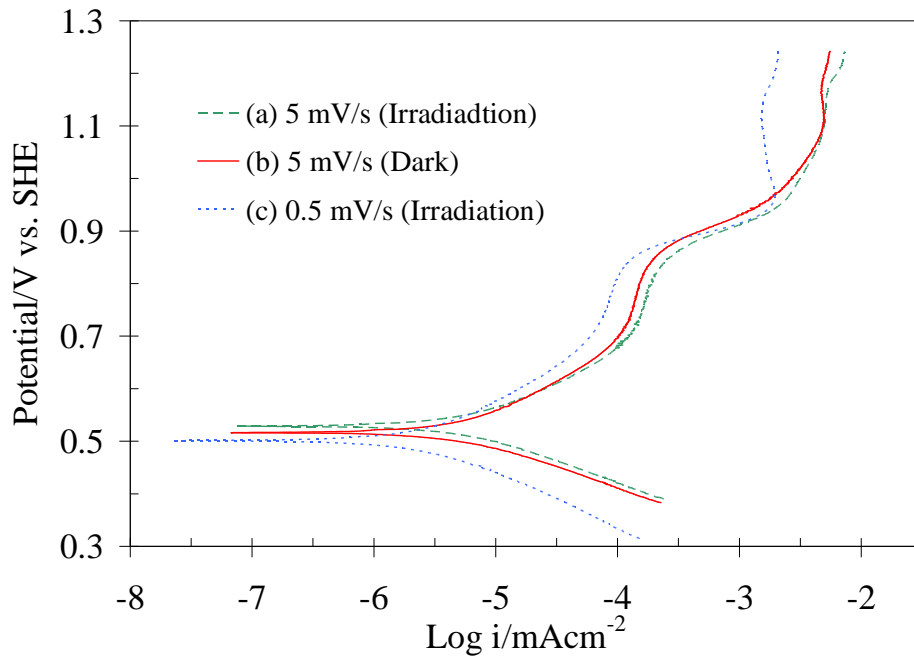
Figure 5-2: Potentiodynamic curves for the pyrrhotite electrode in 1 M HCl electrolyte.

5.2.3 Electrochemical impedance spectroscopy study

Figure 5-3 presents impedance spectra for the pyrrhotite electrode at different potentials. Figure 5-3a shows a response at the OC potential which is associated with mass transfer. Asselin *et al* [2007] have related this kind of behavior to the formation of a thin surface layer on the electrode. Perhaps, this layer was formed during sample preparation at the polishing stage or, alternatively, during the 10 min stabilization time in the electrolyte prior to each electrochemical experiment. Figure 5-3b shows the same behavior of Figure 5-3a, but with smaller total impedance at 692 mV$_{SHE}$. Furthermore, in Figure 5-3b a deviation from pure

linear behavior is seen as a partially resolved semicircle is formed at high frequencies. Hence, the stability of the surface layer decreases with an increase of the potential and simultaneously the effect of charge transfer in the system increases [Asselin *et al.,* 2007]. Similar frequency response has been observed, also at low potentials, on chalcopyrite as reported by Velásquez et al. [2005]. In Figure 5-3c, at 782 mV$_{SHE}$, a partially resolved semi-circle at high frequencies (normally attributed to charge transfer resistance at the solution/surface layer interface) and an inductive loop at low frequencies are apparent. The latter is characteristic of the dissolution of the passive layer through transpassive dissolution [Betova *et al.,* 2002; Bojinov and Tezvetkoff 2003; Erne and Vanmaekelbergh 1997]. Figure 5-3d presents impedance spectra for the electrode at 917 mV$_{SHE}$ which contains a charge transfer related semicircle at high frequencies, an inductive loop at medium frequencies and a loop consisting of combination of a capacitance impedance and a related resistance at lower frequencies (0.1 – 0.01 Hz). A comparison of Figures 5-3c and d shows that, by increasing the potential from 782 to 917 mV$_{SHE}$, a secondary surface layer forms as the behavior at the lowest frequencies changes from inductive to capacitive [Bojinov *et al.,* 2002]. Both Figures 5-3e and f demonstrate the growth of this second layer at lower frequencies through the increase in the total impedance of the system. It is worth mentioning that in Figure 5-3f there is an apparently large difference between the impedance of the first (small semicircle) and second (larger partially resolved semicircle) surface layers – a finding which will be supported with Mott-Schottky studies discussed below. Figure 5-3g presents the behavior of the electrode at 1092 mV$_{SHE}$ which exhibits negative real impedance at this potential and which can be attributed to the transpassive dissolution of the second surface layer. This is a finding similar to that presented by Keddam *et al.* [1985] for transpassive dissolution of nickel. Other researchers have further attributed these inductive loops to small, localized areas of increased anodic activity and transpassive dissolution [Vanmaekelbergh and Erne 1999; Bojinov et al., 2000].
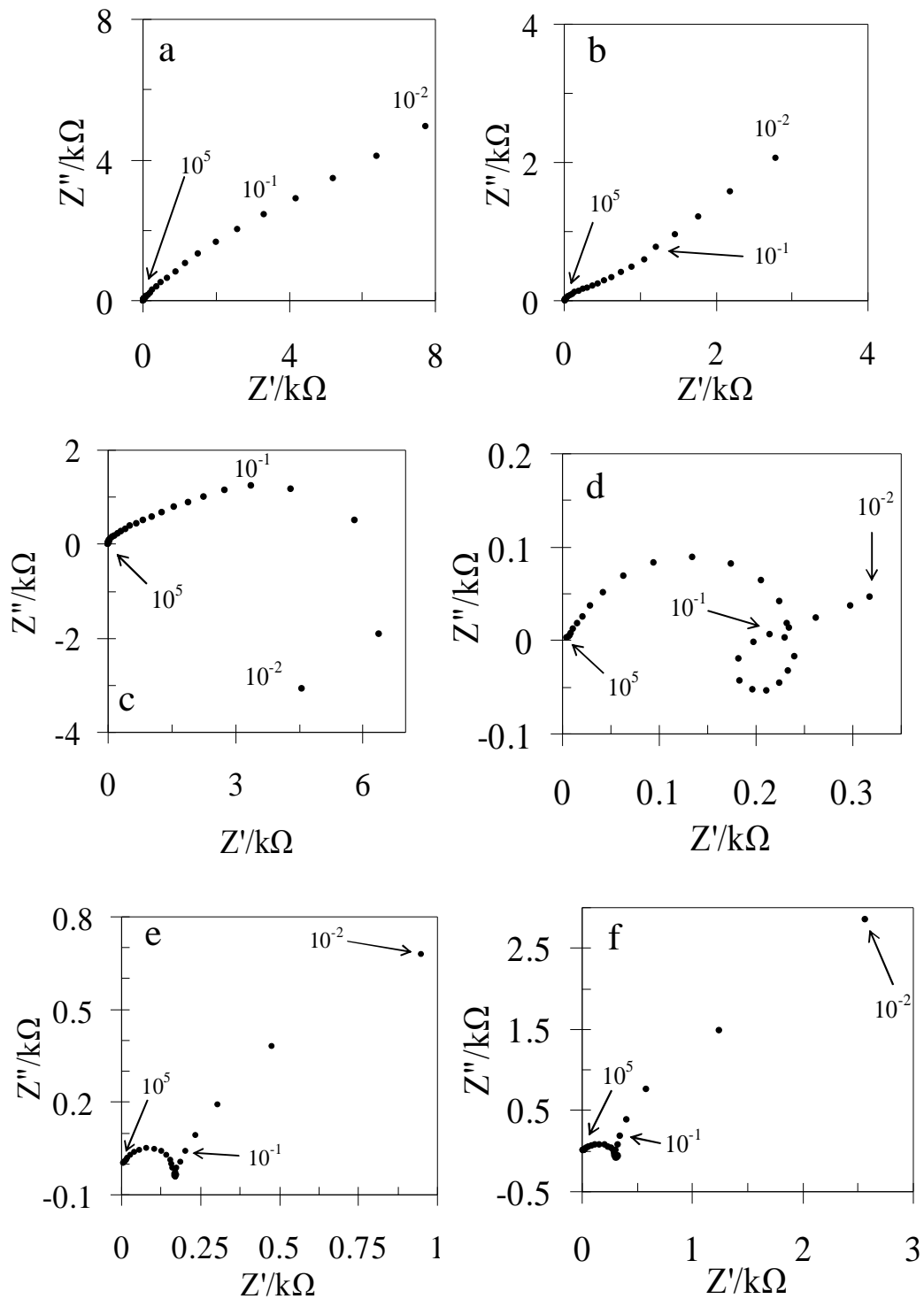
Figure 5-3: Impedance spectra of a pyrrhotite electrode in 1 M HCl at (a) OCP, (b) 692, (c) 782, (d) 917, (e) 967, (f) 1042, (g) 1092 mV *vs.* SHE. Parameter is frequency in Hz.
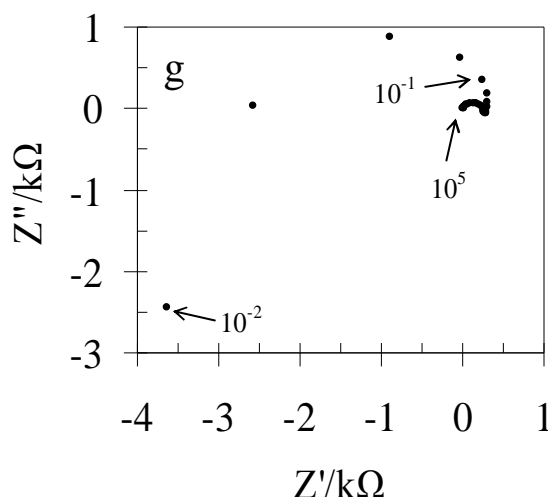
Figure 5-3: continued.

As a brief conclusion to this section, the EIS studies have shown the formation of two distinct surface layers on pyrrhotite as a function of potential. The first quasi-passive layer forms during preparation or upon immersion of the electrode and the dissolution of this layer begins at around 782 mV$_{SHE}$ (cf. Figure 5-2). This layer would be the reason for the change in slope observed through the potential range of 712 to 842 mV$_{SHE}$. The formation of the first layer can be considered independent of the concurrent process which also occurs at low anodic potentials (about 100 mV above the OCP) and results in the production of ferrous ions (cf. reaction 5-1) and elemental sulfur [Hamilton and Woods 1981]. This sulfur layer product would remain on the surface of the sample and could impede the rate of dissolution of the electrode, thus contributing to the apparent passivation or slowing of the reaction as potential is increased. However, Figure 5-3c shows that this quasi-passive layer, which is dissolving between 712 and 842 mV$_{SHE}$, is not stable and so the effect of the sulfur layer on the surface could in fact be more dominant than the effect of this passive film. This idea is substantiated by the potentiodynamic study undertaken at different scan rates (Figure 5-2) which demonstrated that the resistance to polarization in the potential range of 712 to 842 mV$_{SHE}$ is not because of the formation or thickening of a true passive film on the surface. Beyond this primary film, and as potential is increased to the range of 842 to 917 mV$_{SHE}$, the dissolution rate of pyrrhotite increases (Figure 5-2). Studies by Hamilton and Woods [1981] and Almeida and Giannetti [2003] have attributed this to the oxidation of Fe^{2+}. EIS results of the present study show that the dissolution of the quasi-passive layer in this potential region

55

is the dominant process. It is possible that this quasi-passive film is an Fe^{2+} compound which at higher potentials oxidizes to Fe^{3+}. At more anodic potentials (917 mV_{SHE} and higher) the dissolution of the first layer and formation of the second layer occurs simultaneously which is in accordance with the results of potentiodynamic scans. Almeida and Giannetti [2003] have suggested that this second surface layer would be a sulfate layer which forms by reaction 5-4. Increasing the potential of the electrode from 917 to 1042 mV_{SHE} increases the total real impedance of the electrode by about a factor of ten, which means that the second layer is substantially more passivating than the first.

5.2.4 Mott-Schottky study

In order to understand the electrical properties of the passive layers which are observed here, Mott-Schottky studies were undertaken. Figures 5-4 and 5-5 show the Mott-Schottky plots for the pyrrhotite electrode which were constructed from capacitance *vs.* electrode potential measurements at 1, 10 and 50 kHz. Experimentally, the total capacitance value of an electrode (C) can be determined from the measured imaginary part of the impedance (Z'') at sufficiently high ac frequency (f) using Eq. 5-6 [Stansbury and Buchana 2000]:

$$Z'' = \frac{-1}{2\pi fC}$$
5-6

Generally, in the case of semiconductor electrochemistry, the interface between a semiconductor electrode and an electrolyte can be considered as two capacitors in series: the space charge region of the semiconductor and the Helmholtz layer. Thus the measured capacitance of the film-electrolyte interface can be described by the following relationship:

$$\frac{1}{C} = \frac{1}{C_H} + \frac{1}{C_{SC}}$$
5-7

where C_{sc} and C_H are the space charge region and the Helmholtz capacitance, respectively. The capacitance for the space charge region is much smaller than that for the double layer ($C_{SC} \ll C_H$) [Bard and Faulkner, 2001; Kareh *et al.,* 2009; Schmuki *et al.,* 1995], such that one can neglect the Helmholtz double layer capacitance in most calculations. Therefore, the measured capacitance value (C) is equal to the space charge capacitance which is presented as the Mott-Schottky relation in the following expression:

$$\frac{1}{C_{SC}^2} = \frac{2}{e\varepsilon\varepsilon_o n_o}\left(E - E_{fb} - \frac{kT}{e}\right) \qquad\qquad 5\text{-}8$$

where e represents the charge of an electron, ε the dielectric constant of the semiconductor, ε_o the permittivity of free space, n_o the donor density, E the applied potential, E_{fb} flat band potential, k the Boltzmann constant, and T the absolute temperature, where the term kT/e is 25 mV at 25°C [Gryse et al., 1975]. The Nyquist plots presented in the previous section show complex responses with several time constants for each studied potential. This means that the capacitance obtained via Mott-Schottky analysis cannot represent the definitive space charge capacitance. However, a change in slope in the Mott-Schottky plots is necessarily due to a change of the electrical nature of the surface of the electrode. The Mott-Schottky plots of Figure 5-4 show that the surface layers of pyrrhotite (in the potential range of 0.2 to 1.25 V *vs.* SHE) are *n*-type semiconductors, based on the increasing slopes of the curves. An interesting feature of the plots of Figure 5-4 is the sharp break at around 942 mV$_{SHE}$. The break was observed for all the samples around this potential under both dark and irradiated conditions. Not surprisingly this potential is very close to the potential of formation of the second passive layer shown in the potentiodynamic and EIS studies (Figures 5-2 and 5-3). Therefore, it is thought that the change in slope of the Mott-Schottky plots is a consequence of the formation of a separate surface layer on the electrode during the dissolution process.
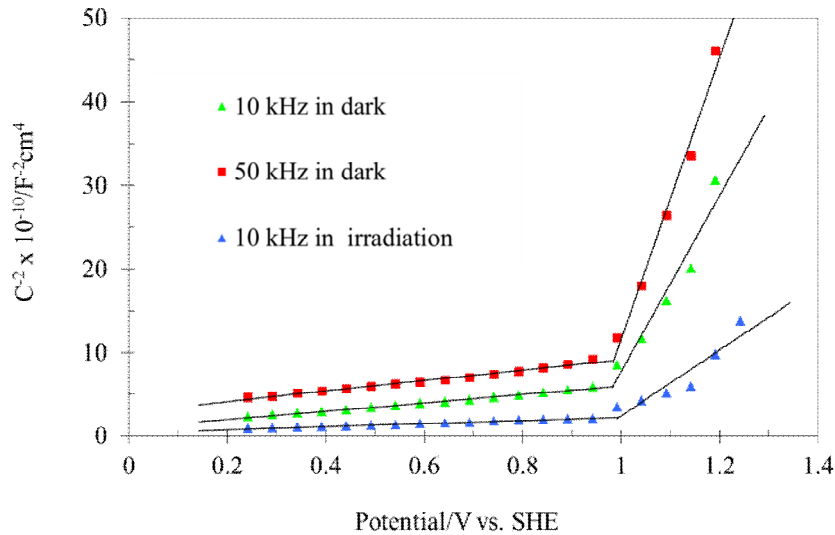
Figure 5-4: Mott-Schottky plots for pyrrhotite in 1 M HCl electrolyte in the dark and under irradiation.

Kennedy and Frese [1978] have suggested that the break in the Mott-Schottky curve can also be explained by assuming the existence of two different kinds of donors in the semiconductor surface layer of pyrrhotite. Hence, the two Mott-Schottky slopes could be:

$$S_1 = \frac{2}{e\varepsilon\varepsilon_o n_1} \qquad (E < E_B) \qquad\qquad 5\text{-}9$$

and

$$S_2 = \frac{2}{e\varepsilon\varepsilon_o n_2} \qquad (E > E_B) \qquad\qquad 5\text{-}10$$

where E_B is the break potential and n_1 and n_2 are the densities of donors before and after E_B, respectively. This suggests that one kind of donor is very close to the conduction band and the second kind is deeper (*i.e.*, far from the conduction band). Assuming the scenario suggested by Kennedy and Frese [1978], increasing the potential of the semiconductor up to potentials more than that of the break potential will cause the ionization of deep donors in the space charge region. A consequence of this phenomenon is an increase in the charge carrier density in the space charge region and a decrease in the slope of the Mott-Schottky plots as potential is increased. In the present study we have an increase in the slope of the Mott-Schottky plots which means that the mechanism proposed by Kennedy and Frese [1978] is likely not the case here. As a result, from Figure 5-4, the linear behavior of the Mott-Schottky plots over the potential interval of 200 to 950 mV$_{SHE}$ is related to the first quasi-passive layer which forms during sample preparation and the break in the plots near 950 mV$_{SHE}$ is due to the formation of the second surface layer which is described in the EIS studies. The semiconductive properties of the second layer are to some extent different from those of the first layer.

From a practical hydrometallurgical perspective, the dissolution of pyrrhotite at lower potentials (< 950 mV *vs.* SHE) is more interesting. Thus, more study on the properties of the first surface layer is essential. For this reason we have focused on the properties of the surface layer formed over the potential range of 200 to 950 mV$_{SHE}$. Figures 5-5a and b present the Mott-Schottky plots for pyrrhotite under irradiation and in the dark, respectively. Figure 5-5a shows good linear behavior for potentials lower than 750 mV$_{SHE}$ while increasing the potentials above 750 mV causes a scattering of the data. It is thought that the dissolution of the first passive layer would be the reason for such scattered behavior and

Figure 5-3c supports this idea by presenting the dissolution of this layer in this potential region. Table 5-1 shows the flat band potentials which were obtained from the intercepts of $1/C^2$ vs. potential by subtracting the term $kT/e = 25$ mV from the intercept (refer to Eq. 5-7). The dielectric constant, ε, of pyrrhotite is around 82 [Rosenholtz and Smith 1936] and the donor density in the electrode for the two different potential regions was determined using this number (Table 5-1). Table 5-1 also contains the effective Debye length which was calculated according to the Debye equation [Memming 2001]:

$$L_{D,eff} = \left(\frac{\varepsilon \varepsilon_o kT}{2ne^2} \right)^{1/2}$$

5-11
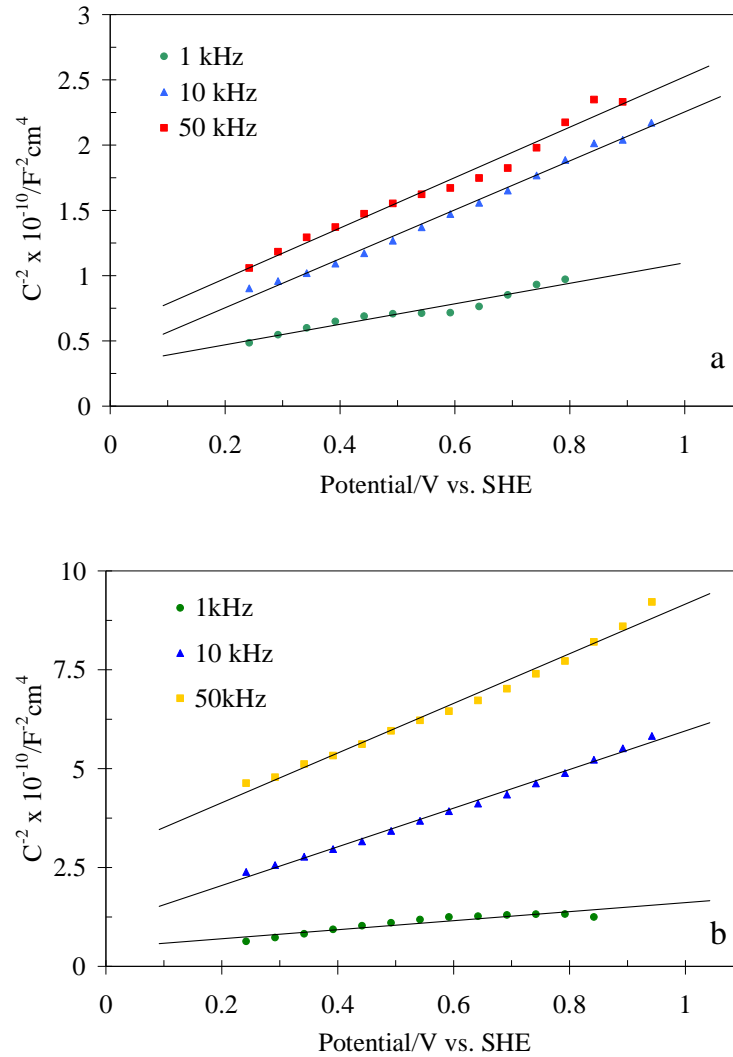
Figure 5-5: Mott-Schottky plots for pyrrhotite electrode in 1M HCl electrolyte, (a) under irradiation and, (b) in dark.

Table 5-1 clearly shows that the charge carrier density of the quasi-passive surface layer in the dark is lower than that under irradiation. This is the case at higher potentials as well. Table 5-1 also shows that the values of the donor density and effective Debye length for pyrrhotite change dramatically at the break potential. This significant difference between the two surface films was also observed by EIS (cf. Figure 5-3f). Figure 5-6 shows the thickness of space charge region, d_{SC}, as a function of potential, $\Delta\varphi_{SC}$, which is obtained by [Azumi $et\ al.$, 1987]:

$$d_{SC} = 2L_{D,eff}\left[\frac{e\Delta\phi_{SC}}{kT} - 1\right]^{1/2} \qquad\qquad 5\text{-}12$$

Eq. 5-12 considers a semiconductor electrode with simple dissolution behavior which is not the case for the pyrrhotite electrode presented in this study with complex Nyquist responses. For this reason, the thickness of the space charge region presented in Figure 5-6 might not be very accurate but does, nevertheless, present evidence for a significant change in the space charge region's thickness at the break potential. A comparison of the two distinct surface layers reveals that the second, higher potential, layer has a lower donor density and consequently will have lower capacitance. This lower donor density infers that the second layer is less conductive than the first and, therefore, is likely better at hindering the dissolution of pyrrhotite. These results are similar to the results of Hamilton and Woods [1981], Almeida and Giannetti [2003], and Mikhlin [2000] who suggest the formation of different sulfur species during the electrochemical dissolution of sulfide minerals.

Table 5-1: Flatband potentials for pyrrhotite in 1 M HCl electrolyte in dark and under irradiation.

	f kHz	E_{fb} mV $vs.$ SHE	n_1 cm^{-3}	$L_{D,eff,1}$ nm	n_2 cm^{-3}	$L_{D,eff,2}$ nm
	1	−423	2.19×10^{20}	0.810	7.15×10^{18}	4.505
Irradiated	10	−227	0.92×10^{20}	1.258	4.37×10^{18}	5.769
	50	−332	0.89×10^{20}	1.277	3.98×10^{18}	6.041
	1	−436	1.51×10^{20}	0.981	5.21×10^{18}	5.275
Dark	10	−243	0.35×10^{20}	2.031	1.64×10^{18}	9.420
	50	−483	0.27×10^{20}	2.302	1.02×10^{18}	11.914

5.2.5 Model development

The EIS data of section 5.2.3 were fitted to three equivalent electrochemical circuits of Figure 5-6. These equivalent circuits represent a preliminary step in the elucidation of the electrochemical processes taking place at the electrolyte/electrode interface. The observed Nyquist impedance plot at high anodic potential (1092 mV$_{SHE}$; Figure 5-3g) is complex due to the existence of the negative real resistance.
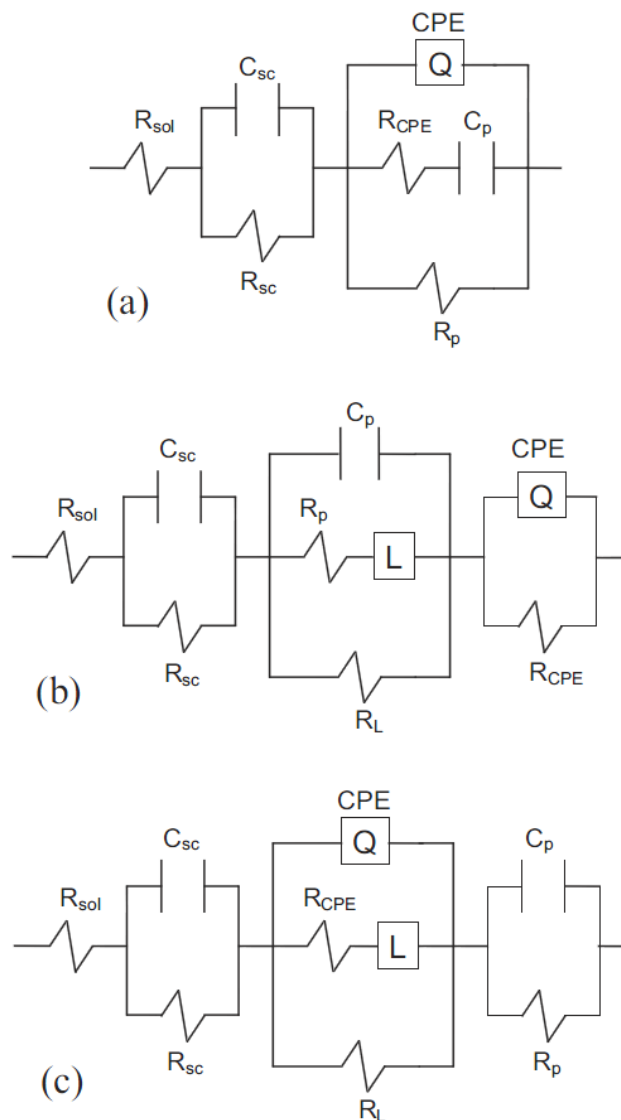
Figure 5-6: Equivalent electrochemical circuit for the Pyrrhotite/electrolyte interface at, (a) low anodic potentials (OC – 692 mV), (b) 782 mV, (c) high anodic potentials (917 – 1042 mV).

The authors have tried to fit the plot by using the circuits previously applied, such as [Epelboin and Keddam 1972; Bojinov *et al.,* 1993]. The proposed circuit by Epelboin and

Keddam [1972] considers the dissolution and passivation of metals (iron and nickel) in sulfuric aqueous media. Also, the paper by Bojinov *et al.* [1993] studies the impedance response of a tin metal electrode in sulfuric aqueous media. Their work and also the work by Glarum and Marshall [1985] have proposed that the negative real impedance, like that of Figure 5-3g, is associated with a time constant which includes a negative resistance connected with a negative capacitance. However, the results of the fitting process were not completely satisfactory and needed more study. The present author is of the opinion that almost all of the publications to date which have dealt with such complex impedance behavior have been done on simple metallic electrodes such as iron, nickel [Epelboin and Keddam 1972], tin [Bojinov et al., 1993] and copper [Glarum and Marshall 1985]. Hence, it is reasonable to consider that since mineral electrodes have a substantially intricate nature than metallic electrodes, the observed complex behavior of the pyrrhotite electrode, as a mineral, would be more complicated to interpret. However, the proposed mechanisms for the metallic electrodes may still be applicable for the pyrrhotite electrode. Therefore, in the present contribution, instead of proposing an electrochemical circuit model for the observed behavior at 1092 mV$_{SHE}$, the authors have looked into the physical meaning of such behavior as is consistent with previous efforts in the literature (this interesting feature of the pyrrhotite mineral electrode at high anodic potentials will be studied in a subsequent paper). Keddam and Takenouti [1985] have attributed the negative real impedance for a nickel electrode to transpassive dissolution. Elsewhere, Epelboin and Keddam [1972] have related this behavior to the competitive dissolution and passivation reactions of nickel. Studying the dissolution of a tin electrode, Bojinov *et al.* [1993] have suggested that the low frequency response is a complicated coupling between the passivation and active dissolution processes at the film/solution interface. In their work, a negative capacitance has been applied in the modeled electrochemical circuit and has been considered to be a measure of the degree of coverage of intermediate species - those which are assisting the dissolution of the passive film. However, studying the dissolution of copper in phosphoric acid solution, Glarum and Marshall [1985] have explained the complex impedance behavior by the dependence of the dissolution process on high mobility hydrogen ions. From their work, by increasing the potential of the electrode, the electrical fields external to the barrier lower the concentration of H$^+$ and so the dissolution rate will be reduced. Considering a kinetic system including two adsorbed

intermediates and two dissolution paths, Bojinov [1996] has reproduced the general features of the impedance spectra of copper, nickel, tin and antimony in sulfuric acid solutions. However, the proposed model does not take into account the possibility of bilayer film formation on the electrode.

The modeled circuit for low anodic potentials (OCP – 692 mV$_{SHE}$) is presented in Figure 5-6a. Figure 5-6b shows the modeled circuit at 782 mV$_{SHE}$ where transpassive dissolution of the surface layer occurs. The model for high anodic potentials (917 – 1042 mV$_{SHE}$) is illustrated in Figure 5-6c. In all of the models the R_{sol} element represents the solution resistance. The C_p/R_p and the C_{SC}/R_{SC} pairs represent the capacitive and resistive behavior of the surface layer and the space charge region of the surface layer, respectively. The constant phase element (*CPE*) presents the effect of defects in the surface layer [Chen et al., 2008] and R_{CPE} represents the resistance of the *CPE* in the equivalent circuit. The CPE element, which compensates for the non-homogeneity in the system, is defined by two values, Q and n. The impedance, Z, of CPE is presented by Eq. 13 [Hsu and Mansfeld 2001; Orazem and Tribollet 2008]:

$$Z_{CPE} = Q^{-1}(j\omega)^{-n} \qquad\qquad 5\text{-}13$$

where Q is the CPE parameter, $i = (-1)^{1/2}$, ω is the frequency in rad s^{-1}, $\omega = 2\pi f$, f is the frequency in Hz, and n is the measure of the non-ideality of the capacitor and has a value in the range $0 < n < 1$. If n equals 1, then, Z_{CPE} is identical to that of a capacitor, $Z_C = (i\omega C)^{-1}$, where C is the capacitance. In fact, a capacitor is a constant phase element with a constant phase angle of -90°. Generally, a CPE behaves like a capacitance which varies with frequency. The presence of the CPE behavior may explain the frequency dependence of the capacitance measured in Figure 5-5. The element L may be due to the transfer of ions across the double layer or an increase of the area of the electrode by the partial dissolution of the surface layer [Vanmaekelbergh and Erne 1999] and R_L represents its resistance. In these circuits, contributions of the double layer capacitance and charge transfer resistance as well as the sample resistance have been neglected. This can be justified by the relatively high values of the double layer capacitance compared to those of the space charge region (C_{SC}) and capacitance of the surface layer C_p. Since these three capacitances are in series the double layer capacitance makes only a minor contribution to the total system capacitance. On the other hand, the electrode resistance is typically smaller than the resistance of the solution,

thus the sample resistance may be ignored. Otherwise, it may introduce a slight error in the obtained values for R_{sol}. Figure 5-7 presents the experimentally measured and calculated Nyquist curves obtained with the equivalent circuits of Figure 5-6 and the values of different elements of the equivalent circuits are shown in Table 5-2.
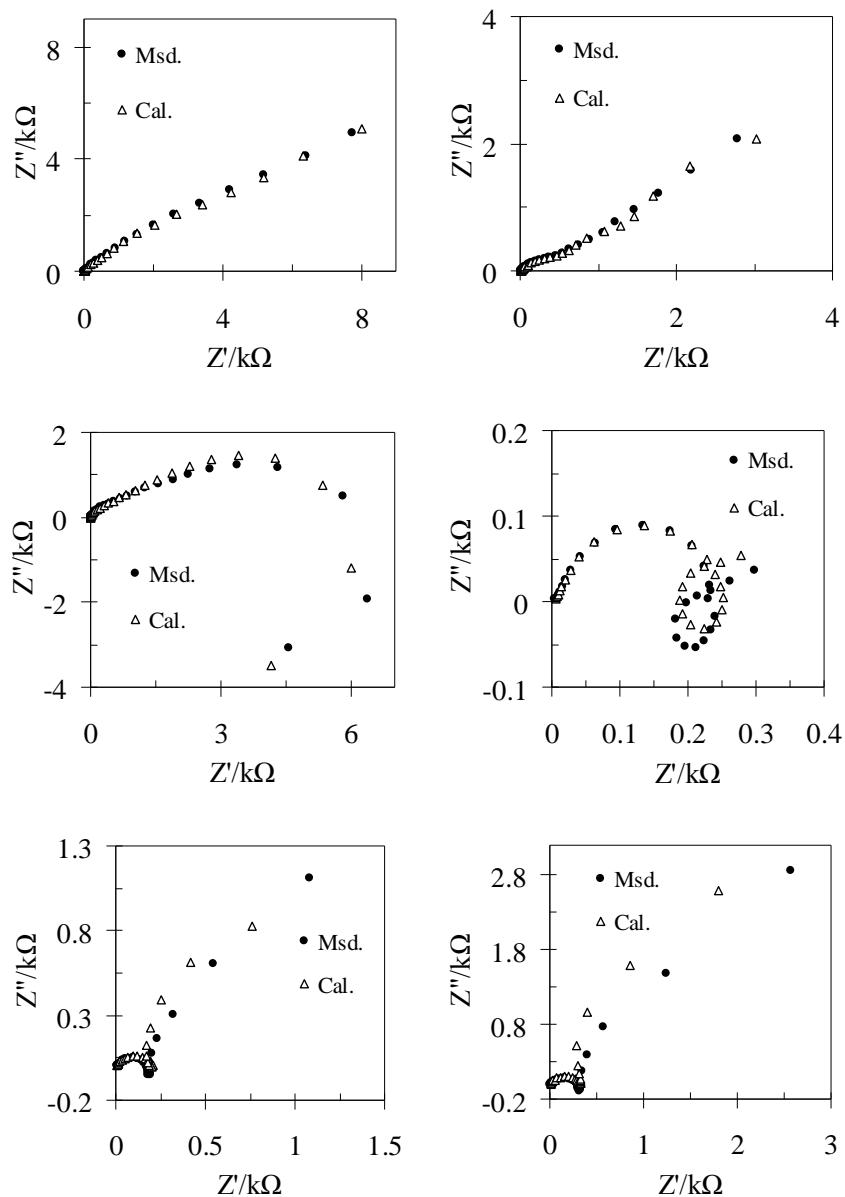
Figure 5-7: Measured and calculated Nyquist plots for pyrrhotite electrodes at (a) OCP, (b) 692 mV, (c) 782 mV, (d) 917 mV, (e) 992 mV, and (f) 1042 mV *vs.* SHE.

Table 5-2: Model parameters for equivalent circuits of Figure 5-6.

E (mV)	R_{SC} (Ω cm^2)	$10^6\ C_{SC}$ (F cm^{-2})	R_P (Ω cm^2)	$10^3\ C_P$ (F cm^{-2})	R_{CPE} (Ω cm^2)	$10^5\ Q$ (Ω s^{-n})	n	R_L (Ω cm^2)	L (H)
OCP	952.1	116.80	21710.0	0.39	24510.0	24.03	0.56	-	-
692	716.6	136.00	5434.0	2.95	975.2	21.15	0.56	-	-
782	5.2	2.40	19140.0	0.28	5.1	0.20	0.36	24.0	91150.0
917	11.0	0.55	8.9	35.40	243.3	1.58	0.74	8.9	88.0
942	8.8	0.41	4156.0	23.15	276.4	2.45	0.72	4156.0	51.4
967	7.0	0.44	1137.0	12.49	175.2	2.55	0.80	1137.0	951.1
992	8.4	0.43	1743.0	12.61	19.6	3.34	0.66	1743.0	267.3
1042	16.7	0.34	4355.0	4.43	308.8	1.61	0.68	4355.0	945.4

In order to determine the capacitance value of the electrode (C) from the measured impedance spectra, a simple circuit shown in Figure 5-8 was fitted. Here, R_{ohmic} is representing the ohmic resistance of the electrode and the CPE and R_t are describing the capacitance and resistance of the electrode's surface, respectively.
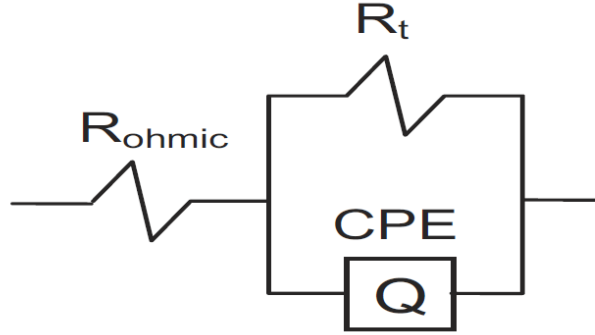
Figure 5-8: Simplified equivalent circuit model for the electrode.

In the potential region of active dissolution of the electrode ($842 - 912$ mV$_{SHE}$), the R_t element of the Figure 5-8 represents the resistance of the surface (which can be the resistance of the space charge region, Helmholtz double layer, or a combination of both). Then, the effective capacitance of the CPE will be calculated by Eq. 5-14 [Hirschorn et al., 2010]:

$$C_{eff} = Q^{1/n} \left(\frac{R_{ohmic}R_t}{R_{ohmic} + R_t} \right)^{(1-n)/n} \qquad \text{5-14}$$

where n and Q are the CPE parameters, as described before, R_{ohmic} and R_t are representing the ohmic resistances of the system and the surface, respectively. Considering $R_t \rangle\rangle R_{ohmic}$, then the Eq. 5-14 will be [Hirschorn et al., 2010]:

$$C_{eff} = Q^{1/n} R_{ohmic}^{(1-n)/n} \qquad \text{5-15}$$

where the C_{eff} represents an estimation of the capacitance of the electrode (C) as a function of R_{ohmic}. However, in the potential range of OC – 842 mV$_{SHE}$ and also potentials > 912 mV$_{SHE}$ the surface of the electrode is blocked with the surface layers. Therefore, the effective capacitance of the CPE element at these potential ranges will be calculated by Eq. 5-16 [Chen et al., 2008; Hirschorn et al., 2010]:

$$C_{eff} = Q^{1/n} R_t^{(1-n)/n} \qquad \text{5-16}$$

where the R_t shows the resistance of the surface layer (equal to the R_p values in Table 5-2) and other parameters have the same meaning of those in Eq. 5-15.

The results from electrochemical studies and modeled electrochemical circuits can be used to propose a reaction sequence for the dissolution of the pyrrhotite electrode. The first stage of the dissolution which takes place at potentials ranging between OC – 692 mV$_{SHE}$ may be related to the formation of a metal–deficient sulfide layer:

$$\text{Fe}_{1-x}\text{S} \longrightarrow \text{Fe}_{1-x-y}\text{S} + y\text{Fe}^{2+} + 2y\text{e}^- \qquad \text{5-17}$$

where the Fe$_{1-x-y}$S layer is a semiconductor layer with donor density of around 10^{20} cm^{-3} (ref. Table 5-1). Both of the C_{SC}/R_{SC} and C_p/R_p pairs of Figure 5-6a are referring to this layer and the constant phase element of the model indicates the effect of surface imperfections. If the electrode obeys Tafel kinetics from OC - 692 mV$_{SHE}$, then the Tafel slope, β_a, will be [Marcus 2002]:

$$\beta_a = \frac{2.03RT}{\alpha_a nF} \qquad\qquad\qquad 5\text{-}18$$

where α_a is the anodic transfer coefficient which can usually be approximated by 0.5 [Bard and Faulkner 2002], and n is the number of electrons taking place in the charge transfer limited reaction. For the case of reaction 5-17, Eq. 5-18 becomes:

$$\beta_a = \frac{2.03RT}{\alpha_a(2y)F} \qquad\qquad\qquad 5\text{-}19$$

and by applying Tafel analysis on Figure 5-9 the β_a value was calculated to be 131 mV/decade. Hence, the $2y$ value will be 0.796 and it is possible to rewrite the dissolution reaction 5-17 for the case of $x = 0.125$ (Fe_7S_8) with the stoichiometry of:

$$Fe_{0.875}S \longrightarrow Fe_{0.477}S + 0.398Fe^{2+} + 0.796e^- \qquad\qquad 5\text{-}20$$
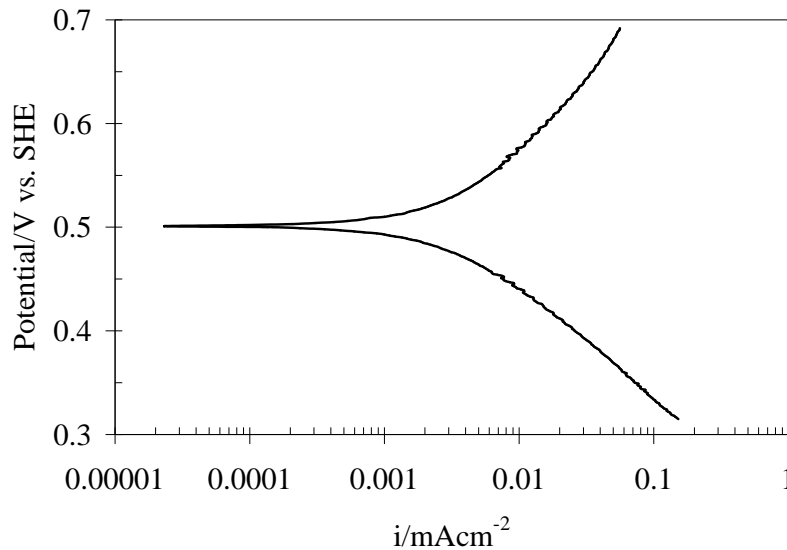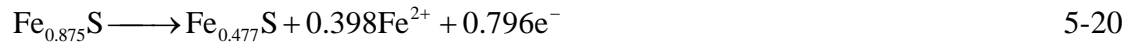
Figure 5-9: Tafel region polarization of the pyrrhotite electrode in 1 M HCl electrolyte.

The metal–deficient sulfide layer of $Fe_{0.602-x}S$ (or $Fe_{0.477}S$ when $x = 0.125$) is stable up to around 742 mV_{SHE} and by increasing the potential to higher values (i.e. 782 mV_{SHE}) this layer will dissolve:

$$Fe_{1-x-y}S \longrightarrow (1-x-y-\lambda)Fe^{2+} + \lambda Fe^{3+} + S + (2-2x-2y+\lambda)e^- \qquad 5\text{-}21$$
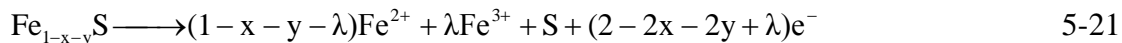
where λ is a constant ($0\langle\lambda\langle 1$) at each given potential (the ferric ion formation will be considered in more detail below). After complete dissolution of this first layer, the pyrrhotite might start to dissolve via Eq. 5-22:

$$Fe_{1-x}S \longrightarrow (1-x-\nu)Fe^{2+} + \lambda Fe^{3+} + S + (2-2x+\nu)e^- \qquad 5\text{-}22$$
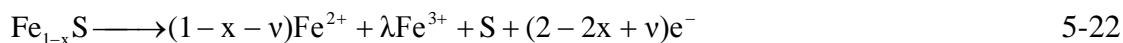
From the proposed reaction sequence for the dissolution of the pyrrhotite electrode, the first stage of the dissolution which takes place at potentials ranging between OC – 692 mV_{SHE} is related to the formation of a metal–deficient sulfide, by reaction 5-17. The results of the EIS experiments support this passive anodic behavior at low anodic potentials (see Figures 5-2a and b and related discussion). However, at higher potentials (i.e. 782 mV_{SHE}) the EIS experiments provide evidence of transpassive dissolution (see Figure 5-2c and related discussion) which we believe is associated with reaction 5-21. According to this reaction, in the potential range of 712 to 842 mV_{SHE}, the $Fe_{1-x-y}S$ passive film dissolves. However, elemental sulfur is also a product of reaction 5-21. Being a poor conductor, elemental sulfur film will impede the dissolution rate of the electrode. Thus, we have concluded that the decrease in the polarization current observed by lowering the scan rate from 5 to 0.5 mVs^{-1} (compare curves (a) and (c) of Figure 5-1) is due to the formation of an elemental sulfur reaction product and not because of the passivation process proposed in reactions 5-17 and 5-20.

This dissolution sequence of the electrode was also studied by chronoamperometry. Figure 5-10a shows the current (density)–time transient for the electrode after applying a potential step from OC potential to 782 mV_{SHE}. After a peak current (67 μAcm^{-2}) at initial immersion due to double layer formation, the Faradaic current results in the dissolution of iron atoms at the electrode surface. Consequently, a layer of the semiconductor $Fe_{1-x-y}S$ (or generally metal–deficient sulfide layer) forms on the surface and further thickening of this layer as time progresses slows down the dissolution rate. The dissolution rate reaches a minimum value after 60 sec (see inset of Figure 5-10a). Therefore, in the early stage of dissolution at 782 mV_{SHE}, reaction 5-17 –or more specifically reaction 5-20 – is believed to be the major dissolution reaction. However, because 782 mV is higher than the reversible potential for the ferrous to ferric ion oxidation reaction (770 mV_{SHE}), the production of ferric ion should also be considered at 782 mV_{SHE}. The sources of the ferric ion could be: (1)

ferrous to ferric oxidation on the surface of the mineral and (2) direct dissolution of the mineral as ferric (and ferrous) ions.

Studying the rate of the ferrous to ferric oxidation reaction on the pyrrhotite electrode was not the goal of this work. Determining the rate of the ferrous to ferric oxidation reaction on the pyrrhotite electrode (and generally mineral electrodes) is difficult due to existence of some other co-current oxidation reactions such as that of the pyrrhotite electrode itself, as Fe^{2+} and/or Fe^{3+}, and the oxidation of impurities which may also be present. On the other hand, it is possible to discuss about the ferrous to ferric oxidation reaction according to the literature. The ferrous to ferric oxidation reaction is a fast reaction on the surface of oxide free metals such as platinum and has been reported to have the exchange current density of 15 mA cm^{-2} [Makrides 1964]. However, superficially oxidizing the surface of metals will cause a ten thousand fold decrease in the exchange current density of Fe^{2+}/Fe^{3+} couple [Stansbury and Buchana 2000]. Reported values for superficially oxidized Fe, Ti, Fe-13.2% Cr, and 304 stainless steel electrodes are 10, 26, 1, 0.045 µA.cm^{-2}, respectively [Makrides 1964; Stern 1957]. Figure 5-11 shows the Tafel region of ferrous to ferric oxidation reaction on different oxidized (passive) metals and also compares those curves with the polarization curve of the pyrrhotite electrode measured in our work. Also it have been demonstrated that the oxidation of ferrous ion on the surface of the chalcopyrite ($CuFeS_2$) mineral, a mineral similar to that used in the present study, in HCl solution is extremely slow and almost negligible [Hirato *et al.,* 1986]. Thus, it can be assumed that the ferrous to ferric oxidation reaction is a slow reaction on the pyrrhotite electrode too. Indeed, from the literatures on the electrochemistry of pyrrhotite, this is a proper assumption. Cyclic voltammetry studies on pyrrhotite electrodes conducted in acidic solutions by different researchers have reported existence of an anodic peak related to the formation of Fe^{3+}. The peaks are reported to be at 0.43 V vs. SHE in 0.5 M CH_3COOH solution (pH 4.6) [Hamilton and Woods 1981], 0.45 V vs. sat. Ag|AgCl in 0.5 M CH_3COOH solution (pH 4.5) [Almeida and Giannetti 2003], and 0.48 V vs. sat. Ag|AgCl in 1M HCl solution [Mikhlin 2000]. However, it has been observed by Hamilton and Woods [1981] that running the cyclic voltammetry experiment either with a solid stationary electrode or rotating disk electrode does not significantly change the current measured at this peak. Therefore, they have concluded that the oxidation reaction which gives rise to the peak is originated directly from the mineral and is not produced from a

diffusion dependent dissolved species. In other words, if the source of the Fe^{3+} is the dissolved Fe^{2+} ion in the vicinity of the electrode surface, then by increasing the rate of diffusion of this species away from the mineral surface (through the use of a rotating disk electrode) one would expect to eliminate (or decrease) this peak. Consequently, the peak has been assigned to the direct oxidation of pyrrhotite electrode as ferric ion [Hamilton and Woods 1981]. Hence, the oxidation of the ferrous ions to ferric ions on the surface of the pyrrhotite electrode can be neglected. Therefore, in the first 60 s of the chronoamperometry curve of Figure 5-10a at 782 mV_{SHE}, it should be considered that iron dissolves as ferrous and ferric (both by direct oxidation of the electrode) and thus the reaction for the early stage of dissolution at 782 mV_{SHE} might be:

$$Fe_{1-x}S \longrightarrow Fe_{1-x-m-n}S + mFe^{2+} + nFe^{3+} + (2m + 3n)e^{-} \qquad \qquad 5\text{-}23$$
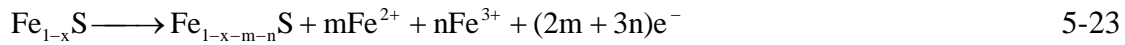
After reaching a critical thickness of the metal–deficient sulfide layer ($Fe_{1-x-m-n}S$) at approximately 60 seconds –see Figure 5-10a– transpassive dissolution of this layer will be the dominant reaction according to reactions 5-21 and 5-22. Subsequently, a layer of elemental sulfur will form on the surface which hinders the dissolution rate (Figure 5-10a). Application of this proposed dissolution sequence to the electrochemical circuit of Figures 5-6b, infers that the C_{SC}/R_{SC} and C_{p}/R_{p} pairs represent the semiconducting and passivation behavior of the metal–deficient sulfide layer, respectively, while the constant phase element may be representative of the thin elemental sulfur layer at the electrode/solution interface. The inductive element, L, is related to the transpassive dissolution of the semiconducting metal–deficient sulfide layer. The chronoamperometry curve of Figure 5-10a shows a gradual increase in dissolution current after 2000 sec. The current increases up to a steady state value of approximately 40 μAcm^{-2}. The reason behind this behavior is not clear, however, either oxidation of the elemental sulfur layer to sulfate or further oxidation of ferrous ions to ferric might be the cause.
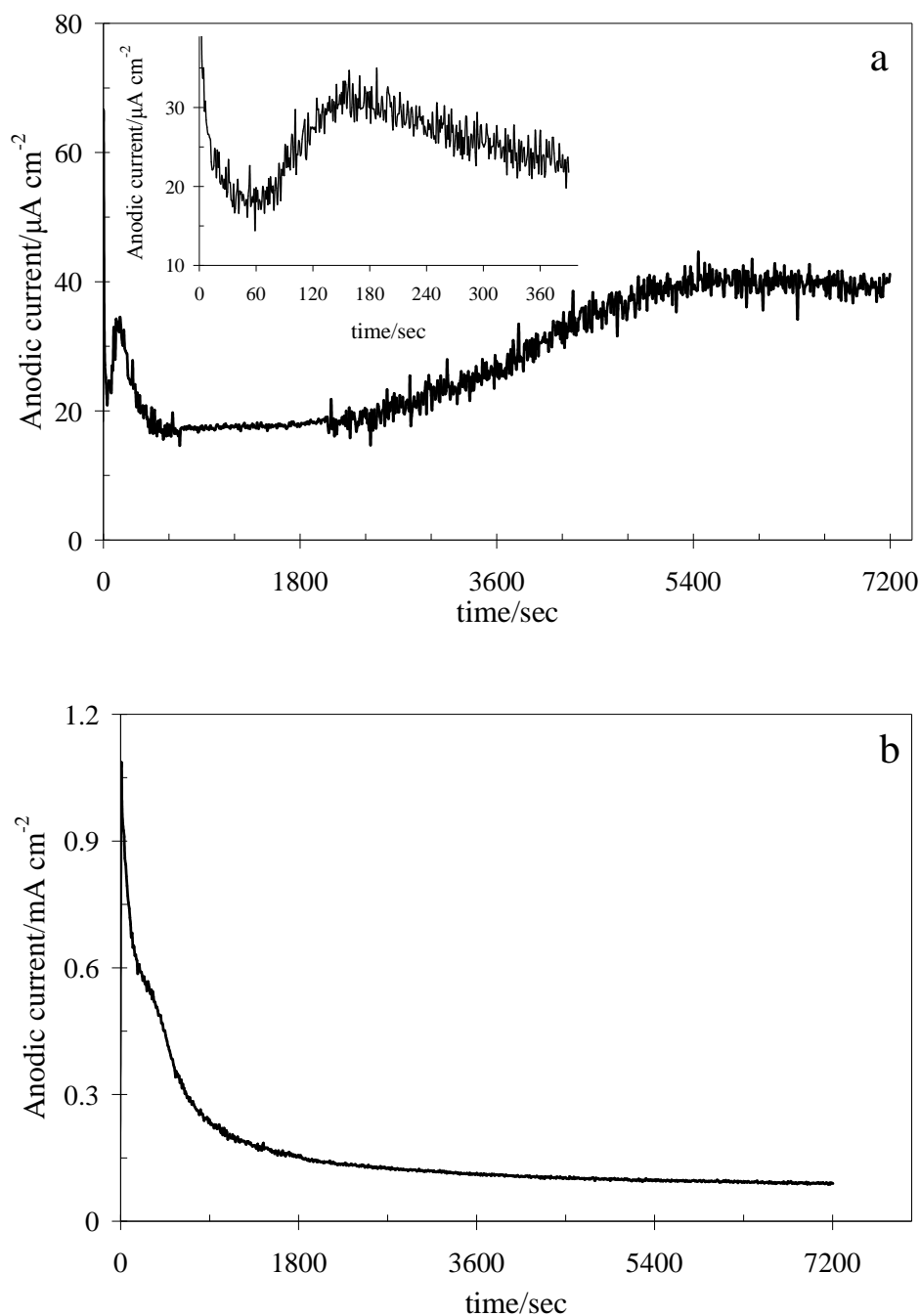
Figure 5-10: Anodic current density-time transient in response to potential step from the OC potential to, (a) 540, and (b) 850 mV; inset of figure (a) shows the earlier stage of dissolution of the corresponding condition with higher resolution.

The dissolution path for the electrode changes when potential is increased to more anodic regions (> 917 mV_{SHE}). Figure 5-10b shows an almost uniform decrease in the dissolution current density of the electrode which is clearly due to the formation of a surface

layer on the electrode. Reaction 5-55 is the likely overall reaction at very high anodic potentials which considers the dissolution of iron as ferric ion and formation of both elemental sulfur and sulfate ions. Due to the high dissolution rates which are observed (steady state dissolution current is 0.12 mAcm^{-2}) a thick, relatively un-protective, sulfur layer or sulfate product is believed to form on the electrode surface. The Mott-Schottky plots of Figure 5-3 show semiconducting behavior for the surface layer which means that the layer cannot be a perfect insulator layer of elemental sulfur. For these reasons, the layer likely consists of a sulfate product (or other sulfur species) or contains a considerable amount of sulfate. In the electrochemical circuit of Figure 5-6c for high anodic potentials the C_{SC}/R_{SC} and L/R_L pairs are related to the formation of the space charge region and dissolution of the semiconductive pyrrhotite, respectively. C_p/R_p represents the capacitive and resistive properties of the surface layer and constant phase element and its corresponding resistance may be due to the imperfections on the surface of film.
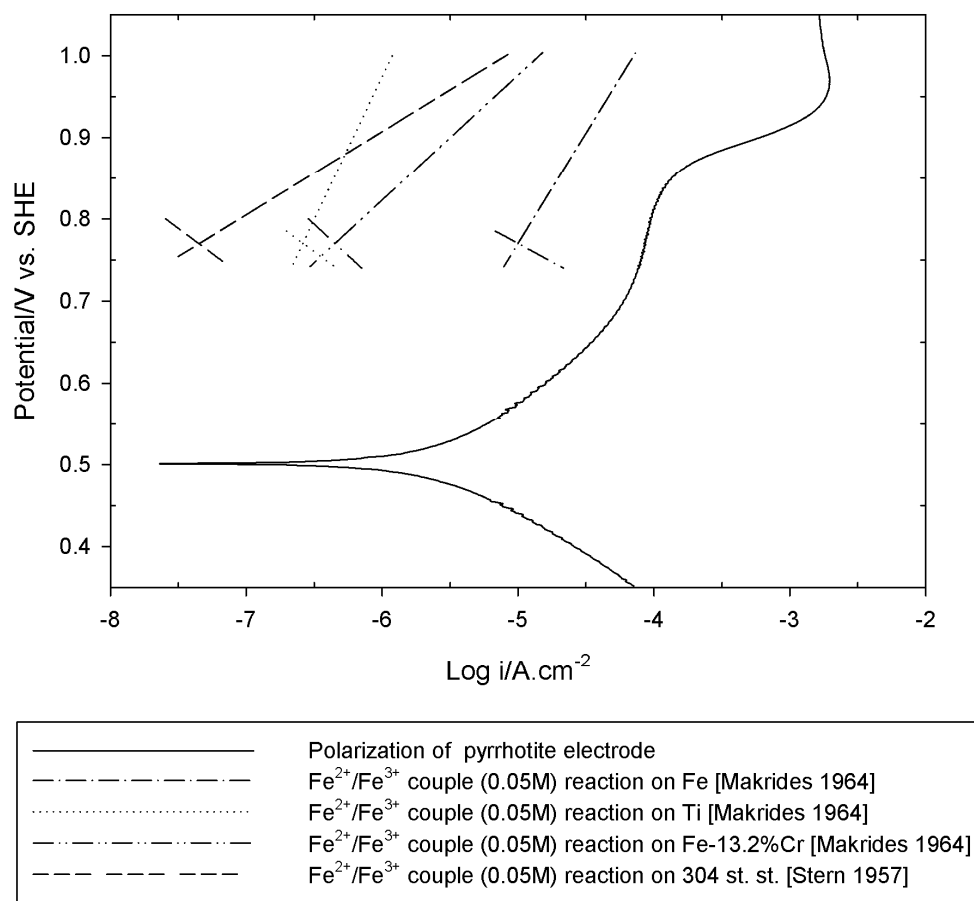
Figure 5-11: Tafel region of ferrous to ferric oxidation reaction on different oxidized metals compared to the polarization curve of pyrrhotite electrode in HCl solution.

5.2.6 SEM studies

Considering reactions 5-5 and 5-22, elemental sulfur is the main product of the dissolution process. In order to observe the morphology of the sulfur layer formed on the surface of the electrode, samples were kept at different constant potentials for two hours and then analyzed by scanning electron microscope (SEM). Figures 5-12a and b show the morphology of the sulfur layer formed at 782 and 1042 mV_{SHE}, respectively. The sulfur layer formed at lower potentials (Figure 5-12a) is rough and discontinuous and does not cover the whole surface of the electrode and, as a result, this film likely would not be very successful at impeding dissolution as demonstrated through electrochemical measurement. The layer formed at higher potentials after two hours (Figure 5-12b) is thicker and contains fewer

74

cracks and discontinuities. The latter appears to cover the whole surface of the sample and, as a result, this layer is more successful at hindering the dissolution rate of the electrode. This is consistent with the results obtained in the electrochemical study.
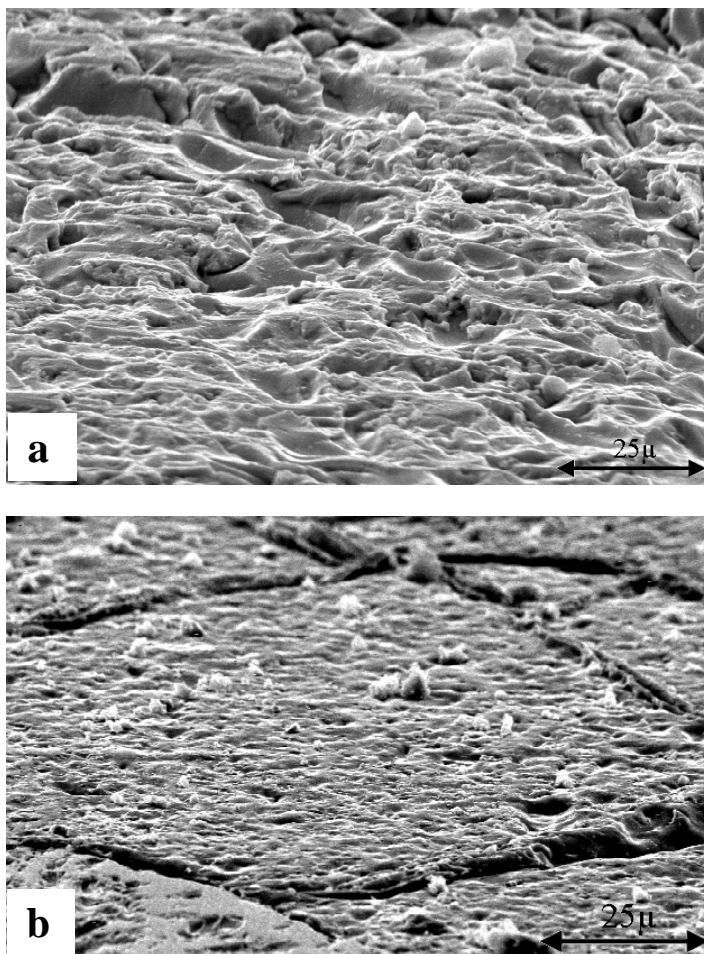
Figure 5-12: SEM images of the pyrrhotite electrode after 2 hrs dissolution in 1 M HCl solution at (a) 782, (b) 1042 mV$_{SHE}$.

Indeed, from Figure 5-10, the steady dissolution current at 782 mV and at 1092 mV$_{SHE}$ are 18 μAcm^{-2} and 160 μAcm^{-2}, respectively. Thus, increasing the potential by 310 mV (from 782 to 1092 mV) increases the dissolution current by less than an order of magnitude (around 8.9 times). As a comparison, the anodic Tafel slope for the electrode in the potential region of OCP – 692 mV$_{SHE}$ is 131 mVdecade^{-1}, which is 2.47 times higher than that of 782 – 1092 mV$_{SHE}$ range. This comparison shows that the dissolution kinetics increases very slowly in the higher potential range (782 – 1092 mV$_{SHE}$) which we believe is a result of the physical properties of the second surface layer (> 912 mV$_{SHE}$). Viz. the donor

density of the second surface layer ($\sim 10^{18}$ cm^{-3}) is lower than that of the first ($\sim 10^{20}$ cm^{-3}, ref. to Table 5-1), and the total impedance of the electrode increases rapidly through the formation of this second layer (roughly from 0.3 kΩ to 3.5 kΩ, ref. to section 5.2.3 and Figure 5-2).

5.3 Conclusion

In this chapter, the electrochemical dissolution behavior of pyrrhotite has been studied in 1M HCl solution with in-situ electrochemical methods. Results show formation of two distinct surface layers on the electrode. The first layer forms during the preparation of the sample or during initial immersion of the pyrrhotite in the test solution. At the initial time, the iron atoms from the pyrrhotite structure partially dissolve into the solution and a metal–deficient sulfide layer with semiconducting properties ($Fe_{1-x-y}S$) forms on the surface of the electrode. The donor density of the layer is around 10^{20} cm^{-3} and the thickening of the layer decreases the dissolution rate of the mineral. The layer is stable up to potential of 842 mV$_{SHE}$. The second film forms at higher anodic potentials (> 912 mV$_{SHE}$) and is substantially more resistant to dissolution than the first layer. Considering reaction 5-5 as the overall dissolution path for this potential range, the ferric ion, elemental sulfur and sulfate ion are the main products of reaction.

The results of this chapter relate to those presented below, and pertaining to chalcopyrite dissolution, as the pyrrhotite electrode (a Fe-S system) is a simplified model for the chalcopyrite electrode (Cu-Fe-S system). The electrochemical methods developed in this chapter for the simplified Fe-S system were then applied below to help elucidate the mechanism of chalcopyrite dissolution.

6 Electrochemical evaluation of chalcopyrite's surface during dissolution in 0.5 M H_2SO_4 solution[2]

6.1 Introduction

Different in-situ electrochemical techniques (i.e. cyclic voltammetry, potentiodynamic and potentiostatic polarization, and chronoamperometry) as well as ex-situ spectroscopic methods (i.e. X-ray photoelectron spectroscopy, auger electron spectroscopy, Raman spectroscopy) have been applied to understand the dissolution mechanism of chalcopyrite, and furthermore, to characterize the surface layers on electrodes (refer to chapter 2 of the thesis). However, there remains uncertainty about the dissolution procedure. The trouble with most of the DC electrochemical techniques used so far is that only circumstantial evidence is derivable to help with the elucidation of possible reaction mechanisms. The ex-situ analytical methods are plagued with controversy associated with the possible evaporation of elemental sulfur under experimental conditions [Buckley and Woods 1994]. In this chapter, the electrochemical dissolution of chalcopyrite in simple sulfuric acid solution will be studied. In order to characterize the surface properties of the chalcopyrite electrode at different anodic potentials and understand the growth sequence of surface layers, we will apply electrochemical impedance spectroscopy. As chalcopyrite is a semiconducting material, Mott-Schottky plots will be extracted to understand the electrolyte/electrode interface. The lessons learned from the pyrrhotite electrochemistry (EIS and Mott-Schottky) study were significantly useful to the development of the methods and analysis applied in this chapter.

6.2 Results and discussion

6.2.1 Characterization of used chalcopyrite electrodes

A high quality natural polycrystalline chalcopyrite sample originating from the Creighton Mine (Sudbury, Ontario) was used for electrode fabrication. The quantitative phase analysis of the chalcopyrite ore was determined using the Rietveld method and X-ray powder diffraction and is shown in Table 6-1. Massive electrodes were prepared by cutting

---

[2] A version of this chapter has been published: "Ghahremaninezhad, A., Asselin, E., Dixon, D.G., 2010, Electrochimica Acta, 55, 5041–5056".

the chalcopyrite into approximately cubic shapes with areas of 1 cm^2 exposed to the solution. Electrical contact with copper wires was made in the back of the sample with silver-loaded epoxy resin. The electrode contacts were protected from the solution by mounting the whole assembly in epoxy resin, leaving only one face of the electrode exposed to the solution. Before each test, the exposed face of the electrode was polished with no. 1200 carbide paper to begin each experiment with a fresh surface. The *reference electrode* in all of the performed tests was a Mercury/mercury Sulfate electrode which is 0.600 mV *vs.* SHE. The microstructure of a polished electrode is shown in Figure 6-1a. Also, Figure 6-1b presents an SEM picture and its associated EDX mapping for elemental distribution which shows the presence of the siderite phase in the chalcopyrite electrode structure.

Table 6-1: Composition of the as received chalcopyrite ore.

Mineral	Chemical Formula	Mass Percentage
Chalcopyrite	$CuFeS_2$	98.1
Siderite	$Fe^{2+}CO_3$	1.9
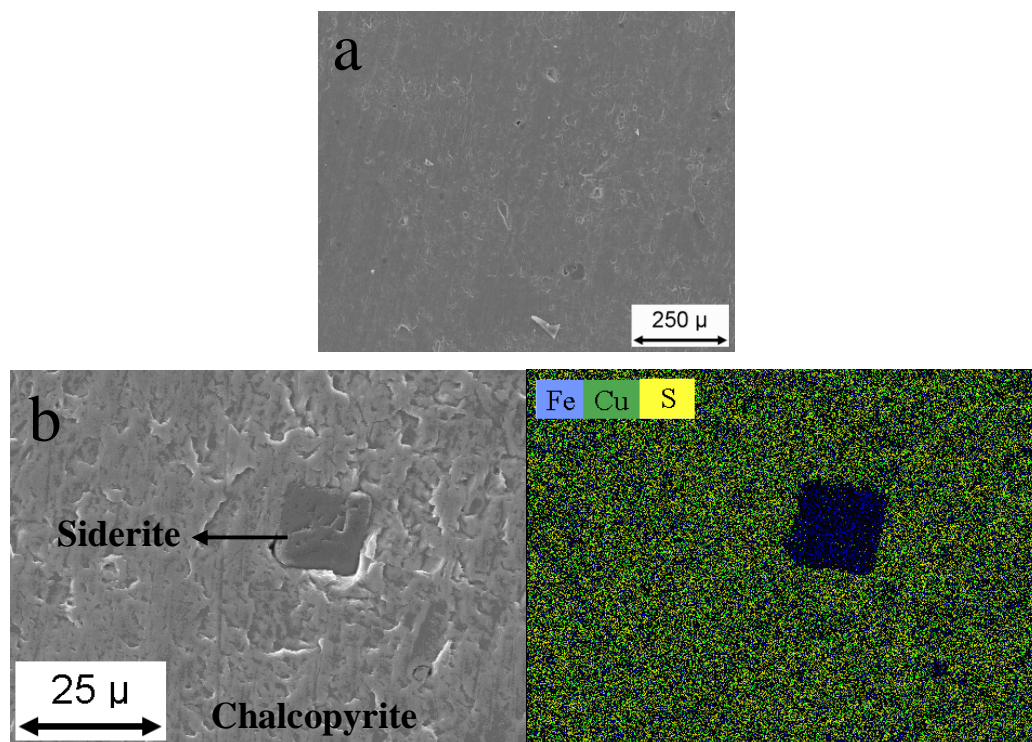
Figure 6-1: SEM images of (a) polished electrode surface, (b) siderite phase and EDX mapping for element distribution on the surface of prepared electrode.

6.2.2 Open circuit potential study

In order to elucidate the surface activity of the electrode after 10 min immersion in the test solution, the open circuit potential curves of different chalcopyrite electrodes as a function of time are shown in Figure 6-2. In all of the curves the potential of the electrode increases for 10 min and afterward almost reaches to a steady state. The rapid increase in the potential during the first 10 min of immersion in the electrolyte is approximately 60 mV which indicates the spontaneous growth of a passive film on the surface of the electrodes. The steady-state OC potential was found to be approximately -0.25 V_{MSE} (0.35 V_{SHE}) and was established within roughly 10 min (where the steady-state was defined here as a change of less than 2 mV/min). All of the electrodes used in the experiments shown here displayed an open circuit potential of -250 ± 10 mV_{MSE} (350 ± 10 mV_{SHE}) after 10 min of stabilization time in the electrolyte.
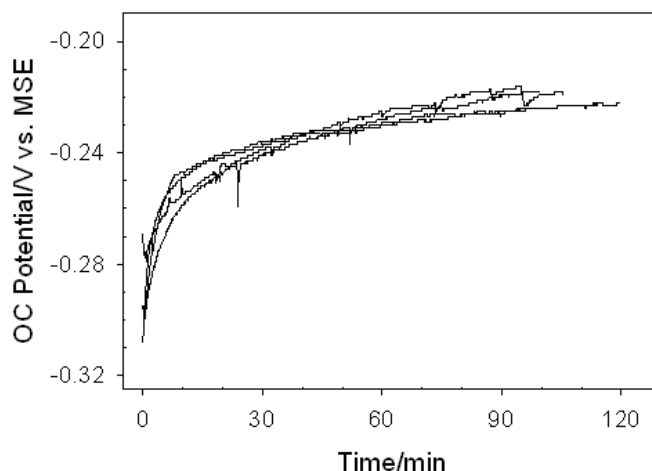
Figure 6-2: Open circuit potential (OCP) of different chalcopyrite electrodes *vs.* time.

6.2.3 Potentiodynamic study

Figure 6-3 shows the potentiodynamic curves for the chalcopyrite electrode at different scan rates of 0.05, 0.5, 5, and 50 mVs^{-1}. Generally, applying a lower scan rate will reveal a closer approximation of steady state electrode behavior. In the case of the present study, the polarization current decreases with decreasing scan rate which is similar to the results published by Warren *et al.* [1982] for $CuFeS_2$ in 1 M sulfuric acid solution. For cathodic potentials, all of the curves show similar E-I profiles which means that the initial sample surfaces have similar properties. In general, three different potential regions are

apparent in Figure 6-3. At low anodic potentials, OC to 0.3 V_{MSE} (0.9 V_{SHE}), the dissolution current is a function of scan rate which is clearly related to the formation of a surface layer. Within the small potential range of 0.30 to 0.42 V_{MSE} (0.90 to 1.02 V_{SHE}), the measured current is the same for all scan rates. In other words, the surface of the electrode is electrochemically active in this region. At higher anodic potentials (> 0.42 V_{MSE}) another film(s) forms on the surface of the electrode and hinders the dissolution rate of the electrode again.
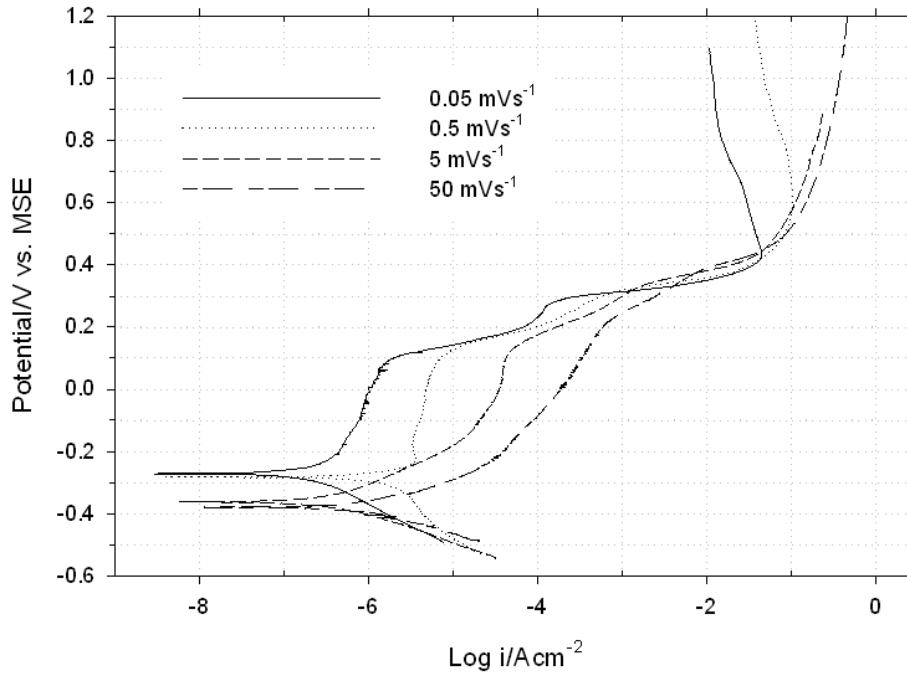
Figure 6-3: Potentiodynamic curves for the chalcopyrite electrode in 0.5 M H₂SO₄ electrolyte at different scan rates.

A closer look at Figure 6-3 reveals further details about the anodic behavior of chalcopyrite. In the case of the low anodic potentials, OC to 0.3 V_{MSE} (OC to 0.9 V_{SHE}), the measured current at lower scan rates is less than that registered at higher scan rates. This behavior, decrease in current by descending the scan rate, is likely related to the formation of a thin surface layer(s) via prewave reactions [Nava and Gonzalez 2006]:

$$CuFeS_2 + 4zH_2O \longleftrightarrow Cu_{1-x}Fe_{1-y}S_{2-z} + xCu^{2+} + yFe^{3+}$$

$$+ zSO_4^{2-} + 8zH^+ + (2x + 3y + 6z)e^- \qquad\qquad 6\text{-}1$$

$$CuFeS_2 + 4pH_2O \longleftrightarrow Cu_{1-m}Fe_{1-n}S_{2-p} + mCu^{2+} + nFe^{3+}$$

$$+ pSO_4^{2-} + 8pH^+ + (2m + 3n + 6p)e^- \qquad\qquad 6\text{-}2$$
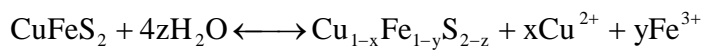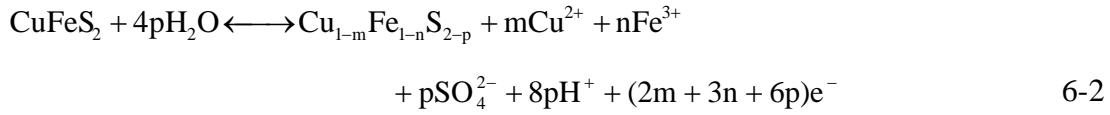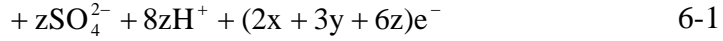
For lower scan rates the layer can have more coverage on the surface. Also, the layer would be thicker or would have less porosity (more time to react) than at higher scan rates. As a result, the anodic current would be smaller (as seen in Figure 6-3). Performing the experiments at very low scan rate reveals the existence of two different passivation regions at low anodic potentials. According to the low scan rate polarization curves of Figure 6-3 (0.05 and 0.5 mVs^{-1}), the first passive layer forms in the potential range of OC to 0.125 V$_{MSE}$ (0.725 V$_{SHE}$) and afterward the second passive layer forms during a small potential window of 0.19 to 0.3 V$_{MSE}$ (0.79 to 0.9 V$_{SHE}$). The formation and dissolution of these layers will be studied in more detail in the next section.

At more anodic potentials of 0.30 to 0.42 V$_{MSE}$ (0.90 to 1.02 V$_{SHE}$), changing the scan rate does not significantly affect the dissolution current. This is likely due to the electrochemically active dissolution of the passive surface layers. At potentials higher than 0.42 V$_{MSE}$, the lower scan rate shifts the curve to lower currents which could again be considered as evidence for the formation of another surface layer(s) on the electrode. At an even higher potential of around 0.68 V$_{MSE}$ (1.28 V$_{SHE}$) there is a further decrease in the measured current which could be considered as resulting from the formation of a second, and different, layer on the surface of the electrode. These findings will be discussed in more detail in the next section.

6.2.4 Electrochemical impedance spectroscopy study

EIS studies on the chalcopyrite electrodes were conducted in three different potential regions: at low anodic potentials of OC to 0.3 V$_{MSE}$ (OC – 0.9 V$_{SHE}$) with a passive electrode surface, in a mid-potential region of 0.3 to 0.42 V$_{MSE}$ (0.9 – 1.02 V$_{SHE}$) with an active electrode surface and at higher anodic potentials of 0.42 to 1.10 V$_{MSE}$ (1.02 – 1.70 V$_{SHE}$). The interpretation of the measured Nyquist and Bode plots shown in this section will be supported by model development in section 6.2.6.

The impedance spectra for the chalcopyrite electrode at low anodic potentials are presented in Figure 6-4. The Nyquist curve obtained at OC potential is similar to that obtained by Asselin *et al* [2007] where it was shown that such behavior is related to the existence of a thin surface layer on the electrode. The EIS study by Velásquez *et al.* [2005] in alkaline solution also revealed the formation of a coating layer which is initially present on the electrode and spontaneously forms during the polishing of the sample. Generally, this layer forms during the preparation of the sample or during initial immersion in the electrolyte for stabilization purposes as studied by Biegler [1977]. Nava and Gonzalez [2006] and Nava *et al.*, [2008], have proposed the formation of a non stoichiometric passive layer of $Cu_{1-x}Fe_{1-y}S_{2-z}$ on the surface of chalcopyrite (reaction 6-1). In alkaline solutions, Yin *et al.*, [2000] and Vaughan *et al.*, [1997] have suggested that, at low anodic potentials (near OCP), a monolayer of surface iron should dissolve first while the Cu and S atoms remain unchanged as CuS_2* and inhibit further dissolution. According to their findings, a small increase in potential will cause further dissolution of iron atoms from deeper sections of the chalcopyrite surface while the CuS_2* layer remains stable and, due to its thickening, the dissolution current will decrease quickly. Possibly, in the case of the present study, the following reaction may occur as considered by Hackl *et al.*, [1995]:

$$CuFeS_2 \longrightarrow Cu_{1-x}Fe_{1-y}S_2 + xCu^{2+} + yFe^{2+} + 2(x+y)e^- \qquad y\rangle\rangle x \qquad 6\text{-}3$$
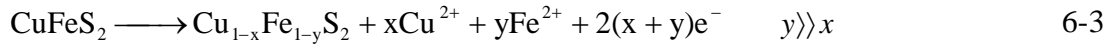
The $Cu_{1-x}Fe_{1-y}S_2$ layer is a passive layer and is responsible for a decrease in dissolution rate. The electrode shows similar behavior for higher anodic potentials of –0.1 and 0.0 V_{MSE} (0.5 and 0.6 V_{SHE}, respectively) as presented in Figure 6-4. It could be concluded that by increasing the potential, more atomic layers are involved in reaction 6-3 such that the passive film grows into the electrode surface. Simultaneously, the thickness of the passive layer increases and inhibits dissolution [Yin *et al.*, 1995]. Increasing the potential shows a partially resolved semi-circle at high frequencies which is related to charge transfer process on the electrode. This result is close to that of Velasquez *et al.*, [1998]. The passive surface layer is stable at higher potentials (up to 100 mV) and furthermore the effect of charge transfer increases.

The impedance curve at 150 mV_{MSE} (750 mV_{SHE}), presented in Figure 6-4, shows a dramatic change in electrochemical behavior. Three well pronounced time constants are detectable in the curve. The first time constant, at high frequencies, is a capacitive loop

related to the combination of the double-layer capacitance impedance combined with a charge transfer resistance (due to the electrochemical dissolution of the electrode) and the second one, at middle frequencies (0.49 – 1.5 Hz) is a capacitive loop related to the combination of a pseudo-capacitance impedance (due to the passive layer) and a resistance. At very low frequencies (0.01 – 0.29 Hz) the Nyquist curve reveals inductive behavior. Most probably, the inductive loop (third time constant) is related to the transpassive dissolution of the passive layer [Betova *et al.,* 2002; Bojinov and Tezvetkoff 2003; Erne and Vanmaekelbergh 1997].
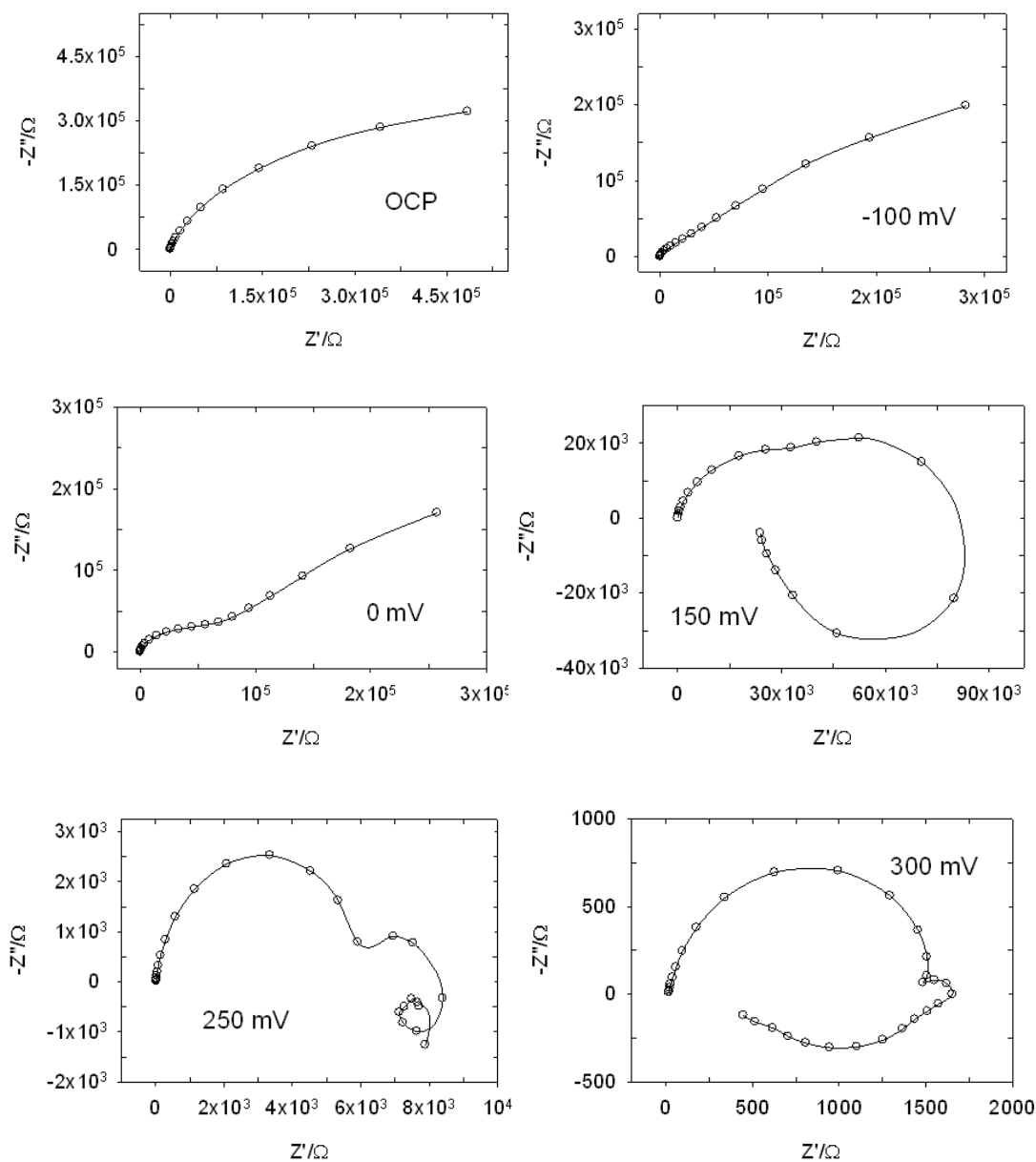
Figure 6-4: Electrochemical impedance spectra of chalcopyrite electrode for anodic potentials of OC to 300 mV$_{MSE}$.

The phase angle diagrams at the low anodic potentials are presented in Figure 6-5a. In the potential range of OC to 0 mV$_{MSE}$ (OC to 600 mV$_{SHE}$) the electrode shows a maximum phase angle of around 80 degrees which is considered to be related to a solid state mass transport process (through passive layer) and at 150 mV$_{MSE}$ (750 mV$_{SHE}$) the electrode has a negative phase angle at high frequencies which supports the inductive behavior shown in Nyquist curve of Figure 6-4 for 150 mV$_{MSE}$. As a result, at 150 mV$_{MSE}$ the passive layer on the electrode is porous due to the transpassive dissolution of the electrode.

84
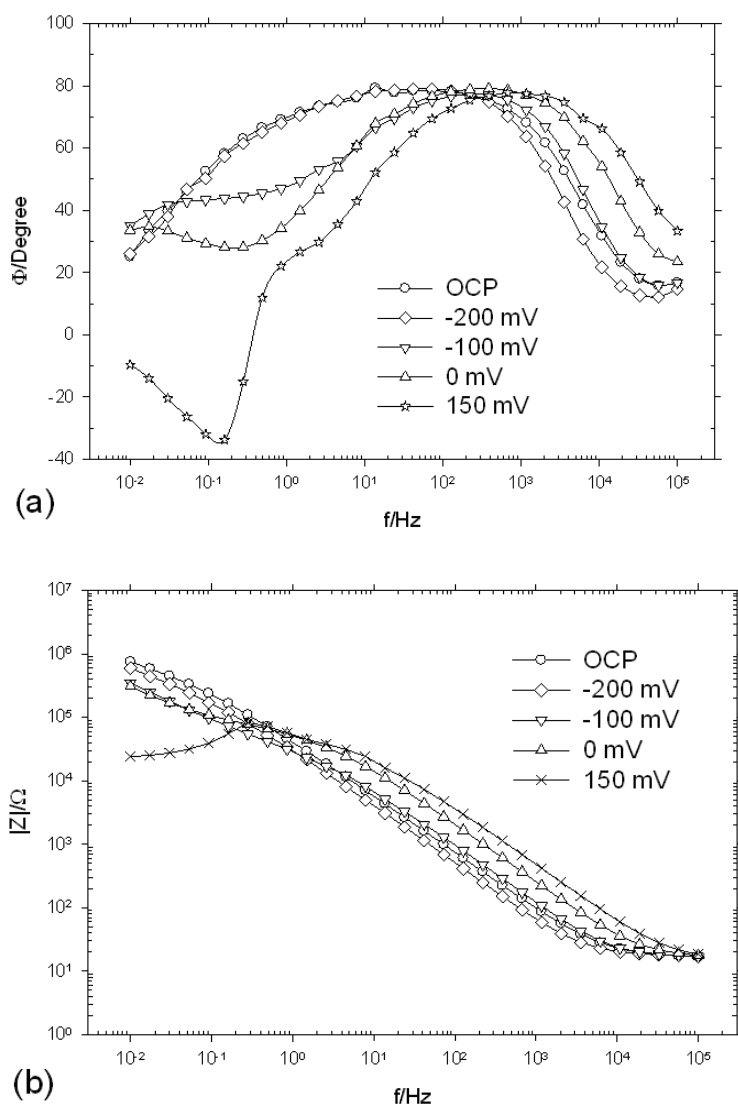
Figure 6-5: Bode diagrams of (a) phase angle, and (b) total impedance magnitude of the chalcopyrite electrode at potential range of OC–150 mV$_{MSE}$ (OC to 750 mV$_{SHE}$).

Figure 6-5b shows the total impedance magnitude diagram for the low anodic potentials. From Figure 6-5b, by increasing potential from 0 to 150 mV$_{MSE}$ (600 to 750 V$_{SHE}$) the total impedance of the electrode at low frequencies decreases more than an order of magnitude. This is believed to be related to transpassive dissolution of the passive layer and its concomitant increase in porosity. The porous nature of the passive layer in this potential range has also been described by Velásquez *et al.,* [2005] and Nava and Gonzalez [2006]. If the $Cu_{1-x}Fe_{1-y}S_2$ compound identified by reaction 6-3 is assumed to be the passive layer

formed from OCP to 0.1 V_{MSE} then it electrochemically dissolves at higher anodic potentials according to Hackl *et al.,* [1995] as:

$$Cu_{1-x}Fe_{1-y}S_2 \longrightarrow Cu_{1-x-z}S_2 + zCu^{2+} + (1-y)Fe^{2+} + 2(z+1-y)e^- \qquad \text{6-4}$$
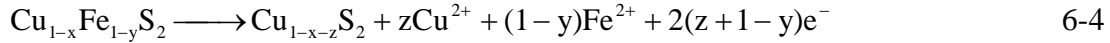
where the $Cu_{1-x-z}S_2$ layer is also passive. The presented Nyquist plot for the chalcopyrite electrode at 250 mV_{MSE} (850 mV_{SHE}) in Figure 6-4 shows five different time constants; a capacitive loop related to the combination of the double-layer capacitance impedance combined with a charge transfer resistance (100 kHz – 14 Hz), a capacitive loop in the 13 – 4.5 Hz related to the combination of a pseudo-capacitance impedance (due to the passive layer) and a resistance, an inductive loop in middle frequencies (5 – 0.85 Hz), and third capacitive and second inductive loops at very low frequencies (0.5 – 0.01 Hz). The capacitive loop at very low frequencies (third capacitive loop) can be related to the formation of a new surface layer on the electrode which according to reaction 6-4 would be *Cu₁₋ₓ₋zS₂*. Similar behaviors have been reported in the case of transpassive dissolution of highly alloyed stainless steels [Betova *et al.,* 2002; Erne and Vanmaekelbergh 1997; Betova *et al.,* 2004]. Figure 6-6a presents the total impedance magnitude diagram for the chalcopyrite electrode at 250 mV_{MSE} (850 mV_{SHE}).
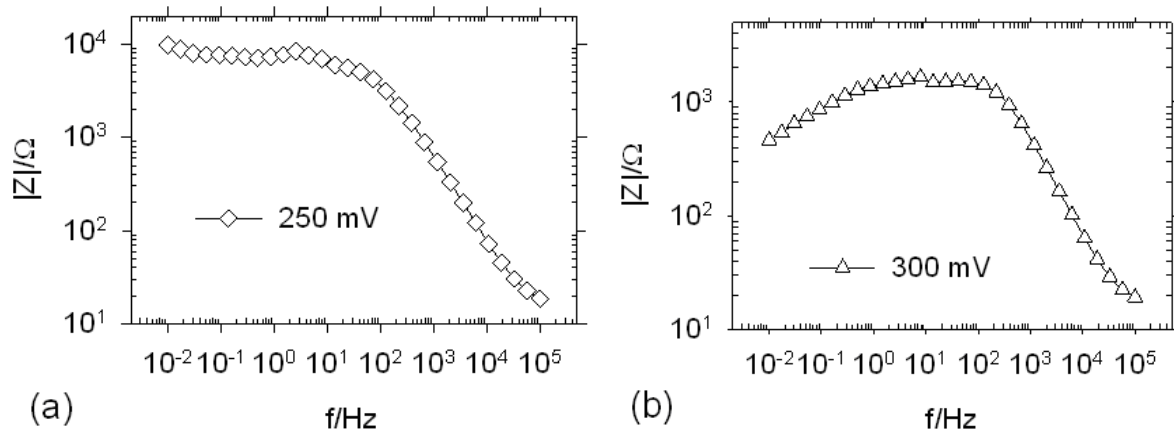
Figure 6-6: Bode diagrams of total impedance magnitude of the chalcopyrite electrode at (a) 250, (b) 300 mV_{MSE}.

At the lowest frequencies (Figure 6-6a) the total impedance of the electrode increases which means that the second inductive loop for 250 mV_{MSE} (inductive loop at the lowest frequencies) is not related to the dissolution of the passive layer. This inductive behavior between 0.15 and 0.01 Hz may be related to the relaxation of negative surface charges on the

passive layer which form by accumulation of metal vacancies at the passive layer/solution interface [Bojinov et al., 1999]. In the case of the anodic behavior of iron in sulfuric acid, Gabrielli *et al.* [1996] explains this behavior as the relaxation of the mobile Fe^{3+} ion. Both of the interpretations of the second inductive loop are analogous from an electrical circuit perspective. The last curve of Figure 6-4 shows the Nyquist plot at 300 mV_{MSE} (900 mV_{SHE}) for the electrode. Two capacitive time constants are visible at high frequencies and one inductive loop at low frequencies. From the low scan rate polarization curve of Figure 6-3, the potential of 300 mV_{MSE} is the very early stage of active dissolution region for the electrode. In other words, 300 mV_{MSE} is a transient potential from passive state to active dissolution state. Also comparing Figures 6-6a and b shows a rapid decrease (around order of magnitude) of total impedance of electrode by increasing the electrode potential from 250 to 300 mV_{MSE} (850 to 900 mV_{SHE}). Consequently, at this potential, the $Cu_{1-x}Fe_{1-y}S_2$ passive film is almost dissolved by reaction 6-4, and the $Cu_{1-x-z}S_2$ layer is the only present passive film on the surface (which also is the product of reaction 6-4). Thus, in Nyquist plot of 300 mV_{MSE} (refer to Figure 6-4), the high frequency loop will be due to the combination of a double layer capacitance impedance and a charge transfer resistance, the combination of a capacitance impedance and a resistance for mid frequencies (due to $Cu_{1-x-z}S_2$ passive layer) and the combination of a inductance impedance and a resistance for low frequencies (due to a transpassive dissolution of the film). The effect of low frequency transpassive dissolution of the electrode can be seen in the Bode diagram for the electrode at 300 mV_{MSE} (Figure 6-6b), which shows a decrease in the total impedance magnitude of the system. The decrease is due to the transpassive dissolution of the passive film and decrease in their thickness. Hackl *et al.* [1995] have suggested a reaction for the dissolution of the passive layer:

$$Cu_{1-x-z}S_2 \longrightarrow (1-x-z)Cu^{2+} + 2S^0 + 2(1-x-z)e^- \qquad\qquad 6\text{-}5$$
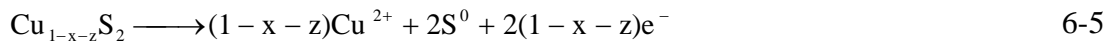
In summary, the EIS studies at low anodic potentials of OC – 0.3 V_{MSE} (OC to 0.9 V_{SHE}) show evidence for the formation of two distinct passive layers according to reactions 6-3 and 6-4 which is in accordance with the findings of the potentiodynamic polarization studies. Generally, the first passive layer forms during sample preparation and is stable in the potential range of OC to 0.1 V_{MSE} (Reaction 6-3). Afterward, a second passive layer forms on the surface (0.1 to 0.3 V_{MSE}) and, at same time, the dissolution of the first passive layer is occurring (Reaction 6-4).

Figure 6-7 shows the impedance spectra for the electrode at 325–390 mV$_{MSE}$ (925 to 990 mV$_{SHE}$). In this potential range the electrode shows a capacitive time constant at high frequencies and an inductive loop at low frequencies. The high frequency impedance loop is the result of charge transfer resistance and double layer capacitance coupling. The inductive impedance loop at low frequencies is characteristic of anodic dissolution of semiconductor electrodes [Gomes and Vanmaekelbergh 1996; Vanmaekelbergh and Searson 1994; Hiskey 1993]. In this potential range, electrochemically active dissolution of the electrode occurs and none of the passive layers formed at lower potentials are stable. Figure 6-8a presents the total impedance magnitude Bode diagram for the dissolution of chalcopyrite in the potential range of 250–390 mV$_{MSE}$ (850–990 mV$_{SHE}$). Increasing the potential from 275 to 325 mV$_{MSE}$ causes a two order of magnitude decrease in the total impedance of the electrode. Simultaneously, the phase angle diagram of Figure 6-8b shows a decrease in capacitive behavior of the electrode at the same potentials. Hence, at the potential window of 300 to 390 mV$_{MSE}$ the anodic dissolution of the electrode occurs.
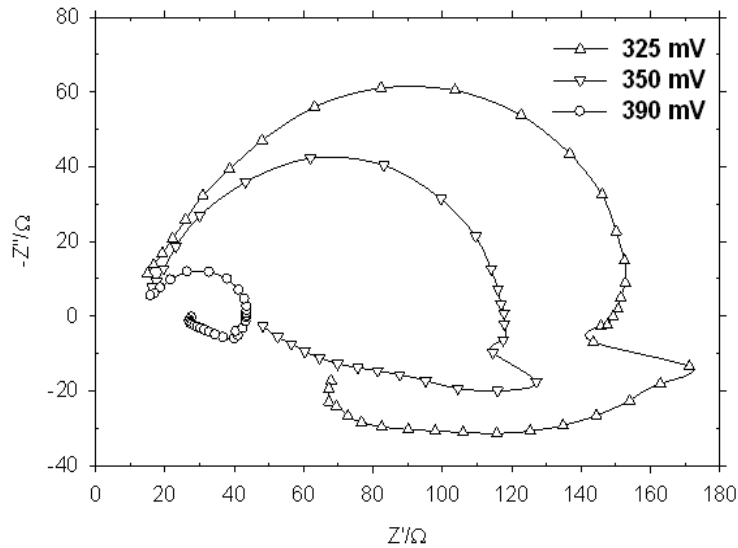
Figure 6-7: Electrochemical impedance spectra of chalcopyrite electrode for anodic potentials of 325–390 mV$_{MSE}$ (925–990 mV$_{SHE}$).

Biegler and Swift [1979] suggest that this dissolution reaction occurs as:

$$CuFeS_2 + 8H_2O \longrightarrow Cu^{2+} + Fe^{3+} + 2SO_4^{2-} + 16H^+ + 17e^-$$ 6-6
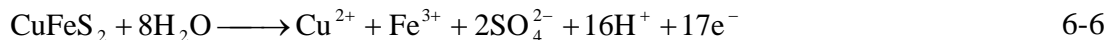
A study by Lazaro and Nicol [2006] has indicated that soluble sulfur species are involved in the dissolution of chalcopyrite. Their results show that $S_2O_3^{2-}$ would be the soluble sulfur species and the proposed reaction is:

$$CuFeS_2 + 3H_2O \longrightarrow Cu^{2+} + Fe^{2+} + S_2O_3^{2-} + 6H^+ + 8e^-$$ 6-7
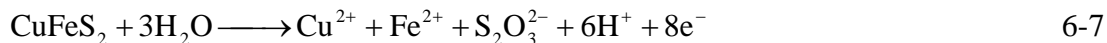
which considers the formation of thiosulfate as a product of chalcopyrite dissolution. An interesting feature of Nyquist plots at these potentials (Figure 6-7) is a jump in real impedance values around the frequency of 10 Hz. This behavior occurs in the potential range of 300 to 400 mV_{MSE} and by increasing the potential the jump in the real impedance decreases. It is possible to consider that a frequency dependent adsorption of a dissolution product occurs at this point. The sulfur species from reactions 6-6 and 6-7 could be good candidates for this phenomenon. However, more studies are needed here and the present authors are not sure about the nature of this process.

Impedance spectra for the chalcopyrite electrode at high anodic potentials of 0.50 – 1.10 V_{MSE} (1.1 to 1.7 V_{SHE}) are presented in Figure 6-9. At 500 mV_{MSE} (Figure 6-9a), three major time constants are detectable; a capacitive loop at high frequencies related to Faradaic resistance and double layer formation on the electrode (10^5 – 386 Hz); an inductive loop at middle frequencies which is a characteristic of anodic dissolution of semiconductor electrodes (386 – 4.5 Hz); and finally a second capacitive loop (4.5 – 10-2 Hz) which is related to the formation of a new film (surface layer). The potentiodynamic studies presented in the previous section (Figure 6-3) also show evidence of film growth on the surface of the electrode. Moreover, the total impedance magnitude Bode diagram of Figure 6-10 shows an increase at low frequencies which is related to formation of the surface layer. Nava and Gonzalez [2006] suggest the formation of ferric sulfate at this potential according to the reaction:

$$2CuFeS_2 + 13H_2O \longrightarrow 0.75CuS + 1.25Cu^{2+}$$

$$+ Fe_2(SO_4)_3 \downarrow + 0.25SO_4^{2-} + 26H^+ + 28e^-$$ 6-8
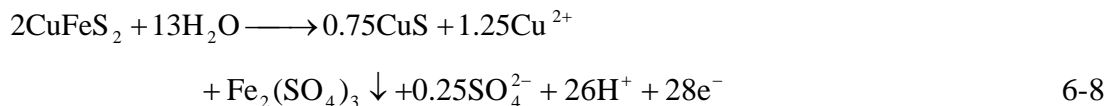
The formation of covellite (CuS) at these potentials has also been proposed by Warren *et al.,* [1982] as well.
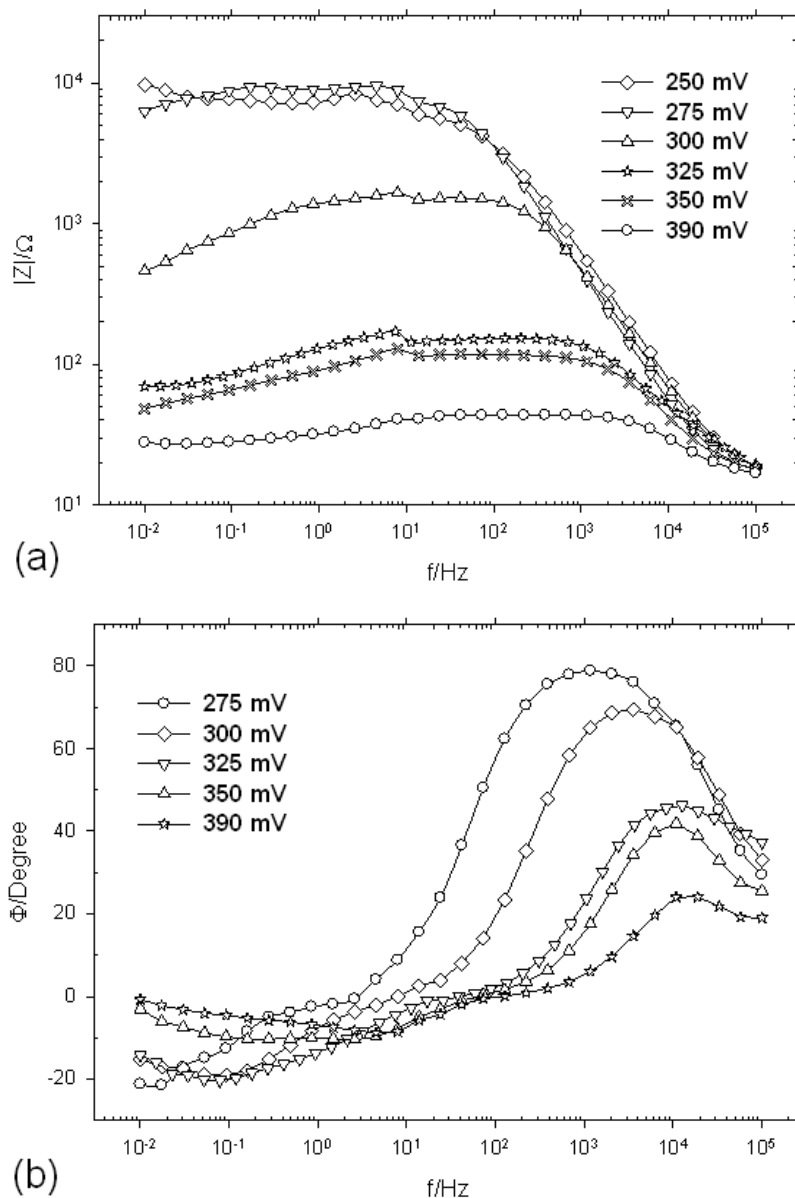
Figure 6-8: Bode diagrams of (a) total impedance magnitude, and (b) phase angle of the electrode at potential range of 250–390 mV.

CuS might be the surface layer which results in the pseudo-passive behavior of the electrode at 0.50 mV$_{MSE}$ (1.10 V$_{SHE}$). Increasing the potential by more than 250 mV to a value of 750 mV$_{MSE}$ (1.35 V$_{SHE}$) adds one more time constant to the Nyquist plot of the electrode (Figure 6-9b). The low frequency capacitive behavior would be related to either the formation of a new surface layer on the electrode or a notable change in the morphology and roughness of the previously formed surface layer. As presented in Figure 6-10, there are two

steps in the total impedance magnitude of the electrode at 0.75 V_{MSE} (1.35 V_{SHE}). The first step (around the frequency of 10 Hz) is thought to result from the formation of the former surface layer (CuS layer) and the second step, at lower frequencies (around the frequency of 0.1 Hz), is thought to be related to the latter phenomenon.
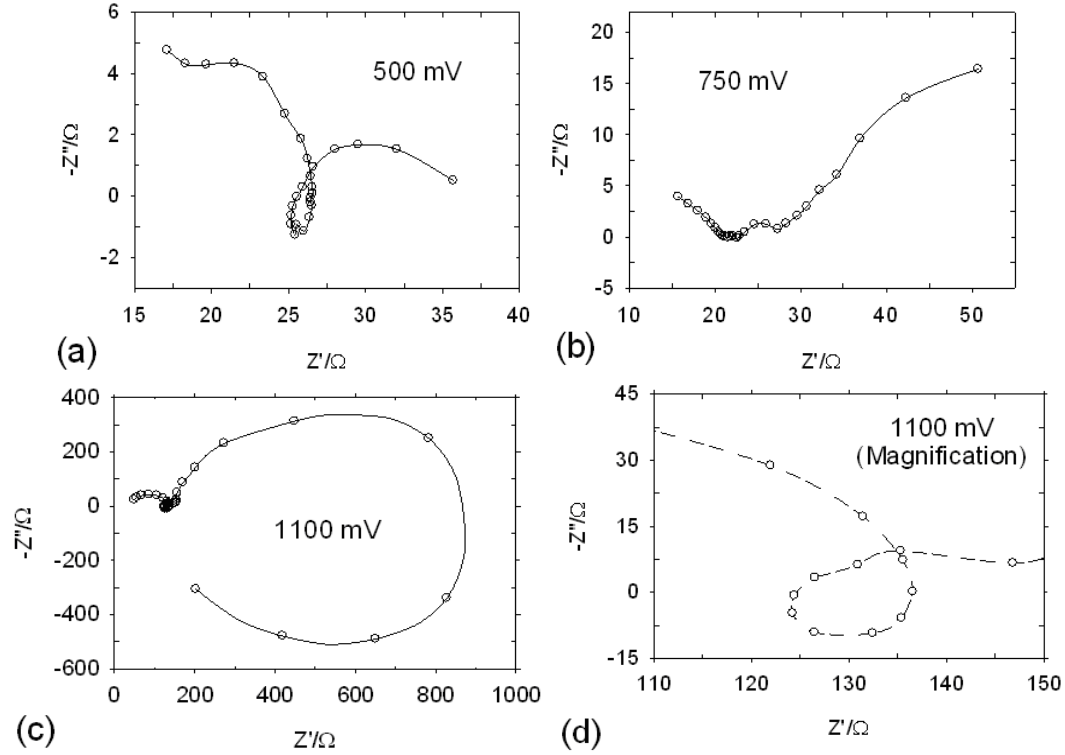
Figure 6-9: Electrochemical impedance spectra of chalcopyrite electrode for anodic potentials of 0.50–1.10 V_{MSE} (1.10 to 1.7 V_{SHE}).

Increasing the potential to 1.10 V_{MSE} (1.7 V_{SHE}) result in an inductive loop at very low frequencies of 92 – 10 mHz (Figure 6-9c) and the Bode diagram of total impedance magnitude at 1.10 V_{MSE} (Figure 6-10) shows a drop in total impedance at the same frequency range. It may thus be assumed that the low frequency inductive loop is related to a transpassive dissolution process. Figure 6-9d presents a higher magnification of the inductive loop for the anodic dissolution of the electrode and the capacitive loop associated with the formation of surface layer which occur at 1.10 V_{MSE}. Studies by Nava and Gonzalez [2006] indicate that the covellite layer which forms around 0.50 V_{MSE} (1.10 V_{SHE}) is not stable at higher potentials (>750 mV_{MSE}) and the suggested dissolution reaction is:

$$CuS + 4H_2O \longrightarrow Cu^{2+} + SO_4^{2-} + 8H^+ + 8e^- \hspace{3cm} 6\text{-}9$$
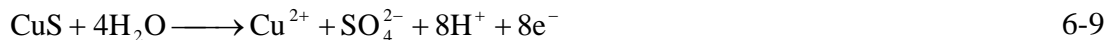
where the covellite decomposes to cupric ions (Cu^{2+}). Furthermore, some authors previously have proposed the formation of jarosite at high anodic potentials [Klauber 2008; Dutrizac 1982; Dutrizac 1989]. X-ray photoelectron spectroscopy studies by Parker *et al.* [2003] indicate that having ferric sulfate on the surface of the chalcopyrite electrode acts as a nucleation template for jarosite formation which hinders the dissolution of the electrode. Ferric sulfate could be directly produced by reaction 6-8 or by the formation of sulfate in the system. For example, further oxidation of the thiosulfate formed according to reaction 6-7 forms sulfate in the system. The proposed reaction for jarosite formation is [Klauber 2008]:

$$2Fe_2(SO_4)_3 + (K, Na, H_3O)_2SO_4 + 12H_2O \longrightarrow$$

$$2(K, Na, H_3O)Fe_3(SO_4)_2(OH)_6 \downarrow + 6H_2SO_4 \hspace{2cm} 6\text{-}10$$
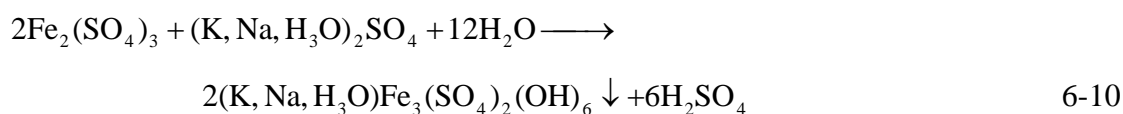
The jarosite formation rate increases very quickly by increasing the temperature and the rate is maximum at pH around 2. The presence of a nucleation template enhances the jarosite formation significantly [Klauber 2008, Parker *et al.,* 2003]. Thus, the formation of jarosite on the surface of electrode could explain the very low frequency capacitive behavior of the electrode at 750 mV$_{MSE}$ (1350 mV$_{SHE}$) of Figure 6-9b.
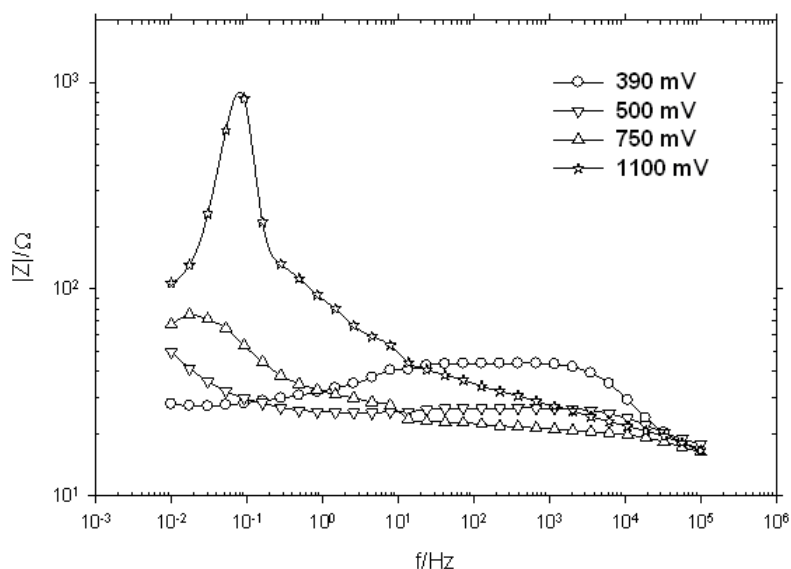
Figure 6-10: Bode diagram of total impedance magnitude for the chalcopyrite electrode at potential range of 390–1100 mV$_{MSE}$ (990 to 1700 mV$_{SHE}$).

6.2.5 Mott-Schottky study

It is useful here to summarize the results of the impedance work provided above: (1) It was observed that for the potential range of OC to 0.3 V_{MSE} (0.9 V_{SHE}) two different passive films formed on the surface of chalcopyrite; (2) in the potential range of 0.3 to 0.42 V_{MSE} (0.9 – 1.02 V_{SHE}) the surface of the chalcopyrite dissolves actively without any passive layer formation; and (3) at higher potentials of 0.42 – 1.1 V_{MSE} (1.02 – 1.7 V_{SHE}) another surface film forms. In this section, Mott-Schottky tests are used to probe the semiconducting properties of the chalcopyrite and its surface films as a function of potential. Figure 6-11 shows the Mott-Schottky plots for chalcopyrite electrodes at different frequencies of 1 and 10 kHz. A polarization curve is also included in Figure 6-11.

Generally, as explained in the previous chapter, the imposed potential at a semiconductor/electrolyte interface results in the formation of the electrical equivalent of two capacitors in series. The first capacitance results from the Helmholtz (double) layer while the second is associated with the space charge region. The overall capacitance of the interface can be described as:

$$\frac{1}{C} = \frac{1}{C_H} + \frac{1}{C_{SC}}$$

6-11

where C_{sc} and C_H are the space charge and the Helmholtz capacitances, respectively. The capacitance for the space charge region is much smaller than that of the double layer (2 to 3 orders of magnitude), such that one can neglect the Helmholtz double layer capacitance in most calculations. Therefore, the measured capacitance value is equal to the space charge capacitance which is presented as the Mott-Schottky relation in the following expression:

$$\frac{1}{C_{SC}^2} = \frac{2}{e\varepsilon\varepsilon_o n_o}\left(E - E_{fb} - \frac{kT}{e}\right)$$

6-12

where e represents the charge of an electron, ε the dielectric constant of the semiconductor, ε_o the permittivity of free space, n_o (or p_o for p-type semiconductors) the donor density, E the applied potential, E_{fb} flat band potential, k the Boltzmann constant, and T the absolute temperature, where the term kT/e is 25 mV at 25°C [Memming 2001].

Figure 6-11 shows 5 specific potential ranges, each with particular slope. The slopes of the Mott-Schottky plot reveal the electronic behavior of the outer surface layers of the electrode which are near the electrolyte. The Nyquist plots presented in the previous section

show complex responses with several time constants for each studied potential. This means that the capacitance obtained through Mott-Schottky analysis cannot represent the definitive space charge capacitance. However, a change in slope in the Mott-Schottky plots is necessarily due to a change of the electrical nature of the surface of the electrode. In the case of Figure 6-11, for potentials less than around 0.3 V the electrode surface has *n-type* semiconductive properties due to the positive slope of the Mott-Schottky plot. For higher potentials the slope is negative, which means that the electrode surface has changed to *p-type* behavior. Minor slope changes are noticeable at different potentials of around -0.1, 0.2, 0.3, and 0.4 V_{MSE} (0.5, 0.8, 0.9 and 1.0 V_{SHE}, respectively) for both curves. The potentiodynamic and EIS studies of previous sections have revealed the formation and dissolution of different surface layers at these critical potentials.
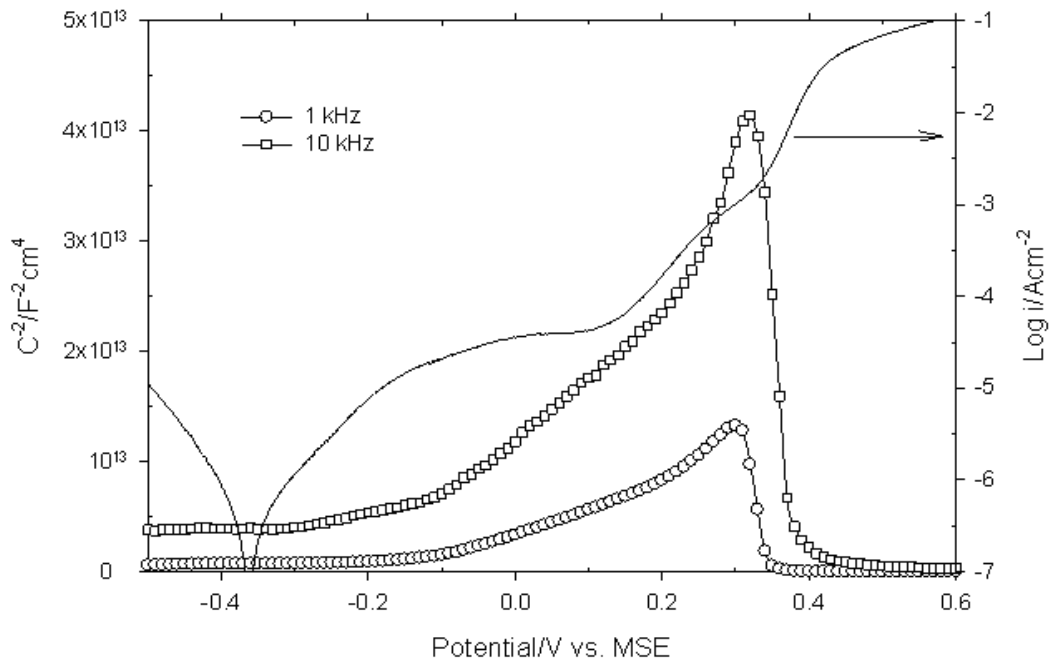
Figure 6-11: Mott-Schottky plots for chalcopyrite electrode at different frequencies.

For potentials less than -0.1 V_{MSE} (0.5 V_{SHE}), the surface is *n-type* and most probably this is associated with the surface layer formed on the electrode during sample preparation. The first break in the Mott Schottky plots occurs at around -0.1 V_{MSE}. Some authors have suggested that a monolayer thick passive film forms –reaction (6-3)– on the surface of the electrode in this potential region (around -0.1 V_{MSE}) [Yin et al., 1995; Vaughan et al., 1997]

94

while other studies propose the formation of a layer with thickness around 2 to 4 nm [Biegler 1977; Biegler and Horne 1985]. Thus, the thin passive film explains the break at -0.1 V_{MSE} (0.5 V_{SHE}). This observed increase in slope implies a decrease in the charge carrier density of surface layer compared to the surface at lower potentials. Increasing the anodic potential causes the deeper layers of the chalcopyrite electrode to be involved in reaction 6-3 and the thickness of the $Cu_{1-x}Fe_{1-y}S_2$ layer (product of reaction 6-3) increases on the surface. As a result the conductivity and capacitance of the surface layer decreases. The second break in the plot occurs around 0.2 V_{MSE} (0.8 V_{SHE}). This break as seen in the Mott-Schottky plot is very close to the potential at which reaction 6-4 is believed to start. As a result, it is suggested that the formation of the $Cu_{1-x-z}S_2$ layer on the surface –reaction 6-4– changes the electrical properties of the surface in this potential region. It has already been mentioned that chalcopyrite actively dissolves in the potential range of 0.3 – 0.42 V_{MSE} (potentiodynamic and EIS studies section) and reactions 6-6 and 6-7 are the suggested reactions. Since the dissolution of the chalcopyrite is electrochemically active in this potential region, it is likely that either no surface layer is present on the chalcopyrite surface or that which is present is ineffective. Thus, the observed behavior of the electrode in the Mott Schottky plots of Figure 6-11 in the potential range of 0.3 – 0.42 V_{MSE} (0.9 – 1.02 V_{SHE}) is directly associated with the properties of the chalcopyrite. The Mott Schottky curves of Figure 6-11 show a negative slope for the electrode in this potential region which means that the chalcopyrite electrode of the present study is a *p-type* semiconductor. At close to 0.4 V_{MSE} (1.1 V_{SHE}) another break in Figure 6-11 appears which is be related to the formation of a *CuS* layer on the chalcopyrite surface according to reaction 6-8.

Table 6-2 shows the charge carrier density and effective Debye length for chalcopyrite and its surface layers in 0.5 M H_2SO_4 electrolyte for different frequencies. In the development of this table it is assumed that the capacitance measured by the Mott-Schottky method is very close to the space charge region capacitance. Actually, for potentials less than –0.1 V_{MSE} (0.5 V_{SHE}) and in the potential range of 0.3 to 0.4 V_{MSE} (0.9 to 0.1.1 V_{SHE}) the Nyquist curves are not very complex. It is therefore acceptable to employ the Mott-Schottky technique for the measurement of the space charge region capacitance and the calculated charge carrier density and effective Debye length likely represent good estimates in these potential ranges. For other potential ranges (for example –0.1 to 0.3 V_{MSE}) the Nyquist

curves are very complex and calculated numbers in Table 6-2 are likely poor estimates. The dielectric constant, ε, of chalcopyrite at room temperature is close 10 [Salsman *et al.*, 1996]. Assuming that the dielectric constant of all surface layers ($Cu_{1-x}Fe_{1-y}S_2$ and $Cu_{1-x-z}S_2$) are close to that of the chalcopyrite, the donor density of surface layers for four different potential regions are determined using the slope of Eq. 6-12 (refer to Table 6-2). Table 6-2 also contains the effective Debye length which was calculated according to the Debye equation [Memming 2001]:

$$L_{D,eff} = \left(\frac{\varepsilon \varepsilon_0 kT}{2ne^2} \right)^{\frac{1}{2}} \qquad\qquad 6\text{-}13$$

Table 6-2 shows that the charge carrier density and effective Debye length of the interface decreases and increases by increasing the potential, respectively. Under the assumption that there is no surface layer on the electrode in the 0.3 to 0.4 V_{MSE} (0.9 to 1.1 V_{SHE}) range (active dissolution range), the charge carrier density in this region is that of the electrode (chalcopyrite) and is calculated to be close to 10^{22} m^{-3}.

Table 6-2: Charge carrier density and effective Debye length for chalcopyrite and its surface layers at 0.5 M H_2SO_4 electrolyte.

	< -0.1 V_{MSE}		-0.1 to 0.2 V_{MSE}		0.2 to 0.3 V_{MSE}		0.3 to 0.4 V_{MSE}	
f	n_1	$L_{D,eff,1}$	n_2	$L_{D,eff,2}$	n_3	$L_{D,eff,3}$	P_4	$L_{D,eff,4}$
kHz	m^{-3}	nm	m^{-3}	nm	m^{-3}	nm	M^{-3}	nm
1	8.8×10^{24}	0.9	6.2×10^{23}	3.3	2.6×10^{23}	5.2	5.3×10^{22}	11.5
10	1.9×10^{24}	1.9	2.5×10^{23}	5.3	0.8×10^{23}	9.5	2.8×10^{22}	15.8

6.2.6 Model development

Considering the surface properties and dissolution processes already elucidated at various potentials, the EIS data were fitted to different equivalent electrochemical circuits. Figure 6-12a shows the modeled circuit for the potential range of OC to 0 V_{MSE} (OC to 0.6 V_{SHE}) and the calculated Nyquist plots according to the model. In this model, the constant phase element (CPE) most probably presents due to defects in the passive layer [Chen *et al.*, 2008]. Another physical explanation for the CPE would be electrode roughness [Mulder *et al.*, 1990]. R_{CPE} represents the resistance of the CPE in the equivalent circuit. The C_p/R_p pair and the C_{SC}/R_{SC} pair represent the capacitive and resistive behavior of the passive film on the

surface and in the space charge region of the passive film, respectively. In all of the models R_{sol} is the contribution of the solution resistance to the electrochemical circuit. This model was also previously considered for the Si/SiO_2 electrode in HCl electrolyte [Kareh *et al.,* 2009]. Figures 6-12b to e present the measured and modeled (calculated) Nyquist plots for the anodic dissolution potentials of OC to $0\ V_{MSE}$. The passive layer formed at this potential is believed to be the $Cu_{1-x}Fe_{1-y}S_2$ layer which forms through reaction 6-3. The values of the different elements in the equivalent circuit of Figure 6-12a are shown in Table 6-3.

Table 6-3: Model parameters for equivalent circuit of Figure 6-12a (presented in next page).

Potential (mV)	R_{SC} ($\Omega\,cm^2$)	$10^6\ C_{SC}$ ($F\,cm^{-2}$)	$10^5\ R_P$ ($\Omega\,cm^2$)	$10^5\ C_P$ ($F\,cm^{-2}$)	R_{CPE} ($\Omega\,cm^2$)	$10^5\ Q$ ($\Omega\,s^{-n}$)	n
OCP	14.5	5.83	9.5	1.51	13.4	4.26	0.710
-200	9.0	12.70	7.5	2.43	12.6	5.48	0.685
-100	7959.0	6.69	7.9	1.21	16.6	12.75	0.606
0	51210.0	12.10	3.4	35.24	5690.0	1.77	0.800

Increasing the potential to $0.15\ V_{MSE}$ ($0.75\ V_{SHE}$) results in transpassive dissolution of the passive layer formed at lower potentials. This transpassive dissolution results in a porous surface layer as shown by Velásquez *et al*. [2005]. Figure 6-13a shows the proposed model for such a surface layer in which the surface roughness is taken into account. In this model (Figure 6-13a) C_1/R_1 pair refers to the passive layer at sections with maximum thickness and C_2/R_2 pair refers to the passive layer at sections with minimum thickness. Such a model has previously been used by Mansfeld and Kendig [1988] for modeling the interfacial behavior of Al with a porous alumina passive layer on the surface. The $C_{SC}||R_a||(LR_b)$ section of the model refers to the dissolution of the semiconductor at the electrolyte as used by different researchers [Gomes and Vanmaekelbergh 1996; Vanmaekelbergh and Searson 1994]. The parallel connection of the $R_a||(LR_b)$ corresponds to the real impedance values during the depletion layer control of the dissolution process while the Helmholtz layer control of the process corresponds to the imaginary impedance values [Vanmaekelbergh and Searson 1994]. Figures 6-13b and c represent the measured and modeled Nyquist plots and total magnitude of the impedance Bode plot for the chalcopyrite electrode at $0.15\ V_{MSE}$ ($0.75\ V_{SHE}$).
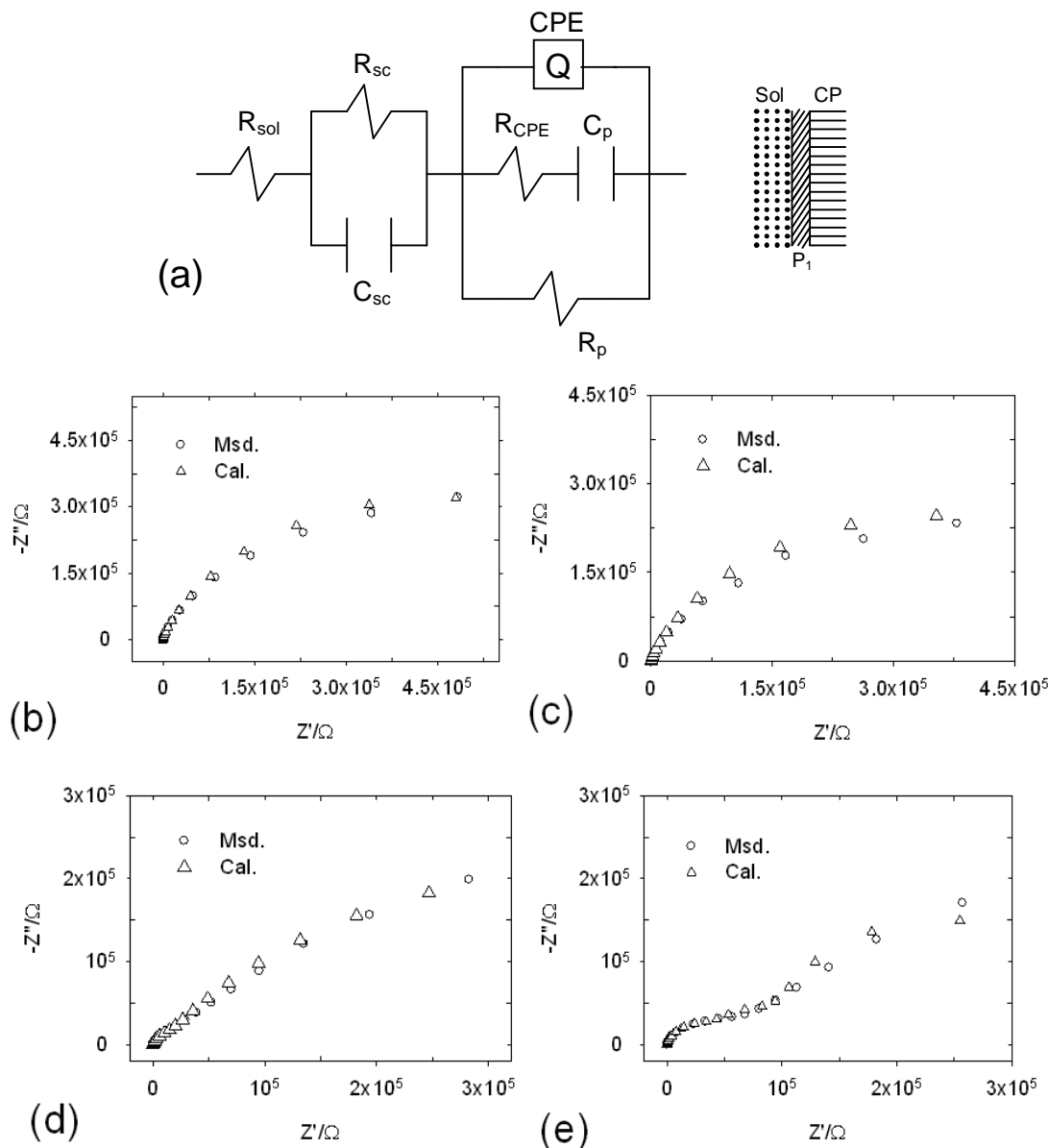
Figure 6-12: (a) Equivalent electrochemical circuit for the Chalcopyrite/electrolyte interface at low anodic potentials; Measured and calculated Nyquist plots for chalcopyrite electrode at (b) OC potential, (c) -200 mV, (d) -100 mV, (e) 0.0 mV.

From the EIS and polarization studies presented above, a second passive layer ($Cu_{1-x-z}S_2$) forms on the surface of the electrode through reaction 6-4 in the potential range of 0.2 – 0.3 V_{MSE} (0.8 to 0.9 V_{SHE}). The model for the electrochemical circuit at this potential range is illustrated in Figure 6-14a. In this figure, the R_p/C_p represent the resistance and capacitance of the inner passive film (i.e. directly on the chalcopyrite surface) while CPE and R_{CPE} are used to model the outer surface layer. The parallel connection of the $R_a||(LR_b)$ corresponds to

the dissolution of the semiconductor electrode and the C_{SC}/R_{SC} pair represent the capacitive and resistive behavior of the space charge region of the passive film. The calculated and measured Nyquist plots and impedance magnitude Bode plots are shown in Figures 6-14e – b for 0.2 and 0.25 V_{MSE} (0.8 to 0.85 V_{SHE}).
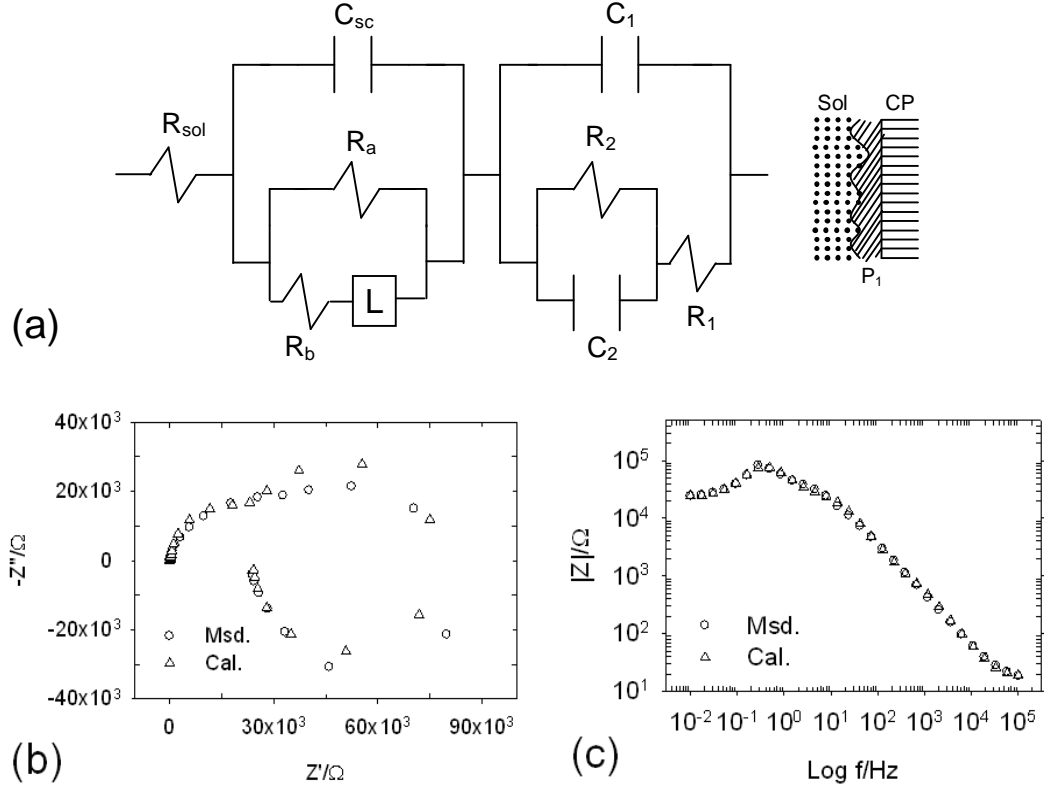
Figure 6-13: (a) Equivalent electrochemical circuit for the Chalcopyrite/electrolyte interface at 0.15 V_{MSE} (0.75 V_{SHE}); Measured and calculated (b) Complex-impedance plane representation, and (c) Bode representation of the magnitude of the impedance.

Figure 6-14: (a) Equivalent electrochemical circuit for the Chalcopyrite/electrolyte interface at potential range of 0.2 to 0.25 V_{MSE} (0.8 – 0.85 V_{SHE}); Measured and calculated (b) Nyquist representation at 0.2 V_{MSE}, (c) Bode representation of the magnitude of the impedance at 0.2 V_{MSE}, (d) Nyquist representation at 0.25 V_{MSE}, (e) Bode representation of the magnitude of the impedance at 0.25 V_{MSE}.

In the potential range of 0.3 to 0.4 V_{MSE} (0.9 to 1.0 V_{SHE}) active dissolution of chalcopyrite electrode occurs. The model chosen for this potential range is shown in Figure 6-15a. The $C_{ss}||R_L||(LR_{SS})$ section of the model represents the dissolution of semiconductor electrodes in which C_{SS} and R_{SS} contribute to the surface (or interface) states on electrode and L, R_L denote the imaginary part of the impedance. A model close to this has been used by Cardon [1972] for the dissolution of a semiconductor-electrolyte interface with electron

100

transfer through surface states. The model considers surface state interactions with both the conduction and valence bands and with the filled and empty states of a redox system. The R_{sol} and C_{SC}/R_{SC} pair addresses the solution resistance and capacitive and resistive properties of the space charge region, respectively. As discussed before, the Nyquist plots at these potentials show a jump in real impedance values around the frequency of 10 Hz. However, the nature of this phenomenon is not clear to these authors. As a result, the proposed model for the $0.3 - 0.4$ V_{MSE} potential range (Figure 6-15a) does not address the jump in EIS results. In order to generate best fit results, the data points at the frequencies less than 10 Hz are disregarded for models fit at 325 and 350 mV_{MSE}. At the potential of 390 mV_{MSE} (990 mV_{SHE}) the 10 Hz jump is very small and considered to be of negligible importance to the modeling procedure. Figures 6-15b – d present the measured and modeled Nyquist plots for the three potentials tested between 300 and 400 mV_{MSE}. The values of the different elements in the equivalent circuit of Figure 6-15a are shown in Table 6-4.

Table 6-4: Model parameters for equivalent circuit of Figure 6-15a.

Potential (mV)	R_{SC} (Ω cm^2)	$10^7 C_{SC}$ (F cm^{-2})	R_{SS} (Ω cm^2)	$10^5 C_{SS}$ (F cm^{-2})	R_L (Ω cm^2)	L (H)
325	122.2	5.55	20.2	1.92	1087.0	15.61
350	92.9	5.47	9.3	2.79	117.2	9.77
390	24.9	8.52	7.5	1.64	21.9	2.04
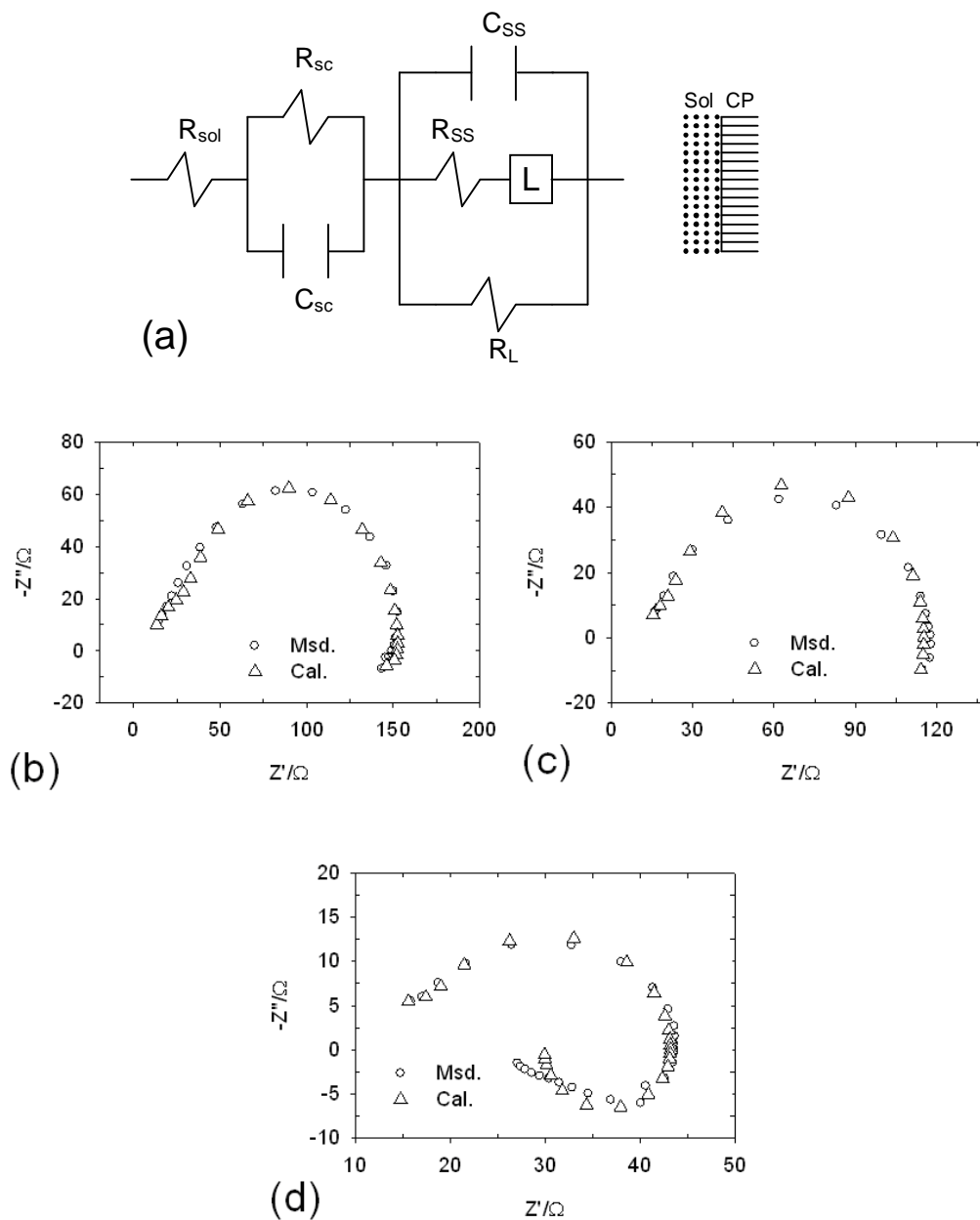
Figure 6-15: (a) Equivalent electrochemical circuit for the Chalcopyrite/electrolyte interface at potential range of 0.3 to 0.4 V_{MSE} (0.9-1.0 V_{SHE}); Measured and calculated Nyquist representations at (b) 325, (c) 350, and (d) 390 mV_{MSE}.

Figure 6-16a shows the model applied for the 0.5 V_{MSE} (1.1 V_{SHE}) Nyquist plot. In this model the circuit components CPE||R_L||L_1R_{CPE} represent the formation and associated properties of the surface layer on the electrode. The surface layer is a *CuS* layer which forms as a product of reaction 6-8. The element L_1 represents ion transfer from the double layer or an increase in the surface area of the electrode due to partial dissolution [Vanmaekelbergh

and Erné 1999]. The components labeled $C||R_b||L_2R_a$ represent the dissolution of the semiconductor electrode as discussed previously. Figure 6-16b shows the measured and calculated Nyquist plots at 0.5 V_{MSE}.

(a)

(b)
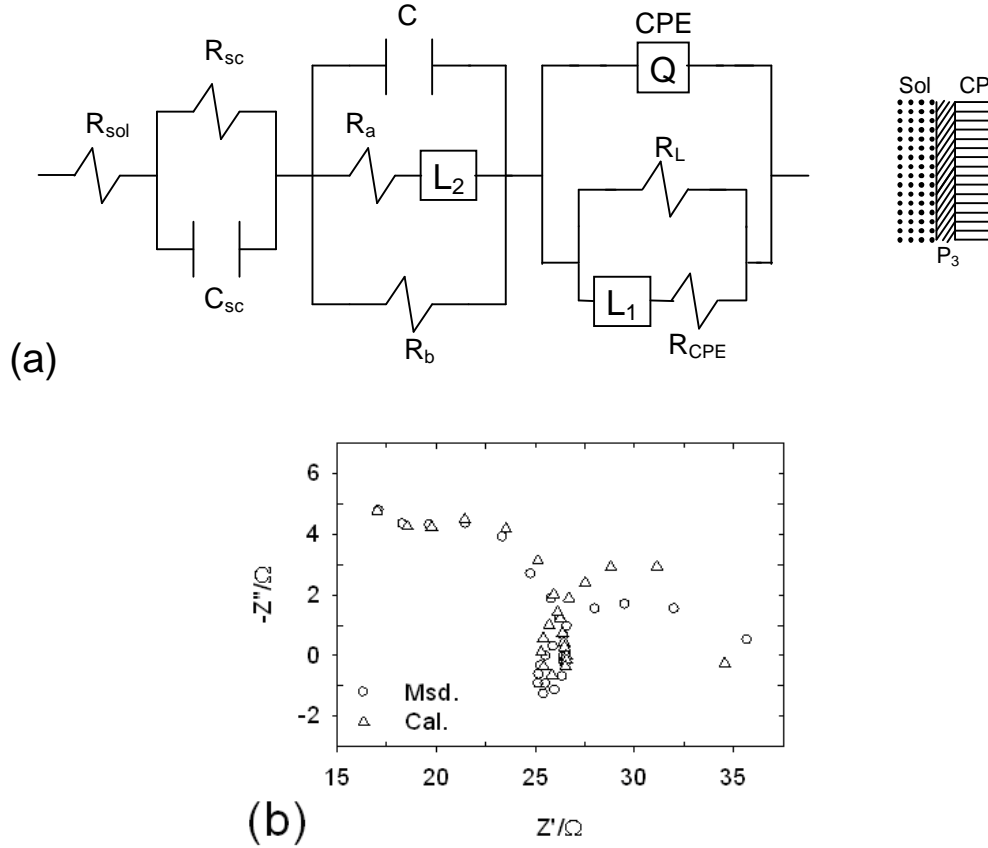
Figure 6-16: (a) Equivalent electrochemical circuit for the Chalcopyrite/electrolyte interface at potential of 0.5 V_{MSE} (1.1 V_{SHE}), (b) Measured and calculated Nyquist representation at 0.5 V_{MSE}.

The modeled electrochemical circuit for the potential of 0.75 V_{MSE} (1.35 V_{SHE}) is presented at Figure 6-17a and the modeled Nyquist plot in Figure 6-17b. At this potential the effect of the negative imaginary part is not very significant and so the $CPE||R_p||C_pR_{CPE}$ part of the modeled circuit does not contain any inductive elements. Thus, the $CPE||R_p||C_pR_{CPE}$ section of circuit represents the mass transport in solid state for both of the surface layers. As discussed before, the surface layers are considered to be the *CuS* layer from reaction 6-8 and the gradual formation of jarosite on the surface is expected to occur according to reaction 6-10. The $C_{SC}||R_L||LR_{SC}$ section addresses the dissolution of the semiconductor. Generally, the $C||R||LR$ circuit could be considered as a general model for the dissolution of semiconductors

103

[Gomes and Vanmaekelbergh 1996] and the physical meaning of the elements depends upon the details of the entire dissolution (or electrochemical reactions) mechanism. So, the C in the equivalent circuit of Figure 6-16a might be related to the surface states or the reaction intermediates at the surface which are separate from the space charge capacitance, C_{SC}. However, at a potential of 0.75 V_{MSE}, the mechanism of dissolution changes such that the $C_{SC}||R_{SC}$ section of the circuit dissolves into the main circuit representing semiconductor dissolution ($C_{SC}||R_L||LR_{SC}$). This could be attributed to the importance of charge transfer in the space charge region at this potential. Clearly, the proposed reactions for high potential anodic dissolution of chalcopyrite are very complex in mechanism. For example, reaction 6-8 has been proposed for chalcopyrite dissolution around 0.5 V_{MSE} and this reaction involves the transfer of 28 electrons. At higher potentials, Nava and Gonzalez [2006]:

$$2CuFeS_2 + 16H_2O \longleftrightarrow 2Cu^{2+} + Fe_2(SO_4)_3 + SO_4^{2-} + 32H^+ + 34e^- \qquad\qquad 6\text{-}14$$
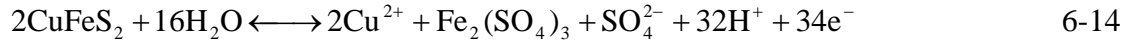
which involves the transfer of 34 electrons. As a consequence, any increase in potential results in significant dissolution mechanism changes which are illustrated in this work by the significant changes in circuit parameterization.

The simulated electrochemical circuit for 1.1 V_{MSE} (1.7 V_{SHE}) is presented in Figure 6-18a. In this model, the C_4/R_4 and C_3/R_3 represent jarosite as a surface film (P_4) and *CuS* as an inner surface layer (P_3), respectively. L_1 is most probably present due to the change in surface area from partial surface layer dissolution [Vanmaekelbergh and Erné 1999]. Physically this can be explained by transpassive dissolution of the inner or outer surface layers. Another explanation for this inductive behavior could be the relaxation of surface charges as discussed before. The $C||R_b||L_2R_a$ section of the circuit refers to the dissolution of the chalcopyrite (as the general reaction occurs at high anodic potential) and the C_{SC}/R_{SC} pair addresses the capacitance and resistance of the space charge region. Figure 6-18b shows the best fit for the Nyquist plot at 1.1 V_{MSE} which is fitted by the proposed model for this potential. Higher magnification of the Nyquist plot for the frequency region related to the formation of the first surface layer (CuS layer) is presented in Figure 6-18c.

(a)

(b)
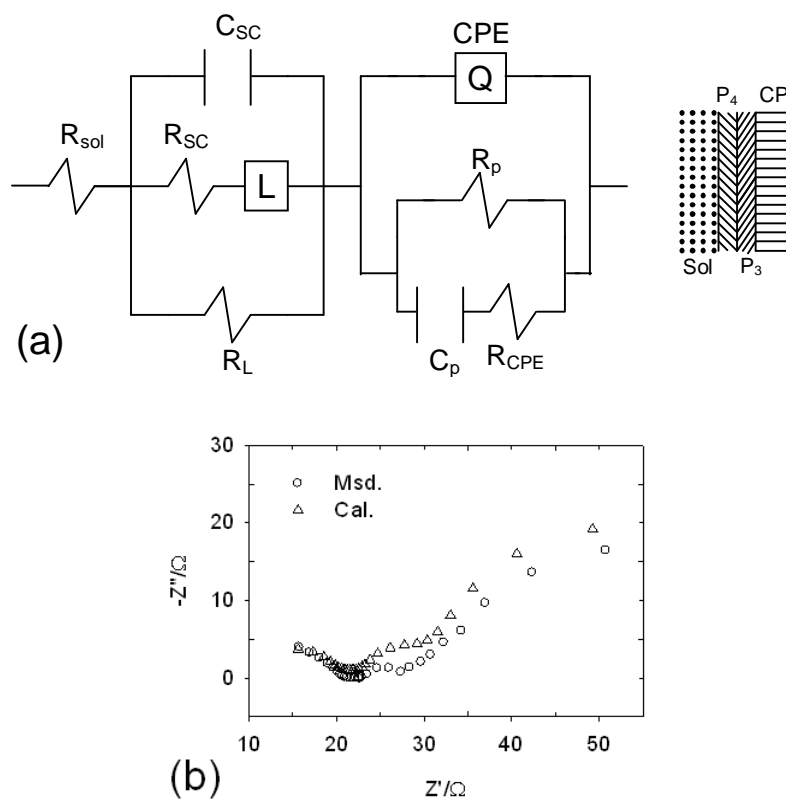
Figure 6-17: (a) Equivalent electrochemical circuit for the Chalcopyrite/electrolyte interface at potential of 0.75 V_{MSE} (1.35 V_{SHE}), (b) Measured and calculated Nyquist representation at 0.75 V_{MSE}.
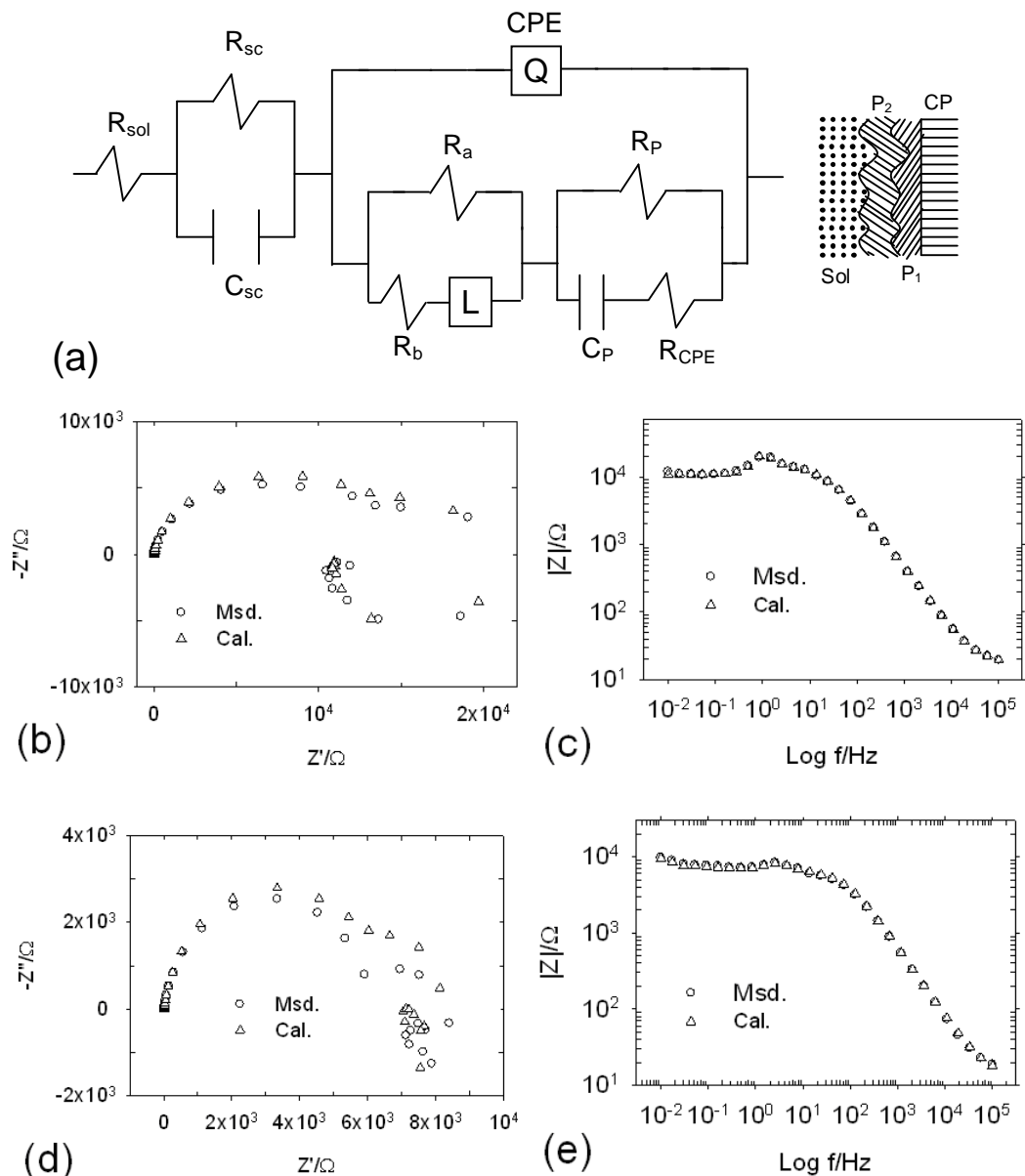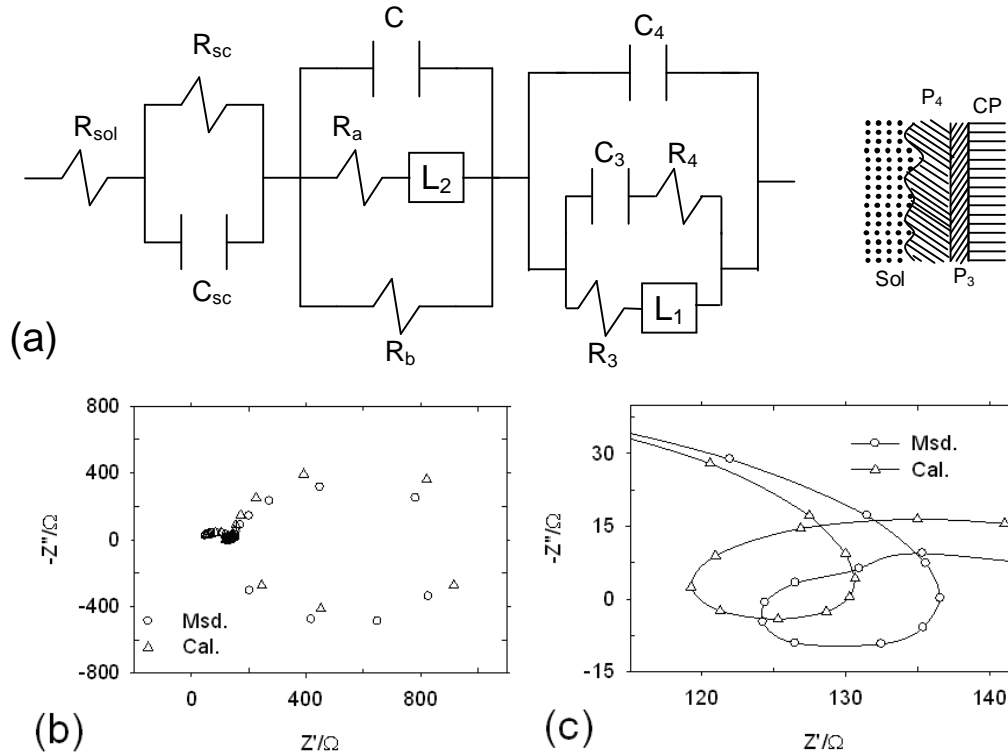
Figure 6-18: (a) Equivalent electrochemical circuit for the Chalcopyrite/electrolyte interface at potential of 1.1 V_{MSE} (1.7 V_{SHE}), (b) Measured and calculated Nyquist representation at 1.1 V_{MSE}, (c) magnification of Figure 6-18b.

All of the equivalent electrochemical circuit models are generated by considering the sequence of proposed electrochemical reactions of section 6.2.4. Several points are worth mentioning when summarizing the results of this chapter:

- At the outset, a thin $Cu_{1-x}Fe_{1-y}S_2$ layer is present on the surface of the electrode. This is a passive layer which forms during the sample preparation and by application of an anodic potential its thickness increases via reaction 6-3. The layer is stable up to the potential of 0.1 V_{MSE} (0.7 V_{SHE}).

- In the potential range of the 0.1 – 0.3 V_{MSE} (0.7 – 0.9 V_{SHE}) the $Cu_{1-x}Fe_{1-y}S_2$ layer dissolves and a second passive layer of $Cu_{1-x-z}S_2$ forms through reaction 6-4. Generally, in the lower half of the potential range (around 0.1 – 0.15 V_{MSE}) the transpassive dissolution of the $Cu_{1-x}Fe_{1-y}S_2$ layer is the major phenomenon on the surface (Nyquist curve of Figure 6-4 at 0.15 V_{MSE}) and by increasing the potential to the upper half of the range (0.15 – 0.3 V_{MSE}) a complete film of $Cu_{1-x-z}S_2$ forms on the outer surface of the porous $Cu_{1-x}Fe_{1-y}S_2$ layer (Nyquist curve of Figure 6-4 at 0.25 V_{MSE}). The model of Figure 6-13 addresses the transpassive dissolution of the $Cu_{1-x}Fe_{1-y}S_2$ layer while the

106

model of Figure 6-14 elucidates the effect of the $Cu_{1-x-z}S_2$ film as a second passive layer formed on the surface of the first passive layer of $Cu_{1-x}Fe_{1-y}S_2$. At this point, the $Cu_{1-x}Fe_{1-y}S_2$ layer is a thin porous layer directly on the surface of chalcopyrite.

- In the potential range of 0.3 – 0.42 V_{MSE} (0.9 – 1.02 V_{SHE}) the chalcopyrite electrode dissolves with an electrochemically active surface. Dissolution of the previously formed $Cu_{1-x-z}S_2$ layer occurs through reaction 6-5 and chalcopyrite dissolves via reaction 6-6 and/or 6-7.

- Increasing the potential of the electrode into the range of 0.42 – 0.7 V_{MSE} (1.02 – 1.3 V_{SHE}) causes the formation of a *CuS* layer on the surface of the electrode via reaction 6-8. This layer impedes the dissolution rate of the electrode (ref. to the low scan rate potentiodynamic curves of Figure 6-3). However, considering the high dissolution current, the layer is not a passive layer.

- For the potentials higher than 0.7 V_{MSE} (1.3 V_{SHE}), the previously formed surface layer of *CuS* dissolves through reaction 6-9. Moreover, the conditions are favorable for the formation of jarosite on the surface via reaction 6-10.

Thermodynamic data (via *E*-pH diagrams [Garrels and Christ, 1965]) indicate that chalcopyrite will dissolve at pH less than 6 and an oxidizing potential higher than –0.4 V_{MSE} (0.2 V_{SHE}). However, the main issue in the dissolution of chalcopyrite under atmospheric conditions appears to be the passivation of chalcopyrite through the formation of $Cu_{1-x}Fe_{1-y}S_2$ and $Cu_{1-x-z}S_2$ passive layers.

6.3 Conclusion

The present chapter considered the electrochemical dissolution of chalcopyrite in 0.5 M sulfuric acid solution. Potentiodynamic polarization, electrochemical impedance spectroscopy, and Mott-Schottky techniques were applied. Initially, during the sample preparation a thin layer of $Cu_{1-x}Fe_{1-y}S_2$ forms on the surface of the electrode where $y \rangle\rangle x$. During electrochemical dissolution of chalcopyrite this layer is stable and its thickness increases with potential by reaction 6-3 (OC – 0.1 V_{MSE}). At higher potentials (0.1 – 0.3 V_{MSE}) the previously formed surface layer partially dissolves and a second passive layer ($Cu_{1-x-z}S_2$) forms via reaction 6-4. Both of these layers display the characteristics of passive layers at low scan rate (0.05 mVs^{-1}) and for high scan rates they are observed to be pseudo-

passive. In the potential range of 0.3 to 0.4 V_{MSE}, none of the surface layers are stable and electrochemically active dissolution of the electrode occurs by reactions 6-6 and/or 6-7. By increasing the potential to 0.5 V_{MSE}, CuS is believed to form through reaction 6-8 and this only slightly impedes the dissolution of chalcopyrite. In fact, due to the high dissolution current observed at this potential (around 0.1 Acm^{-2}) this layer cannot be considered a passive layer. At higher potentials (around 0.75 V_{MSE}) the conditions are suitable for the formation of jarosite on the surface of electrode. The ferric sulfate phase (which is produced through reaction 6-8) has been shown to act as a nucleation template for jarosite. Jarosite forms according to reaction 6-9 and this reaction product does decrease the dissolution rate.

Understanding the surface behavior of chalcopyrite during the electrochemical dissolution was the main goal of this study. The observations of the present study were explained based on the literature and results of previous studies. Since EIS was the main electrochemical technique applied in the present study, different equivalent electrochemical circuits were modeled and compared to experimental results to support the proposed sequence of chalcopyrite dissolution and surface layer formation. The models have been used to describe the experimental data in a satisfactory way. In the next chapter, the XPS method will be applied to explore the composition of chalcopyrite's passive film. XPS can provide very useful information about the chemistry of the passive film and the information obtained will be used to understand further details of the dissolution mechanism.

7 X-ray photoelectron spectroscopy analysis of chalcopyrite's surface in sulfuric acid solution

7.1 Introduction

In the previous chapter, electrochemical methods were applied to analyze the surface of a chalcopyrite electrode in 0.5 M sulfuric acid. All the discussion and the proposed reactions were extracted from literature. In the present chapter, X-ray photoelectron spectroscopy will be applied to study the surface of chalcopyrite and link the results to the previous electrochemical studies.

7.2 Results and discussion

7.2.1 Passivation of chalcopyrite; a brief introduction

Figure 7-1a shows the multi-cyclic voltammogram (10 cycles) of the chalcopyrite electrode in the potential window of 0.1 to 1 V_{SHE}. In this experiment, the potential of the electrode was initially swept from 0.55 to 1 V_{SHE} then 10 cycles, from 1 V_{SHE} to 0.1 V_{SHE}, were performed continuously (scan rate was 50 mV s^{-1}). Two anodic peaks at 0.48 V_{SHE} (peak a1) and 0.84 V_{SHE} (peak a2) and a cathodic peak c1 at 0.29 V_{SHE} are clear in Figure 7-1a. Both cathodic and anodic current peaks declined as the experiment proceeded due to the passivation of the electrode surface. The decline of the associated charge with the peak a1, as the number of cycles increased, is shown in Figure 7-1b.

The anodic peak a2 has been shown to be related to the initial dissolution of chalcopyrite [Yin *et al.*, 1995]. This peak is completely undetectable in all of the following cycles due to passivation of chalcopyrite (this point is very clearly shown in Fig. 7-1c). In other words, during the following cycles, the surface of chalcopyrite appears to be in the passive state and the dissolution rate seems to be controlled by mass transfer through the passive film which substantially reduces the dissolution rate [Yin *et al.*, 1995]. For the same reason, the associated charge with this peak of Fig. 1a decreases significantly to a negligible value and the peak is not detectable in the second cycle. The anodic peak at 0.84 V_{SHE} (peak a2) has been attributed to the following reaction [Yin *et al.*, 1995]:

$$CuFeS_2 = CuS_2^* + Fe^{2+} + 2e^-$$ 7-1
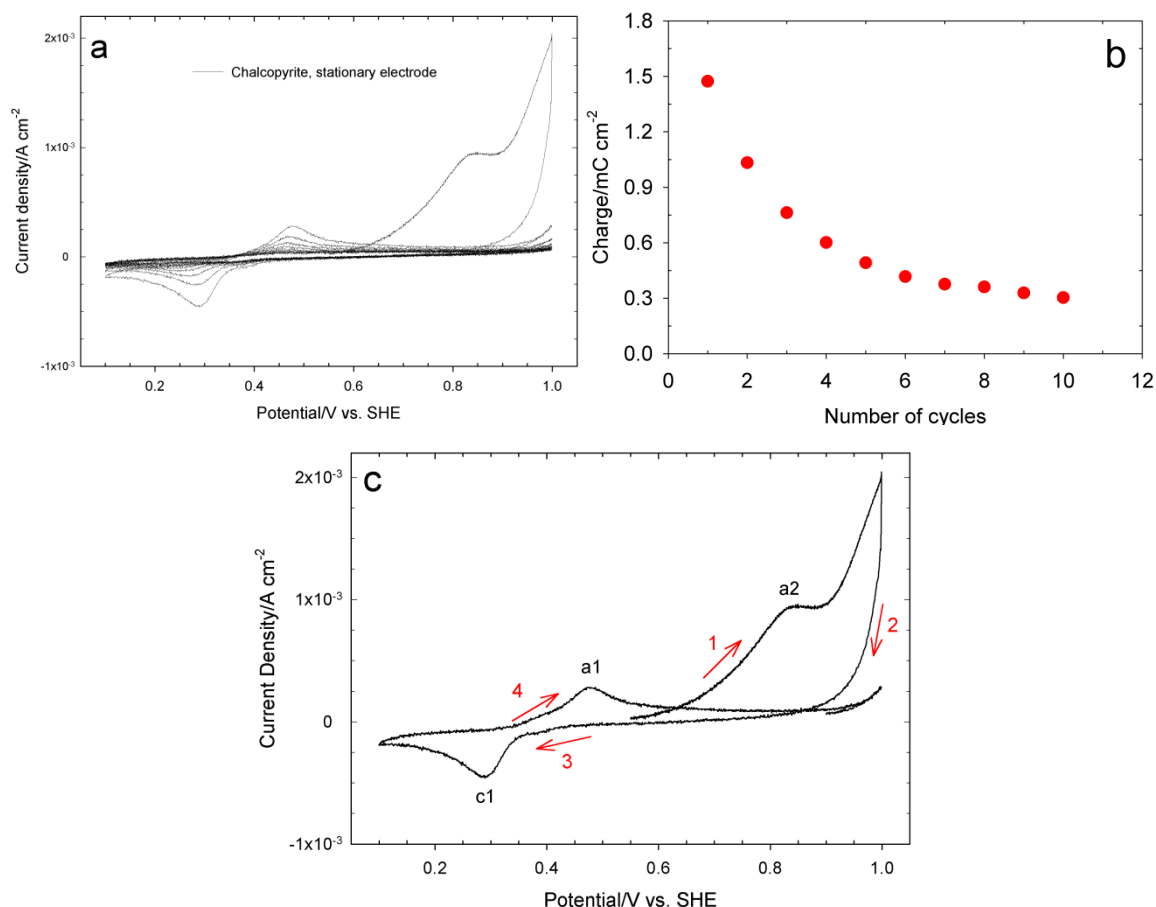
Figure 7-1: (a) Multicyclic voltammogram (10 cycles) of a chalcopyrite electrode in the potential window of -0.1 to 1 V_{SHE}, (b) associated charge with the anodic peak of Figure 7-1a at 0.476 V at each cycle, (c) first cycle of Figure 7-1a.

It has been suggested that the initial chalcopyrite dissolution at 0.84 V_{SHE} results in formation of a metastable copper sulfide phase with the stoichiometry of Cu:2S shown as CuS_2^*. In addition, it has been proposed that this phase is responsible for the subsequent passivation of chalcopyrite [Yin *et al.,* 1995]. It is worth mentioning that peaks c1 and a1 of Fig. 7-1c are not related to the direct oxidation of chalcopyrite; however, the observed decrease in the associated charge at peak a1 (and also c1) is indirectly due to chalcopyrite passivation.

Fig. 7-2a presents the potentiodynamic polarization of chalcopyrite. After stabilizing the electrode in solution at OCP for 6 hours, the electrode was polarized in the cathodic direction (solid-blue curve in Fig. 7-2a). The anodic part of the curve was separately obtained

110

by anodic polarization of a fresh chalcopyrite electrode, also after 6 hours of stabilization at OCP (dashed-red curve in Fig. 7-2a). The applied scan rate in both of the polarization experiments was 0.1 mV s^{-1} and the solution was gently aerated during the experiment. The separate experiments for the measurement of the anodic and cathodic branches were conducted to avoid the impact of cathodic dissolution of chalcopyrite on the anodic section of the curve.

The registered OCP for the electrode after 6 hours, before starting the polarization experiment of Fig. 7-2a, was ca. 0.55 V_{SHE} and the OCP was typically reached after 1 hour of immersion. At potentials between OCP and 0.94 V_{SHE} the electrode shows a slow dissolution rate owing to the passivation of the electrode in this potential window [Viramontes-Gamboa et al. 2007]. This result is in agreement with our previous chapter. It is important to note that a scan rate of 0.1 mV s^{-1} would be sufficiently low to obtain a steady-state polarization response from most metallic electrodes; however, this scan rate is not low enough if one seeks to measure the most stable E-I response of chalcopyrite [Viramontes-Gamboa *et al.,* 2007]. This is clearly shown by comparison of the potentiodynamic polarization diagram of Fig. 7-2a with the potentiostatic polarization diagram of Fig. 7-2b. The passivation of chalcopyrite in sulfuric acid solution is more evident in Fig. 7-2b which shows a decrease in current density as the potential is increased above 0.67 V_{SHE}.
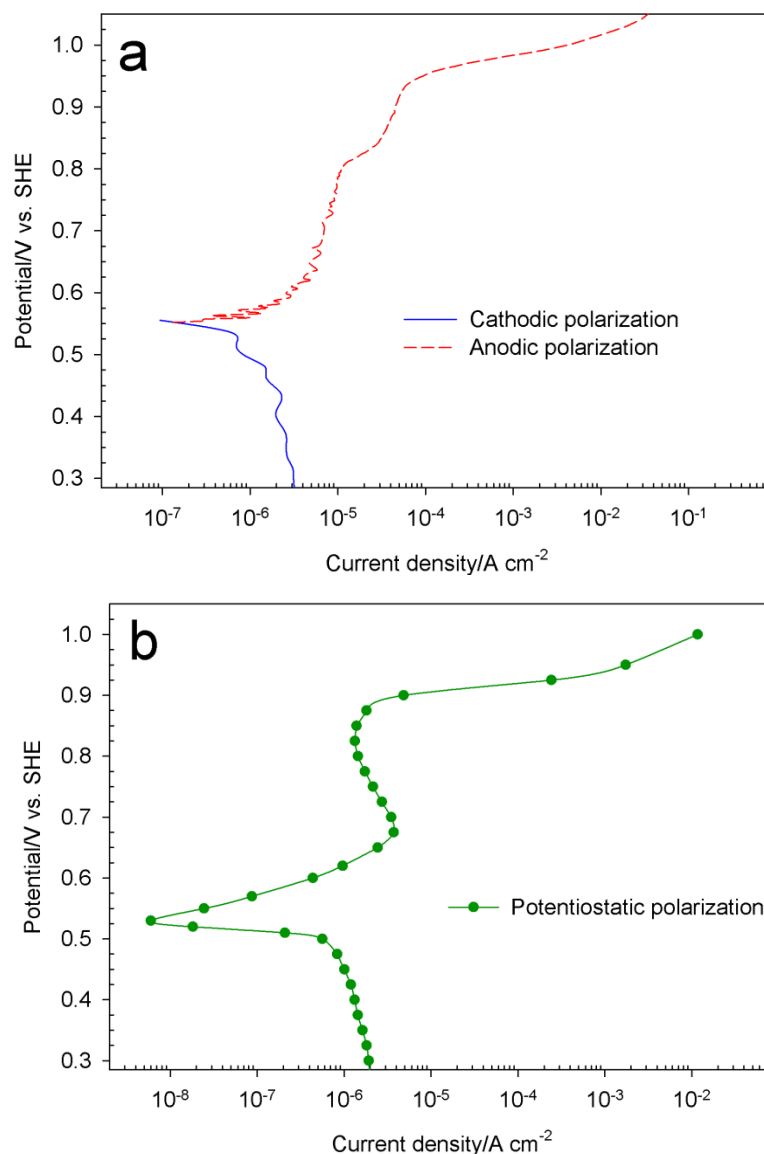
Figure 7-2: (a) Potentiodynamic (SR = 0.1 mV sec^{-1}) and (b) potentiostatic polarization of chalcopyrite electrode in 0.5 M sulfuric acid.

The formation of a stable passive film on the surface of chalcopyrite is the reason for the sharp decrease in current prior to the steady state dissolution current density in the passive potential region being established. This can be confirmed by long term potentiostatic polarization of chalcopyrite at a passive potential, as shown in Fig. 7-3. Fig. 7-3a presents *i-t* behavior of chalcopyrite at potentials of 0.5, 0.55 and 0.65 V_{SHE}. All the curves of Fig. 7-3a show a sharp decrease in the current density during the first few hours of the experiment, which is due to the formation of a passive film. Fig. 7-3b presents the long-term potentiostatic polarization of chalcopyrite at a passive potential. This figure presents the

polarization behavior of chalcopyrite in sulfuric acid solution for about 60 hours at 0.80 V_{SHE}. From Fig. 7-2b, it is obvious that the potential of 0.80 V_{SHE} is within the passive range. Under this polarization condition the electrode reaches the steady state current in about 3 hours and afterwards the current density is almost constant (ca. 1.3 $\mu A\ cm^{-2}$) for the rest of the experiment. This confirms the formation of a stable film on the surface and suggests that the thickness of the passive film most probably remains constant during the 60 hours of experiment. Considering that diffusion is the rate-limiting mechanism in the passive film, which is shown to be the case in chapter 9 of the present thesis, from Fick's first law of diffusion one would expect a substantial decrease in the current density of Fig. 7-3b if the passive film were thickening. For instance, if the thickness of the passive film were to double (during the 60 h of experiment), then the current density should decrease by half. However the current density of Fig. 7-3b (and also Fig. 7-3a) is almost constant, suggesting a passive film of constant thickness.

The formation of a compact elemental sulfur film is also very unlikely at this potential since accumulation of elemental sulfur (as an insulating material) on the surface must lower the current density as a function of time. Additionally, after this experiment (about 60 h), there was no visible product layer on the surface of the electrode. This is in agreement with the findings of other workers [Warren *et al.* 1982; Holliday and Richmond, 1990; Yin *et al.,* 1995] and will be further verified by our XPS results. The noise observed in the current density of Fig. 7-3b (sudden increases in dissolution current) is most probably related to the formation of pits on the electrode [Biegler and Swift, 1979]. Chemical characterization of the species in the passive film is very complicated or impossible by electrochemical methods. Hence, in the next section, XPS was used to provide detailed information about the oxidation state of different species and the composition of the surface film(s).
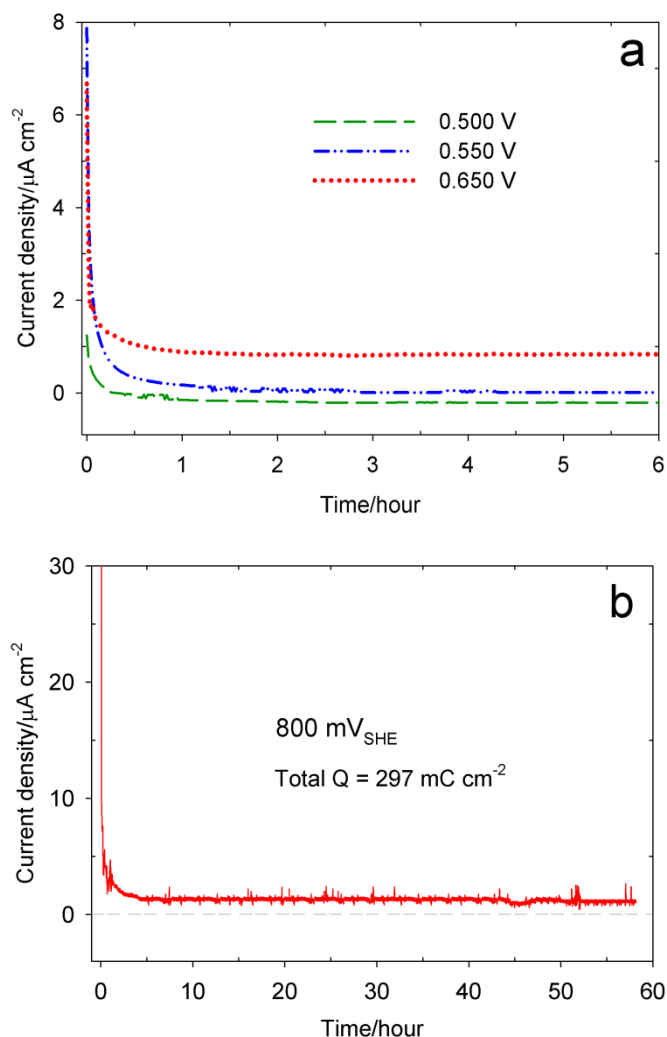
Figure 7-3: Potentiostatic polarization of chalcopyrite at (a) 0.5, 0.55 and 0.6 V for 6 hours, and (b) 800 mV$_{SHE}$ for 60 hours.

7.2.2 XPS study of chalcopyrite (survey spectra)

XPS is a very successful surface analytical tool for mineral dissolution research. Although XPS requires sample transfer from the electrolyte to ultrahigh vacuum (UHV) with a concomitant loss of contact with the electrolyte and loss of electrode potential control, it can provide reliable data on the chemical situation of the surface at the time of removal. This information is required to obtain a sound basis for the interpretation of the mechanisms and kinetics of dissolution processes. In this section we have studied the general XPS spectra of chalcopyrite and also the high-resolution spectra of copper, iron and sulfur species. In some of the experiments the XPS data were obtained after Ar$^+$ ion etching of the sample. These

results will be used as reference for the peak position of copper, iron and sulfur atoms in the chalcopyrite structure. As mentioned above, the ion etching might alter the chemical state of the surface species. In order to eliminate possible errors in the registered results, a low beam energy (1 keV) was applied (for further details refer to the experimental section). Also, all the acquired results were compared with the available results from the literature, in order to ensure the validity of the results.

The survey (full range) XPS spectrum of a chalcopyrite sample is provided in Fig. 7-4. Fig. 7-4a presents the spectrum for polished chalcopyrite after 6 hours of air exposure which shows the carbon, oxygen, copper, iron and sulfur peaks. The binding energy of C1s at 284.6 eV is characteristic of aromatic/aliphatic carbons. The O1s peak may be related to air contamination of the samples and/or surface oxidation of the chalcopyrite. Figure 7-4b presents the spectrum of the same sample after ion etching (in order to remove the passive film) inside the XPS chamber. Etching of the sample removed the oxygen and carbon peaks from the spectrum and only copper, iron and sulfur related peaks remained.

7.2.3 Cu2p peaks in chalcopyrite

Fig. 7-5a shows a typical high-resolution spectrum of Cu 2p for chalcopyrite obtained after ion etching. The fitting results of peaks by XPSPeak 4.1 software revealed that the Cu $2p_{3/2}$ peak is centered at 932.4 eV (FWHM = 1.19), and the Cu $2p_{1/2}$ peak is centered at 952.3 eV (FWHM = 2.43). The suggested binding energies for the Cu $2p_{3/2}$ and Cu $2p_{1/2}$ peaks of chalcopyrite are 932.4 eV and 952.1 eV, respectively [Nakai *et al.* 1978], which are in excellent agreement with our data. It is worth mentioning that the presence of Cu^{2+} usually results in the appearance of a satellite peak around the binding energy of 942 eV [Yin *et al.* 2005; Chusuei *et al.,* 1995]. In the case of the spectrum presented in Fig. 5a, no evidence for such a satellite peak exists and subsequently the divalent state of copper (Cu^{2+}) is not observed. This agrees with the results of other workers suggesting the presence of only monovalent copper atoms in the chalcopyrite structure [Nakai *et al.* 1978]. Fig. 7-5b presents the copper auger spectrum ($Cu_{L3M45M45}$) excited with X-rays, which is centered at 568.9 eV. This value is close to that measured by Brion [1980], which was 568.65 eV. The $Cu_{L3M45M45}$ values for the Cu-Cu bond, CuS and Cu_2S are 568.1, 568.5 and 569.5 eV, respectively [Ghahremaninezhad *et al.,* 2011].
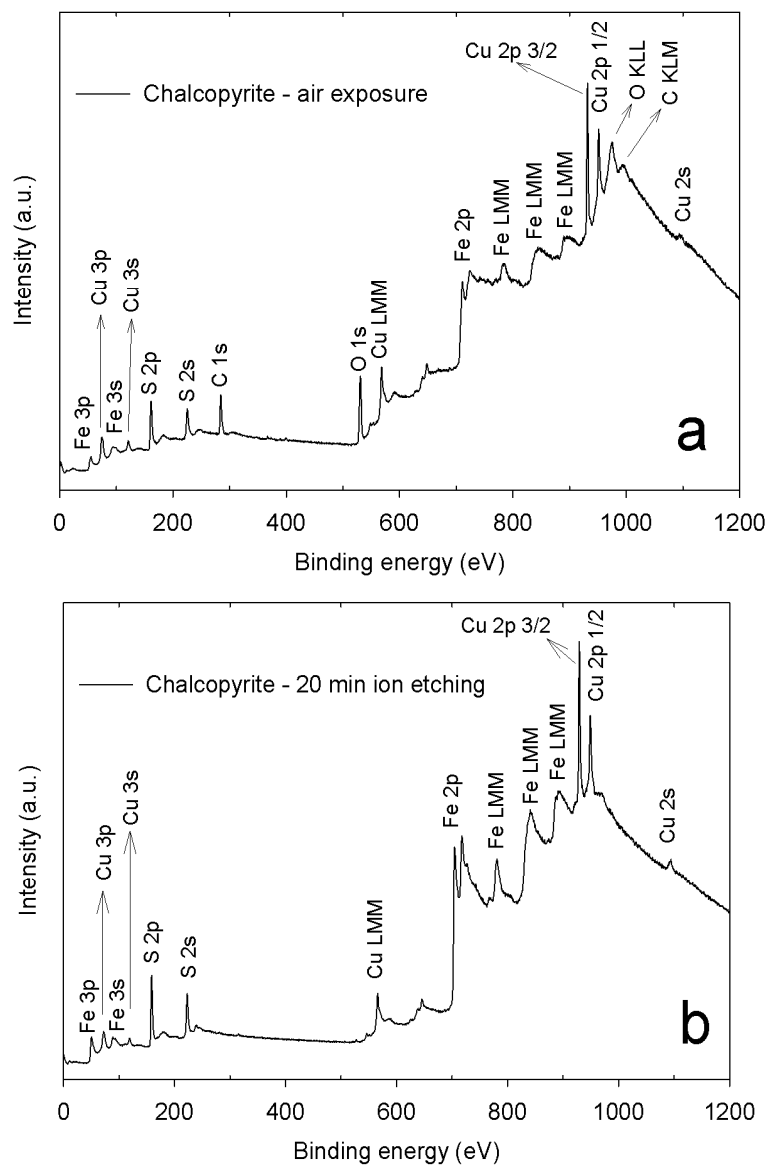
Figure 7-4: The survey (full range) XPS spectrum of chalcopyrite (a) after polishing and 6 hours of air exposure, (b) after ion etching inside the XPS chamber.
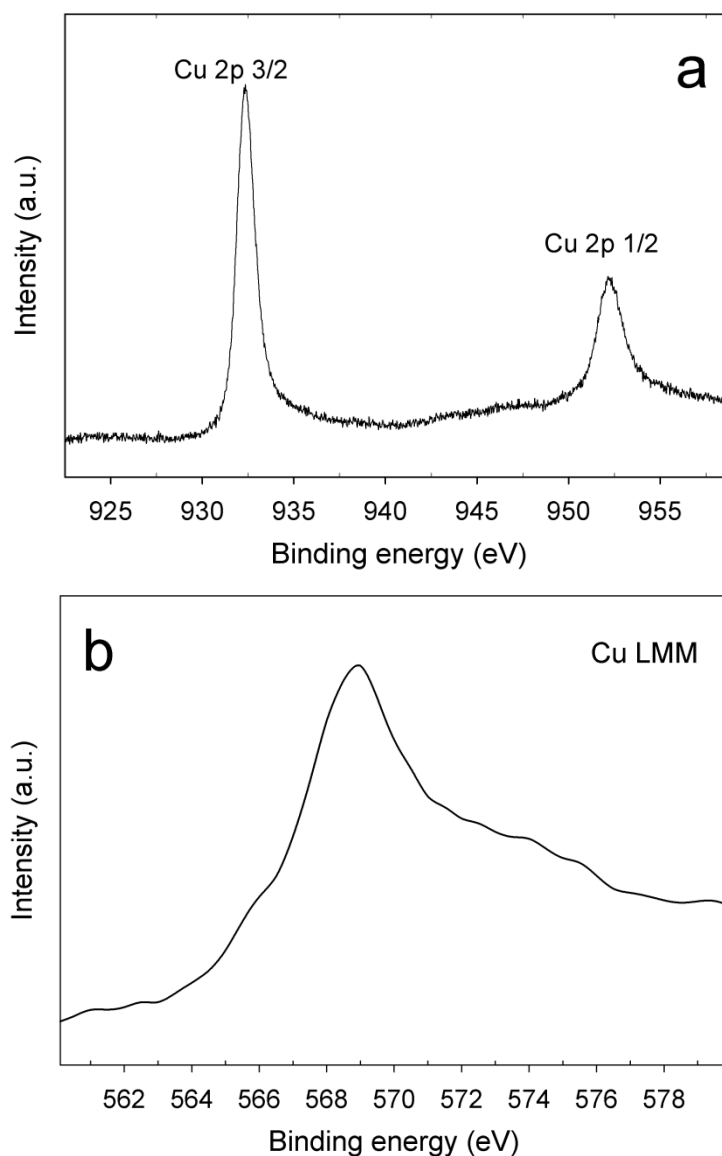
Figure 7-5: (a) XPS spectrum of Cu2p, and (b) copper Auger spectrum excited by X-rays, obtained after ion etching.

7.2.4 Fe2p and Fe3p peaks of chalcopyrite

A typical high-resolution spectrum of Fe 2p for chalcopyrite obtained after ion etching is presented in Fig. 7-6. The spectrum shows two strong peaks of Fe $2p_{3/2}$ and Fe $2p_{1/2}$ at 707.8 eV and 721.1 eV, respectively. These are related to fully coordinated Fe atoms in the chalcopyrite structure and are consistent with the results of other workers [Brion, 1980].
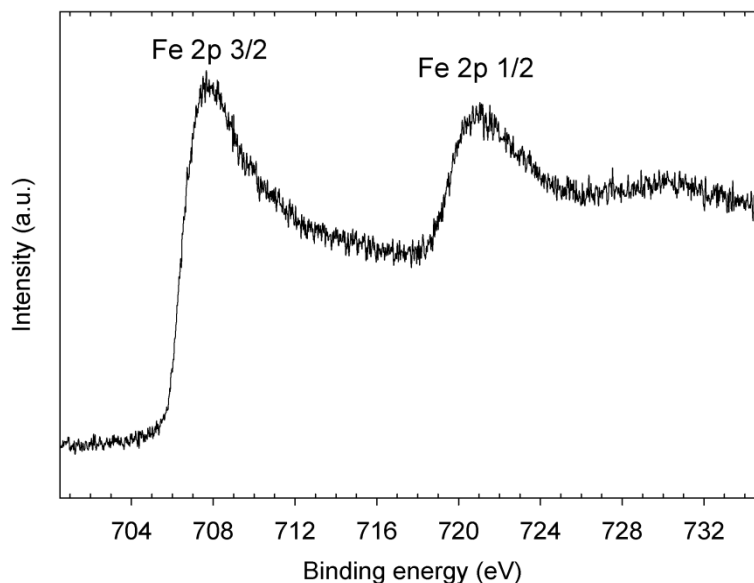
Figure 7-6: XPS spectra of (a) Fe2p, and (b) Fe3p of chalcopyrite, obtained after ion etching.

7.2.5 S2p and S2s peaks of chalcopyrite

Fig. 7-7 shows the S 2p core level peak after ion etching. The S 2p peaks also occur as doublets, S $2p_{3/2}$ and S $2p_{1/2}$, as a result of spin–orbit splitting. XPSPeak 4.1 software was used to fit the peaks of the S 2p spectra. The S 2p spectra were fitted using a 2:1 peak area ratio for S $2p_{3/2}$ to S $2p_{1/2}$ and 1.2 eV splitting. The peaks fitted to the spectra use a summed Gaussian-Lorentzian (SGL) function to describe the convoluted Gaussian-Lorentzian line shapes of the peaks. The weighting used was 80% Gaussian and 20% Lorentzian. The background of the spectrum was obtained using the Shirley method [Shirley 1972]. The extracted peak positions from literature were used to assign species to the peaks. The presented S 2p spectrum of Fig. 7-7 consists of two major doublets representing bulk monosulfide and disulfide. The S $2p_{3/2}$ peaks of two doublets of Fig. 7-7 are centered at 161.4 eV and 162.5 eV. The two S $2p_{3/2}$ peaks are 1.1 eV apart. It has been reported that the S $2p_{3/2}$ peak originating from fully coordinated sulfur atoms in chalcopyrite's crystal structure, i.e. monosulfide (S^{2-}), centers at 161.4 eV [Mielczarski *et al.,* 1996] and elsewhere it has been reported to be at 161.5 eV [McCarron *et al.*, 1990]. These results agree well with those of our experiments (S $2p_{3/2}$ peak of Fig. 7-7, centered at 161.4 eV). On the other hand, the position of the S $2p_{3/2}$ peak for the disulfide species (S_2^{2-}) is reported to be 162.48 eV [Klauber *et al.,* 2001], and this again agrees well with the position of the second S $2p_{3/2}$ peak

118

in our data. In fact, it is well established that sulfur anions in the chalcopyrite structure (S^{2-}) undergo a dimerization process to form S_2^{2-} species once they reach the surface of the mineral [Klauber 2003]. Hence, the detected sulfur species on the surface of chalcopyrite are sulfide species (i.e. sulfur species bonded to metallic atoms of copper and iron).

In addition to the two S 2p doublets, Fig. 7-7 presents another peak positioned at 163.7 eV. This peak is a broad peak (FWHM = 2.8) and has previously been related to the formation of polysulfide (S_n^{2-}, n > 2) [Hackl *et al.,* 1995, Klauber *et al.,* 2001]. On the other hand, it has been shown by other researchers [Fujisawa *et al.,* 1994; Goh *et al.,* 2010] that this high-energy feature is a small tail related to the S 3p→Fe 3d interband excitation. In other words, the tail is related to the energy-loss satellite due to the S 3p→Fe 3d excitation [Chernyshova and Andreev 1997; Buckley *et al.,* 1994]. In order to prove that this result is valid in our study, a systematic XPS study was conducted to compare the S 2p core level peaks obtained from Fe-S minerals (i.e. pyrite and pyrrhotite) and Cu-S minerals (i.e. chalcocite and covellite). Table 4-1 shows the compositions of the minerals used in this study; minerals 2 (pyrite rich) and 3 (pyrrhotite rich) were used as Fe-S minerals and minerals 4 (chalcocite rich) and 5 (covellite rich) were used as Cu-S minerals. The results are presented in Fig 7-8a to d. Figs. 7-8a, b, c and d show the high-resolution sulfur spectrum of minerals 2 (pyrite), 3 (pyrrhotite), 4 (chalcocite) and 5 (covellite), respectively. From the comparison of the figures, it is clear that the energy loss feature at high binding energy (~ 163.5 eV) is present in Fe-S minerals (Figs. 7-8a and b), while it is absent in Cu-S minerals (Figs. 7-8c and d). This result further clarifies that the high-energy feature in sulfur species spectra is most likely related to the S 3p→Fe 3d excitation and does not originate from polysulfide.

The S 2s core level peak of chalcopyrite after ion etching is presented in Fig. 7-9. The peak is positioned at binding energy of 225.6 eV. The S 2s peaks of the S ions in CuS and Cu_2S are reported to be 225.6 and 225.3 eV, respectively; while the S 2s peak of elemental sulfur occurs at a binding energy of 228.4 eV [Chernyshova and Andreev 1997; Buckley *et al.,* 1994]. The energy difference between the S 2s level of elemental sulfur and sulfides is appreciably wide (~3 eV) and this fact can be used to confirm sulfur formation on the surface of leached chalcopyrite samples. The XPS results obtained for a chalcopyrite sample conditioned with Ar^+ ion is summarized in Table 7-1. These data can be used as the reference

values for XPS analysis of chalcopyrite. In the next section the chalcopyrite electrodes were polarized at different anodic potentials and afterwards the outermost surface of chalcopyrite was analyzed by XPS. In order to eliminate any alteration of surface species during the XPS experiment, no argon ion etching was performed on the surface of the samples.
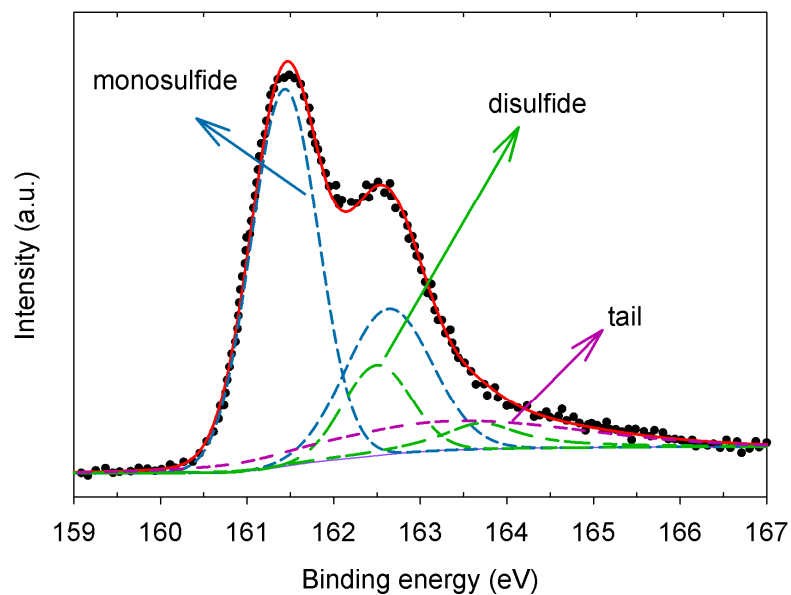
Figure 7-7: XPS spectrum of S 2p peak of chalcopyrite.
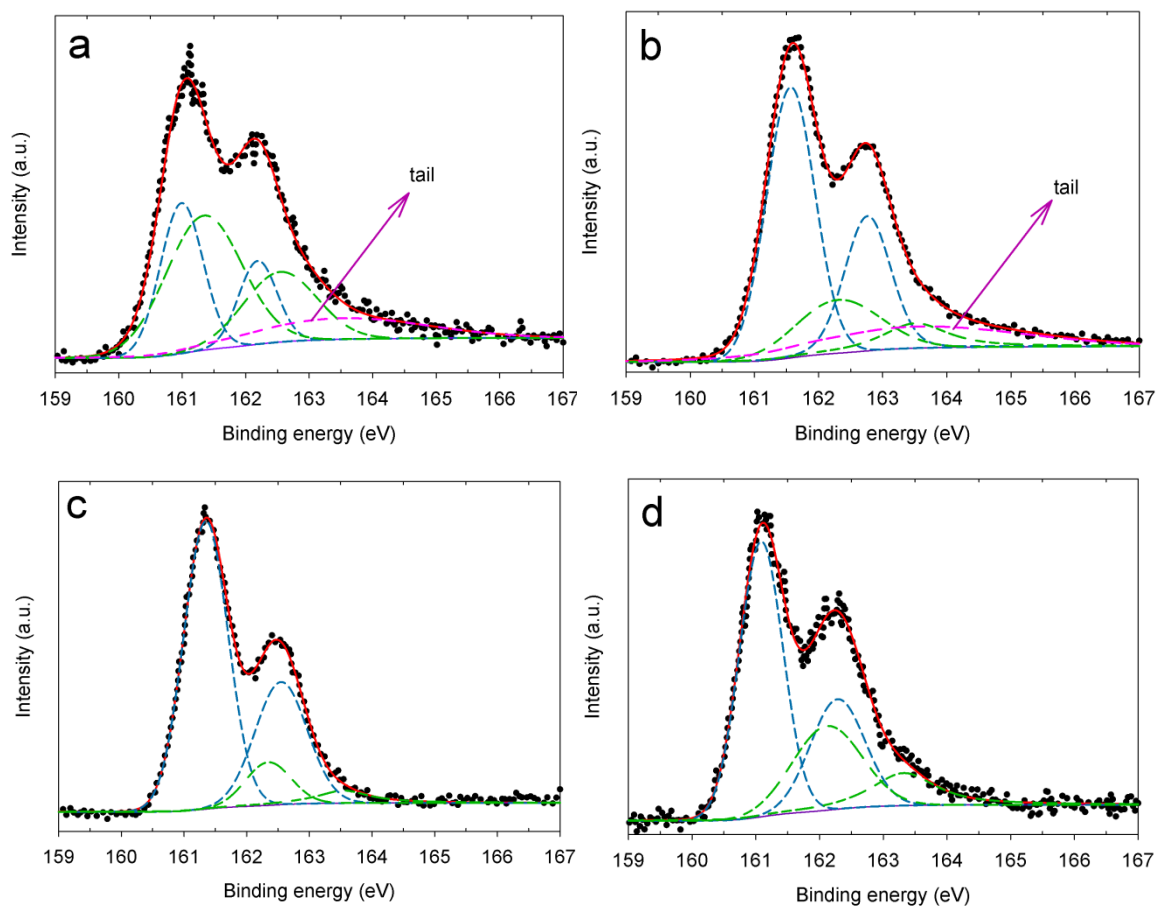
Figure 7-8: S2p core level peaks obtained from minerals (a) 2 (pyrite, FeS$_2$), (b) 3 (pyrrhotite, Fe$_{1-x}$S), (c) 4 (chalcocite, Cu$_2$S), and (d) 5 (covellite, CuS). Composition of each mineral is presented in Table 4-1.
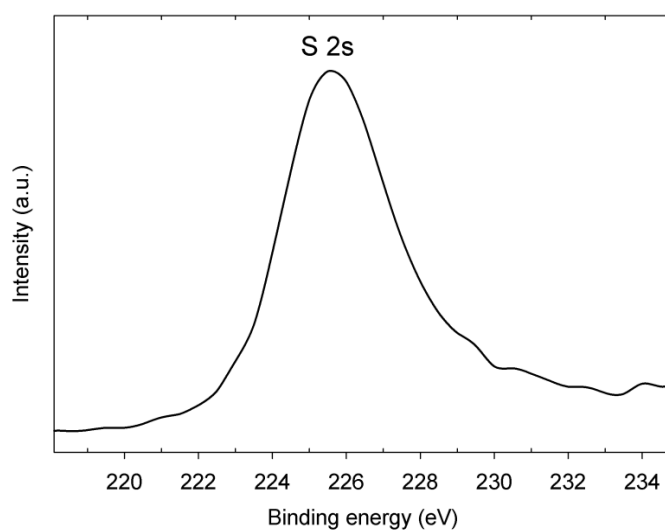
Figure 7-9: S2s core level peak of chalcopyrite.

Table 7-1: Binding energy (eV) of Cu, Fe and S elements for chalcopyrite after Ar$^+$ ion etching.

Cu Valence	Binding energy of core levels (eV)								
	Cu 2p		Cu$_{LMM}$	Fe 2p		Fe 3p	S 2p3/2		S 2s
	3/2	1/2		3/2	1/2		monosulfide	disulfide	
I	932.4	952.3	568.9	707.8	721.1	53.6	161.4	162.5	225.6

7.2.6 XPS study of potentiostatically polarized chalcopyrite

In this section, XPS experiments are applied to study the surface of chalcopyrite electrodes after dissolution in 0.5 M sulfuric acid solution by application of potentiostatic potentials for 6 hours. Dissolution of chalcopyrite for 6 hours will provide information regarding the composition and stoichiometry of the most stable surface film(s) on chalcopyrite. These results are useful for long term dissolution of chalcopyrite, especially the dissolution processes such as acidic leaching of chalcopyrite in hydrometallurgical processes, which typically take several hours. Note again that no Ar$^+$ etching was performed on the experiments of this section.

Fig. 7-10 presents the Cu 2p peaks of chalcopyrite electrodes obtained after 6 hours of potentiostatic polarization at 450, 650, 700, 900, 950 and 1000 mV. Since the satellite peak is absent in the Cu 2p core level peaks of Fig. 10, cupric is absent on the mineral surface even after dissolution at different potentials [Yin *et al.* 2005; Chusuei *et al.,* 1995]. In Fig. 7-10, the two peaks centered at about 931.9 and 951.9 eV represent the Cu 2p3/2 and Cu 2p$_{1/2}$, respectively. Both of the Cu 2p$_{3/2}$ and Cu 2p$_{1/2}$ are centered at lower binding energies than that of non-dissolved chalcopyrite, i.e. 932.4 eV and 952.1 eV (Fig. 7-5a). It has been well established that the Cu 2p$_{3/2}$ peak with high binding energy (about 933.0–933.8 eV) and the presence of a shake-up peak (about 939–944 eV) are two major XPS characteristics of cupric, while a lower Cu 2p$_{3/2}$ binding energy (about 931.8–933.1 eV) and the absence of the shake-up peak are characteristics of reduced copper species [Avgouropoulos and Ioannides 2003; Liu and Flytzani-Stephanopoulos 1995].
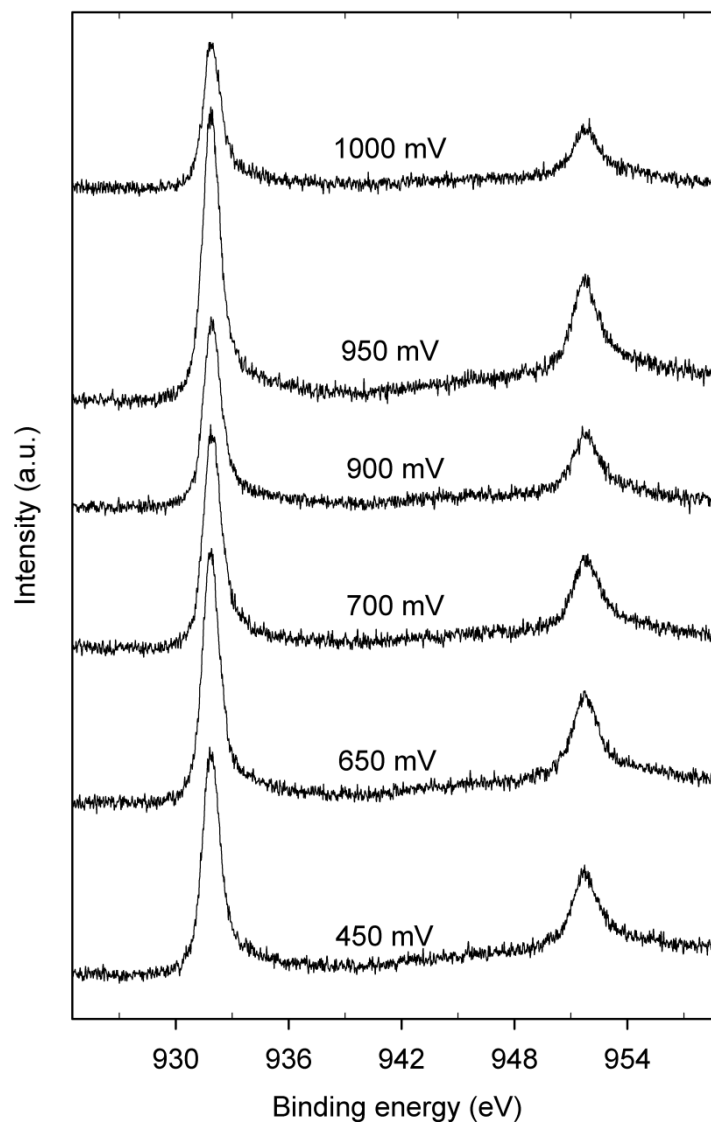
Figure 7-10: Comparison of Cu2p peaks of chalcopyrite after dissolution in 0.5 M sulfuric acid at different potentials for 6 hours.

So again, this means that even after dissolution of chalcopyrite at different potentials between 450 and 1000 mV, surface copper exists only in the monovalent form. Probable cuprous (Cu^+) compounds are cuprous oxide (Cu_2O) and/or cuprous sulfides (CuS and Cu_2S). The Cu $2p_{3/2}$ peak of cuprous species bonded to oxygen and sulfur in Cu_2O, CuS and Cu_2S is reported to be centered at 932.8 [Lefevre *et al.*, 2000], 932.0 [Nakai *et al.,* 1978] and 932.6 [Nakai *et al.,* 1978], respectively. From the compareson of the Cu $2p_{3/2}$ peak value of Fig. 7-10 with these values, one can conclude that the most plausible cuprous specie would be CuS. This conclusion can be further confirmed by using the copper auger spectrum (Cu $L_3M_{45}M_{45}$)

123

excited with X-rays, which is centered at 568.5 eV (Fig. 7-11). The Cu $L_3M_{45}M_{45}$ values for CuS and Cu_2S are 568.5 and 569.5 eV, respectively [Ghahremaninezhad *et al.,* 2011]. This result rules out the possibility of the formation of Cu_2S on the surface. It is worth mentioning that the Cu_{LMM} peak of Cu_2O is reported to be at 569.7 eV [Lefevre *et al.*, 2000], which is about 1.25 eV higher than that of Fig. 7-11.
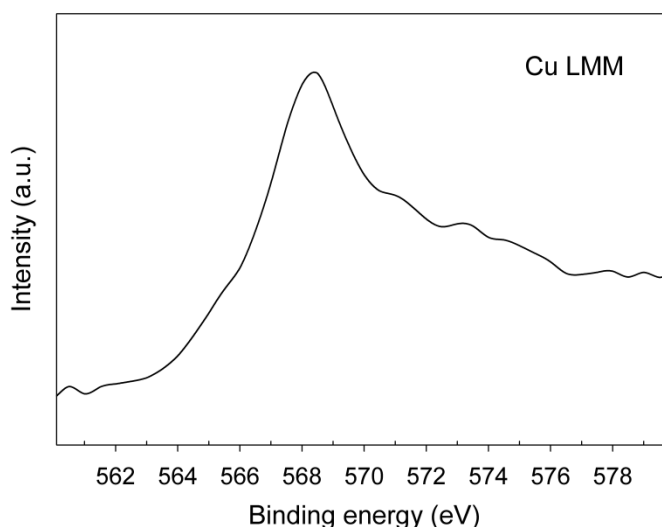
Figure 7-11: Copper auger spectrum ($Cu_{L3M45M45}$) excited with X-rays obtained after potentiostatic polarization of chalcopyrite electrode at 700 mV$_{SHE}$ for 6 hours.

The formation of CuS on the surface of oxidized chalcopyrite has been detected by other researchers as well. In a recent study on electrochemical dissolution of chalcopyrite in 0.1 M sulfuric acid solution by Majuste et al. [2012], the formation of covellite (CuS) has been detected by Raman spectroscopy of chalcopyrite surface after electrochemical dissolution of the electrode at 0.6 and 0.8 V. Covellite (CuS) formation during electrochemical dissolution of chalcopyrite in acid chloride solutions has also been suggested by Ammou-Chokroum et al. [1979]. Elsewhere, Warren et al. [1982] have suggested that the formation of a nonstoichiometric CuS phase on massive chalcopyrite electrode surface during electrochemical dissolution in 1.0 M sulfuric acid is plausible. Yin et al., [1995] and Córdoba et al. [2008] are among other researchers who have suggested the formation of CuS on the surface of chalcopyrite during electrochemical oxidation.

Fig. 7-12 compares the Fe 2p spectra of the chalcopyrite surface after 6 hours of dissolution at 700 mV with that of Fig. 7-6 (non-dissolved chalcopyrite sample). The

124

spectrum of etched chalcopyrite, curve *a* in Fig. 7-12, shows two characteristic Fe $2p_{3/2}$ and Fe $2p_{1/2}$ peaks of chalcopyrite centered at 707.8 eV and 721.1 eV, respectively. On the other hand, the Fe 2p spectrum obtained from the surface of a chalcopyrite electrode after dissolution at 700 mV for 6 hours, curve *b* in Fig. 7-12, has two extra peaks centered around 710 eV and 724 eV. In order to further explore the chemical state of iron species of curve *b*, the Fe $2p_{3/2}$ peak was fitted with three peaks centered at 707.4 (peak 1), 710.3 (peak 2) and 712.6 eV (peak 3), presented in Fig. 7-13a. Peak 1 of Fig. 7-13a at 707.4 eV shows a 0.4 eV left shift versus the Fe $2p_{3/2}$ peak of chalcopyrite (curve *a* of Fig. 7-12). The Fe $2p_{3/2}$ peak at 707.4 eV can be assigned to the binding energy of Fe^{2+} species bonded to sulfur, e.g. FeS which is 707.5 eV [Pratt *et al.,* 1994; Jones *et al.,* 1992] or Fe^{2+} in FeS_2 which is reported to be 707.4 eV [Brion 1980; Pratt *et al.,* 1994] and elsewhere is reported to be 707.5 eV [Ennaoui *et al.,* 1986]. Unfortunately, from this information we were not able to confidently differentiate between FeS and FeS_2, especially due to lack of XPS studies on FeS. It is worth mentioning that the Fe $2p_{3/2}$ peak of FeO and ferrous hydroxide are around 709.1 and 711.6 eV [Nesbitt and Muir 1994; Descostes *et al.,* 2000], respectively. Both of these values are substantially different from the Fe $2p_{3/2}$ peak obtained in this study (i.e. 707.4 eV) which rules out the possibility of the presence of FeO and ferrous hydroxide on the surface.
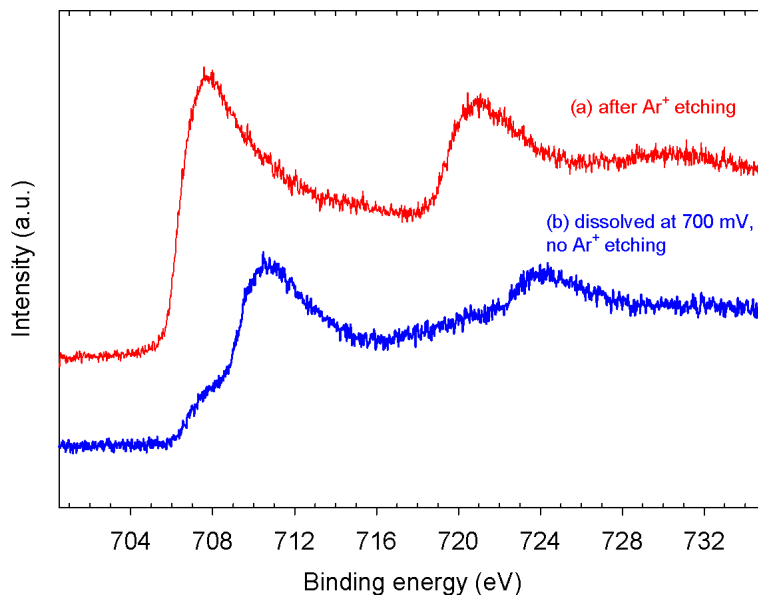
Figure 7-12: Comparison of Fe2p peaks of chalcopyrite (a) after ion etching inside XPS instrument, and (b) after dissolution at 700 mV$_{SHE}$ in 0.5 M sulfuric acid solution.

The peak at 710.3 eV can be attributed to the Fe $2p_{3/2}$ peak of FeOOH or Fe_3O_4 which are both centered at 710.2 eV [Nesbitt and Muir 1994; Descostes *et al.*, 2000]. From the Fe 2p peak of Fig. 7-13a it is not possible (or very risky) to distinguish between FeOOH or Fe_3O_4. For this reason, the Fe 3p spectrum of chalcopyrite under the same condition of Fig. 7-13a is presented in Fig. 7-13b. Two main peaks centered at 53.3 (peak 1) and 55.5 eV (peak 2) have been used for fitting of the main spectrum (Fig. 7-13b). The peak at 53.3 eV perfectly matches with the Fe 3p peak of Fe^{2+} bonded to sulfur in species such as FeS_2, which is 53.3 eV [Descostes *et al.*, 2000] (here it must be mentioned that the Fe 3p value for FeS is not available; hence yet again we are not sure if FeS or FeS_2 or a mixture of both species are present on the surface as iron sulfide). The peak at 55.5 eV matches well with the Fe 3p peak of Fe^{3+} in FeOOH which is 55.6 eV [Descostes *et al.*, 2000]. However, the Fe 3p peak of iron species in Fe_3O_4 occurs at 53.7 eV [Brion 1980] which is about 1.8 eV below the Fe 3p binding energy of curve 2 in Fig. 7-13b. Thus it is most likely that after dissolution of chalcopyrite at constant potential, surface iron exists as iron sulfide and FeOOH. The reported value for the Fe 3p peak of chalcopyrite by Brion [1980] is 54.2 eV which is 0.9 eV higher than peak 1 of Fig. 7-13b and 1.3 eV lower that peak 2 of Fig. 7-13b. These values again confirm that no chalcopyrite is present on the surface.

The formation of FeOOH on chalcopyrite is generally associated with high pH solutions (> 2). Nevertheless, in addition to the results in this study, the formation of ferric oxy-hydroxide (FeOOH) on the surface of chalcopyrite has been previously reported. Córdoba et al. [2008] have detected goethite on chalcopyrite by XRD, after ferric assisted leaching of chalcopyrite in sulfuric acid solution (pH = 1.8) at 35ºC. Elsewhere, Kaplun et al. [2011] and Li et al [2010], have detected goethite as a chalcopyrite leaching product. Kaplun et al. [2011] detected goethite by XPS after leaching chalcopyrite at 0.75 V and pH 1 (experiment at 85 ºC). Li et al. [2010], detected goethite, also by XPS, after leaching of chalcopyrite at pH 1. In another study, Pratesi and Cipriani [2000] have used XPS, Auger electron spectroscopy (AES) and Rutherford backscattering spectrometry (RBS) methods to detect the formation of goethite on chalcopyrite surfaces after air oxidation. Based on all of the above literature and our XPS results, we suggest that the formation of FeOOH in the case of our studies is possible. This will be further discussed below.
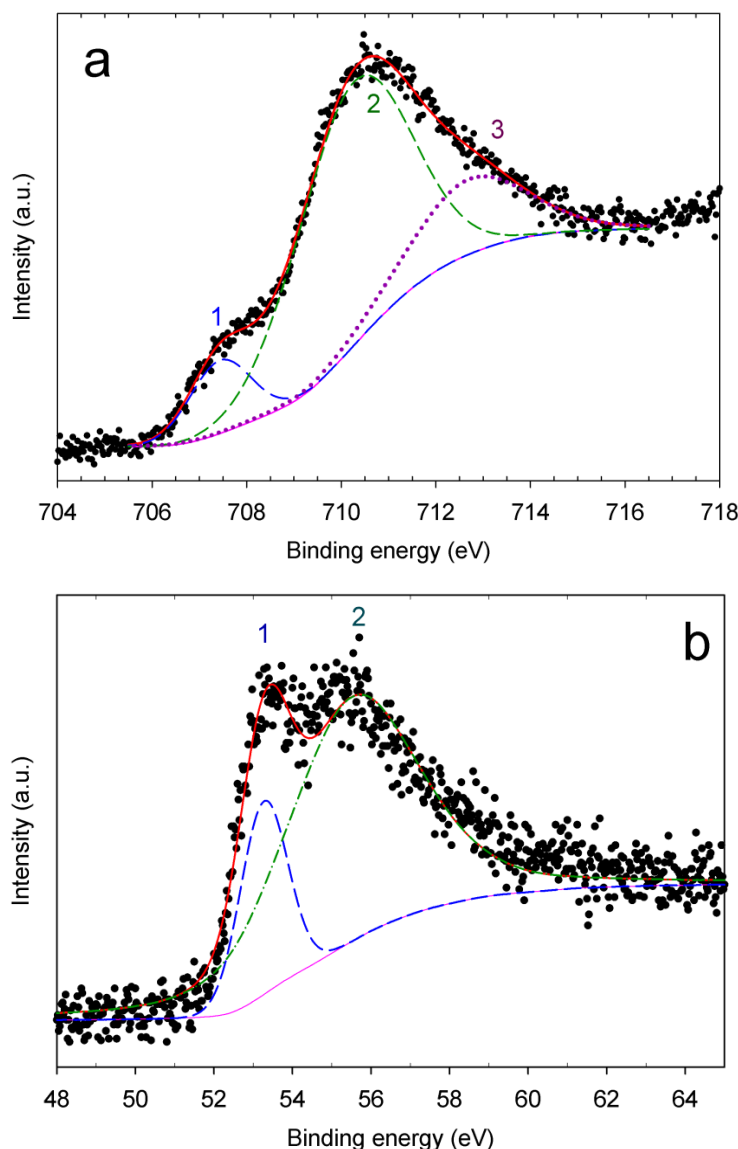
Figure 7-13: XPS spectrum of (a) Fe2p$_{3/2}$ and (b) Fe3p obtained from a chalcopyrite electrode after 6 hours dissolution at 700 mV$_{SHE}$.

The other iron species detected in this study, in addition to FeOOH, are those bonded to sulfur (iron sulfide species). In fact, it is highly plausible that these iron sulfide species may be related to a metal-deficient sulfide film formed during electrochemical oxidation. Several workers have reported the formation of a metal-deficient sulfide film (e.g. $Cu_{1-x}Fe_{1-y}S_2$) on the surface of chalcopyrite during dissolution in acidic media [Hackl *et al.,* 1995; Warren *et al.,* 1982]. This occurs by surface depletion of metallic atoms from the chalcopyrite surface, where the depletion rate of iron atoms is higher than copper atoms due to preferential dissolution of iron (i.e. $y > x$). Additionally, it has been suggested by several

researchers that the metal-deficient layer is the chalcopyrite passive film and is thus responsible for the slow dissolution rate of chalcopyrite [Hackl *et al.,* 1995; Warren *et al.,* 1982; Ghahremaninezhad *et al.,* 2010]. In fact, it seems very probable that the detected iron-sulfide species in our XPS study originates from a metal-deficient sulfide phase such as $Cu_{1-x}Fe_{1-y}S_2$. Cuprous sulfide species were also detected (refer to Fig. 7-10 and related discussion).

The ratio of iron sulfide to FeOOH (i.e. the ratio of Fe-S species to Fe-O species) can be obtained from the ratio of their peak areas. From the Fe 2p spectrum (Fig. 7-13a) the ratio of ferric oxy-hydroxide to iron sulfide is 87:13. Similarly, using the Fe 3p spectrum (Fig. 7-13b) the ratio of ferric oxy-hydroxide to iron sulfide is 85:15. The last peak of Fig. 7-13a (peak 3) is centered at 712.5 eV. This peak does not match with any cited peak of iron species [Wagner *et al.,* 1979]. This peak has been assigned to a Cu_{LMM} auger peak excited with X-rays which is around 712.5 eV [Harmer *et al.,* 2005; Schon 1972]. Based on this analysis, the latter peak at 712.5 eV (Fig. 7-13a) was excluded from the interpretation of the ferric oxy-hydroxide to iron sulfide ratio. Fig. 7-14 presents the Fe 2p spectra of chalcopyrite electrodes obtained after potentiostatic dissolution at different potentials. In addition to the Fe $2p_{3/2}$ peaks centered at 707.4 eV, originating from iron sulfide, the Fe 2p3/2 peak related to FeOOH (centered at 710.3 eV) is clear in all of the samples.
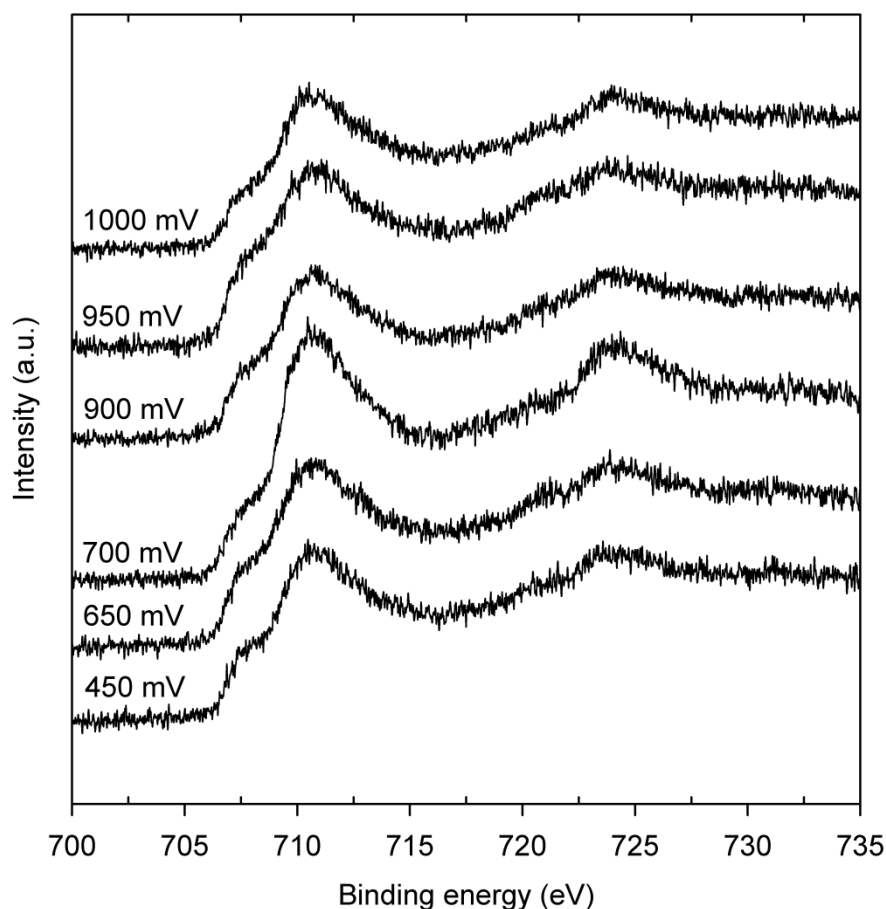
Figure 7-14: Comparison of Fe 2p peaks of chalcopyrite after dissolution at different potentials for 6 hours.

Fig. 7-15 shows a series of S 2p XPS spectra for chalcopyrite electrode surfaces obtained after dissolution at different potentials. The evolution of various sulfur species as a function of applied potential can be seen in this figure. The fitted XPS spectra of S 2p peaks of Fig. 7-15 are presented in Fig. 7-16 and 7-17. For clarity, only the S $2p_{3/2}$ peaks of the fitted curves have been displayed in the Figs. 7-16 and 7-17. The binding energies of the first S $2p_{2/3}$ core level are all in the range of 161.0 to 161.1 eV (peak 1 of Figs. 7-16 and 7-17), and this value is in agreement with what is generally found for monosulfide sulfur (S^{2-}) species of cuprous sulfides (CuS) [Bhide *et al.,* 1981] and/or iron sulfides (FeS) [Yu *et al.,* 1990]. The second S $2p_{2/3}$ core level peak (peak 2 of Figs. 7-16 and 7-17) with the binding energy of about 162.1 eV agrees well with the S $2p_{3/2}$ peak position of disulfide (S_2^{2-}) sulfur species of cuprous sulfide (CuS) [Nakai *et al.,* 1978] and iron disulfide (FeS$_2$) [Descostes *et al.,* 2000]. The formation of cuprous sulfide (CuS) was suggested from the Cu 2p peak

analysis (Fig. 7-10) and iron sulfides (FeS and/or FeS$_2$) were also possible based on Fig. 7-13. It is well established in the literature that all copper atoms in the CuS phase are in the monovalent copper (Cu$^+$) state [Nakai *et al.,* 1978] which implies that the best formulation for the description of copper and sulfur's chemical state in covellite (CuS) is Cu$_3^+$S$_2^{2-}$S$^-$ [Goh *et al.,* 2006; Folmer and Jellinek 1980]. Additionally, it was mentioned above that the detected copper sulfide and iron sulfide species by XPS may be related to Cu-S and Fe-S bonds in a metal-deficient sulfide phase (Cu$_{1-x}$Fe$_{1-y}$S$_2$).

The XPS spectrum of S 2p peaks at potentials of 450, 650, 700 and 870 mV (Figs. 7-15 and 7-16) show a tail in the high binding energy region of about 163 eV which we believe is due the S 3p→Fe 3d interband excitation (peak 3 of Figs. 7-16a to d). The characteristic of this peak is its high FWHM value, i.e. larger than 2 [Klauber 2003; Acres *et al.,* 2010]. The tail of the low potential S 2p XPS spectra of chalcopyrite obtained after potentiostatic dissolution at potentials up to 870 mV$_{SHE}$ has the same characteristics as the S 3p→Fe 3d interband excitation, i.e. a broad peak (high FWHM) centered around 163 eV [Acres *et al.,* 2011]. Figs. 7-16a–d illustrate this point by presenting the XPS spectrum of the S 2p peak of chalcopyrite after dissolution at 450, 550 (OCP), 700 and 870 mV$_{SHE}$. The binding energies and FWHM values for all of the peaks of S 2p$_{3/2}$ spectra at different potentials are presented in Table 7-2. Peak 1 and peak 2 of table 7-2 are the same as explained already in Fig. 7-7. Peak 3 of Table 7-2 has a high FWHM value for the no dissolution condition (not immersed in solution) and chalcopyrite dissolved at 450, OCP, 650, 700 and 870 mV$_{SHE}$ and refers to S 3p→Fe 3d interband excitation (also presented in Figs. 7-16a to d).
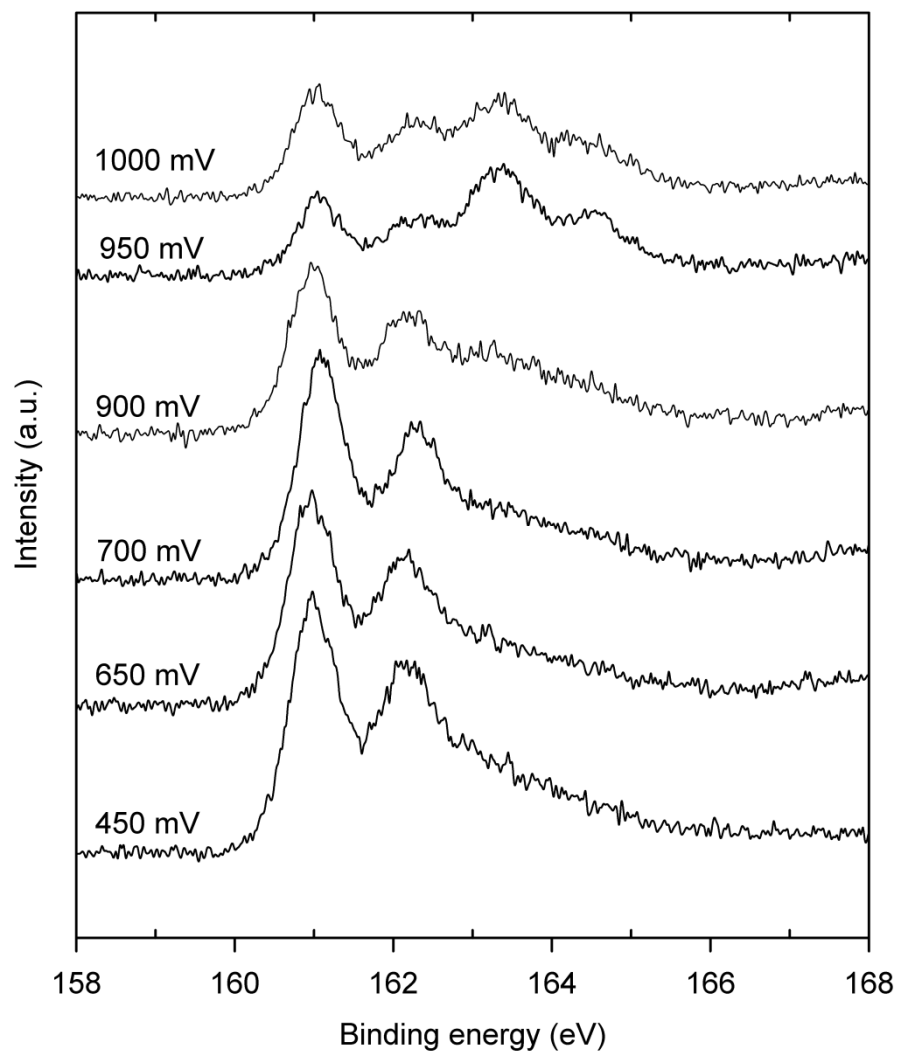
Figure 7-15: Comparison of S2p peaks of chalcopyrite after dissolution at different potentials for 6 hours.

Table 7-2: Binding energy and FWHM values for XPS spectra of S2p peaks.

Condition	Peak 1		Peak 2		Peak 3		Peak 4		Peak 5	
	B.E. (eV)	FWHM	B.E. (eV)	FWHM	B.E. (eV)	FWHM	B.E. (eV)	FWHM	B.E. (eV)	FWHM
No dissolution	161.00	0.74	162.15	1.01	163.17	2.46	–	–	–	–
450 mV	160.97	0.70	162.14	0.99	163.29	2.49	–	–	–	–
OCP	161.04	0.72	162.21	0.91	163.22	2.45	–	–	–	–
650 mV	160.96	0.70	162.12	0.95	163.32	2.46	–	–	168.23	1.54
700 mV	161.08	0.69	162.26	0.95	163.40	2.35	–	–	168.09	1.27
870 mV	161.01	0.73	162.13	0.96	163.44	2.41	–	–	168.04	1.30
900 mV	160.97	0.69	162.18	0.90	163.36	0.98	164.54	0.87	168.43	2.01
950 mV	161.05	0.65	162.17	0.89	163.29	0.98	164.33	0.99	168.36	0.99
1000 mV	161.01	0.67	162.29	1.02	163.36	0.96	164.43	1.05	168.02	1.12

Figure 7-16: S2p XPS spectra for chalcopyrite electrode surface obtained after dissolution at (a) 450, (b) OCP (~550 mV$_{SHE}$), (c) 700 and (d) 870 mV$_{SHE}$ illustrating the characteristics of the S 3p→Fe 3d interband excitation related peaks.

133

In the case of high applied potentials (i.e. 900, 950 and 1000 mV$_{SHE}$) the spectra are significantly different from those obtained at low potentials (Fig. 7-15). From the potentiostatic polarization study presented in Fig. 7-2a, it was clear that, for the potential range up to about 900 mV$_{SHE}$, chalcopyrite is in its passive state. The potentials of 900 mV$_{SHE}$ and above are transpassive dissolution potentials, i.e. the dissolution rate of chalcopyrite increases drastically. Hence, one would expect a substantial change in the sulfur species on the surface of chalcopyrite for potentials above 900 mV$_{SHE}$. It is clear from Fig. 7-15 that the two peaks at ~ 161.0 and 162.1 eV, are still present; this fact can be seen in Table 7-2. However, the area under the peaks has decreased. In addition, two extra peaks centered at higher binding energies of 163.3 and 164.4 eV have grown (Fig. 7-15). The fitted XPS spectra of S 2p peaks for chalcopyrite after dissolution at 900, 950 and 1000 mV$_{SHE}$ are presented in Figs. 7-17a–c (For clarity, only S 2p$_{3/2}$ peaks of fitted curves have been presented). Each XPS spectrum of Fig. 7-17 is fitted with 5 peaks. Peaks 1 and 2 are the same peaks seen in Fig. 7-16 (related to iron sulfide and copper sulfide bonds, which most probably originated from a metal-deficient sulfide film on the surface). The last peak (peak 5) of Figs. 7-17a–c, centered at a very high binding energy of ~168.5 eV, is related to sulfate and most probably originates from sulfate phase formation [Klauber 2008] or electrolyte (sulfuric acid) residue on the surface [Bhide *et al.,* 1981]. This peak was also present on the samples polarized at 650, 700 and 870 mV$_{SHE}$ (Table 7-2 and Figs. 7-16c and d). Peak 3 of Figs. 7-17a–c has similar binding energy to that of the last peaks of Figs. 7-16a–d, however the FWHM is smaller. The binding energy for peak 3 is between 163.3 and 163.4 eV and the FWHM is between 0.96 and 1.04, which is a smaller FWHM value than those obtained at low potentials (~ 2.5). We suggest that this S 2p$_{3/2}$ peak (peak 3 in Figs. 7-17a–c) may be related to polysulfide (S_n^{2-}) formation. This is in agreement with the literature, which suggests the formation of polysulfide sulfur species around the binding energy 163.3 eV and low FWHM of around 1.0 [Hackl *et al.,* 1995]. The S 2p$_{3/2}$ peak 4 of Figs. 7-17a–c, centered around the binding energy of 164.4 eV (Table 7-2) is most probably related to the S 2p$_{3/2}$ of elemental sulfur as the binding energy of this peak is in agreement with the value reported for elemental sulfur (164.4 eV) [Manocha and Park 1977]. The reason for the absence of the S 3p→Fe 3d interband excitation peak in the polarized electrodes at high anodic potentials

(Fig. 7-17) is not clear; however, we suspect that it may be related to elemental sulfur formation on the surface.

A better investigation of the formation of elemental sulfur requires further study of the XPS spectra for S, and the S 2s peak provides a convenient way of doing this. The binding energy of chalcopyrite's S 2s peak is measured to be 225.6 eV (Fig. 7-9). The S 2s peaks of the S atoms in CuS, Cu_2S and FeS_2 are reported to be 225.6, 225.3 and 226.1 eV, respectively; while the S 2s peak of elemental sulfur occurs at a binding energy of 228.4 eV [Chernyshova and Andreev 1997; Panzuner and Egert 1984; Buckley *et al.,* 1994]. Hence, the broad difference between the S 2s level of sulfides vs. elemental sulfur can be used for detection of elemental sulfur formation. Fig. 7-18 presents XPS spectra of S 2s peaks of chalcopyrite after dissolution at different potentials for 6 hours. At low potentials, the S2s peaks are narrow and, by increasing the potential above 900 mV_{SHE}, the peaks become wider. From Fig. 7-18 it is clear that the binding energy of the maximum intensity point (peak point) is almost the same for all the potentials below 870 mV_{SHE} and by increasing potential to 900 mV_{SHE} (or above), the binding energy of the peak point shifts to higher energies. This is due to the formation of elemental sulfur on the surface, which has higher binding energy for the S 2s level.

The above study on the S 2p and S 2s XPS spectra of chalcopyrite (Figs. 7-15 to 7-18) suggest that for elemental sulfur to be formed as a direct product of electrochemical chalcopyrite dissolution, a fairly high potential of 900 mV_{SHE} or above is required. Warren *et al.* [1982] have proposed the formation of elemental sulfur as a product of chalcopyrite dissolution at high potentials (E > 0.7 V):

$$CuFeS_2 = Cu^{2+} + Fe^{3+} + 2S^o + 5e^- \qquad\qquad 7\text{-}2$$

Additionally, they have mentioned that this elemental sulfur may be the product of covellite (CuS) dissolution at high potentials (E > 0.9 V_{SHE}), where covellite was considered to be the product of chalcopyrite dissolution at lower potentials. It was suggested by Warren et al. [1982] that during the electrochemical dissolution of chalcopyrite in 1 M sulfuric acid solution at 25ºC, a nonstoichiometric covellite film forms and passivates the chalcopyrite surface. Our results also agree with the results of Yin *et al*. [1995], as they did not report the formation of elemental sulfur during the dissolution of chalcopyrite electrodes in 0.1 and 1 M HCl solutions at 25ºC. Yin *et al.* [1995] have shown that, in strongly acidic solutions (pH <

2) at potentials below 0.77 V_{SHE}, dissolution of chalcopyrite proceeds through reaction (1), and for higher potentials (up to 1.04 V_{SHE}) the following reaction is proposed [Yin *et al.* 1995]:

$$CuFeS_2 + 8H_2O = Cu^{2+} + Fe^{3+} + 2SO_4^{2-} + 16H^+ + 17e^-$$ 7-3
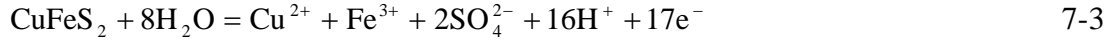
Nevertheless, neither reaction (1) nor (3) suggests the formation of elemental sulfur. A recent synchrotron small-angle X-ray diffraction study by Majuste et al. [2012] has shown that polarization of a chalcopyrite electrode in 0.1 M sulfuric acid solution at 0.8 and 1.0 V_{SHE} yields covellite (CuS) and elemental sulfur (S_8) on the chalcopyrite electrode surface. These researchers did not detect elemental sulfur at low anodic potentials of 0.6 and 0.7 V_{SHE}. These results are also consistent with the observations of the present study.
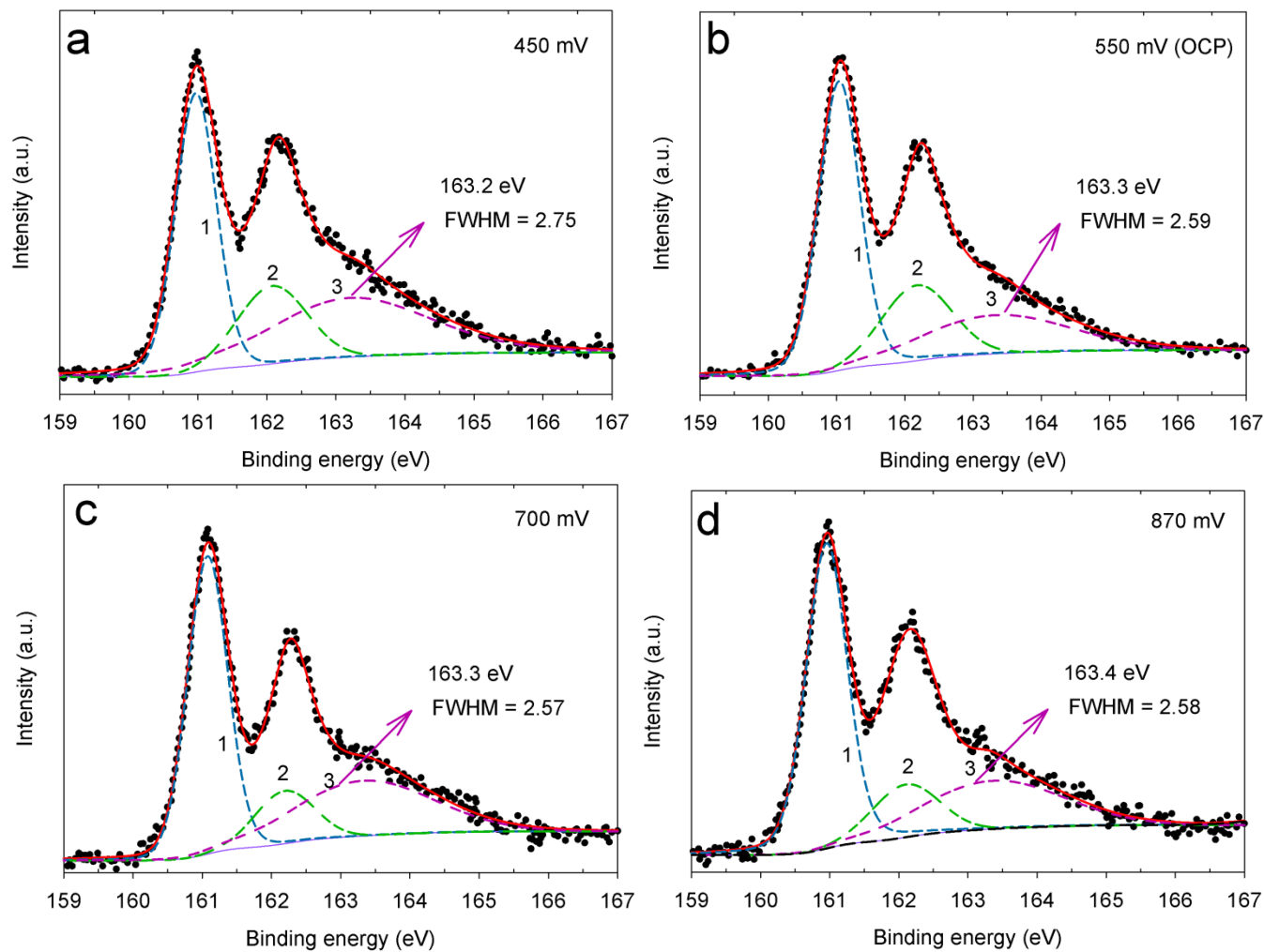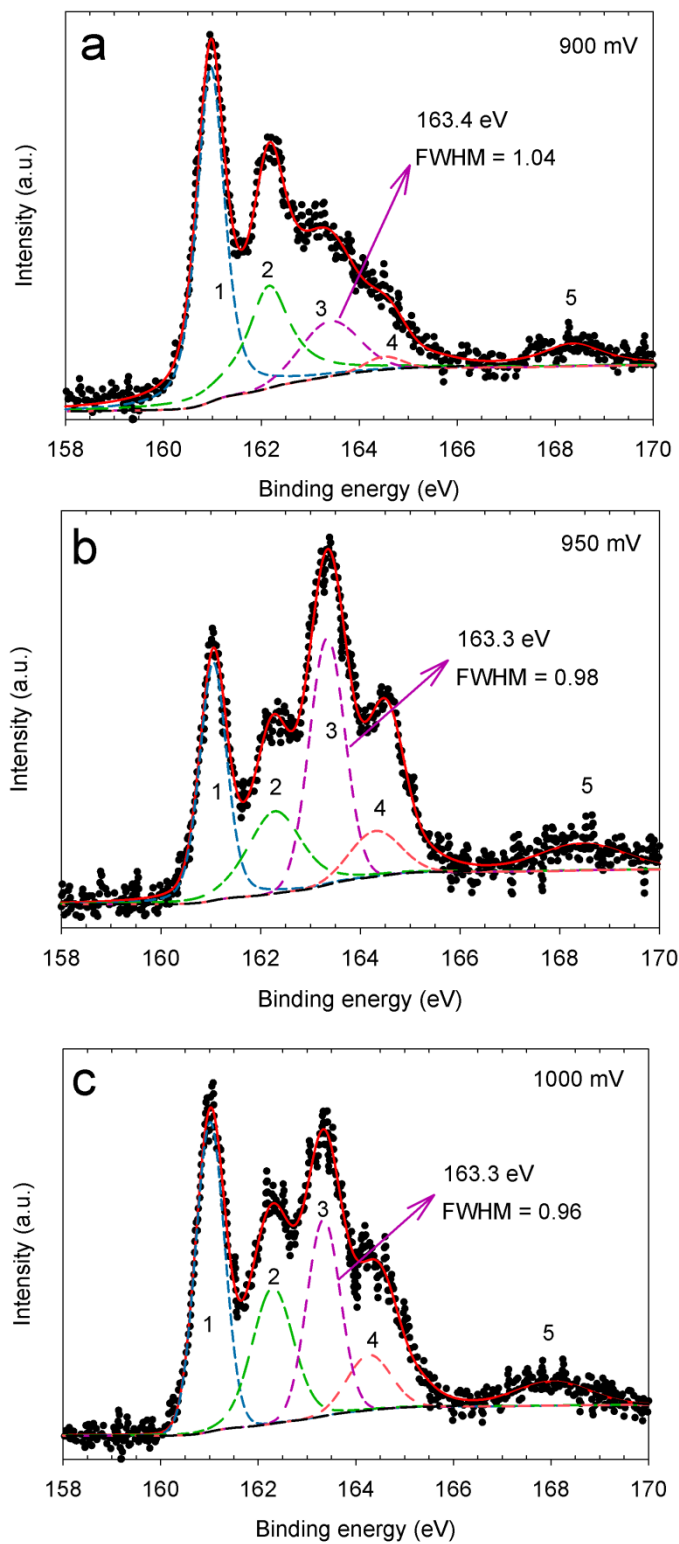
Figure 7-17: S2p XPS spectra for chalcopyrite electrode surface obtained after dissolution at (a) 900, (b) 950, and (c) 1000 mV$_{SHE}$.
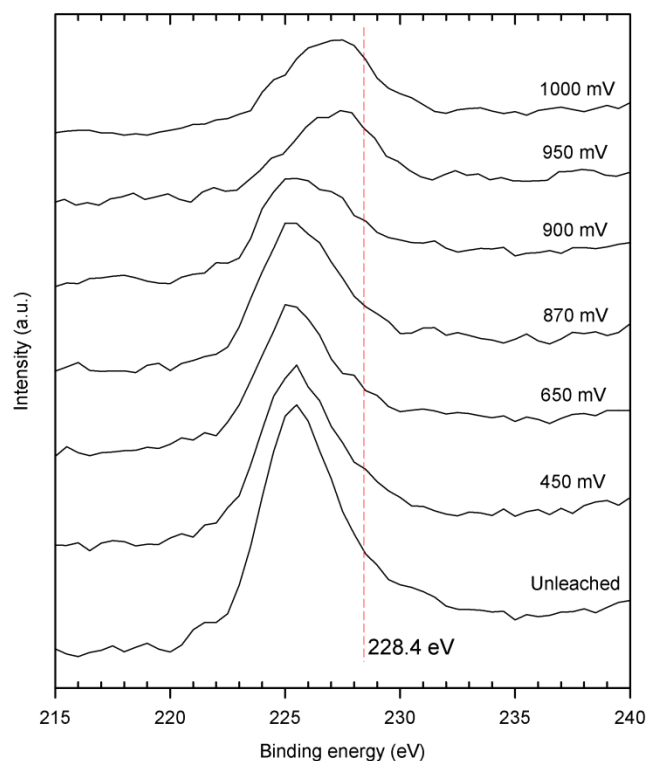
Figure 7-18: Comparison of S2s peaks of chalcopyrite after dissolution at different potentials for 6 hours. Red dashed-line represents the binding energy of S2s peak of elemental sulfur, 228.4 eV.

Fig. 7-19 shows the speciation of sulfur versus potential on the outermost surface of chalcopyrite after 6 hours of dissolution at different constant potentials. To obtain the data of Fig. 7-19, it was assumed that the percentage of each species (S^{2-}, S_2^{2-}, S_n^{2-}, elemental S and SO_4^{2-}) is directly proportional to the area under its S 2p peak presented in Figs. 7-15, 7-16 and 7-17. It is worth mentioning that for the experimental data from the 550 mV$_{SHE}$ condition presented in Fig. 7-19, no potential was applied to the electrode; indeed, the electrode was immersed in solution at open circuit and throughout the 6 hours of immersion the potential was fairly stable at ca. 550 mV$_{SHE}$. From Fig. 7-19, the major species of sulfur at low potentials (450 to 870 mV$_{SHE}$) are monosulfide (S^{2-}) and disulfide (S_2^{2-}). Additionally, about 5% of sulfate (SO_4^{2-}) species form in this potential interval as well. Interestingly, by increasing the potential from 450 mV to 870 mV$_{SHE}$, the fraction of monosulfide increases from 43 to 56% of total sulfur while the fraction of disulfide decreases from 57 to 39%. In the passive potential region, $650 < E < 900$ V$_{SHE}$, the ratio of different sulfide species (S^{2-}/S_2^{2-}) remains relatively constant (at c.a. 1.4). This point can be justified by considering

138

the passive state of chalcopyrite in this potential region; in this region a passive sulfide film is formed on the surface, which has approximately the same composition throughout all passive potentials. Note from Fig. 7-19 that in the transpassive region, $E > 0.90$ V_{SHE}, the fraction of monosulfide and disulfide species show a notable decrease (monosulfide decreases from 56% to 19% and disulfide decreases from 39% to 18%) and the fraction of polysulfides and elemental sulfur shows a sudden increase (polysulfide increase from 0 to 35% and elemental sulfur increases from 0 to 21%). From Fig. 7-19, the concentration of polysulfide and elemental sulfur for potentials below 0.90 V_{SHE} is zero and the concentration of sulfate at potentials below OCP is negligible. Considering the fact that transpassive dissolution of chalcopyrite occurs at potentials greater than 0.90 V_{SHE}, these findings clearly demonstrate that monosulfide and disulfide species are responsible for passivation of chalcopyrite and elemental sulfur would have an insignificant effect on passivation under the conditions tested here. As concluded from the XPS analysis above, copper sulfide (CuS) and iron sulfide bonds were detected on the surface of the electrochemically dissolved chalcopyrite electrode (Figs. 7-10 and 7-13). The literature has previously indicated that copper sulfide and iron sulfide bonds likely originate from the metal-deficient sulfide film which forms on the surface [Warren *et al.,* 1982; Hackl *et al.,* 1995; Viramontes-Gomboa *et al.,* 2007]. If true, this phase should be considered to constitute the passive film on the surface. The following reaction may then be suggested for passivation of chalcopyrite where a metal-deficient sulfide film is the passivating film:

$$CuFeS_2 = Cu_{1-x}Fe_{1-y}S_2 + xCu^{2+} + yFe^{2+} + 2(x+y)e^- \qquad y > x \qquad \qquad 7\text{-}4$$
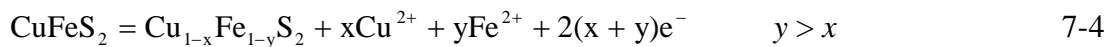
Several other researchers have concluded that a metal-deficient sulfide passive film forms via reaction (7-4) or very similar reactions [Warren *et al.,* 1982; Hackl *et al.,* 1995; Viramontes-Gomboa *et al.,* 2007]. In all of these articles it has been acknowledged that y should be larger than x due to preferential dissolution of iron atoms to copper atoms.

139
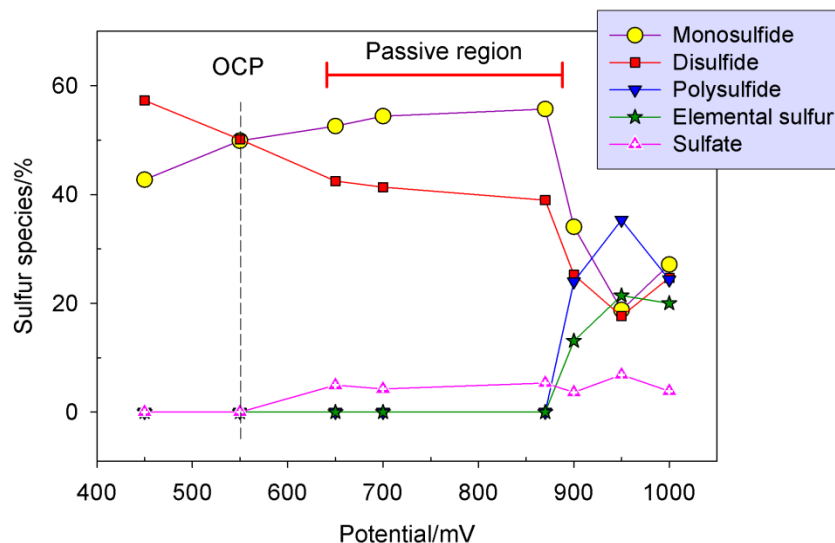
Figure 7-19: Sulfur species on the surface of chalcopyrite formed after dissolution in 0.5 M sulfuric acid solution at different potentials for 6 hours.

Nevertheless, reaction (7-4) or similar reactions such as reaction (7-1) may not be the best way to describe the dissolution of chalcopyrite. The reason for this is the accumulation of sulfur (in sulfide form) by reaction (7-4) and the accumulation of both copper and sulfur by reaction (7-1) on the surface of the electrode. During dissolution by reactions (7-4) and (7-1), as the sulfide film grows on the surface (CuS_2 in reaction 7-1 and metal-deficient sulfide layer in reaction 7-4), it will result in thickening of the film which, in turn, will cause a decrease of the dissolution current density (during potentiostatic polarization of the electrode at a passive potential, OCP $< E <$ 0.9 V_{SHE}). From Fick's law of diffusion, one would estimate that if the passive film thickness doubles, then the dissolution current density of chalcopyrite must decrease by half. However, Fig. 7-3b clearly shows that even after 60 hours of potentiostatic dissolution of chalcopyrite at 0.80 V_{SHE}, the current density remains approximately constant. This means that sulfur species (i.e. monosulfide and disulfide species) and copper ions cannot accumulate on the surface and must dissolve instead. This process can only be described if all the elements of chalcopyrite (i.e. Fe, Cu and S) are considered to dissolve during the dissolution of chalcopyrite.

In fact, through a ring–disk electrode study on a natural chalcopyrite electrode in 0.1 M H_2SO_4 solution, Lazaro and Nicol [2006] proposed the formation of soluble sulfur species such as thiosulfate. In their study, different potentials (in the passive region) were applied on the chalcopyrite disk for 1 h while the platinum ring was held at a constant cathodic potential

140

of –0.06 V_{SHE}. Under this condition, any oxidized species of chalcopyrite dissolution emanating from the disk were reduced on the platinum ring (except ferrous, as the potential for its reduction to metallic iron is very low). Afterwards, during the anodic stripping of the platinum ring, in addition to the peak for the stripping of copper metal, two other peaks were obtained. The potential of the latter two peaks were in the potential region similar to those that are known to be associated with the oxidation of the copper sulfides. Since different copper sulfides can be oxidized in this potential region, it was not easy to assign these peaks to a particular copper sulfide (e.g. CuS, Cu_2S and Cu_xS). Nevertheless, since these peaks are representative of the oxidation of copper sulfides, then in addition to copper ions, it was suggested that soluble sulfur species such as thiosulfate ($S_2O_3^{2-}$) and/or hydrogen sulfide (H_2S) could be formed in the dissolution reaction at the disk [Lazaro and Nicol 2006]. Hence, if one assumes that thiosulfate is a soluble product of chalcopyrite dissolution, then a reaction such as the following may be a good description for chalcopyrite dissolution in the passive region:

$$CuFeS_2 = Cu_{1-x}Fe_{1-y}S_{2-z} + xCu^{2+} + yFe^{2+}$$

$$+ \frac{z}{2}S_2O_3^{2-} + 3zH^+ + 2(x+y+z)e^- \qquad y>x \qquad \qquad 7\text{-}5$$
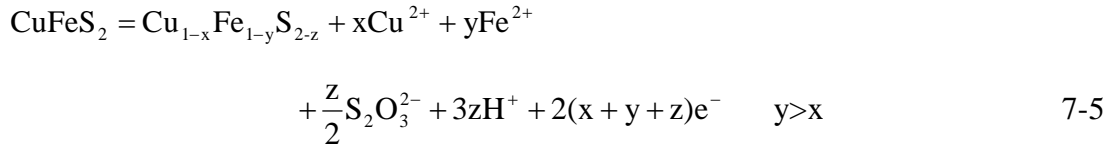
In reaction (7-5), a portion of the iron, copper and sulfur atoms dissolve as cupric, ferrous and thiosulfate species while the metal-deficient sulfide film ($Cu_{1-x}Fe_{1-y}S_{2-z}$) passivates the electrode and hinders the dissolution rate. In fact, reaction (7-5) is similar to reaction (7-4), but reaction (7-5) also accounts for the proposed dissolution of sulfur. It is worth mentioning here that thiosulfate is known to be a major dissolution product of some other sulfide minerals such as pyrite (FeS_2) [Mishra and Osseo-Asare 1988; Rohwerder *et al.*, 2003].

In addition to thiosulfate, one would also consider H_2S as a potential soluble sulfur product. The interaction between water molecules and the (001) plane of chalcopyrite has recently been studied by means of density functional modeling [Ferreira de Lima *et al.*, 2011]. This work has suggested that hydrogen sulfide gas may evolve at anodic potentials. These authors show that in a highly acidic solution, protons adsorb to the surface of the disulfides (S_2^{2-} species) and this causes elongation of the S–S bond and formation of H_2S

species. Additionally, it has been concluded by Ferreira de Lima *et al.,* [2011] that the adsorption of positively charged protons to sulfur dimers on the chalcopyrite surface inhibits the initiation of the polysulfide formation, and H_2S forms instead. The solubility of H_2S in water is very low and has a very strong foul odor (50% of humans can recognize the characteristic odor of hydrogen sulfide at concentrations as low as 0.005 ppm), and we have never noticed this odor during the course of our experiments. Nevertheless, further experimental studies are warranted for analysis of the soluble sulfur species formed during chalcopyrite dissolution.

Fig. 7-20 presents the concentration of various elements (oxygen, sulfur, iron and copper) on the surface of chalcopyrite as a function of potential. Each element of Fig. 7-20 reflects its total concentration after 6 hours of dissolution. From Fig. 7-20, the concentration of copper, iron and sulfur remains relatively constant on the surface in the passive potential region (650 to 900 mV_{SHE}). This result would suggest that a passive film with a defined and time-invariant composition (e.g. $Cu_{1-x}Fe_{1-y}S_{2-z}$) is responsible for hindering the rate of chalcopyrite dissolution in this potential region. This point agrees with our results presented above. However, oxygen concentration increases from ca. 24% to 42% upon increasing the potential from OCP (~ 550 mV_{SHE}) to 870 mV_{SHE}.
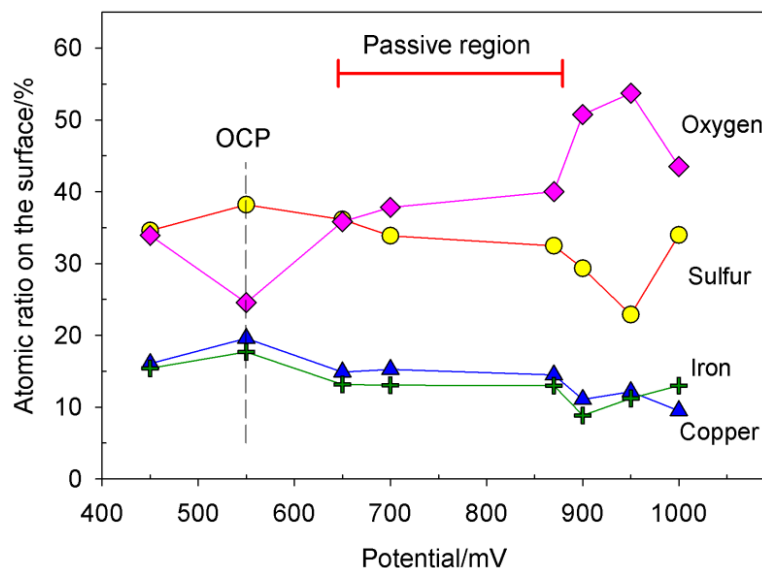
Figure 7-20: Concentration of O, S, Cu and Fe species on the outer-most surface of chalcopyrite after dissolution at different potentials for 6 hours in 0.5 M sulfuric acid solution. C contamination is excluded from the analysis.

To further elucidate the role of oxygen on the passivation of chalcopyrite, its surface speciation is presented in Fig. 7-21 as a function of different potentials. To obtain Fig. 7-21, the XPS spectra of the O 1s peak of oxygen at different potentials were fitted with three peaks; one peak at 529.6 ± 0.1 eV corresponding to O^{2-} in oxide phases [Tan *et al.* 1990], one at 531.5 ± 0.1 eV corresponding to OH^- in hydroxide species [Clayton and Lu 1986] and the last one at high binding energy of 532.8 ± 0.1 eV corresponding to oxygen in sulfate or/and water [Shuxian *et al.,* 1986]. Since oxygen in sulfate and water gives rise to peaks at the same binding energy, we were not able to interpret water and sulfate separately and thus we have excluded water from the data presented in Fig 7-21. A sample of the fitting process for XPS spectra of the O1s peak of chalcopyrite obtained after 6 hours of potentiostatic dissolution at 650 mV is presented in Fig. 7-22. From Fig. 7-21, a major part of the oxygen present at all potentials is in hydroxyl form (OH^-). Fig. 7-21 shows that the concentration of sulfate and/or adsorbed water on the surface increases on the surface as potential increases ($450 < E < 900$ mV$_{SHE}$) and, in contrast, the concentration of O^{2-} and OH^- species is almost constant. This fact would imply that the observed increase of total oxygen fraction on the surface in Fig. 7-20, is most likely due to an increase in sulfate concentration and adsorbed water. This finding is consistent with that of Fig. 7-19 which shows the formation of a sulfate phase on the surface as potential is increased. In addition, the adsorbed water on the electrode constitutes further evidence for the formation of FeOOH on the surface of the electrode. As noted above, the formation of FeOOH is generally associated with pH higher than that used in our experiments (above pH = 2) [Pourbaix 1966]. It appears that adsorption of water to the iron-sulfide species (Fe-S bonds were detected by XPS, as shown above) of the passive film (highly hydrated passive film) provides an environment of H_2O and OH^- (lattice or bound water) around Fe species analogous to a high pH environment where the FeOOH phase can be stable. This suggested path for the formation of FeOOH agrees reasonably well with the anodic dissolution model of pyrite in acidic media suggested by Mishra and Osseo-Asare [1988], which assumes that the first step of pyrite dissolution involves the deprotonation of adsorbed water:
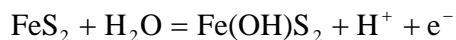
$$FeS_2 + H_2O = Fe(OH)S_2 + H^+ + e^- \qquad\qquad 7\text{-}6$$

This model [Mishra and Osseo-Asare 1988] predicts the formation of thiosulfate as a dissolution product. Hence, we would suggest that the FeOOH species on the surface of the dissolved chalcopyrite (detected by XPS) may originate from the dissolution of the sulfur-bonded iron species of the passive film (i.e. Fe-S species). This pathway for formation of FeOOH is very similar to the proposed model for hydration of molybdenum and chromium atoms in the passive film of stainless steel in acidic solution (0.1 M HCl) which suggests the formation of highly hydrated species such as $MoO(OH)_2$, MoO_4^{2-}, $Cr(OH)_3$ and CrO_4^{2-} [Clayton and Lu 1986]. The latter four species are thermodynamically stable only in high pH solutions, i.e. higher than that of Clayton and Lu's study. We conclude it is likely that, during the dissolution of chalcopyrite in acidic solutions, water molecules adsorb to its surface and provide an environment of H_2O and OH^-, which facilitate the formation of FeOOH.
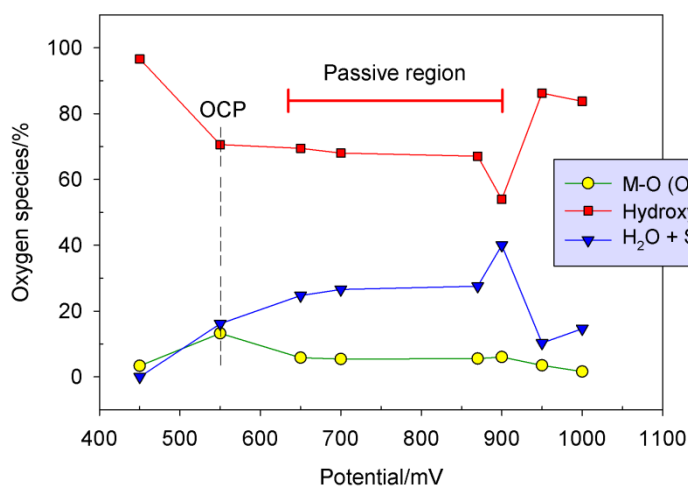
Figure 7-21: Oxygen species on the surface of chalcopyrite formed after dissolution at different potentials for 6 hours.
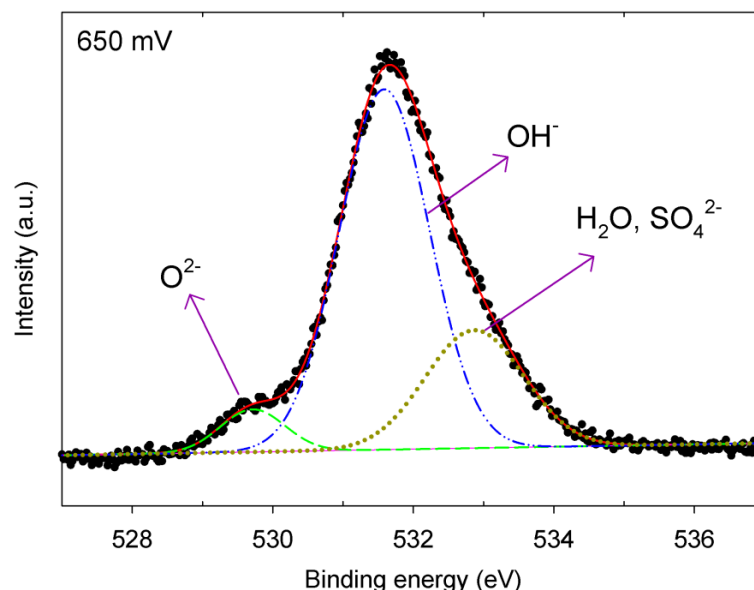
Figure 7-22: O1s core level peak obtained from chalcopyrite after 6 hours of dissolution at 650 mV$_{SHE}$.

7.3 Conclusion

In summary, the surface layers formed during the electrochemical dissolution of chalcopyrite in 0.5 M sulfuric acid solution were studied. It was shown that potentiodynamic polarization of chalcopyrite, even at a very low scan rate, cannot successfully demonstrate the active-passive dissolution of chalcopyrite. On the other hand, the results of potentiostatic polarization have agreed very well with those of XPS studies, which suggest that this technique can accurately demonstrate the active-passive dissolution behavior of chalcopyrite. From potentiostatic polarization it was concluded that chalcopyrite is passive at potentials below 0.90 V$_{SHE}$, beyond which it actively dissolves. Results of XPS studies have shown a substantial change in the oxidation state of sulfur species on the surface of chalcopyrite at potentials above 0.90 V$_{SHE}$. XPS experiments revealed that copper and iron sulfide bonds are present in the passive film of chalcopyrite, but their binding energies are different from those of chalcopyrite. These bonds were believed to originate from a metal-deficient sulfide passive film with composition $Cu_{1-x}Fe_{1-y}S_{2-z}$. In addition, FeOOH was detected on the surface and a possible reaction mechanism for its formation was suggested. XPS results showed that the surface of passive chalcopyrite is blocked by a sulfide film and beyond the passive region (above 0.90 V$_{SHE}$) the percentage of sulfides in the film decreased significantly, i.e. monosulfide decreased from 56% to 19% and disulfide decreased from

39% to 18%. Furthermore, no elemental sulfur or polysulfide was detected on the surface at potentials below 0.90 V_{SHE}. Hence, it is concluded that the transpassive dissolution of chalcopyrite is significantly linked to the oxidation of sulfur (from sulfide in the passive film to elemental sulfur and perhaps to sulfur species with higher oxidation states, e.g. thiosulfate). Additionally, by comparing XPS sulfur spectra of chalcopyrite with the results of sulfur spectra from iron sulfide (pyrite and pyrrhotite) and copper sulfide minerals (chalcocite and covellite) we have concluded that the high energy feature in sulfur species spectra (~ 163.3 eV) is most likely related to the S 3p→Fe 3d excitation and does not originate from polysulfide.

In the next chapter the multi-cyclic voltammetry method will be used to further understand the dissolution mechanism of chalcopyrite in 0.5 M sulfuric acid solution. This study will help us to suggest proper electrochemical reactions for chalcopyrite dissolution.

8 Multiple cyclic voltammetry study of chalcopyrite in 0.5 M sulfuric acid solution

8.1 Introduction

In the last two chapters, the surface of the chalcopyrite electrode was studied mostly by electrochemical impedance spectroscopy and X-ray photoelectron spectroscopy. EIS studies in chapter 6 revealed the formation of two distinct surface layers on chalcopyrite after dissolution in 0.5 M sulfuric acid solution. Also, EIS results have suggested that the outermost surface layer must be the product of the dissolution of the inner passive film. The formation of a metal deficient sulfide passive film on the chalcopyrite surface was further confirmed by XPS studies in chapter 7.

In this chapter, cyclic voltammetry will be used as an additional method to understand the dissolution mechanism of chalcopyrite in 0.5 M sulfuric acid solution.

8.2 Results and discussion

8.2.1 Effect of oxygen content of the solution on the CV experiments

Figure 8-1 presents the multicyclic voltammograms for a stationary chalcopyrite electrode in both deaerated (Fig. 8-1a) and aerated (Fig. 8-1b) 0.5 M H_2SO_4 solutions. In the case of deaerated solution, argon gas was sparged into the solution for 1 hour and was stopped about 2 minutes prior to the experiment. It can be seen from the comparison of these two figures that the position of peak currents are almost identical. All of the anodic and cathodic peaks either increase with time (i.e., the number of cycles) or are invariant in time. None of the peaks vanish. Both experiments show seven anodic peaks at 0.02, 0.10, 0.19, 0.24, 0.35, 0.65 and 0.79 V_{SHE} and four cathodic peaks at 0.37, 0.30, −0.10 and −0.20 V_{SHE}. Hence throughout the rest of this paper, only the results of aerated solution will be discussed. In addition, each of the current peaks of Fig. 8-1 will be explained in depth.
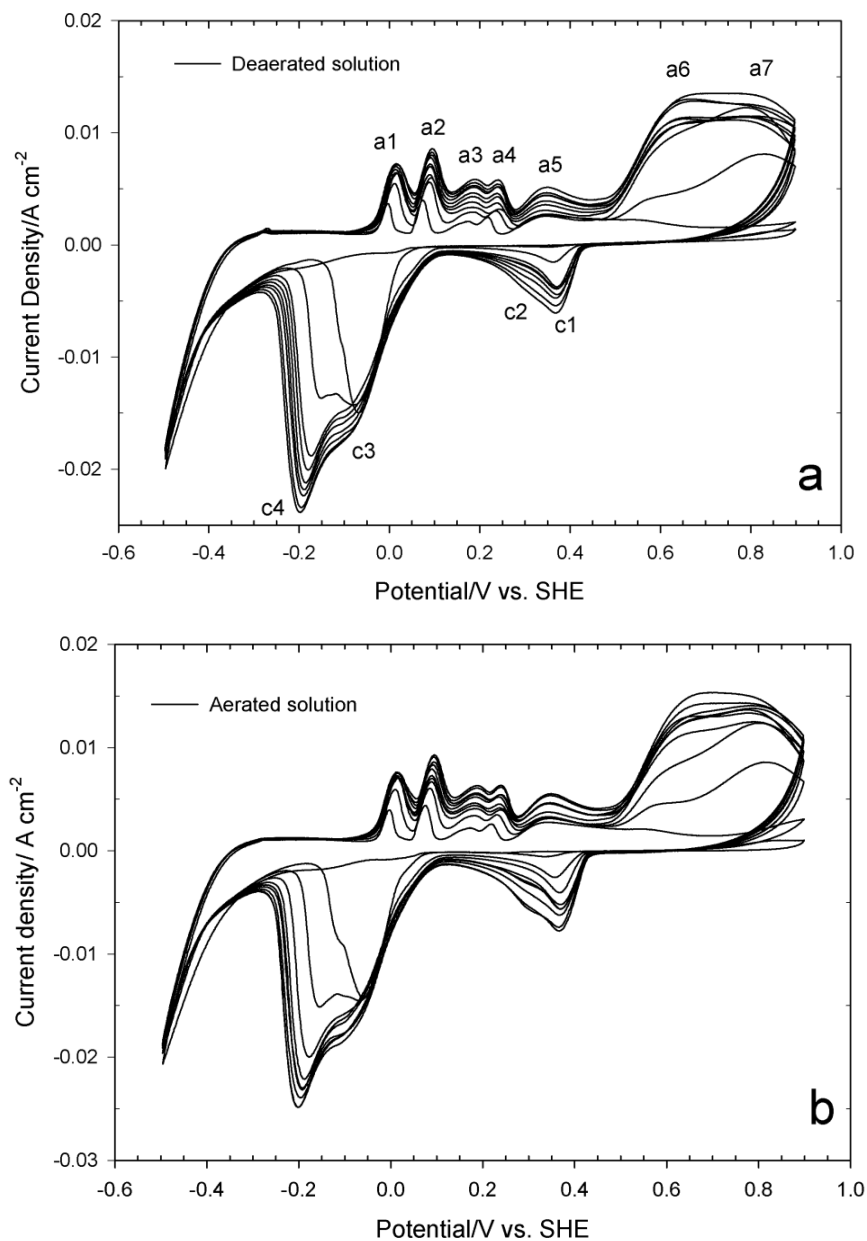
Figure 8-1: Multicyclic voltammogram for stationary chalcopyrite electrode in 0.5 M H₂SO₄ deaerated (a) and aerated (b) solutions. Scan rate is 50 mV s⁻¹.

8.2.2 Cathodic reactions on the surface of chalcopyrite

In general, during the multicyclic voltammetry experiments, anodic and cathodic peaks may grow or vanish in time (i.e. number of cycles) or be insensitive to the number of cycles. The response of current peaks to the number of cycles is indicative of the depletion or accumulation of electroactive species in the vicinity of the electrode.

148

Figure 8-2a presents a typical multicyclic voltammogram for stationary chalcopyrite in 0.5 M H_2SO_4 solution (quiescent condition). In this experiment, the chalcopyrite electrode was polarized at 0.55 V (very close to its OCP) for 20 seconds and afterwards, the potential of the electrode was increased linearly to 0.75 V, followed by 10 cycles from 0.75 V to –0.5 V and back at a scan rate of 50 mV s^{-1}. The evolution of the current peaks as the number of cycles is increased is clear. The current for all of the cathodic and anodic peaks increases with an increasing number of cycles. In the tenth cycle, anodic peaks occur at 0.01, 0.09, 0.19, 0.24, 0.35, 0.64 and 0.84 V and cathodic peaks occur at 0.36, 0.28, −0.11 and −0.20 V. In order to understand the origin of the cathodic peaks, the tenth cycle of the experiment was compared to the tenth cycle of a rotating (500 rpm) chalcopyrite disk electrode in Fig. 8-2b. If a peak originated directly from the oxidation or reduction of chalcopyrite or other solid phases on the surface then it remains in the voltammogram for the rotating electrode; however, peaks originating from the oxidation or reduction of dissolved species should be significantly reduced or entirely absent. From Fig. 8-2b, it is clear that anodic peaks a1, a2, a3 and a4 are related to the oxidation of dissolved species (these peaks are discussed in more detail in section 8.2.3). The same explanation can be provided for cathodic peaks c1 and c2, which may be related to the reduction of ferric and cupric dissolved during the anodic scans (the assigned reactions to all cathodic peaks are presented in Table 8-1). In the case of the stationary electrode, iron and copper dissolve and remain near the electrode surface (quiescent condition), becoming involved in reduction reactions at low potential. In Fig. 8-2a, peak c1 is present from the second cycle and grows with each additional cycle; however, peak c2 is not observed in the first two cycles. Peak c1 can be related to ferric reduction:

$$Fe^{3+} + e^- \rightarrow Fe^{2+} \qquad E(V_{SHE}) = 0.771 + 0.0591 \log \frac{[Fe^{3+}]}{[Fe^{2+}]} \qquad \text{8-1}$$
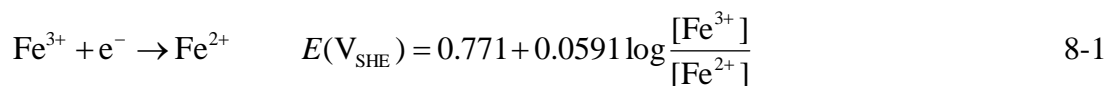
Under the conditions of our experiment (dissolution of chalcopyrite up to 0.75 V, Fig. 8-2a), iron dissolves mostly as ferrous. Hence in the first cycle the cathodic peak c1 is not observed. Nevertheless, after the first cycle, the ferrous concentration in the vicinity of the electrode surface increases rapidly (ferrous ions form during both anodic and cathodic dissolution of chalcopyrite). Hence, the equilibrium potential of reaction 8-1 (cf. Table 8-1) will decrease significantly and even in the high regions of the potential window of Fig. 8-2a,

ferric will be stable. Therefore, after the second cycle and for all further cycles, peak c1 appears in Fig. 8-2a.
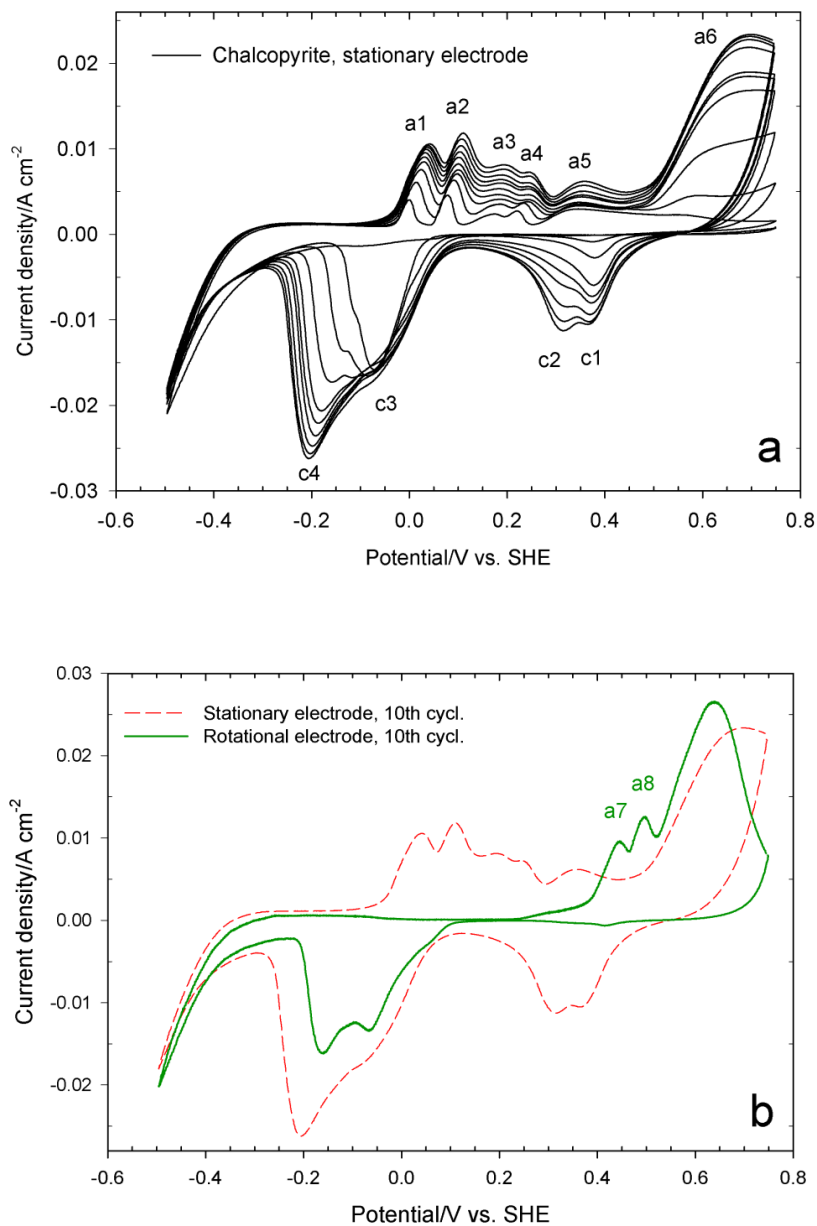
Figure 8-2: Typical multicyclic voltammogram of stationary chalcopyrite in 0.5 M H_2SO_4 solution (a) and effect of the rotation of the electrode on the evolution of the peaks (b). Scan rate is 50 mV s^{-1}.

Table 8-1: Reactions associated with cathodic peaks of chalcopyrite dissolution.

peak	Reaction number	Reaction	Reference
c1	8-1	$Fe^{3+} + e^- \rightarrow Fe^{2+}$	This study
c2	8-4	$CuFeS_2 + 3\,Cu^{2+} + 4\,e^- \Rightarrow 2\,Cu_2S + Fe^{2+}$	Biegler and Horne 1985
c3/c4	8-5	$2\,CuFeS_2 + 6\,H^+ + 2\,e^- \rightarrow Cu_2S + 3\,H_2S_{(aq)} + 2\,Fe^{2+}$	Biegler and Swift 1979
	8-6	$9\,CuFeS_2 + 4\,H^+ + 2\,e^- \rightarrow Cu_9Fe_8S_{16} + 2\,H_2S_{(aq)} + Fe^{2+}$	Hiroyoshi *et al.*, 2002
	8-7	$5\,CuFeS_2 + 12\,H^+ + 4\,e^- \rightarrow Cu_5FeS_4 + 6\,H_2S_{(aq)} + 4\,Fe^{2+}$	Nava and Gonzalez 2006

Peak c2 of Fig. 8-2a has been assigned by various authors to the reduction of a solid ferric sulfate phase [Nava and Gonzalez 2006], cupric reduction to copper [Holliday and Richmond 1990; Eghbalnia and Dixon 2001], and covellite reduction to chalcocite [Yin *et al.*, 1995]. Nava and Gonzalez have assigned the following reaction for peak c2 of Fig. 8-2a [Nava and Gonzalez 2006]:

$$Fe_2(SO_4)_{3(solid)} + 2\,e^- \rightarrow 2\,Fe^{2+} + 3\,SO_4^{2-}$$

$$E(V_{SHE}) = 0.795 - 0.0591 \log[Fe^{2+}] - 0.0887 \log[SO_4^{2-}] \qquad 8\text{-}2$$
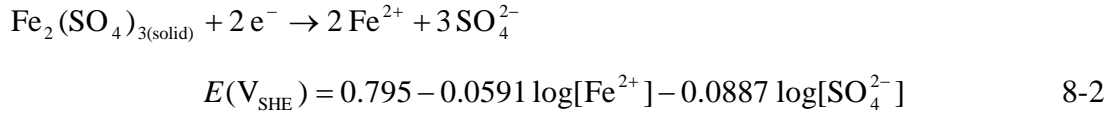
Argument against the validity of reaction 8-2 is that peak c2 must be related to a reduction reaction which involves at least one soluble reactant, since, from Fig. 8-2b, the peak is absent in the case of a rotating electrode. However, reaction 8-2 consumes no soluble species during reduction.

In order to investigate peak c2 further, several cyclic voltammetry experiments were performed on a chalcopyrite electrode after four different conditioning procedures. First, the electrode was polarized at 0.55 V (~OCP) for 20 s. Next, the potential was scanned linearly up to 0.75 V, where it was polarized for 0, 10, 100, or 1000 s, after which cyclic voltammetry was performed from 0.75 to 0.1V and back to 0.75 V. The results of these experiments are presented in Fig. 8-3. From Fig. 8-3 the cathodic reaction seems to be very much related to the anodic reaction which follows at 0.47 V. Yin *et al.* [1995] and Beigler and Horne [1985] have acknowledged that the associated reactions to these peaks must be the forward and reverse portions of a reversible reaction. Indeed, from the observed behavior of the reactions in Fig. 8-3, we also believe that both anodic and cathodic peaks are related to a reversible reaction with a reversible potential of *ca.* 0.4 V.

Additionally, it should be pointed out that the maximum positive potential in this experiment (Fig. 8-3) is 0.75 V which is well below the transpassive dissolution potential of chalcopyrite (~0.90 V) [Ghahremaninezhad et al., 2010; results of chapter 7]. In this potential region mostly ferrous and ferric will be released to solution rather than copper ions; Nova and Gonzales have shown that the concentration of dissolved copper is low and anodic stripping voltammetry (ASV) was unable to detect copper in solution [Nava and Gonzalez 2006]. At this low copper concentration level, the reversible potential of cupric reduction will be well below the reversible potential of Fig. 8-3 (*ca.* 0.4 V). Hence, cupric reduction to metallic copper is not a valid reaction for peak c2 of Fig. 8-2a.
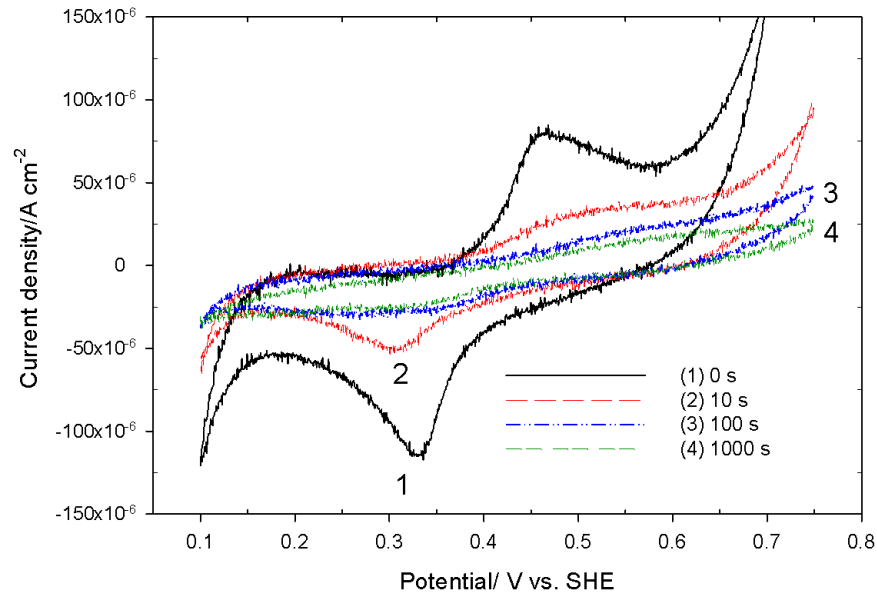
Figure 8-3: Cyclic voltammetry of chalcopyrite electrode between 0.75 to 0.1 V_{SHE} with (1) 0, (2) 10, (3) 100 and (4) 1000 seconds of potentiostatic polarization at 0.75 V_{SHE} before cyclic voltammetry experiment. Scan rate is 50 mV s^{-1}.

The other reaction suggested in the literature is reduction of covellite [Yin *et al.* 1995]:

$$CuS + Cu^{2+} + 2\,e^{-} \rightarrow Cu_2S \qquad E(V_{SHE}) = 0.493 + 0.0295\log[Cu^{2+}]$$ 8-3
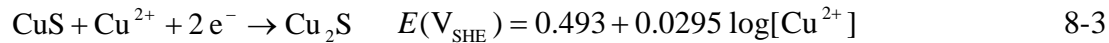
Yin *et al.* [1995] have proposed that CuS and cupric, which are products of chalcopyrite oxidation [Yin *et al.* 1995], form in the positive-going cycle and that these are involved in the cathodic direction of reaction 6 during the negative-going cycle. If reaction 6 were valid, then one would expect to observe a cathodic peak in Fig. 8-3 with increasing magnitude as the polarization time at 0.75 V was increased from 0 to 1000 s (due to the formation of more CuS and Cu^{2+} by further oxidation of chalcopyrite at 0.75 V). However, the results of Fig. 8-3 present exactly the opposite scenario; by increasing the polarization time at 0.75 V from 0 to 1000 s the peak is almost eliminated. This evidence calls the validity of reaction 6 into question.

Lastly, Biegler and Horne [1985] proposed the formation of chalcocite by chalcopyrite reduction according to the following reaction:

$$CuFeS_2 + 3\,Cu^{2+} + 4\,e^{-} \rightarrow 2\,Cu_2S + Fe^{2+}$$

$$E(V_{SHE}) = 0.700 + 0.0443\log[Cu^{2+}] - 0.0148\log[Fe^{2+}]$$ 8-4
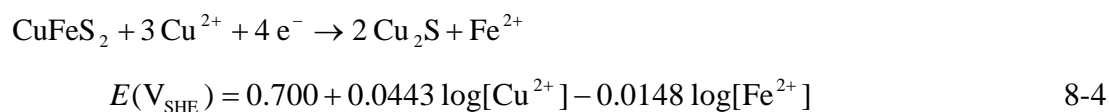
In order to further evaluate this reaction, Biegler and Horne [1985] investigated the influence of 0.5 mM of ferric, ferrous and cupric addition on the magnitude of the cathodic peak of Fig. 8-3. Addition of ferric and ferrous had no effect; however, cupric addition increased the magnitude of the peak significantly.

Now, it remains only to justify why the potentiostatic polarization of chalcopyrite at 0.75 V before a cyclic voltammetry experiment eliminates both the anodic and cathodic peaks (refer to Fig. 8-3) of reaction 8-4. The potential of 0.75 V is a passive potential for chalcopyrite [Ghahremaninezhad *et al.* 2010]; hence, during polarization of the electrode at this potential, a passive film forms on the mineral surface. Anodic polarization of chalcopyrite at 0.75 V extends the area of the passive surface of chalcopyrite, decreasing the exposed surface of chalcopyrite to solution as polarization time is increased. Hence, the extent of reaction 8-4 will decrease as a function of anodic polarization time at 0.75 V. This means that less chalcocite (Cu_2S) will be produced by reaction 8-4 during a negative-going cycle, and therefore less chalcocite will be available for oxidation during the following positive-going cycle; *i.e.*, a decrease in the magnitude of the cathodic peak will lower the magnitude of the corresponding anodic peak.

As a final validation of reaction 8-4, a rotating chalcopyrite disk electrode (500 rpm) was polarized linearly from 0.55 V (*ca.* OCP) to 0.75 V, and two successive potential scan cycles were then applied between 0.75 V and 0.1 V (the same potential window as in Fig. 8-3). The result of this experiment is presented in Fig. 8-4, which clearly shows that both the cathodic and anodic peaks are eliminated by rotation of the electrode. This is due to diffusion of both cupric and ferrous away from the electrode which eliminates the possibility of reaction 8-4.
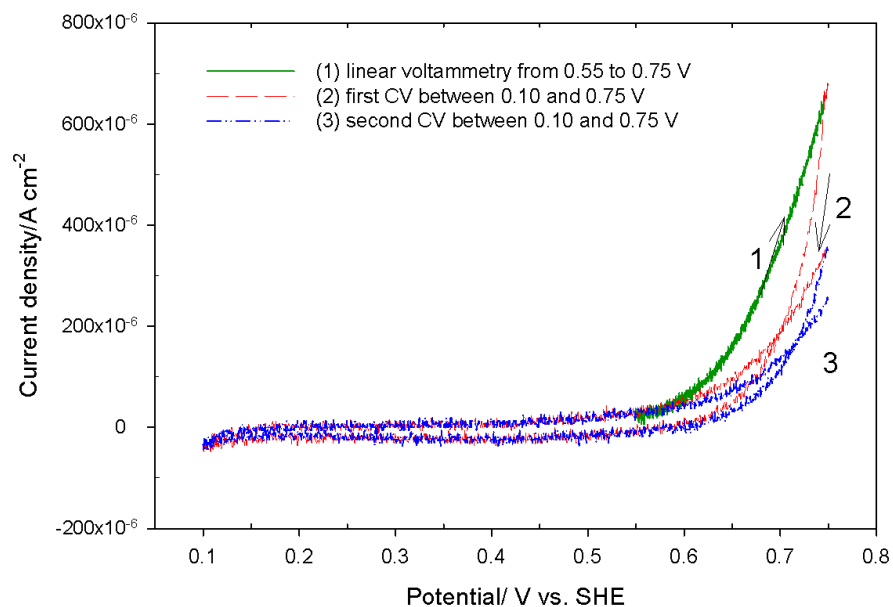
Figure 8-4: Cyclic voltammetry of a rotating chalcopyrite disk electrode (500 rpm) between 0.75 and 0.1 V. Scan rate is 50 mV s^{-1}.

Fig. 8-5 presents the cyclic voltammogram of a chalcopyrite electrode in the potential window from −0.1 to 1 V. Increasing the anodic vertex potential during cyclic voltammetry of chalcopyrite electrodes to potentials above 0.9 V shifts the cathodic peak of Fig. 8-3 to more negative potentials, i.e. from 0.33 V to 0.29 V. In addition, increasing the vertex potential from 0.75 V (Fig. 8-3) to 1.0 V (Fig. 8-5) clearly increases the magnitude of the cathodic peak from about 125 μA cm^{-2} (Fig. 8-3) to about 470 μA cm^{-2} (Fig. 8-5). This increase in the magnitude of the peak may be related to the increase in the concentration of cupric (reactant of reaction 8-4 − cf. Table 2) in the vicinity of the electrode, provided by increasing the anodic dissolution potential up to 1.0 V.

155
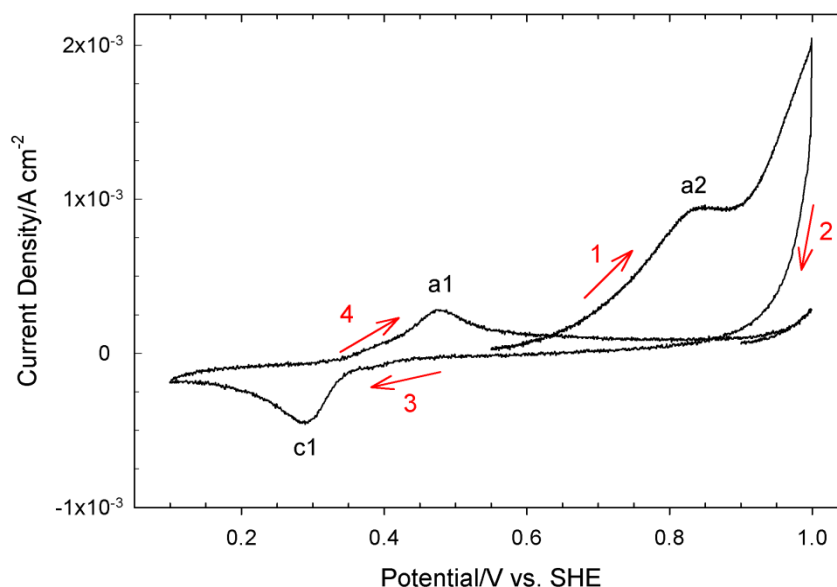
Figure 8-5: Cyclic voltammogram of a chalcopyrite electrode in the potential window of −0.1 to 1 V. Scan rate is 50 mV s⁻¹.

Fig. 8-6 presents the first, second and tenth CV cycles for a stationary chalcopyrite electrode. In this experiment, the electrode was polarized at 0.55 V (*ca.* OCP) for 20 seconds and then scanned up to 0.75 V and finally 10 cycles were performed between 0.75 and −0.5 V. It is clear that both peaks c3 and c4 are absent in the first cycle, appearing only upon (and after) the second cycle. The current of peak c3 remains almost constant regardless of the number of cycles while peak c4 grows as the cycling is continued (Fig. 8-6). Additionally, from Fig. 8-2b, it is clear that rotation of the electrode does not eliminate peaks c3 and c4. The origin of peaks c3 and c4 is most likely reduction of chalcopyrite itself [Li *et al.* 2011]. From the Pourbaix diagram for chalcopyrite [Garrels and Christ 1965], at *ca.* pH 0.3 chalcopyrite is not stable at potentials below −50 mV, i.e. the Pourbaix diagram predicts formation of chalcocite at this condition. Furthermore, again from the same Pourbaix diagram, chalcocite (Cu_2S) is the stable phase at potentials below −0.25 V, and may thus form on the surface. However, partial cathodic dissolution of iron from the chalcopyrite structure may result in the formation of copper-iron-sulfur phases such as $Cu_9Fe_8S_{16}$ or Cu_5FeS_4. A list of possible reactions associated with peaks c3 and c4 of Fig. 8-6 are presented in Table 8-1 (reactions 8-5 to 8-7).
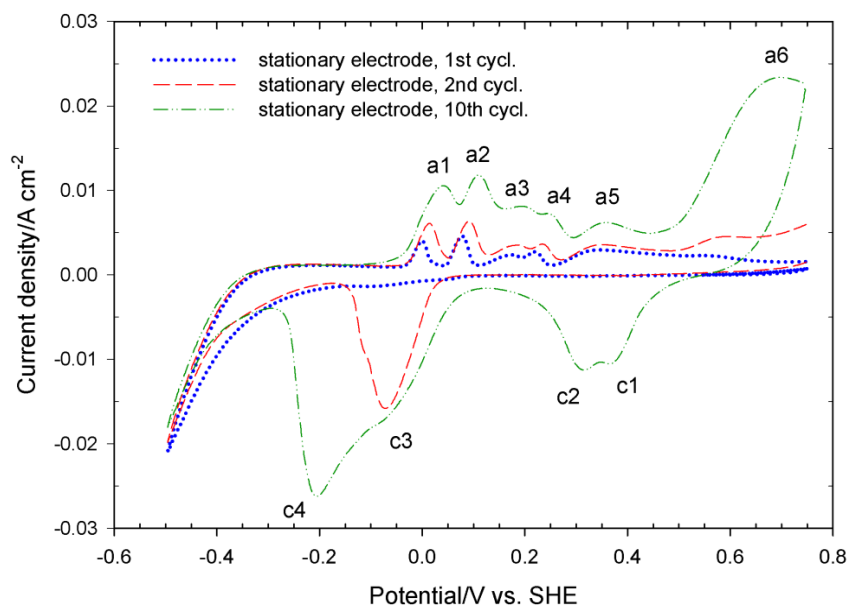
Figure 8-6: Multicyclic voltammetry of chalcopyrite electrode presenting the first, second, and tenth cycles. Scan rate is 50 mV s^{-1}.

8.2.3 Anodic reactions on the surface of chalcopyrite

Fig. 8-1a reveals seven distinct anodic peaks for a typical stationary chalcopyrite electrode. Anodic peaks a1 to a7 are centered at 0.02, 0.10, 0.19, 0.24, 0.35, 0.65 and 0.79 V, respectively. In order to understand the origin of these peaks (the assigned reactions to all anodic peaks are summarized in Table 8-1), the anodic vertex potential was held at 0.75 V (same as Fig. 8-2a) while the cathodic vertex potential was increased from −0.5 V to +0.1 V (Fig. 8-7a) and −0.1 V (Fig. 8-7b). In both experiments, first the electrode was held at 0.55 V (*ca.* OCP) for 20 seconds and afterwards polarized linearly up to 0.75 V (50 mV s^{-1}), and then 10 cycles were applied (50 mV s^{-1}). From Fig. 8-7a, it is clear that anodic peaks a1, a2, a3 and a4 are related to the oxidation of products of cathodic peaks c3 and c4 (cf. Table 8-1); otherwise, they would have appeared in Fig. 8-7a. Moreover, from Fig. 8-2b one can say that the reactions associated with these anodic peaks all involve soluble reactants, such that rotation of the electrode eliminates them. By lowering the cathodic vertex potential from 0.1 V (Fig. 8-7a) to −0.1 V (Fig. 8-7b), cathodic peak c3 (and, to some extent, c4 – cf. Table 8-1) occurs, and subsequently, anodic peaks a2, a3 and a4 also appear. Hence, these anodic peaks are related to the oxidation of soluble reaction products associated with peaks c3 and c4 (ferrous and H$_2$S, based on the reactions given in Table 8-1). Formation of copper sulfides

157

(with different stoichiometries) through oxidation of other copper sulfides (products of reactions 8–5 to 8–7 of Table 8-1) are possible reactions [Biegler and Horne 1985; Vinkevicius *et al.* 1998]. An example of these reactions can be reaction 8-9, presented in Table 8-2. The required H_2S for the above reaction originates from the reactions associated with peaks c3 and c4 of Fig. 8-2a, i.e. reactions 8–5 to 8–7 of Table 8-1. By rotation of the electrode (Fig. 8-2b), any aqueous H_2S product diffuses away from the electrode surface and reaction 8-9 (cf. Table 8-2) is prevented.
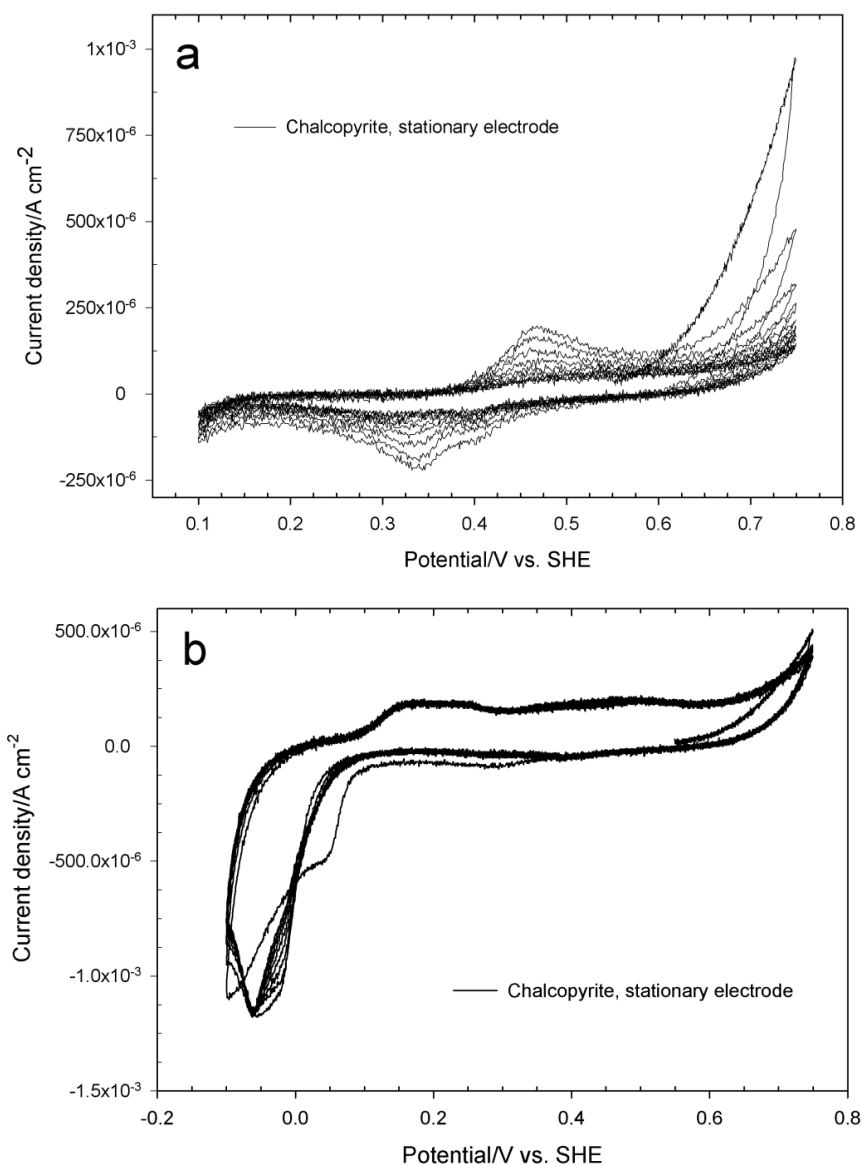
Figure 8-7: Multicyclic voltammetry (10 cycles) of a stationary chalcopyrite electrode in the potential window of (a) 0.1 to 0.75 V, and (b) −0.1 to 0.75 V. Scan rate is 50 mV s^{-1}.

Table 8-2: Anodic reactions on chalcopyrite surface.

peak	Reaction number	Reaction	Reference
a1 – a4	8-8	$Cu_2S + H_2S_{(aq)} \rightarrow 2\,CuS + 2\,H^+ + 2\,e^-$	Biegler and Horne 1995
a5	8-4	$CuFeS_2 + 3\,Cu^{2+} + 4\,e^- \Leftarrow 2\,Cu_2S + Fe^{2+}$	Biegler and Horne 1995
a6	8-9	$CuFeS_2 = Cu_{1-x}Fe_{1-y}S_2 + xCu^{2+} + yFe^{2+} + 2(x+y)e^- \qquad y \gg x$	Nava and Gonzalez 2006
a7	8-10	$Cu_{1-x}Fe_{1-y}S_2 \rightarrow (1-x)Cu^{2+} + (1-y)Fe^{3+} + 2\,S + (5-2x-3y)e^-$	Hackl *et al.* 1995
a8	8-12	$CuFeS_2 + 8\,H_2O \rightarrow Cu^{2+} + Fe^{3+} + 2\,SO_4^{2-} + 16\,H^+ + 17\,e^-$	Yin *et al.* 1995
	8-13	$CuFeS_2 \rightarrow Cu^{2+} + Fe^{3+} + 2\,S + 5e^-$	Yin *et al.* 1995

Fig. 8-8 presents the multicyclic voltammogram of a stationary chalcopyrite electrode over a wide potential range (–0.5 to 1.2 V). In this figure, anodic peaks a1 to a4 are the same peaks as those shown in Figs. 8-6 and 8-7. Peak a5 is the reverse of reaction 8-4 (cf. Tables 8-1 and 8-2) as shown in Figs. 8- 3 to 8-5.

Peak a6 of Fig. 8-8 represents the anodic oxidation of chalcopyrite. At potentials below 0.9 V (transpassive dissolution potential of chalcopyrite [Ghahremaninezhad *et al.* 2010]), iron atoms dissolve preferentially from the surface of chalcopyrite, leaving behind a copper-rich film [Ghahremaninezhad *et al.* 2010; Viramontes-Gamboa *et al.,* 2007]. In fact, it has been claimed by many researchers that a metal-deficient sulfide film is the passive film responsible for slow leaching of chalcopyrite [Ghahremaninezhad *et al.* 2010; Viramontes-Gamboa *et al.* 2007; Biegler and Swift 1979; Yin *et al.* 1995; Nava and Gonzalez 2006; Hackl *et al.* 1995]. Hence, the reaction associated with peak a6 of Fig. 8-8 is [Ghahremaninezhad *et al.* 2010]:

$$CuFeS_2 = Cu_{1-x}Fe_{1-y}S_2 + xCu^{2+} + yFe^{2+} + 2(x+y)e^- \qquad y > x \qquad\qquad 8\text{-}10$$
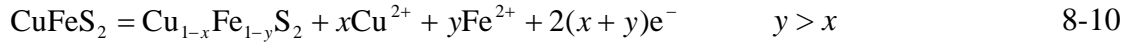
The formation of a metal-deficient sulfide film can be investigated by OCP measurements. If a passivated chalcopyrite electrode is immersed in the electrolyte (at OCP), then the metal-deficient sulfide film will relax as iron and copper atoms diffuse from the bulk of the electrode to the surface (i.e. diffusion will cause the x and y values of reaction 8-9 to approach 0). In order to confirm the formation of such a film, chalcopyrite electrodes were polarized at three different passive potentials of 0.65, 0.75 and 0.85 V for 10 hrs in 0.5 M sulfuric acid solution and afterwards allowed to relax to their OCPs. Fig. 8-9 presents the OCP of each electrode after polarization. In addition to the above three OCP curves, for the sake of comparison, the OCP behavior of an unpolarized chalcopyrite electrode is also presented in Fig. 8-9 (solid black curve). The OCP measurements of Fig. 8-9 were conducted for about 9 hrs. All of the OCP values approach the original OCP value of chalcopyrite (that of an unpolarized sample – *ca.* 0.54 V) after about 4 hrs. This figure provides further evidence that the passive layer of chalcopyrite is a metal-deficient film. Hence reaction 8-9 (Table 8-2) is the reaction associated with the anodic dissolution of chalcopyrite (peak a6 of Fig. 8-8).
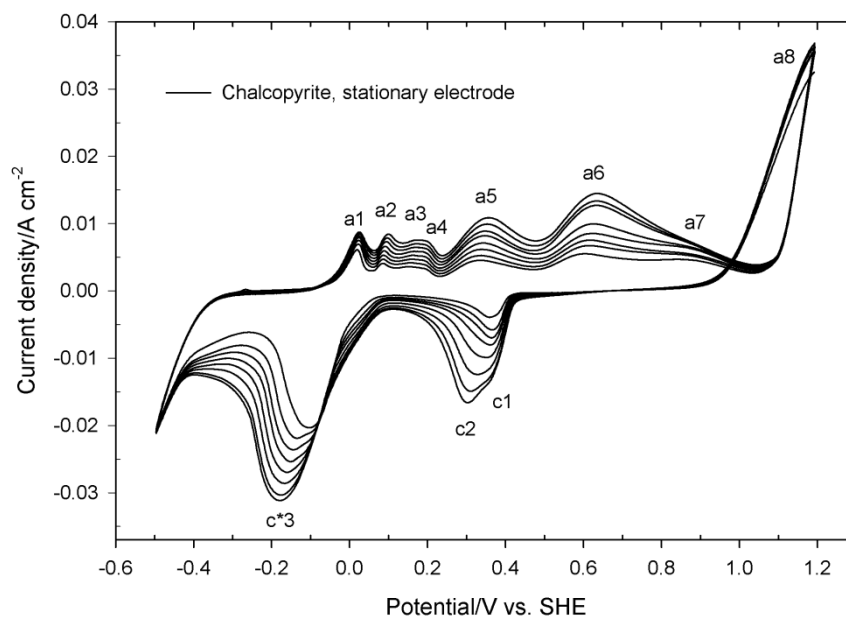
Figure 8-8: Multicyclic voltammetry of a stationary chalcopyrite electrode in the potential window of −0.5 to 1.2 V. Scan rate is 50 mV s⁻¹.
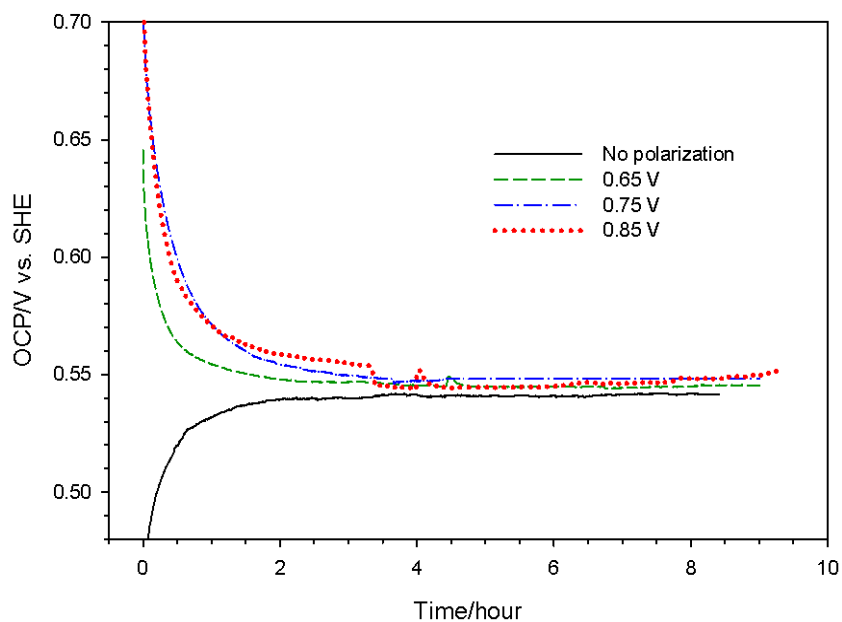
Figure 8-9: OCP measurements of a chalcopyrite electrode after polarizing at different passive potentials of 0.65, 0.75 and 0.85 V for 10 hrs. The OCP behavior of a polished chalcopyrite electrode (without previous polarization) is also presented with a solid black line.

In addition to peaks a1 to a6, Fig. 8-8 presents a new anodic peak observable at 0.90 V (peak a7) and a rapid rise in current in the positive-going direction at potentials above 1.1 V (peak a8). The magnitude of peaks a5 and a6 increased with the number of cycles while the magnitude of peak a7 was almost constant. Interestingly, the potential of peak a7, 0.90 V, is the same as the transpassive dissolution of chalcopyrite [Ghahremaninezhad *et al.,* 2010]. Hence, peak a7 can be assigned to dissolution (oxidation) of the passivating film of chalcopyrite (*i.e.*, the metal-deficient sulfide film). The near-constant magnitude of peak a7 can be justified by the fact that the passive film is only a few nanometers thick [Ghahremaninezhad *et al.,* 2010]. Hence, the charge associated with dissolution of this film (and consequently the peak current magnitude) is always about the same. Elemental sulfur (and polysulfide) is one of the oxidation products of chalcopyrite at (transpassive) potentials above 0.90 V [Ghahremaninezhad *et al.,* 2010]. If peak a7 is in fact associated with the oxidation of the passive film, and if elemental sulfur is one of the oxidation products, then one possible reaction for peak a7 would be:

$$Cu_{1-x}Fe_{1-y}S_2 \rightarrow (1-x)Cu^{2+} + (1-y)Fe^{3+} + 2S + (5-2x-3y)e^- \qquad \text{8-11}$$
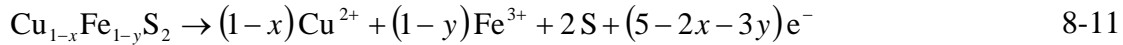
where $y > x$ [Hackl *et al.* 1995]. In reaction 8-11 we have considered the formation of ferric due to the thermodynamic instability of ferrous at 0.90 V and above. In order to calculate the thickness of the passive film, we make the assumption that all of the charge associated with peak a7 is related to CuS dissolution (since y in reaction 8-11 is much larger than x, so one can assume that the iron content of the metal-deficient phase is almost negligible) [Warren *et al.* 1982]. In other words, we assume that the main passivating film of chalcopyrite is CuS. This assumption is also consistent with the results of some other workers who have concluded that the copper sulfides formed at passive potentials are responsible for passivation of chalcopyrite [Biegler and Horne 1985; Yin *et al.* 1995; Lazaro and Nicol 2006; Nava and Gonzalez 2006; Holliday and Richmond 1990]. Under this assumption, it is possible to relate the mass of the dissolved copper sulfide (CuS) through peak a7 to the charge associated with the peak. Integrating the current under peak a7 in Fig. 8-8 gives a charge of 6.2 ± 0.4 mC cm^{-2}. Considering the calculated density of 4.6 g cm^{-3} for CuS [Evans and Konnert 1976], and assuming a surface roughness factor of unity, the thickness of the passivating CuS film on the surface of chalcopyrite can be estimated to be approximately 6.7 nm. This result agrees fairly well with that of Yin *et al.* [1995] who calculated a thickness

of about 4 nm for the passive film. Elsewhere, a passive film consisting of CuS and elemental sulfur with a thickness of 2.9 nm is proposed [Biegler and Horne 1985].

From Fig. 8 it is very clear that above 1.1 V the anodic current density sharply increases. This is due to the dissolution of chalcopyrite via one or both of the following reactions [*Yin et al. 1995*]:

$$CuFeS_2 + 8\,H_2O \rightarrow Cu^{2+} + Fe^{3+} + 2\,SO_4^{2-} + 16\,H^+ + 17\,e^- \qquad\qquad 8\text{-}12$$

$$CuFeS_2 \rightarrow Cu^{2+} + Fe^{3+} + 2\,S + 5e^- \qquad\qquad 8\text{-}13$$
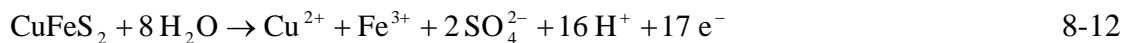
The cathodic peak of Fig. 8-8 at −0.10 V (peak c*3, whose potential increases with cycle number up to −0.18 V) has a different shape and position compared to cathodic peaks c3 and c4 of Fig. 8-2a. Peak positions for c3 and c4 of Fig. 8-2a in the tenth cycle are −0.08 and −0.20 V respectively, while the potential of peak c*3 in Fig. 8-8 is −0.17 V. This dissimilarity may suggest a change in the path of the reactions associated with these peaks. Further evidence for such a change can be obtained by comparing the magnitude of peaks c3 and c4 in Fig. 8-2a with that in Fig. 8-8. In the first cycle shown in Fig. 8-2a peaks c3 and c4 are absent while in Fig. 8-8 the cathodic peak at −0.10 V has an appreciable magnitude during the first cycle, *ca.* 18 mA, and grows to *ca.* 32 mA after several cycles. In order to determine the origin of this difference, multicyclic voltammetry in the potential window of −0.5 to 1.0 V was conducted, as shown in Fig. 8-10. The lower vertex potential of the experiment was kept at −0.5 V but, in order to eliminate the oxidation reaction which begins at 1.1 V, the upper vertex was reduced to 1.0 V. In both of the experiments of Figs. 8-8 and 8-10, the electrodes were held at 0.55 V (*ca.* OCP) for 20 seconds, then the potential was scanned up to the anodic vertex (1.2 V for Fig. 8-8 and 1.0 V for Fig. 8-10), and then 10 cycles were performed. The shape of cathodic peaks c1 and c2 in Fig. 8-10 are the same as those of Fig. 8-2a and different from that of Fig. 8-8 (peak c*3). By comparing Figs. 8-8 and 8-10, one may conclude that the origin of the different magnitudes of peaks c3 and c4 of the first cycle is related to the reaction associated with peak a8 of Fig. 8-8. If peak a8 is associated with dissolution of chalcopyrite via reactions 8-12 and 8-13 (cf. Table 8-2), then at potentials above 1.1 V the surface of the electrode dissolves actively and the exposed surface of the electrode will consist mainly of chalcopyrite and elemental sulfur [1, 22], and all of the other copper sulfide intermediates will have been dissolved. Hence, we conclude that peak c*3 of Fig. 8-8 is related to the reduction of elemental sulfur. By exposure of the

electrode to the very high anodic potential of 1.2 V (Fig. 8-8), a significant amount of elemental sulfur can form on the surface of chalcopyrite (via reaction 8-13). In fact, exposure of the electrode to this potential causes the formation of a thin black film on the surface of the electrode which can be wiped away with a soft cotton swab. Thus, peak c*3 of Fig. 8-8 can be related to the following reaction:

$$S + 2\,H^+ + 2\,e^- = H_2S_{(aq)} \qquad E(V_{SHE}) = 0.148 - 0.0591\,pH \qquad\qquad 8\text{-}14$$
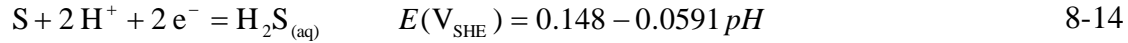
Due to the high concentration of sulfur on the surface, elemental sulfur reduction will be the main cathodic reaction in comparison to cathodic reactions 8–5 to 8–7 of Table 8-1.
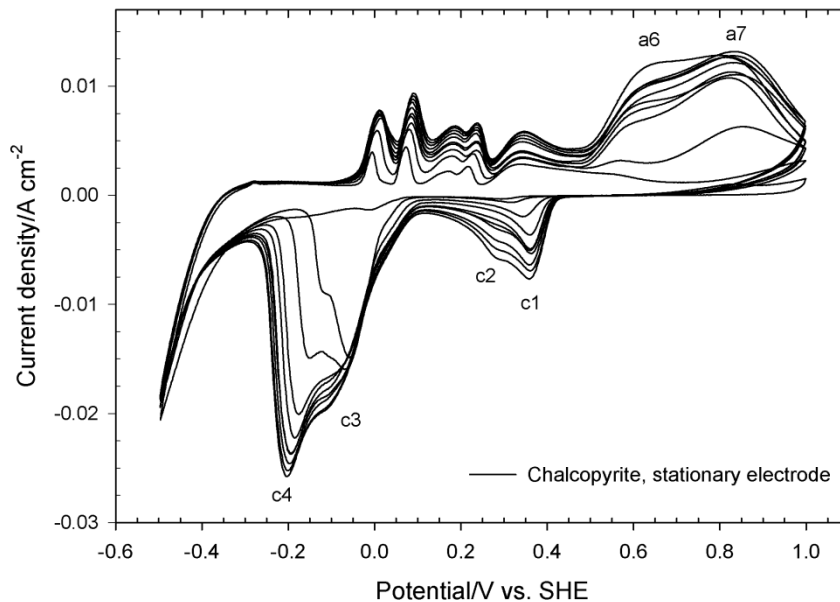
Figure 8-10: Multicyclic voltammetry of a stationary chalcopyrite electrode in the potential window of −0.5 to 1.0 V. Scan rate is 50 mV s⁻¹.

8.3 Conclusion

In summary, electrochemical reactions on the surface of a massive chalcopyrite electrode were investigated in 0.5 M sulfuric acid solution (pH 0.3) at 25ºC by multicyclic voltammetry and open circuit potential measurements. Variation of the scan limits under different experimental conditions (quiescent *vs.* rotating electrodes) was used for analysis of each electrochemical current peak. Oxidation of chalcopyrite proceeds at high anodic potentials ($E > 0.6$ V_{SHE}). It was shown iron atoms dissolve preferentially from the surface of chalcopyrite during anodic dissolution, leaving behind a copper-rich metal-deficient

sulfide passive film (i.e. $Cu_{1-x}Fe_{1-y}S_2$ $y > x$). By integrating the current under the chalcopyrite de-passivation peak (peak a7 of Fig. 8-10), the thickness of the passive film was calculated to be *ca.* 6.7 nm. Additionally, experiments showed that elemental sulfur is a product of chalcopyrite oxidation at anodic potentials higher than 1.0 V_{SHE}.

Cathodic dissolution of chalcopyrite proceeds at potentials below 0 V_{SHE}. The cathodic dissolution process involves the release of ferrous and $H_2S_{(aq)}$ to solution. The cathodic reactions which occur in the potential region of 0.1 to 0.6 V_{SHE} and the anodic reactions which occur at potentials lower that 0.5 V_{SHE} are all related to the reduction and oxidation of soluble species. The soluble species involved in those cathodic reactions are ferric and cupric and the soluble species involved in the anodic reactions is $H_2S_{(aq)}$.

9 Ferric/ferrous redox reaction on anodically passivated chalcopyrite (CuFeS$_2$) electrode[3]

9.1 Introduction

Typical hydrometallurgical copper extraction processes for chalcopyrite concentrates proceed by reduction of an oxidant (e.g. ferric ion, oxygen) and oxidation of chalcopyrite to cupric and ferrous. The oxidation reaction for chalcopyrite in the presence of ferric can be written as [Dutrizac and MacDonald, 1974]:

$$CuFeS_2 + 4Fe^{3+} = Cu^{2+} + 5Fe^{2+} + 2S^o \qquad\qquad 9\text{-}1$$

Oxygen can re-oxidize the ferrous back to ferric via the following reaction:

$$4Fe^{2+} + O_2(aq) + 4H^+ = 4Fe^{3+} + 2H_2O \qquad \Delta G^o_{25^oC} = -193.3 \quad kJ/mole \qquad 9\text{-}2$$

The ferric ion represents one of the most important oxidants in hydrometallurgy [Tshilombo *et al.,* 2002]. The ultimate effects of ferric in leaching solutions are to accept electrons at the mineral surface with rapid kinetics and to maintain a relatively high redox potential, at which the electrochemical dissolution of chalcopyrite (generally the mineral of interest) is thermodynamically favored. From the Pourbaix diagram of chalcopyrite [Garrels and Christ 1965], the acidic oxidation of chalcopyrite is thermodynamically possible at pH values lower than 6 and oxidation potentials higher than 0.2 V$_{SHE}$. Since the ferric-ferrous couple has a relatively high potential, E^o = 0.771 V$_{SHE}$, the desired solution potential during leaching can be obtained by the addition of ferric. The other reason for the use of ferric as an oxidant is its relatively rapid reduction kinetics on the surfaces of some minerals such as pyrite. In the case of chalcopyrite leaching in sulfuric acid solution, it has been claimed that the kinetics of the ferric-ferrous redox reaction are very slow [Beigler and Horne 1985; Parker *et al.,* 1981]. Elsewhere, McMillan *et al.* [1982] have shown that the rate of the ferric-ferrous redox reaction is very slow in comparison with Cu^{2+}/Cu^+ and I_3^-/I^- redox couples. Nevertheless, the kinetic parameters of the ferric-ferrous couple on the surface of chalcopyrite under leaching conditions have not yet been quantified. These kinetic parameters are important for hydrometallurgical process optimization and development. The

---

lack of quantitative information on the kinetic parameters of the ferric-ferrous couple on the surface of chalcopyrite (and almost all other minerals) is due to the interference from chalcopyrite oxidation. In other words, during the dissolution of chalcopyrite, the oxidation reaction of chalcopyrite will be coupled with ferrous oxidation; and in the case of reducing conditions, oxygen and chalcopyrite reduction will be coupled with ferric reduction. The interference from unwanted reactions makes the quantification of ferric reduction kinetics by application of typical electrochemical methods almost impossible.

Another issue with quantifying the kinetics of redox couples is passivation of the substrate. The kinetics of the ferric-ferrous couple on the surface of oxide-free metals [Samec and Weber 1977] and superficially oxidized metals [Makrides 1964a] have been studied previously. The determination of these kinetics on the surface of oxide-free metals is straightforward. On the other hand, the charge transfer rate of the redox reactions at superficially oxidized metals depends on the thickness of the semiconductor oxide film. This can be described with the quantum mechanical theories of electron transfer [Marcus 1964]. According to these theories, the tunneling probability decreases with the thickness of the passive film. However, in the case of semiconductor electrodes, e.g. chalcopyrite and most of the sulfide minerals, the electrochemical reactions proceed by participation in the electron transfer reaction of electronic states inside the semiconductor electrode. Hence, chalcopyrite itself, as a semiconductor material, and its passive film together make the kinetics of the ferric-ferrous couple more complicated (even than that of superficially oxidized metals). Under anodic potentials of about 0.65 to 0.90 V_{SHE} in sulfuric acid solution, chalcopyrite is in the passive state and several metal-deficient-sulfide passive films, e.g. $Cu_{1-x}Fe_{1-y}S_2$ ($y > x$), $Cu_{1-z}S_2$ and CuS, have been suggested to form at potentials between 0 and 1.0 V_{SHE} [Ghahremaninezhad *et al.,* 2010a; Cordoba *et al.,* 2008; Viramontes-Gamboa *et al.,* 2007; Nava and Gonzalez 2006]. In addition, it has been shown that the passive film of chalcopyrite has semiconductive properties [Ghahremaninezhad *et al.,* 2010a; Hiskey 1993]. Hence, in order to analyze the kinetics of the ferric-ferrous couple on chalcopyrite under leaching conditions, one must include the influence of the semiconducting properties of the passive film in the redox reaction kinetics.

In this chapter, the kinetics of the ferric-ferrous couple on the surface of chalcopyrite in acidic sulfate media will be discussed. Despite attempts to measure the kinetics on

chalcopyrite surfaces [Cordoba *et al.,* 2008; Hiroyoshi *et al.,* 2001], to the best of our knowledge, there is no report of the exchange current density values or reaction orders for the ferric-ferrous couple on the surface of chalcopyrite.

9.2 Experimental

A high quality natural polycrystalline chalcopyrite sample (98.1% chalcopyrite, 1.9% siderite $FeCO_3$) originating from the Creighton Mine (Sudbury, Ontario) was used for electrode fabrication. Further characterization of the mineral and morphological distribution of the siderite are given elsewhere in chapter 6 [and also Ghahremaninezhad *et al.,* 2010a]. Massive electrodes were prepared by cutting the mineral into approximately cubic shapes with areas of 1 cm^2 exposed to the solution. In order to have a uniform current distribution on the samples, a thin layer of metallic copper was electrodeposited on the back of the electrodes (the side to which the wire was attached). Copper was electrodeposited from a copper sulfate solution at low current density (4 mA cm^{-2}). An electrical contact with copper wires was made to the back of the samples with silver-loaded epoxy resin (Mg Chemicals). The electrode contacts were protected from the solution by mounting the whole assembly in epoxy resin (LECO), leaving only one face of the electrode exposed to the solution. Prior to each electrochemical experiment the electrodes were checked to ensure that there was no evidence of crevice corrosion in the electrode. This was possible due to the transparent epoxy resin mounts. Before each test, the exposed face of the electrode was polished with new carbide papers, starting from no. 300 and progressing to no. 1200 paper. After this polishing procedure, the surfaces of the electrodes were inspected with an optical microscope to ensure that the morphology of the electrodes was similar. The electrodes were then washed, sonicated and rinsed in deionized (DI) water and dried in a stream of air.

All electrochemical experiments were performed at 25ºC using a VersaSTAT 4 potentiostat/galvanostat controlled by VersaStudio software (version 1.51, Princeton Applied Research). A conventional three-electrode electrolytic cell was used for electrochemical analysis. The test cell was jacketed and water was circulated through the jacket to maintain the desired test temperature of 25ºC. The working electrode was always the prepared chalcopyrite electrode. A graphite counter electrode (99.999%, Alfa Aesar) and a glass-body Ag/AgCl reference electrode filled with 4 M KCl electrolyte saturated with AgCl (Accumet

13-620-523, 199 mV *vs* SHE at 25ºC) were used. All electrode potentials in this study are reported with respect to the SHE. The reference electrode was connected to a saturated K_2SO_4 solution-filled Luggin capillary to minimize IR drop. The electrolyte inside the reference electrodes was refreshed after every 20 h of use and the electrodes were tested against a lab-standard Ag/AgCl electrode before each experiment.

The electrode potential was allowed to stabilize for 6 h before starting the measurements and, in order to ensure reproducibility, tests were begun only after reaching the same OCP to within ±5 mV. The initial solution was 500 mL of 0.5 M H_2SO_4 (pH 0.3), prepared by dissolving reagent grade sulfuric acid (Fisher Scientific) in DI water. In all experiments the oxygen content of the solution was controlled by sparging air through the solution. The potentiostatic polarization experiments were performed by application of a constant potential and the current flow through the sample was registered.

The experiments for the kinetic measurements of ferric-ferrous redox reactions on the chalcopyrite surface were performed in the following order. Before each experiment, the electrode potential was allowed to stabilize for 6 h in 500 mL of 0.5 M H_2SO_4 solution. The solution was stirred during the experiments (250 rpm). The electrode was then passivated potentiostatically at the desired potential for 6 h (the passive potential region of chalcopyrite was obtained from potentiostatic polarization data). The current density during the first two hours of passivation dropped to a steady-state current of less than 10 µA cm^{-2}. Passivation for more than 24 h showed negligible effect on the current, meaning the thickness of the passive film was almost constant after 6 h. 200 mL of solution containing 0.5 M H_2SO_4 and the desired amounts of $Fe_2(SO_4)_3$ and $FeSO_4$ (both from Fisher Scientific) were then added to the solution, in order to change the composition of the original electrolyte to 0.5 M H_2SO_4, 0.1 M $Fe_2(SO_4)_3$ and 0.05 M $FeSO_4$. The applied potential was held constant during the entire process and the current was registered for 20 h after addition of the Fe salts. The current jump in the potentiostatic experiment was related to the ferric-ferrous redox reaction.

EIS tests were conducted at all potentials one hour prior to and one hour after the addition of Fe salts. The frequency range was 10^{-2} to 10^5 Hz with a peak-to-peak amplitude of 5 mV. ZSimpWin 3.20 software (Princeton Applied Research) was used to fit the impedance data.

9.3 Results and discussion

Fig. 9-1 shows a typical potentiostatic polarization curve for the chalcopyrite electrode in 0.5 M H_2SO_4 solution. The curve was obtained by potentiostatically polarizing the chalcopyrite electrode for 6 h at each potential in order to reach the steady-state current (I_{ss}). The *i-t* (current density-time) behavior of the chalcopyrite electrode at selected potentials is presented in Fig. 9-2.
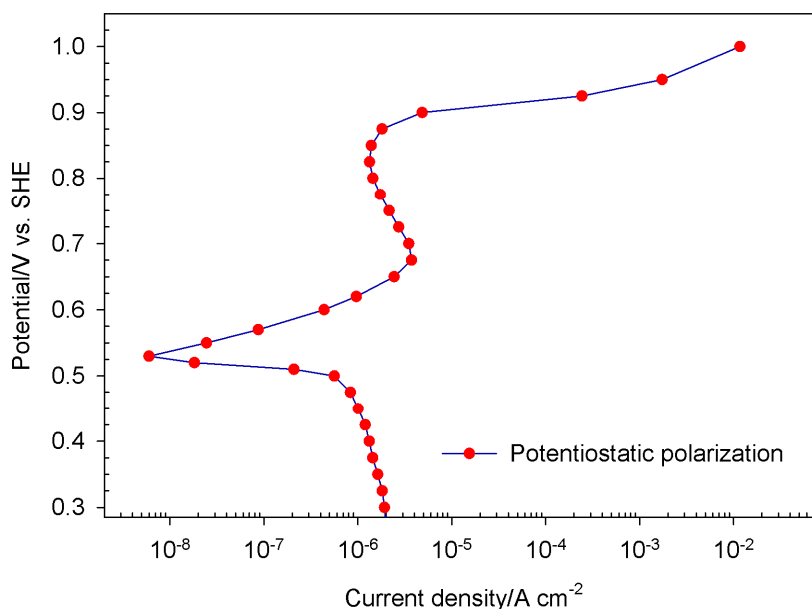
Figure 9-1: Potentiostatic polarization of chalcopyrite in 0.5 M sulfuric acid solution.
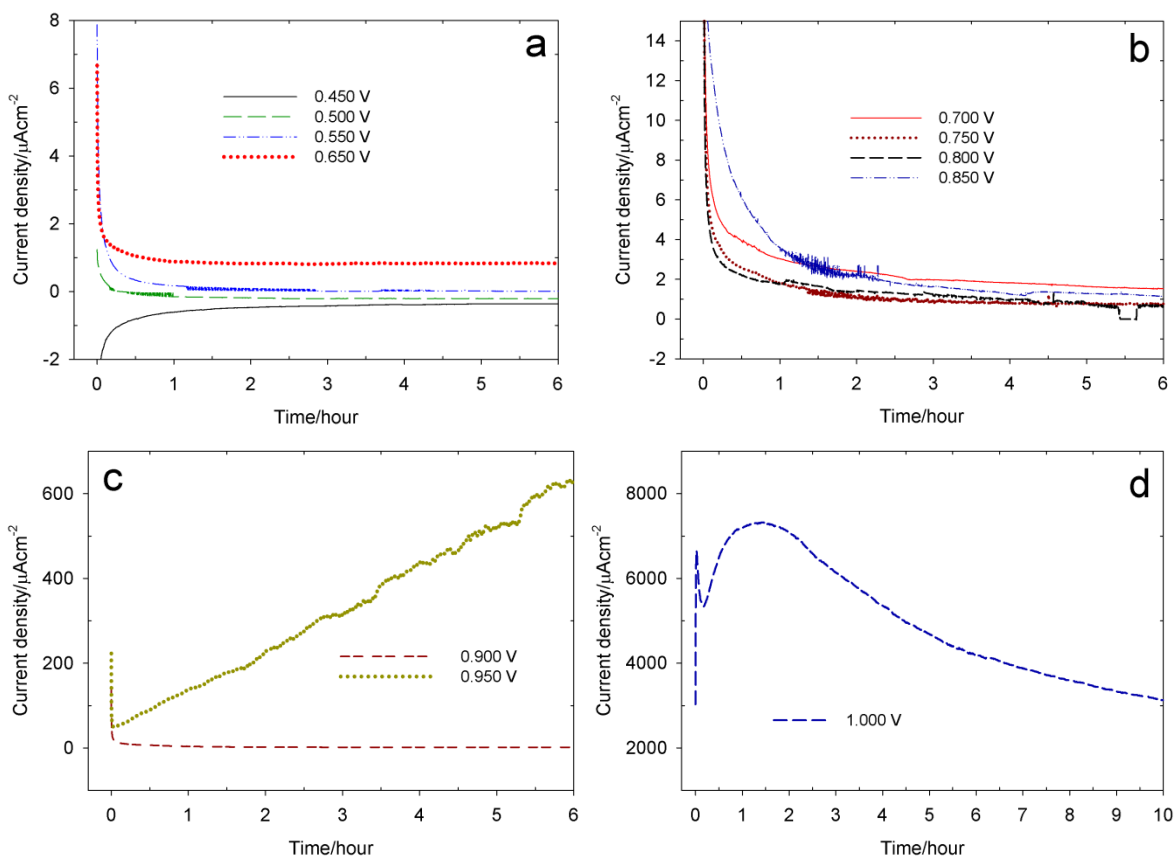
Figure 9-2: *i-t* behavior of chalcopyrite electrode in 0.5 M sulfuric acid solution at between 0.45 to 1.00 V.

From Fig. 9-1 and Figs. 9-2a to c, all potentials between 0.50 to 0.90 V can be considered to lie within the passive region. It is clearly stated in the literature that even at potentials below the open circuit potential (OCP) of chalcopyrite (ca. 0.54 V from Fig. 9-1) the surface of chalcopyrite is covered by a passive film which forms during exposure to air (prior to exposing the mineral to sulfuric acid solution) or during the 6 h stabilization of the electrode in solution prior to polarization [Ghahremaninezhad *et al.,* 2010a; Velasquez *et al.,* 2005]. The passive film on the surface of chalcopyrite is a stable film which causes steady state dissolution of chalcopyrite. This can be confirmed by long term potentiostatic polarization of chalcopyrite at a passive potential, as shown in Figs. 9-2a to c. Indeed, formation of a stable passive film on the surface of chalcopyrite is the reason for the sharp decrease in current prior to reaching the steady state dissolution current density in the potential region of 0.60 to 0.90 V. All of the curves in Figs. 9-2a and 9-2b show a sharp decrease in the current density during the first few hours of the experiment. However, in Fig. 9-2c, only a 50 mV increase in the potential of the electrode (from 0.90 to 0.95 V) causes

171

breakdown of the passive film and active dissolution of chalcopyrite. At the high anodic potential of 0.95 V, the dissolution rate increases as a function of time and, even after 6 h of polarization, the current density has not yet stabilized. Dissolution of chalcopyrite at 1.0 V (Fig. 9-2d) also shows a very high dissolution current density. The dissolution current density at this potential is above 3 mA cm^{-2} and the behavior is very different from the lower potentials. In Fig. 9-2d, the current reaches a peak after only a few minutes due to double layer formation. The decrease in current density observed after 1.5 h at 1.0 V (Fig. 9-2d) is probably due to the precipitation of Fe species on the surface of the electrode. Lu *et al.,* [2001] have suggested that at low pH (< 1, as in our experiments), ferric containing species such as jarosite may precipitate on the surface of chalcopyrite. Nava and Gonzalez [2006] and Klauber [2008] have also suggested the formation of ferric sulfate precipitates in this potential region. Nevertheless, even after 10 h of electrodissolution at 1.0 V (Fig. 9-2d) the current density is very high (*ca.* 1.5 mA cm^{-2}) which suggests that, regardless of a decrease in the current density, none of the layers formed on the surface act as passive films [Ghahremaninezhad *et al.,* 2010a]. Further analysis of the *i-t* behavior of chalcopyrite electrodes at 1.0 V is not relevant to this study.

The potentiostatic polarization diagram of chalcopyrite (Fig. 9-1) shows a negative slope in the anodic passive region (0.65 to 0.85 V). This is presented in Fig. 9-3, which shows the anodic section of the potentiostatic polarization of Fig. 9-1. According to the point defect model of passive films, the negative slope of the anodic passive region is related to the presence of an *n*-type semiconductor passive film with cation interstitial defects or anionic vacancies [Macdonald *et al.,* 1998]. This is in agreement with our previous findings [Ghahremaninezhad *et al.,* 2010a] which have shown that the passive film formed on the same chalcopyrite sample used in this study in the same solution has characteristics of an *n*-type semiconductor material.

Fig. 9-4a shows the points of the measured differences between the current density of the potentiostatic experiments ($0.56 \leq E \leq 0.95$ V) before and after addition of Fe salts to the electrolyte. This process is illustrated in Fig. 9-4b, which shows the current-time behavior of the electrode after addition of Fe salts at 0.70 V. The Δi value, shown in the inset of Fig. 9-4b, is the current density used to plot Fig. 9-4a.
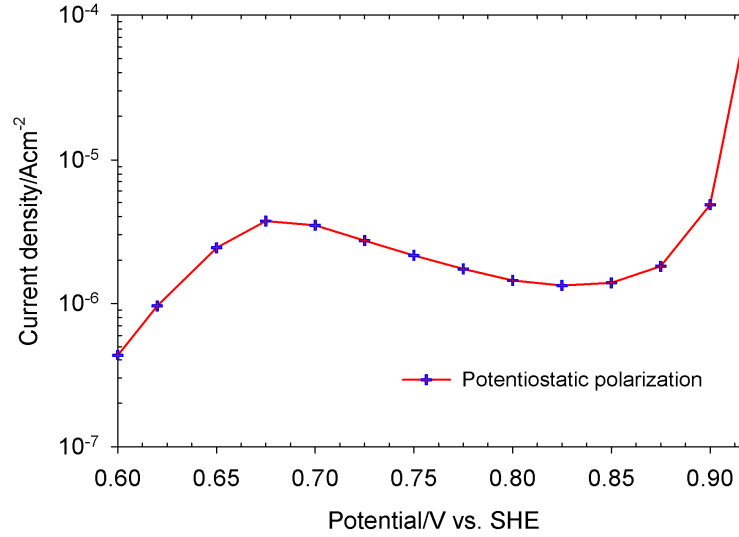
Figure 9-3: Potentiostatic polarization of chalcopyrite in 0.5 M sulfuric acid solution. This figure magnifies the anodic region as shown in Fig. 9-1.

In order to ensure that the data points of Fig. 9-4a are reliably presenting the Tafel region for the ferric-ferrous couple, two conditions must be met. First, the passive film must be stable on the surface of the chalcopyrite. The electrode was potentiostatically polarized at a constant potential ($0.56 \leq E \leq 0.95$ V) for 6 h and for all of the potentials the current–time curve had the characteristics of the passive state, i.e. decline of current until nearly constant, e.g. Fig 9-4b. Second, excessive overpotential must be avoided. High overpotential can change the charge-transfer-controlled kinetics to diffusion-controlled kinetics. An estimate of the limiting current density for the ferric-ferrous couple was calculated. The solution used in these experiments contains 0.2 M Fe^{3+} and 0.05 M Fe^{2+} and, considering the concentration of ferrous, the limiting current density is about 10 mA cm^{-2}, from:

$$i_d^{Fe^{3+}/Fe^{2+}} = \frac{FDc}{\delta}$$

9-3

where D is the diffusion coefficient and δ is the thickness of the Nernst layer. In the above calculation we have assumed that $D = 10^{-5}$ cm^2 s^{-1} and $\delta = 5\times10^{-3}$ cm [Makrides 1964b]. In this study, the registered highest current density, before addition of the iron salts, was less than 10^{-5} A cm^{-2} (Fig. 9-3), and the current density for the ferric-ferrous couple was always less than 3×10^{-4} A cm^{-2} (Fig. 9-4a). In addition to the above argument, the data points of Fig. 9-4a show two reasonably straight lines corresponding to the Tafel region. This means that any possible contribution from diffusion current can be neglected and that the major

contribution comes from charge transfer. Hence, it is safe to conclude that Fig. 9-4a represents the Tafel behavior of the ferric-ferrous redox couple on the surface of the passivated chalcopyrite electrode.
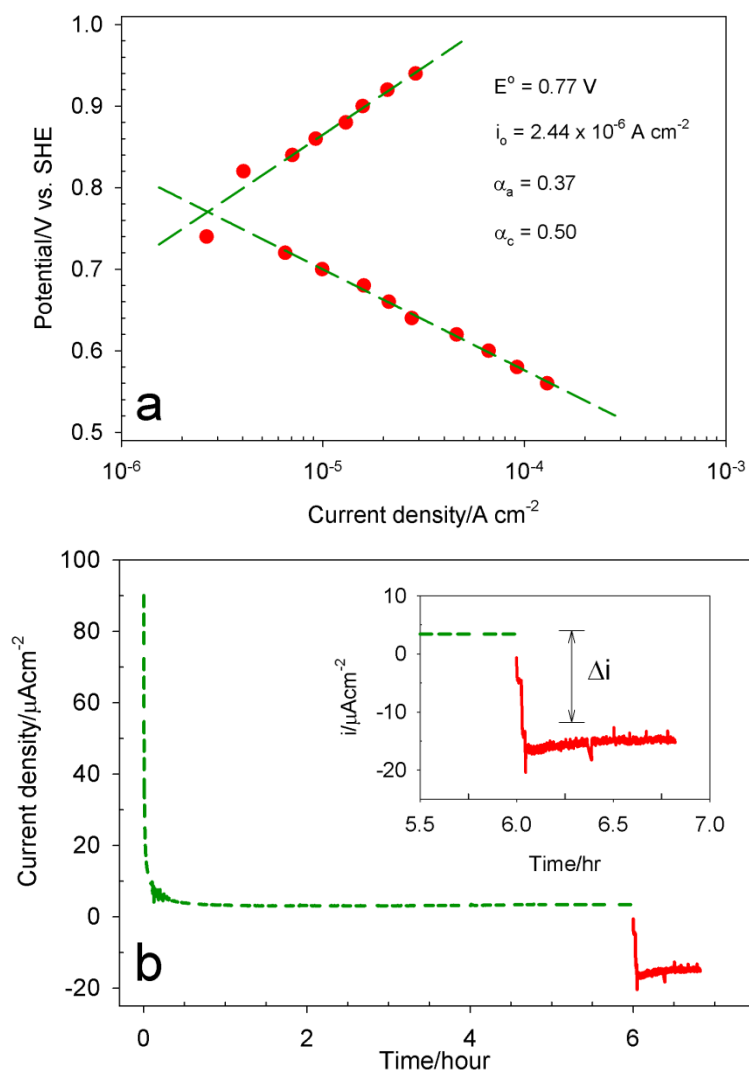
Figure 9-4: (a) Tafel region of the Fe^{3+}/Fe^{2+} couple, and (b) potentiostatic behavior of a chalcopyrite electrode at 0.70 V before and after addition of the Fe^{3+}/Fe^{2+} couple (the difference in current was used to derive Fig. 9-4a).

A typical plot of charge density *vs* time for potentiostatic polarization at 0.60 V is presented in Fig. 9-5. The curve for the Fe-containing part of the experiment (solid-red line) presents a constant slope which is due to the ferric reduction reaction. The inset of Fig. 9-5 presents an expanded view of the first 6 h of polarization in Fe-free solution (dashed green line). After two hours the slope of the curve is almost constant (inset of Fig. 9-5). However,

174

the reaction rate is higher in the Fe-containing segment due to the rapid ferric reduction reaction.
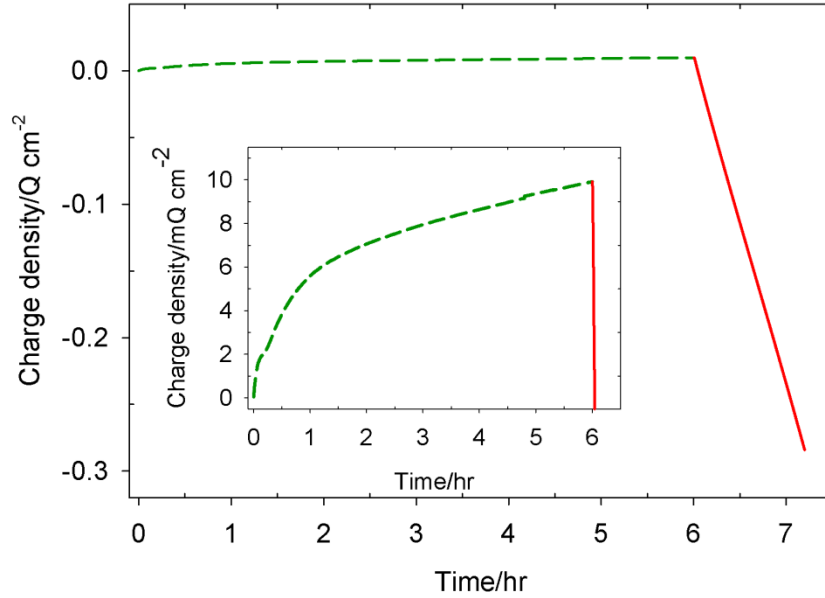
Figure 9-5: (a) A typical plot of charge density vs time for potentiostatic polarization at 0.60 V. The solid-red line represents the stage at which Fe-containing solution was added to the original solution. The inset figure shows an expanded view of the first 6 hours of polarization in Fe-free solution (dashed-green line).

From Fig. 9-4a, the equilibrium potential of the ferric-ferrous couple is calculated to be 0.77 V. From the Nernst equation, this value should be:

$$E(V_{SHE}) = 0.770 + 0.059 \log\left(\frac{Fe^{3+}}{Fe^{2+}}\right) = 0.805 \qquad\qquad 9\text{-}4$$

which is higher than the measured potential of this study. This is justified for two reasons: (1) the formation of species such as $Fe(OH)^{2+}$ and possibly $Fe(OH)^{+}$ [Makrides 1964a] and/or other ferric sulfate complexes [Hirato *et al.,* 1987] can reduce the free ferric and ferrous concentrations and cause the reversible potential of the ferric-ferrous couple to be different from the calculated one; (2) experimental measurements may contain an appreciable liquid junction potential which is, however, constant during the experiment. The exchange current density, i_o, and the anodic and cathodic transfer coefficients, α_a and α_c, were calculated to be 2.44 $\mu A\ cm^{-2}$, 0.37 and 0.50, respectively. Reported i_o values for superficially oxidized Fe, Ti, Fe-13.2% Cr, and 304 stainless steel electrodes are 10, 26, 1, and 0.045 $\mu A\ cm^{-2}$, respectively [Makrides 1964a, 1964b; Stern 1957; Ghahremaninezhad *et*

175

al., 2010b], which are close to the above results. The reaction order obtained from the summation of the anodic and cathodic transfer coefficients is 0.87. Theoretically, for the ferric-ferrous couple on the surface of bare metal this number should be 1.00. However, blocking of the anodic reactions is a typical property of *n*-type semiconductors [Kapusta and Hackerman 1981], which lowers the anodic transfer coefficient, α_a, to less than 0.4 while the cathodic transfer coefficients, α_c, remain around 0.5. In fact, this result matches with that of our previous work [Ghahremaninezhad *et al.,* 2010a] which suggested that at high anodic potentials (e.g. 0.80 V or above) the surface of the electrode is negatively charged due to the accumulation of metal vacancies in the passive film/solution interface. This negative charge on the surface is in fact responsible for blockage of oxidation reactions at the electrode surface. Additionally, it should be noted that the formation of *n*-type passive films on the surface of chalcopyrite was suggested by the potentiostatic experiments (Fig. 9-3) presented above and the Mott-Schottky experiments discussed in a previous paper [Ghahremaninezhad *et al.,* 2010a].

Electrochemical impedance spectroscopy (EIS) has also been used to further investigate the ferric-ferrous couple on a passivated chalcopyrite electrode. The EIS method provides a kinetic model in the form of an equivalent circuit, and one can typically attribute a clear physical meaning to each of the parameters (circuit elements) of the model. EIS is a powerful technique for the study of charge transfer kinetics, and is used here to study the charge transfer rate on the surface of chalcopyrite in the presence and absence of iron salts in solution. Fig. 9-6 shows the measured and calculated Nyquist impedance spectra for iron-free (Fig. 9-6a) and iron-containing (Fig. 9-6b) solutions, measured at 0.70 V. In both figures, two time constants are clearly evident. The first time constant is a well-defined capacitive loop related to the combination of the double-layer capacitive impedance with a charge transfer resistance. The second time constant is one part of a capacitive loop, which is related to the influence of diffusion processes occurring at the electrode surface [MacDonald 1990; Ghahremaninezhad *et al.,* 2010a]. During the application of an anodic potential of 0.70 V to the chalcopyrite electrode in iron-free solution (Fig. 9-6a), iron atoms dissolve preferentially from the surface of chalcopyrite, leaving behind a copper-rich passive film [Hackl *et al.,* 1995; Ghahremaninezhad *et al.,* 2010a]. Hence, the second time constant may be due to the diffusion of iron atoms through the copper rich passive film. Alternatively, the second time

constant may be related to ferric reduction on the electrode surface. At the applied potential of 0.70 V, ferric reduction contributes significantly to the overall electrochemical processes occurring on the chalcopyrite electrode. This is clearly demonstrated in Fig. 9-4b, where the addition of iron salts to the solution caused the current density to increase from *ca.* 3 μA cm^{-2} (anodic) to *ca.* –17 μA cm^{-2} (cathodic). In addition, the second time constant of the Nyquist plot of Fig. 9-6b is a straight line with a slope of *ca.* 1 (characteristics of Warburg impedance), which suggests a diffusion process in solution [Bard and Faulkner 2001]. Hence, the second time constant in iron-containing solution (Fig. 9-6b) may be due to the diffusion of ferric towards the electrode surface.
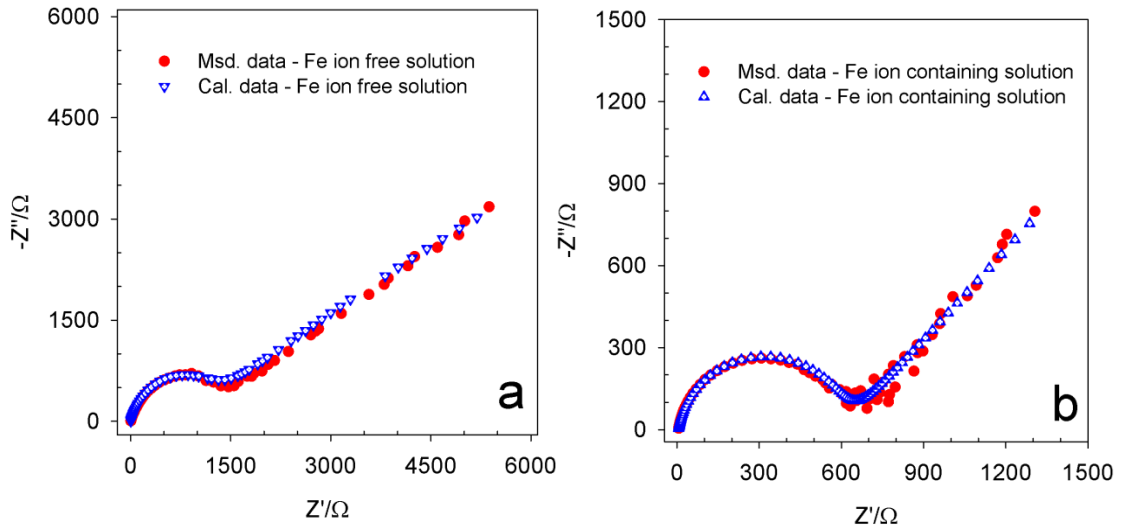
Figure 9-6: Measured and calculated Nyquist plots for the chalcopyrite electrode at 0.70 V in (a) Fe^{3+}/Fe^{2+}-free, (b) Fe^{3+}/Fe^{2+}-containing solution.
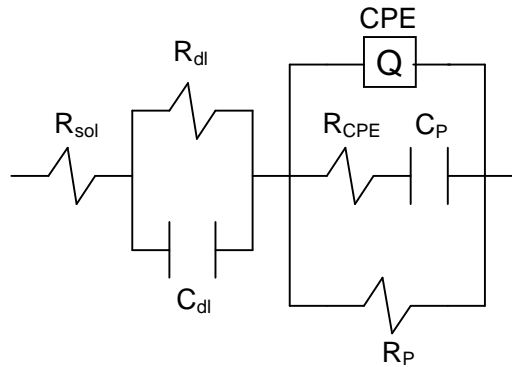
Figure 9-7: Equivalent electrochemical circuit for the chalcopyrite/electrolyte interface.

177

The equivalent electrical circuit chosen to model the measured impedance spectra is shown in Fig. 9-7, and its electrical parameters are given in Table 1. The low chi-squared (χ^2) values given in Table 9-1 indicate a good fit to the experimental data. R_{sol} represents the solution resistance and, not surprisingly, this resistance is decreased by the addition of iron salts. R_{dl} and C_{dl} represent the resistance and capacitance of the double-layer, respectively. Note the significant decrease in the double-layer resistance (R_{dl}) upon the addition of iron salts. The double-layer resistance can be defined as follows [Bard and Faulkner 2001]:

$$R_{dl} = \frac{RT}{nFi_o} \qquad\qquad 9\text{-}5$$

where R, T, n and F represent the ideal gas constant, temperature in Kelvin, number of transferred electrons and Faraday constant, respectively, and i_o is the exchange current density of the electrochemical reaction. In iron-free solution, the slow anodic dissolution of chalcopyrite is the electrochemical reaction on the chalcopyrite electrode and its exchange current density value must be applied in Eq. 9-5. In contrast, by addition of iron salts to the solution, ferric reduction will be the predominant reaction on the surface and in this case the exchange current density of ferric reduction should be used in Eq. 9-5. The exchange current density of ferric reduction is higher than that of chalcopyrite oxidation. Hence, one would expect a decrease in the R_{dl} value by addition of iron salts to the solution. This agrees well with the data of Table 9-1, which shows the R_{dl} value decreases from 1714 to 470 Ω cm^2 upon the addition of iron salts to the solution.

Table 9-1: Model parameters for equivalent circuit of Fig. 9-7.

Solution	R_{Sol} (Ω cm^2)	R_{dl} (Ω cm^2)	C_{dl} (F cm^{-2})	R_P (Ω cm^2)	C_P (F cm^{-2})	R_{CPE} (Ω cm^2)	Q (Ω s^{-n})	n	Chi-squared
Fe^{3+}/Fe^{2+} free	3.50	1714.0	2.07×10^{-4}	5655.1	8.53×10^{-6}	1765.4	6.57×10^{-4}	0.84	6.34×10^{-4}
Fe^{3+}/Fe^{2+} containing	2.65	470.0	2.39×10^{-6}	2335.4	5.77×10^{-6}	592.6	1.45×10^{-3}	0.51	9.59×10^{-4}

Double-layer resistance is a characteristic quantity for the charge-transfer step of an electrochemical reaction which indicates its inherent speed (the higher the charge transfer resistance, the lower the reaction rate). From the R_{dl} values given in Table 9-1, the ferric reduction reaction ($R_{dl} = 470$ Ω cm^2) proceeds faster than chalcopyrite oxidation ($R_{dl} = 1714$ Ω cm^2). This means that the passivated chalcopyrite electrode is able to transfer charge at higher rates than its passive state would suggest. This finding agrees with our chronoamperometry results (Fig. 9-4b); and is also made clear in Fig. 9-5, which shows a much higher reaction rate for the iron-containing part of the curve (solid line) than for iron-free solution (dashed line). In general, a passive film (a copper sulfide film such as CuS_2, in the case of chalcopyrite [Yin *et al.,* 1995]) on the surface of a material impedes the dissolution rate owing either to its low electronic or low ionic conduction. It is worth mentioning here that the electrochemical dissolution of the passive film at the film/solution interface cannot be the rate-controlling process [Macdonald 1999]. In fact, if this process were rate controlling then increasing the electrode potential would result in an exponentially increasing current as per the Butler-Volmer equation. In other words, if the electrochemical dissolution of the passive film governed the kinetics then the *E*-log *i* diagram of Fig. 9-1 would not show declining current densities at between *ca.* 0.65 and 0.85 V.

Low electronic conduction of a passive film imposes a very high double-layer resistance on electrochemical reactions, while low ionic conduction of a passive film significantly reduces the diffusion rate of atoms through the passive film to the solid-solution interface. In the case of a passivated chalcopyrite electrode, our findings show that the passive film can transfer charge at high rates, indicating that the electronic conduction of the passive film is relatively high. Hence, the passive film of chalcopyrite impedes chalcopyrite dissolution due to its low ionic conduction. In other words, the passive dissolution of chalcopyrite is mass-transport-controlled by the passive film.

The C_{dl} values (double-layer capacitance) of Table 9-1 also show a decrease from 207.00 to 2.39 μF cm^{-2} by addition of iron salts to the solution. The double-layer capacitance of an electrode can be estimated as follows [Bard and Faulkner 2001]:

$$C_{dl} = \frac{\varepsilon \varepsilon_o A}{d}$$

9-6

where ε_o, A and d represent the permittivity of free space (8.85×10^{-14} F cm^{-2}), the exposed surface area of the electrode, and the thickness of the double-layer, respectively, and ε is the dielectric constant of the medium (*i.e.*, solution in the double layer). The dielectric constant of sulfuric acid solutions *ca.* 25°C is about 90 and addition of ferrous to the solution lowers the value to below 10 [Greenwood and Earnshaw 1997]. Assuming these values can be applied for our condition, then Eq. 9-6 would give double-layer capacitances of about 100 and 1 μF cm^{-2} for iron-free and iron-containing solutions, respectively (note that the thickness of the double-layer was assumed to be 1 nm for these estimates). These estimated values agree very well with data given in Table 9-1.

R_P and C_P represent the resistance and capacitance of the passive film, respectively. Table 9-1 shows similar values in both iron-free and iron-containing solution. In general, R_P and C_P values mostly depend on the thickness of a passive film, and typically this thickness depends on the applied potential. During the related experiment of Figs. 9-6a and b, the applied electrode potential was constant (0.70 V), thus one would not expect a considerable change in R_P and C_P values, as suggested by data given in Table 9-1. The thickness of a passive film can be estimated simply by rearranging Eq. 6 thus:

$$d_P = \frac{\varepsilon \varepsilon_o A}{C_P}$$

9-7

where d_P represents the thickness of the passive film. The capacitance values of the passive film are presented in Table 9-1. If one assumes that the relative dielectric constant ε for the passive film of chalcopyrite is about 10 [Ghahremaninezhad *et al.*, 2010a], then one can obtain a thickness of *ca.* 1 to 1.5 nm from Eq. 9-7. Calculations by Biegler [1977] have shown that the thickness of the passive film of chalcopyrite formed in sulfuric acid solution is *ca.* 2 nm and in another paper [Biegler and Horne 1985] this layer is reported to be *ca.* 3 nm thick. Both results agree fairly well with our estimates, indicating that the equivalent electrochemical circuit model of Fig. 9-7 and the calculated passive film capacitances given in Table 9-1 are likely valid.

The constant phase element (CPE) and its associated resistance (R_{CPE}) are the final elements of Fig. 9-7 to consider. In general, the CPE element behaves as a capacitance which

varies with frequency and R_{CPE} represents its resistance in the equivalent circuit. The impedance of a CPE is presented by [Brug *et al.*, 1984]:

$$Z_{CPE} = Q^{-1}(j\omega)^{-n} \qquad \qquad 9\text{-}8$$

where Q is the CPE parameter; $j = (-1)^{1/2}$; ω is the frequency in rad s^{-1}, $\omega = 2\pi f$; f is the frequency in Hz; and n is the measure of the non-ideality of the capacitor and has a value in the range $0 < n < 1$. If $n = 1$, then Z_{CPE} is identical to that of a capacitor, $Z_C = (j\omega C)^{-1}$, where C is the capacitance. Indeed, a capacitor is a constant phase element with a phase angle of 90°. Usually, CPE elements represent the effect of crystal defects in the passive film [Hirschorna *et al.*, 2010]. Interestingly, in the case of chalcopyrite dissolution in sulfuric acid solution, the suggested passive film is a metal-deficient sulfide layer which forms by preferential dissolution of iron atoms from the mineral surface and, therefore, contains a high density of point defects (vacancies at iron positions within the chalcopyrite structure). Hence, in the case of iron-free solution, the CPE element and its associated resistance may be related to the point defects in the structure of the chalcopyrite passive film. The suggested n value for such a defective passive film is usually between 0.8 and 0.9 [Jorcin *et al*, 2006], which agrees well with the results given in Table 9-1 (n = 0.84).

In contrast, the addition of iron salts to the solution decreased the value of n to 0.51. A value of n close to 0.5 (together with slope of the second time constant of the Nyquist plot in Fig. 6b which is *ca.* 1.0) are two independent indicators of a significant diffusion process in solution [Bard and Faulkner 2001]. Thus, in the presence of iron in solution, the CPE element of Fig. 7 most probably represents the diffusion of ferric towards the electrode surface.

The potentiostatic polarization diagram of Fig. 9-1 and the *i-t* curves of Figs. 9-2a to c have shown that a steady-state passive film forms on the surface of chalcopyrite. Additionally, the chronoamperometry results shown in Fig. 9-4b, the results shown in Fig. 9-5 and a comparison of R_{dl} values given in Table 9-1 prove that the passive film of chalcopyrite is a better electronic conductor than an ionic conductor. Subsequently, one may safely conclude that the chalcopyrite passive film impedes the dissolution rate of chalcopyrite due to its low ionic conductivity (rather than its low electronic conductivity). In other words, the passive dissolution of chalcopyrite is mass transport-controlled by the passive film. If one assumes that iron dissolves preferentially to copper during chalcopyrite

leaching and a passive film of metal-deficient sulfide layer forms on the surface [Hackl *et al.*, 1995], then the diffusion of atoms (of mostly Fe) from the bulk of chalcopyrite to the passive film/solution interface is essential for chalcopyrite to be oxidized. In fact, copper and iron atoms must diffuse through the passive film to reach the passive film/electrolyte interface in order to be oxidized. However, as we have shown above, this diffusion step is slow and therefore controls the dissolution rate of chalcopyrite.

During the ferric-assisted leaching of chalcopyrite concentrates, ferric reduction represents the major contribution to the total cathodic current. On the other hand, the diffusion of atoms through the passive film is slow, and therefore the number of electrons available for ferric reduction on the surface will be controlled by the diffusion of atoms through the passive film. This is illustrated in the schematic of Fig. 9-8, which shows that the rate of ferric reduction is completely dependent on the diffusion of iron and copper atoms within the passive film and their subsequent oxidation at the passive film/solution interface. Even high concentrations of ferric in solution cannot increase the rate of chalcopyrite dissolution because the electrons for the ferric reduction reaction must be provided by diffusion of atoms through the passive film lattice. Therefore, considering the fact that the main anodic reaction in chalcopyrite leaching is chalcopyrite oxidation, the slow rate of chalcopyrite oxidation (due to the slow diffusion process) will control the rate of ferric reduction on the surface of chalcopyrite. In other words, sluggish chalcopyrite oxidation (dissolution) is the reason for slow ferric reduction on the surface of chalcopyrite.

These findings are different from the proposed idea that pyrite-assisted galvanic leaching of chalcopyrite in ferric-containing solution results in a substantially higher dissolution rate [Berry *et al.,* 1978; Koleini *et al.,* 2011]. In fact, the results of a recent study by Eghbalnia and Dixon [2011] have shown that copper extraction from pyrite-assisted leaching in iron sulfate media is only slightly faster than in the absence of pyrite when the pyrite has little or no silver content [Eghbalnia and Dixon 2011; Nazari *et al.*, 2011]. Generally, it is true that the addition of pyrite to a chalcopyrite concentrate leach solution will speed up the ferric reduction rate, as it has already been suggested that the ferric-ferrous couple is rapid on pyrite surfaces [Mishra and Osseo-Asare 1988]. However it cannot be stated conclusively that the rate of chalcopyrite oxidation will also be increased. Indeed, a recent study by Nazari *et al.* [2011] demonstrated that not all pyrite minerals increase the

dissolution rate of chalcopyrite leaching significantly, and that silver content of the pyrite is a key factor in determining the leaching rate of chalcopyrite concentrates. Furthermore, Nazari's study has shown that the co-presence of pyrite and silver is essential for rapid leaching of chalcopyrite, and that the addition of silver or pyrite alone do not result in a substantial increase in the chalcopyrite dissolution rate. It should be mentioned that Nazari *et al.* [2011] have suggested that chalcopyrite leaching is difficult due to the slow kinetics of ferric reduction on its surface, whereas, the results of this work present a different scenario. Findings of the present study support the idea that the presence of silver in chalcopyrite leach solutions may alter the properties of the chalcopyrite passive film, and this idea will be revisited in a future paper. Nevertheless, a detailed and alternative mechanism of chalcopyrite leaching in the co-presence of pyrite and silver is suggested and discussed elsewhere [Nazari *et al.,* 2012].
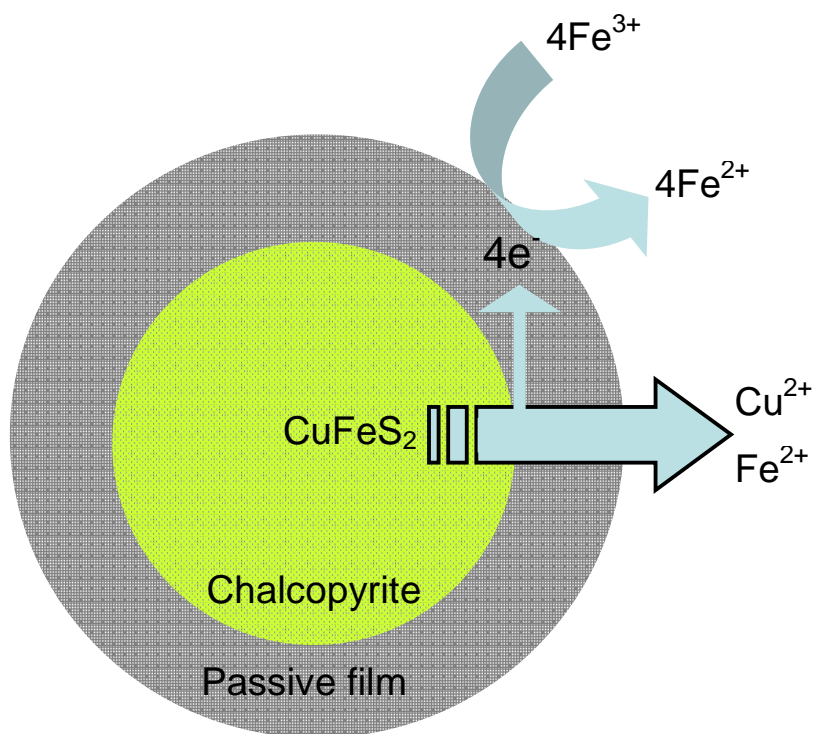
Figure 9-8: Schematic illustration for the dissolution process of a passivated chalcopyrite mineral particle in ferric-containing sulfuric acid solution. High concentration of ferric (0.1 M) is available on the surface for cathodic reduction, and anodic oxidation of chalcopyrite must provide the required electrons for ferric reduction. However, diffusion of iron and copper atoms through the passive film is slow (rate-controlling step) and so the electron production rate will be slow and consequently so will be the ferric reduction rate.

9.4 Conclusions

In summary, the kinetics of the ferric-ferrous couple on an anodically passivated chalcopyrite surface in 0.5 M sulfuric acid solution at 25ºC was investigated for the first time. For this redox reaction, the exchange current density of 2.44 μA cm^{-2} and the anodic and cathodic transfer coefficients of 0.37 and 0.50 were obtained, respectively. In addition, it was shown that the ferric reduction reaction on the surface of chalcopyrite is relatively fast (i.e. faster than oxidation of chalcopyrite itself). It was shown that the slow kinetics of ferric reduction on chalcopyrite surfaces during the leaching process is due to slow diffusion of Fe atoms through a passive film.

10 A proposed electrochemical dissolution model

10.1 Introduction

In this chapter, a possible anodic dissolution model for chalcopyrite in 0.5 M sulfuric acid solution based on the findings of the previous chapters will be proposed.

10.2 Model development

The general dissolution behavior of chalcopyrite in 0.5 M sulfuric acid solution can be considered to occur in two different modes: (1) passive dissolution, and (2) transpassive dissolution [Ghahremaninezhad *et al.* 2010] (note that the anodically active dissolution of chalcopyrite is not an option here since the chalcopyrite surface at potentials even slightly above its OCP (or OCP itself) is covered with a thin layer of passive film [Ghahremaninezhad *et al.* 2010]). In the passive state, a passive film blocks the surface of the electrode and hinders the dissolution rate, while in the transpassive state, the passive film is not stable, and dissolution of chalcopyrite proceeds without any serious barrier (formation of non-passive surface films is possible at elevated potentials). From our XPS results (chapter 7), the ultimate passivating agent for chalcopyrite may be copper sulfide (CuS) and metal-deficient sulfide (e.g. $Cu_{1-x}Fe_{1-y}S_{2-z}$).

There is a distinct difference between the transpassive dissolution of sulfide minerals (e.g. chalcopyrite) and that of most metals and alloys (e.g. stainless steel). In the case of passive metals, a metal oxide film forms on the surface and passivates the metal (e.g. chromium oxide film on the surface of stainless steel). In the transpassive region, metal atoms of the passive film structure on metals oxidize to higher oxidation states and dissolve in solution. In the case of sulfide minerals, e.g. chalcopyrite, the transpassive dissolution proceeds after oxidation of sulfide species to higher oxidation states such as thiosulfate, sulfate or elemental sulfur. Hence, in the case of this study, sulfide ions in the passive film must oxidize to higher oxidation states in order for chalcopyrite to dissolve. We have shown that copper sulfide (CuS) and metal-deficient sulfide ($Cu_{1-x}Fe_{1-y}S_{2-z}$) are the most plausible phases present on the surface of chalcopyrite in the passive state (cf. chapter 7). In addition, iron oxyhydroxide (FeOOH) was also detected on the surface (cf. chapter 7). It was proposed

that the low potential anodic dissolution of chalcopyrite proceeds through a reaction such as reaction 7-5 (cf. chapter 7).

Reaction 7-5 is an overall anodic reaction which takes into account the formation of a metal-deficient sulfide film (as a passive film phase). In addition, this reaction includes the formation of soluble ions of iron, copper and sulfur as ferrous, cupric and thiosulfate ions, respectively. Indeed, from the characteristics of chalcopyrite dissolution, the formation of the latter soluble ions (or other soluble species of Fe, Cu and S) seems to be a mandatory requirement. One of the most important characteristics of chalcopyrite dissolution, which also was discussed in a previous study (cf. chapter 7), is presented in Fig. 10-1, i.e. potentiostatic dissolution of chalcopyrite at 0.80 V for about 60 hours results in a sharp decrease in the current density value and afterwards a very low steady state current density. In other words, if one considers a reaction such as [Yin *et al.* 1995]:

$$CuFeS_2 = CuS_2^* + Fe^{2+} + 2e^-$$
$$\text{10-1}$$

as the general passivation reaction of chalcopyrite, the charge associated with the experiment of Fig. 10-1, i.e. total q = 297 mC cm^{-2}, will result in a relatively thick passive film after some hours of dissolution. An estimate of the thickness of the CuS_2^* film (product of reaction 10-1, suggested by Yin *et al.,* [1995]) is presented in Fig. 10-2. This figure shows a thickness of the passive film of ca. 200 nm after 20 hours and the thickness increases to ca. 400 nm after 60 h. One would expect a significant decrease in the dissolution current density as a function of time (from Fick's first diffusion law). For instance, if the thickness of the passive film doubles (during the 60 h of experiment), then the current density (current flux) should decrease to half. However the current density of Fig.10-2 is almost steady state (i.e. not decreasing).
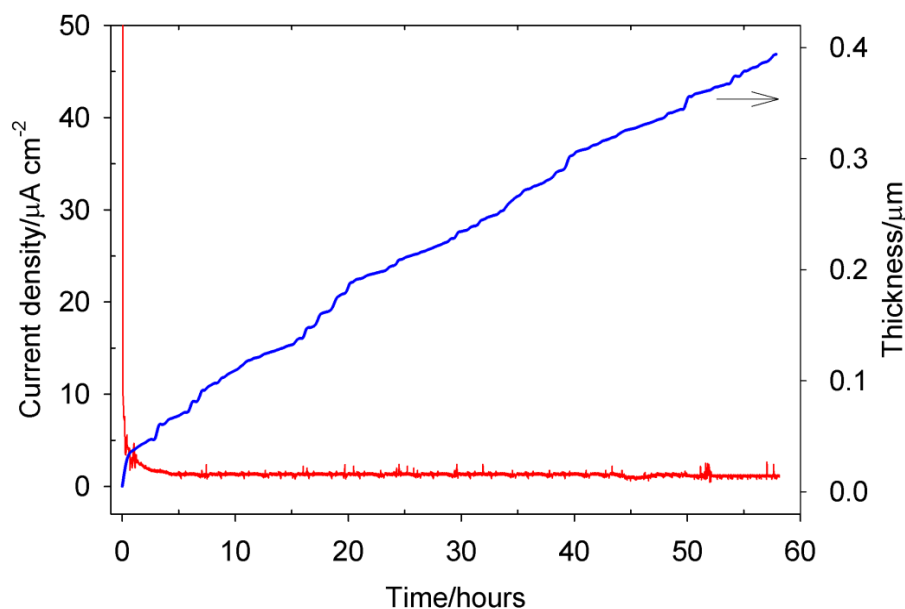
Figure 10-1: Passive current vs. time respond of a chalcopyrite electrode to potentiostatic polarization at 800 mV, and related thickness of the passive film (CuS_2^*) calculated from reaction 10-1.

On the other hand, the reaction suggested in this study, i.e. reaction 7-5, considers both passivation of chalcopyrite, by formation of metal-deficient sulfide phase, and dissolution of all three elements present in the structure of chalcopyrite. In addition, a fraction of the iron-sulfide species (Fe-S bonds in the passivating film) may react with water to form FeOOH (formation of iron oxyhydroxide (FeOOH) was suggested by our XPS studies in chapter 7). It has been proven that Fe-S species (species with iron-sulfide bond) are good catalysts for oxygen reduction [Susac *et al.* 2007]. In fact, it has been suggested that pyrite electrodes (Fe-S bonds) can successfully coordinate OH⁻ and water molecules on their surface and promote the associated reactions [Mishra and Osseo-Asare 1988]. If this is true, then one would expect that the Fe-S bonds of the chalcopyrite passive film coordinate water molecules and form Fe-O species (FeOOH). Then it would be expected that the passive surface of chalcopyrite could be covered with a FeOOH product layer. This schematic is presented in Fig. 10-2. In order to confirm the order of surface films (formation of a FeOOH product layer on top of sulfide passive film), an angle-resolved XPS experiment was performed on the surface of a chalcopyrite electrode after 6 hours of dissolution at 0.70 V. In this experiment (presented in Fig. 10-3) the take-off angle of the photoelectrons for Fig. 10-3a was 45° and in the experiment of Fig. 10-3b the take-off angle of photoelectrons was

increased to 90º. The penetration depth for the photoelectrons with the high angle (90º) is about 10 nm while at low angles, e.g. 45º, a lower penetration depth is expected. Under this condition, if the position of the FeOOH film is on top of the sulfide passive film, i.e. the $Cu_{1-x}Fe_{1-y}S_{2-z}$ film as presented in schematic of Fig. 10-2, then the ratio of Fe-O species to Fe-S species must show an increase. The fitting procedure of the Fe 3p level spectrum has been explained elsewhere (rf. Chapter 7) and the ratio of Fe-O to Fe-S can be acquired from the area ratio under the related peaks for iron oxyhydroxide and iron sulfide species. The Fe 3p spectra of Figs. 10-3a and b show two main peaks centered at 53.3 (peak 1) and 55.5 eV (peak 2). The peak at 53.3 eV agrees well with the Fe 3p peak of Fe^{3+} in Fe-S species and the peak at 55.5 eV matches well with the Fe 3p peak of Fe^{3+} in FeOOH (rf. Chapter 7). The ratio of Fe-O to Fe-S is *c.a.* 91:9 and 85:2 for Figs. 10-3a and 10-3b, respectively. The reason for this slight increase in the Fe-O to Fe-S ratio, obtained by decreasing the take-off angle of the photoelectrons, is that the FeOOH layer covers the sulfide passive film as shown in Fig. 10-2. Note that the partial dissolution of the passive film, to form FeOOH, might result in flaws on its outer layer and consequently the FeOOH film may be porous. In addition, the thickness of the FeOOH film must be less than 10 nm, otherwise we wouldn't be able to detect the Fe-S and Cu-S species by XPS.
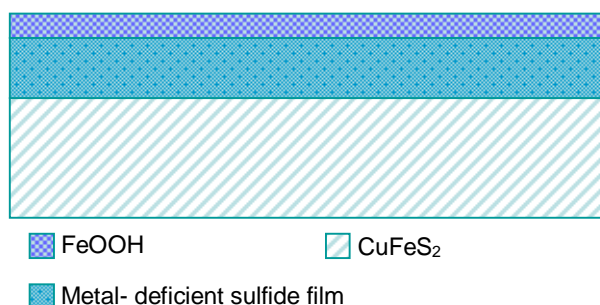
Figure 10-2: Schematic illustration for the growth of surface films on chalcopyrite surface.
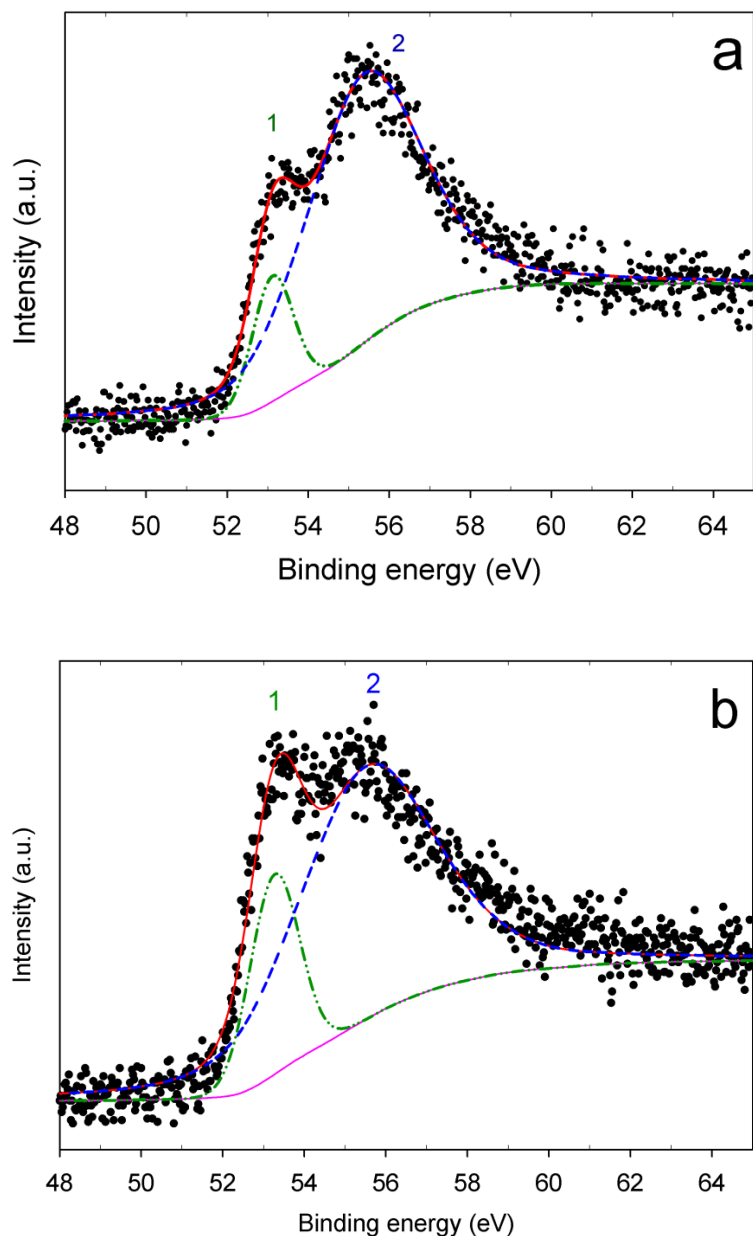
Figure 10-3: XPS spectrum of Fe 3p level obtained from a chalcopyrite electrode after 6 hours dissolution at 700 mV. The take-off angle of the photoelectrons was (a) 45º, (b) 90º.

The results presented here are very similar to those of chapter 6 which employed EIS to elucidate the nature of the passive film. However, in our previous study, since we didn't perform any analytical methods on the surface of the electrode for compositional characterization of the surface films, reactions proposed by other workers were selected to explain the dissolution/passivation behavior that we observed. In this previous work the

dissolution reaction of chalcopyrite at low anodic potentials, which results in passivation of chalcopyrite, was suggested to be:

$$CuFeS_2 \longrightarrow Cu_{1-x}Fe_{1-y}S_2 + xCu^{2+} + yFe^{2+} + 2(x+y)e^- \qquad y\rangle\rangle x \qquad 10\text{-}2$$
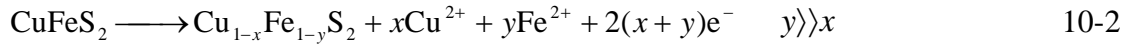
and it was suggested that the layer on top of the passive film forms by the following reaction:

$$Cu_{1-x}Fe_{1-y}S_2 \longrightarrow Cu_{1-x-z}S_2 + zCu^{2+} + (1-y)Fe^{2+} + 2(z+1-y)e^- \qquad 10\text{-}3$$
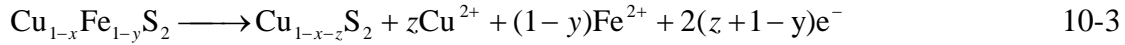
This conclusion was made based on the measured and modeled impedance spectra, which revealed that in the passive state, there must be two surface layers on the surface of chalcopyrite - the topmost layer forming by partial dissolution of the passive film (reaction 10-3). This conclusion is in good agreement with the results of chapter 7 which suggests the formation of a second layer (FeOOH film) by partial dissolution of the passive film (metal-deficient sulfide film of $Cu_{1-x}Fe_{1-y}S_{2-z}$). In addition, the main product of reaction 10-2 is very similar to the product of reaction 7-5, as they both produce a passive metal-deficient sulfide film. For complete dissolution of chalcopyrite (transpassive dissolution), we would suggest that at high enough potentials (above 0.90 V), the passive film of chalcopyrite dissolves by reaction 8-10. Complete dissolution of chalcopyrite starts after this stage and proceeds according to reactions such as 8-11 to 8-12, but not exclusive to these reactions.

One final and very important point which must be discussed is the elemental sulfur yield in the low temperature acidic (around 80ºC) leaching processes of chalcopyrite reported by different workers [Klauber *et al.* 2001; Koleini *et al.* 2011; Nazari *et al.* 2011]. This elemental sulfur yield has led to the conclusion by several authors that passivation is caused by a sulfur film [Klauber *et al.* 2001]. In contrast, results of electrochemical studies on chalcopyrite dissolution tend to support the passivation of chalcopyrite by a sulfide passive film [Viramontes-Gamboa *et al.* 2007; Parker *et al.* 1981; Linge 1976]. We believe that the thiosulfate present in solution, originated from chalcopyrite dissolution by reactions such as 7-5, can be the precursor for elemental sulfur formation. Indeed, the formation of elemental sulfur from thiosulfate is a reduction reaction that may be presented as [Marcus and Protopopoff 1977]:

$$S_2O_3^{2-} + 2O_{ads} + 10H^+ + 8e^- = 2S + 5H_2O \qquad 10\text{-}4$$

Reaction 10-4 is consistent with many experimental leaching process results, as it has been observed that an increase in the oxygen pressure during the chalcopyrite leaching

increases the elemental sulfur yield [Dixon and Tshilombo 2010]. Furthermore, it has been shown that higher acidity of chalcopyrite leach solution will result in higher elemental sulfur yield [Marsden and Wilmot 2007] which is consistent again with reaction 10-4. Further evidence for the validity of reaction 10-4 may be gleaned from pyrite leaching studies in acidic ferric sulfate solutions [Bouffard *et al.* 2006]. The main product of pyrite leaching is known to be thiosulfate [Schippers and Sand 1999]. Studies by Bouffard et al. [2006] has shown that increasing the redox potential in pyrite leaching, lowers the elemental sulfur yield (i.e. increases the sulfate formation, instead). In fact, this can be explained by reaction 10-4, as by increasing of the redox potential the rate of thiosulfate reduction decreases, i.e. increase of redox potential will impose a more oxidizing condition in the leach solution and reduction reactions such as reaction 10-4 will be less favorable).

Alternatively, it has been shown by Johnston and McAmish [1973] that in a dilute acidic thiosulfate solution (HCl concentration between 1.95 – 8.16 mM), colloidal sulfur can form with a rapid third-order reaction. The suggested overall reaction is:

$$H^+ + S_2O_3^{2-} = S + HSO_3^- \qquad \frac{d[S]}{dt} = k[H^+][S_2O_3^{2-}]^2 \qquad \text{10-5}$$
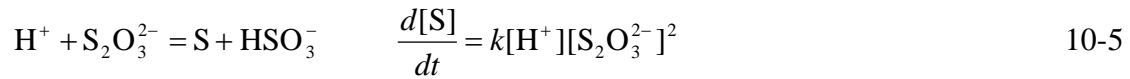
and the reaction is shown to be a rapid reaction with the *k* value of:

$$k = (1.64 \pm 0.13) \times 10^{11} \exp(\frac{-15930 \pm 160}{RT}) \frac{l^2}{mole^2 \sec^1} \qquad \text{10-6}$$

Reaction 10-5 is the disproportionation reaction of thiosulfate which simultaneously reduces and oxidizes the thiosulfate reactant to elemental sulfur and bisulfate products, respectively. If the above pathways for formation of elemental sulfur in leaching of chalcopyrite are true, then reaction 10-4 and 10-5 suggest that the sulfur yield in the concentrate leaching experiments originates from thiosulfate, which itself is a product of chalcopyrite dissolution. Thus S^o does not form directly from chalcopyrite dissolution. Such a reaction scheme, i.e. the formation of elemental sulfur from thiosulfate in acidic solutions, has also been suggested for the leaching of pyrite [Chandra and Gerson 2010]. Nonetheless, reaction 10-5 can form at most 50% elemental sulfur from its reactant thiosulfate while the reported elemental sulfur yield for chalcopyrite is around 90% or above [Dutrizac 1989]. This means that reaction 10-4 is likely the main sulfur producing reaction, in comparison to

reaction 10-5. If this is true, then there is need for further studies to evaluate the validity of reaction 10-4 in the case of chalcopyrite leaching.

10.3 Conclusion

In summary, thiosulfate is proposed to be the soluble sulfur species which forms during the dissolution of chalcopyrite. The absence of elemental sulfur during electrochemical dissolution of chalcopyrite and its presence in leaching processes were discussed. Elemental sulfur is believed to be the product of thiosulfate reduction. However, this needs further study to be confirmed as we do not have any direct evidence for this type of reaction.

11 Conclusions and recommendations

The results of the electrochemical and surface analysis experiments of this study on the electrochemistry of pyrrhotite and chalcopyrite minerals have generated the following conclusions and recommendations.

11.1 Conclusions

- The electrochemical dissolution behavior of pyrrhotite has been studied in 1M HCl solution with in-situ electrochemical methods (chapter 5). Results showed the formation of two distinct surface layers on the electrode. At low anodic dissolution potentials, the iron atoms from the pyrrhotite structure partially dissolve and a metal–deficient sulfide layer with semiconducting properties ($Fe_{1-x-y}S$) forms on the surface of the electrode. This layer is stable up to potential of 0.84 V_{SHE}. The second film forms at higher anodic potentials (> 0.91 V_{SHE}) and is substantially more resistant to dissolution than the first. The results of this study are directly related to those of chalcopyrite electrodissolution. As pyrrhotite represents a simplified case of chalcopyrite dissolution, we would expect to observe relatively similar morphology for the passive film of chalcopyrite. More specifically, in the case of chalcopyrite dissolution, a copper sulfide surface film forms on its surface which is analogous to that in pyrrhotite electrodissolution, i.e. both films are semiconductor films and both form by partial dissolution of atoms from the mineral structure.

- From EIS studies on the chalcopyrite electrode (chapter 6), it was shown that at low potentials (below 0.7 V_{SHE}) a surface layer forms on the surface of chalcopyrite. Above this potential (0.7 – 0.9 V_{SHE}) the previously formed surface layer partially dissolves and a second passive layer forms. Both of these layers display the characteristics of passive layers at low scan rate (0.05 mV s^{-1}) and for high scan rates they are observed to be pseudo-passive. In the potential range of 0.9 to 1.02 V_{SHE}, none of the surface layers are stable and electrochemical active dissolution of the electrode occurs.

- From the electrochemical experiments of chapter 7 it was concluded that potentiodynamic polarization of chalcopyrite, even at a very low scan rate, cannot reliably and successfully demonstrate active-passive dissolution of chalcopyrite. On the other hand,

the results of potentiostatic polarization have agreed very well with those of XPS studies, which suggest that this technique can accurately demonstrate the active-passive dissolution behavior of chalcopyrite. From potentiostatic polarization it was concluded that chalcopyrite is passive at potentials below 0.90 V_{SHE}, beyond which it actively dissolves.

- Results of XPS studies (chapter 7) have shown a substantial change in the oxidation state of sulfur species on the surface of chalcopyrite at potentials above 0.90 V_{SHE}. XPS experiments revealed that copper and iron sulfide bonds are present in the passive film of chalcopyrite, but their binding energies are different from those of chalcopyrite. These bonds were believed to originate from a metal-deficient sulfide passive film with composition $Cu_{1-x}Fe_{1-y}S_{2-z}$. In addition, FeOOH was detected on the surface and a possible reaction mechanism for its formation was suggested.

- XPS results of chapter 7 also showed that the surface of passive chalcopyrite is blocked by a sulfide film and beyond the passive region (above 0.90 V_{SHE}) the percentage of sulfides in the film decreased significantly, i.e. monosulfide decreased from 56% to 19% and disulfide decreased from 39% to 18%. Furthermore, no elemental sulfur or polysulfide was detected on the surface at potentials below 0.90 V_{SHE}. Hence, it is concluded that the transpassive dissolution of chalcopyrite is significantly linked to the oxidation of sulfur (from sulfide in the passive film to elemental sulfur and perhaps to sulfur species with higher oxidation states, e.g. thiosulfate). Additionally, by comparing XPS sulfur spectra of chalcopyrite with the results of sulfur spectra from iron sulfide (pyrite and pyrrhotite) and copper sulfide minerals (chalcocite and covellite) we have concluded that the high energy feature in sulfur species spectra (~ 163.3 eV) is most likely related to the S 3p→Fe 3d excitation and does not originate from polysulfide.

- From the cyclic voltammetry experiments of chapter 8, it was shown that iron atoms dissolve preferentially from the surface of chalcopyrite during anodic dissolution, leaving behind a copper-rich metal-deficient sulfide passive film (i.e. $Cu_{1-x}Fe_{1-y}S_2$ $y > x$). By integrating the current under the chalcopyrite de-passivation peak, the thickness of the passive film was calculated to be *ca.* 6.7 nm. Additionally, experiments showed that elemental sulfur is a product of chalcopyrite oxidation at anodic potentials higher than 1.0 V_{SHE}.

- Results of chapter 8 also showed that cathodic dissolution of chalcopyrite proceeds at potentials below 0 V_{SHE}. The cathodic dissolution process involves the release of ferrous and $H_2S_{(aq)}$ to solution. The cathodic reactions which occur in the potential region of 0.1 to 0.6 V_{SHE} and the anodic reactions which occur at potentials lower that 0.5 V_{SHE} are all related to the reduction and oxidation of soluble species. The soluble species involved in those cathodic reactions are ferric and cupric and the soluble species involved in the anodic reactions is $H_2S_{(aq)}$.

- Chapter 9, for the first time, presents the kinetics of the ferric-ferrous couple on an anodically passivated chalcopyrite surface in 0.5 M sulfuric acid solution at 25ºC was investigated. For this redox reaction, the exchange current density of 2.44 μA cm^{-2} and the anodic and cathodic transfer coefficients of 0.37 and 0.50 were obtained, respectively. In addition, it was shown that the ferric reduction reaction on the surface of chalcopyrite is relatively fast (i.e. faster than oxidation of chalcopyrite itself). It was shown that the slow kinetics of ferric reduction on chalcopyrite surfaces during leaching processes is due to slow diffusion of Fe atoms through the passive film.

- Coupling the results of chapters 5-9, a reaction model for the anodic chalcopyrite dissolution was proposed. Thiosulfate is proposed to be the soluble sulfur species which forms during the dissolution of chalcopyrite. The absence of elemental sulfur during electrochemical dissolution of chalcopyrite and its presence in leaching processes were discussed. Elemental sulfur is believed to be the product of thiosulfate reduction. However, this needs further studies to be confirmed.

11.2 Recommendations

The recommended future work is the following:

- Dissolution of chalcopyrite through the formation of soluble sulfur species should be further investigated. In this regard, one might put a platinum plate in front of a chalcopyrite electrode. The chalcopyrite electrode should be dissolved at anodic potentials and the platinum plate must be kept at a cathodic potentials. Note that for this experiment two potentiostats are required. Then the platinum electrode can be analyzed for sulfur species by means of different techniques such as XPS, SIMS etc.

- The effect of the temperature increase on the passivity of chalcopyrite was not considered in this study. Since typical leaching processes of chalcopyrite proceed at elevated temperatures, this effect should be studied.

- The aim of this study was to produce very fundamental knowledge about the dissolution of chalcopyrite in a simple solution. However, the effect of the different acids and acid concentrations on the passivation of chalcopyrite needs to be further elucidated.

- The findings of this study, i.e. composition of passive film and its chemical and semiconductor properties, are helpful regarding the selection of reagents for leaching. Leaching of chalcopyrite at low anodic potentials (below 0.75 V_{SHE}) requires an aggressive reagent (e.g. Cl^-) which can break down chalcopyrite's passive film by pit formation. The selection of proper reagents for further study requires comprehensive knowledge of the physio-chemical properties of chalcopyrite's passive films, which are provided in this thesis.

References

Abraitis, P.K., Pattrick, R.A.D., Kelsall, G.H., Vaughan, D.J., 2004, Mineralogical Magazine, 68(2), p. 343.

Acres, R.C., Harmer, S.L., Beattie, D.A., 2010, Minerals Engineering 23, p. 928.

Acres, R.C., Harmer, S.L., Shui, H.W., Chen, C.H., Beattie, D.A., 2011, J. Synchrotron Radiation, 18, p. 649.

Almeida, C.M.V.B., Giannetti, B.F., 2003, J. Electroanal. Chem., 553, p. 27.

Asselin, E., Alfantazi, A., Rogak, S., 2007, J. Electrochem. Soc. 154, p. C215.

Austin, I.G., Goodman, C.H.L., Pengelly, A.E., 1956, J. Electrochem. Soc. 103, p. 609.

Avgouropoulos, G., Ioannides, T., 2003, Appl. Catal. A, 244, p. 155.

Aznar, J.C., Richer-Lafleche, M., Cluis D., 2008, Environmental Pollution, 156, p. 76.

Azumi, K., Ohtsuka, T., Sato, N., 1987, J. Electrochem. Soc. 134, p. 1352.

Bard, A.J., Faulkner, L.R., 2001, Electrochemical methods, 2nd Ed., John Wiley & Sons, NY, p. 745.

Beolchini, F., Veglio, F., 1999, Ind. Eng. Chem. Res., 38, p. 3296.

Berry, V.K., Murr, L.E., Hiskey, J.B., 1978, Hydrometallurgy, 3, p. 309.

Betova, I, Bojinov, M., Laitinen, T., Makela, K., Pohjanne, P., Saario, T., 2002, Corr. Sci. 44, p. 2675.

Betova, I., Bojinov, M., Tzvetkoff, T., 2004, Electrochim. Acta 49, p.2295.

Bevilaqua, D., Diéz-Perez, I., Fugivara, C.S., Sanz, F., Benedetti, A.V., Garcia, O., 2004, Bioelectrochemistry, 64, p. 79.

Biegler, T., 1977, J. Electrochem. Soc. 85, p. 101.

Biegler, T., Horne, M.D., 1985, J. Electrochemical Soc. 132, p. 1363.

Biegler, T., Swift, D.A., 1979, J. Appl. Electrochem. 9, p. 545.

Biernat, R.J, Robins, R.G., 1972, Electrochimica Acta 17, p. 1261.

Biswas, A.K., Davenport, W.G., 1976, Extractive Metallurgy of Copper, Pergamon Press, Oxford.

Boekema, C., Krupski, A.M., Varaste, M., Parvin, K.,VanTil, F.,VanDerWoude, F., Sawatzky, G.A., 2004, J. Magn. Magn. Mater. 272–276, p. 559.

Bojinov, M, 1996, J. Electroanal. Chem. 405, p. 15.

Bojinov, M., Betova, I., Fabricius, G., Laitinen, T., Raicheff, R., Saario, T., 1999, Corr. Sci. 41, p. 1557. AND, Bojinov, M., Fabricius, G., Laitinen, T., Saario, T., 1999, Electrochim. Acta 44, p.4331.

Bojinov, M., Fabricius, G., Kinnunen, P., Laitinen, T., Makela, K., Saario, T., Sundholm, G., 2000, Electrochimica Acta 45, p. 2791.

Bojinov, M., Fabricius, G., Kinnunen, P., Laitinen, Y., Mäkelä, K., Saario, T., Sundholm, G., Yliniemi, K., 2002, Electrochim. Acta 47 p. 1697.

Bojinov, M., Salmi, K., Sundholm, G., 1993, J. Electroanal. Chem. 347, p. 207.

Bojinov, M., Tezvetkoff, T., 2003, J. Phys. Chem. B 107, p. 5101.

Brion, D., 1980, Appl. Surf. Sci., 5, p. 133.

Buckley, A.N., Kravets, I.M., Shchukarev, A.V., Woods, R., 1994, J. Appl. Electrochem., 24, p. 513.

Buckley, A.N., Woods, R., 1994, J. Electroanal. Chem. 370, p. 295.

Buckley, A.N., Woods, R., 1996, The galena surface revisited, in: R. Woods, P. Richardson, F. Doyle (Eds.), Electrochemistry in Minerals and Metals Processing IV, The electrochemical Society, Pennington, NJ, p. 1.

Burdick, C.L., Ellis, J.H., 1917, J. Am. Chem. Soc., 39, p. 2518.

Cardon, F., 1972, Physica 57, p. 390.

Chandra, A.P., Gerson, A.R., 2010, Surf. Sci. Reports, 65, p. 293.

Chen, L., Zhou, Y., Krause, S., Munoz, A.G., Kunze, J., Schmuki, P., 2008, Electrochim. Acta 53, p. 3395.

Chernyshova, I.V., Andreev, S.I., 1997, Appl. Surf. Sci. 108, p. 225.

Chusuei, C.C., Brookshier, M.A., Goodman, D.W., 1995, Langmuir, 15, p. 2806.

Clayton, C.R., Lu, Y.C., 1986, J. Electrochemical Soc. 133, p. 2465.

Córdoba, E.M., Muñoz, J.A., Blázquez, M.L., González, F., Ballester, A., 2008, Hydrometallurgy 93, p. 81.

Descostes, M., Mercier, F., Thromat, N., Beaucaire, C., Gautier-Soyer, M., 2000, Appl. Sur. Sci. 165, p. 288.

Dixon, D.G., Mayne, D.D., Baxter, K.G., 2008, Can. Metall. Q. 47, p. 327.

Donovan, B., Reichenbaum, G., 1958, J. Appl. Phys. 9, p. 474.

Donnay, G., Coliss, L.M., Donnay, J.D.H., Elliott, N., Hastings, J.M., 1958, Phys. Rev. 112, p. 1917.

Dreisinger, D., 2006, Hydrometallurgy 83, p. 10.

Dreisinger, D., Abed, N., 2002, Hydrometallurgy 66 p. 37.

Droppert, D.J., Shang, Y., 1995, Hydrometallurgy 39, p. 169.

Dutrizac, J.E., 1978, Metall. Trans. B 9B, p. 431.

Dutrizac, J.E., 1982, Jarosite-type compounds and their application in the metallurgical industry, In: Osseo-Asare, K., Miller, J.D. (Eds.), Hydrometall. Res., Dev. Plant Pract., Proc. Int. Symp., 3rd, Metall. Soc. AIME, Warrendale PA, pp. 531–551.

Dutrizac, J.E., 1989, Can. Metall. Q. 28, p. 337.

Dutrizac, J.E., 1996, Hydrometallurgy 42, p. 293.

Dutrizac, J.E., MacDonald, R.J.C., 1974, Miner. Sci. Eng. 6, p. 59.

Eghbalnia, M., Dixon, D.G., 2011, Hydrometallurgy 110, p. 1.

Ellisa, S., Senanayake, G., 2004, Hydrometallurgy 72, p. 39.

Elsherief, A.E., 2002, Minerals Eng. 15, p. 215.

Ennaoui, A., Fiechter, S., Jaegermann, W., Tributsch, H., 1986, J. Electrochem. Soc. 133, p. 97.

Epelboin, I., Keddam, M., 1972, Electrochimica Acta 17, p. 177.

Erne, B.H., Vanmaekelbergh, D., 1997, J. Electrochem. Soc. 144, p. 3385.

Evans, H.T., Konnert, J.A., 1976, Am. Mineral., 61, p. 996.

Farquhar, M.L., Wincott, P.L., Wogelius, R.A., Vaughan D.J., 2003, Appl. Surf. Sci. 218, p. 34.

Ferreira de Lima, G. Oliveira, C., Avelino de Abreu, H., Duarte, H.A., 2011, J. Phys. Chem. C, 115, p. 10709.

Filippou, D., Konduru, R., Demopoulos, G.P., 1997, Hydrometallurgy, 47, p. 1.

Folmer, J.C.W., Jellinek, F., 1980, J. Less Common Metals 76, p. 153.

Fujisawa, M., Suga, S., Mizokawa, T., Fujimori, A., Sato, K., 1994, Phys. Review B, 49, p. 7155.

Gabrielli, C., Keddam, M., Minouflet, F., Perrot, H., 1996, Electrochim. Acta 41, p. 1217.

Garrels, R.M., Christ, C.L., 1965, Solution, Minerals, and Equilibria, Harper & Row, NY, p. 213.

Ghahremaninezhad, A., Asselin, E., Dixon, D.G., 2011, J. Phys. Chem. C, 115, p. 9320.

Ghahremaninezhad, A., Asselin, E., Dixon, D.G., 2010, Electrochim. Acta, 55, p. 5041a.

Ghahremaninezhad, A., Asselin, E., Dixon, D.G., 2010, J. Electrochem. Soc. 157, p. C248b.

Glarum, S.H., Marshall, J.H., 1985, J. Electrochem. Soc. 132, p. 2878.

Glatzel, T., Fuertes-Marrón, D., Schedel-Niedrig, T., Sadewasser, S., Lux-Steiner, M.C., 2002, Appl. Phys. Lett., 81, p. 2017.

Goh, S.W., Buckley, A.N., Skinner, W.M., Fan, L.L., 2010, Phys. Chem. Minerals, 37, p. 389.

Goh, S.W., Buckley, A.N., Lamb, R.N., 2006, Minerals Engineering 19, p. 204.

Gomes, W.P., Vanmaekelbergh, D., 1996, Electrochim. Acta 41, p. 967.

Gordon, R.B., Bertram, M., Graedel, T.E., 2006, PNAS 103, p. 1209.

Greenwood, N.N., Whitfield, H.J., 1968, J. Chem. Soc. A. London 7, p. 1697.

Gryse, R.D., Gomes, W.P., Cardon, F., Vennik, J., 1975, J. Electrochem. Soc. 122, p. 711.

Habashi F., 1997, Handbook of Extractive Metallurgy, Vol. 2, Wiley-VCH, Weinheim, Germany, p 491.

Habashi F., 1978, Chalcopyrite, its chemistry and metallurgy, McGraw-Hill, New York.

Hackl, R.P., Dreisinger, D.B., Peters, E., King, J.A., 1995, Hydrometallurgy 39, p. 25.

Hall, S.R., Stewart, J.M., 1973, Acta Cryst. B29, p. 579.

Hamajima, T., Kambara, T., Gondaira, K.I., 1981, Phys. Rev. B, 24, p. 3349.

Hamilton, I.C., Woods, R., 1981, J. Electroanal. Chem, 118, p. 327.

Harmer, S.L., Pratt, A.R., Nesbitt, H.W., Fleet, M.E., 2005, Canadian Mineralogist 43, p. 1619.

Harmer, S.L., Thomas, J.E., Fornasiero, D., Gerson, A.R., 2006, Geochim. et Cosmochim. Acta 70 p. 4392.

Hedberg, E., Gidhagen, L., Johansson, C., 2005, Atmospheric Environment 39, p. 549.

Hiroyoshi, N., Arai, M., Miki, H., Tsunekawa, M., Hirajima, T., 2002, Hydrometallurgy 63, p. 257.

Hiroyoshi, N., Kuroiwa, S., Miki, H., Tsunekawa, M., Hirajima, T., 2004, Hydrometallurgy 74, p. 103.

Hiroyoshi, N., Miki, H., Hirajima. T., Tsunekawa, M., 2001, Hydrometallurgy, 60, p. 185.

Hirschorn, B., Orazem, M.E., Tribollet, B., Vivier, V., Frateur, I., Musiani, M., 2010, Electrochimica Acta 55, p. 6218.

Hiskey, J.B., 1993, chalcopyrite semiconductor electrochemistry and dissolution, In: Reddy, R.G.,Weizenbach, R.N. (Eds.), The Paul E. Queneau International Symposium, Extractive Metallurgy of Copper, Nickel and Cobalt, Volume I: Fundamental Aspects, The Minerals, Metals & Materials Society, p. 949.

Holliday, R.I., Richmond, W.R., 1990, J. Electroanal. Chem. 288, p. 83.

Hsu, C.H., Mansfeld, F., 2001, Corrosion 57, p. 747.

Hu, J., Lu, Q., Deng, B., Tang, K., Qian, Y., Li, Y., Zhou, G., Liu, X., 1999, Inorg. Chem. Commun. 2 p. 569.

Johnston F., McAmish, L., 1973, J. Colloids Interface Sci. 42, p. 112.

Jones, C.F., LeCount, S., Smart, R.S., White, T.J., 1992, Appl. Surf. Sci. 55, p. 65.

Kaplun, K., Li, J., Kawashima, N., Gerson, A.R., 2011, Geochimi. et Cosmochimi. Acta, 75, p. 5865.

Kapusta, S., Hackerman, N., 1981, J. Electrochem. Soc. 128, p. 327.

Kareh, K., Ghahremaninezhad, A., Asselin, E., 2009, Electrochim. Acta 54, p. 6548.

Karthe, S., Szargan, R., Suoninen, E., 1993, Appl. Surf. Sci. 72, p. 157.

Ke, J., Li, H., 2006, Hydrometallurgy 82, p. 172.

Keddam, M., Takenouti, H., Yu, N., 1985, J. Electrochem. Soc. 132, p. 2561.

Kennedy, J.H., Frese Jr., K.W., 1978, J. Electrochem. Soc. 125, p. 723.

Klauber, C., 2008, Int. J. Miner. Process. 86, p. 1.

Klauber, C., 2003, Surf. Inter. Anal., 35, p. 415.

Klauber, C., Parker, A., Bronswijk, W.V., Watling, H., 2001, Int. J. Miner. Process., 62, p. 65.

Koleini, S.M.J., Aghazadeh, V., Sandström, Å., 2011, Minerals Engineering, 24, p. 381.

Lazaro, I., Nicol, M.J., 2006, J. Appl. Electrochem. 36, p. 425.

Lefevre, G., Walcarius, A., Ehrhardt, J.J., Bessiere, J., 2000, Langmuir, 16, p. 4519.

Lehmann, M.N., Kaur, P., Pennifold, R.M., Dunn, J.G., 2000, Hydrometallurgy 55, p. 255.

Li, J., Kawashima, N., Kaplun, K., Absolon, V.J., Gerson, A.R., 2010, Geochimi. et Cosmochimi. Acta, 74, p. 2881.

Li, L.C., Lan, X.J., Yi, Y., Yuan, N.Z., Juan, Z.X., Lei, Z., Yan, M.C., Dong, Z.Y., 2011, Hydrometallurgy, 107, p. 13.

Linge, H.G., 1976, Hydrometallurgy 2, p. 51.

Liu, W., Flytzani-Stephanopoulos, M., 1995, J. Catal. 153, p. 317.

Lu, Z.Y., Jeffrey, M.I., Lawson, F., 2000, Hydrometallurgy 56, p. 145.

Macdonald, D.D., Ismail, K.M., Sikora, E., 1998, J. Electrochem. Soc., 145, p. 3141.

Majuste, D., Ciminelli, V.S.T., Osseo-Asare, K., Dantas, M.S.S., Magalhães-Paniago, R., 2011, Hydromettalurgy, doi:10.1016/j.hydromet.2011.11.003.

Makrides, A.C., 1964, J. Electrochem. Soc., 111, p. 392.; Makrides, A.C., 1964, J. Electrochem. Soc., 111, p. 400.

Manocha, A.S., Park, R.L., 1977, Appl. Surf. Sci. 1, p. 129.

Mansfeld, F., Kendig, M.W., 1988, J. Electrochem. Soc. 135, p. 828.

Marcus, P., 2002, Corrosion Mechanisms in Theory and Practice, 2nd ed., Chap. 1, Marcel Dekker, New York.

Marcus, P., Mansfeld, F. (Eds.), 2006, Analytical methods in corrosion science and engineering, Taylor & Francis Group, CRC Press, Boca Raton, FL, pp. 1-102.

Marcus, R.A., 1964, Ann. Rev. Phys. Chem., 15, p. 155.

McCarron, J.J., Walker, G.W., Buckley, A.N., 1990, Intr. J. Mineral Process., 30, p. 1.

McMillan, R.S., MacKinnon, D.J., Dutrizac, J.E., 1982, J. Appl. Electrochem. 12, p. 743.

Memming, R., 2001, Semiconductor electrochemistry, Wiley-VCH, Weinheim, chapters 1-7.

Mielczarski, J.A., Cases, J.M., Alnot, M., Ehrhardt, J.J., 1996, Langmuir, 12, p. 2519.

Mikhlin, Y., 2000, Phys. Chem. Chem. Phys. 2, p. 5672.

Mikhlin, Y.L., Tomashevich, Y.V., Asanov, I.P., Okotrub, A.V., Varnek, V.A., Vyalikh, D.V., 2004, Appl. Surf. Sci. 225, p. 395.

Mishra, K.K., Osseo-Asare, K., 1988, J. Electrochem. Soc. 135, p. 1898.

Mishra, K.K., Osseo-Asare, K., 1992, J. Electrochem. Soc. 139, p. 749.

Morrison, S.R., 1980, Electrochemistry at semiconductor and oxidized metals electrodes, Plenum Press, NY, chapters 1-6.

Mulder, W.H., Sluyters, J.H., Pajkossy, T., Nyikos, L., 1990, J. Electroanal. Chem. 285, p. 103.

Munoz, J.A., Gomez, C., Ballestrer, A., Blazquez, M.L., Gonzalez, F., Figueroa, M., 1998, J. Appl. Electrochem. 28, p. 49.

Munoz, P.B., Miller, J.D., Wadsworth, J.D., 1979, Metall. Trans. B 10B, p. 149.

Nakai, I., Sugitani, Y., Nagashima K., Niwa, Y., 1978, J. Inorg. Nucl. Chem. 40, p. 789.

Nava, D., Gonzalez, I., 2006, Electrochim. Acta 51, p. 5295.

Nava, D., Gonzalez, I., Leinen, D., Ramos-Barrado, J.R., 2008, Electrochim. Acta 53, p.4889.

Nazari, G., Dixon, D.G., Dreisinger, D.B., 2011, Hydrometallurgy 105, p. 251.

Nazari, G., Dixon, D.G., Dreisinger, D.B., 2012, Hydrometallurgy doi:10.1016/j.hydromet.2011.12.011.

Nesbitt, H.W., Muir, I.J., 1994, Geochim. et Cosmochim. Acta 58, p. 4667.

Orazem, M.E., Tribollet, B., 2008, Electrochemical Impedance Spectroscopy, John Wiley & Sons, NJ, p. 233.

Otte, K., Lippold, G., Hirsch, D., Schindler, A., Bigl, F., 2000, Thin Solid Films, 498, p. 361.

Panzuner, G., Egert, B., 1984, Surf. Sci. 144, p. 651.

Parker, A.J., Paul, R.L., Power, G.P., 1981, J. Electroanal. Chem. 118, p. 305.

Parker, A., Klauber, C., Kougianos, A., Watling, H.R., Bronswijk, W., 2003, Hydrometallurgy 71, p. 265.

Paul, R.L., Nicol, M.J., Dcggle, J.W., Saunders, A.P., 1978, Electrochimica Acta, 23, p. 625.

Plieth, W., 2008, Electrochemistry for Materials Science, Elsevier, Oxford, UK, p. 263.

Pratesi G., Cipriani, C., 2000, Eur. J. Mineral., 12, p. 397.

Pratt, A.R., Muir, I.J., Nesbitt, H.W., 1994, Geochim. et Cosmoch. Acta, 58, p. 827.

Price D.W., Warren, G.W., 1986, Hydrometallurgy 15, p. 303.

Robie, R.A., Bethke, P.M., Beardsley, K.M., 1967, U.S. geological Survey Bulletin 1248, p. 8.

Rockett, A., 2008, The Materials Science of Semiconductors, Springer, NY, p. 21.

Rosenholtz, J.L., Smith, D.T., 1936, J. American Mineralogist 21, p. 115.

Pourbaix, M., 1966, "Atlas of Electrochemical Equilibrium Aqueous Solutions," Pergamon Press, Ltd., Oxford.

Salsman, J.B., Williamson, R.L., Tolley, W.K., Rice, D.A., 1996, Minerals Eng. 9, p. 43.

Samec, Z., Weber, J., 1977, J. Electroanal. Chem., 77, p. 163.

Schmuki, P., Bohni, H., Bardwell, J.A., 1995, J. Electrochem. Soc. 142, p. 1705.

Schon, G., 1972, J. Electron Spectrosc., 73, p. 377.

Shirley, D.A., 1972, Physical Review B, 5, p. 4709.

Shreir, L.L., Jarman, R.A., Burstein, G.T., 2000, Corrosion, 3rd Rev., Metal/Invironment Reactions, Vol. 1, Butterworth-Heinemann, Oxford, p. 143.

Shuey, R.T., 1975, Semiconducting ore minerals, Elsevier Scientific Publishers Co., NY, p. 242.

Shuxian, Z., Hall, W.K., Ertl, G., Konzinger, H., 1986, J. Catalysis 100, p. 167.

Stansbury, E.E., Buchana, R.A., 2000, Fundamentals of Electrochemical Corrosion, ASM International, Materials Park, OH, p. 260.

Stern, M., 1957, J. Electrochem. Soc., 104, p. 559.

Subramanian, K.N., Jennings, P.H., 1972, Can. Metall. Q. 11, p. 387.

Susac, D., Zhu, L., Teo, M., Sode, A., Wong, K.C., Wong, P.C., Parsons, R.R., Bizzotto, D., Mitchell, K.A.R., Campbell, S.A., 2007, J. Phys. Chem. C, 111, p. 18715.

Tan, B.J., Klabunde, K.J., Sherwood, P.M.A., 1990, Chem. Mater. 2, p. 186.

Tell, B., Shay, J.L., kasper, H.M., 1972, J. Appl. Phys. 43, p. 2469.

Teranishi, T., 1961, J. Phys. Soc. Jap. 16, p. 1881.

Teranishi, T., Sato, K., Kondo, K., 1974, J. Phys. Soc. Jap. 36, p. 1618.

Torma, A.E., 1991, Electrochemistry of a semiconductor chalcopyrite concentrate leaching by Thiobacillus ferrooxidans. In: Cooper, W.C., Kemp, D.O., Lagos, G.E., Tan, K.G. (Eds.), Hydrometallurgy and Electrometallurgy of Copper. Pergamon Press, NewYork, p. 73.

Tshilombo, A.F., Petersen, J., Dixon, D.G., 2002, Minerals Eng., 15, p. 809.

Vanmaekelbergh, D., Erné, B.H., 1999, J. Electrochem. Soc. 146, p. 2488.

Vanmaekelbergh, D., Searson, P.C., 1994, J. Electrochem. Soc. 141, p. 697.

Vaughan, D.J., Becker, U., Wright, K., 1997, Int. J. Miner. Process. 51, p. 1.

Vasquez, B.R., Viramontes-Gamboa, G., Dixon D.G., 2012, J. Electrochem. Soc. 159, p. C8.

Velásquez, P., Gómez, H., Leinen, D. Ramos-Barrado, J.R., 1998, Colloids and Surfaces A 140, p. 177.

Velásquez, P., Gómez, H., Ramos-Barrado, J.R., Leinen, D., 1998, Colloids and Surfaces A 140, p. 369.

Velásquez, P., Leinen, D., Pascual, J., Ramos-Barrado, J.R., Grez, P., Gómez, H., Schrebler, R., Río, R.D., Córdova, R., 2005, J. Phys. Chem. B 109, p. 4977.

Vinkevicius, J., Mozginskiene, I., Jasulaitiene, V., 1998, J. Electroanal. Chem., 442, p. 73.

Viramontes-Gamboa, G., Rivera-Vasquez, B.F., Dixon, D.G., 2006, ECS Transactions 2, p. 165.

Viramontes-Gamboa, G., Rivera-Vasquez, B.F., Dixon, D.G., 2007, J. Electrochem. Soc. 154, p. C299.

Wagner, C.D., Riggs, W.M., Davis, L.E., Moulder, J.F., Muilenberg, G.E., 1979, Perkin-Elmer Corporation/Physical Electronics Division, Eden Prairie, Minnesota, pp. 76-77.

Wang, H., 2008, Mineral Processing & Extractive Metall. Rev. 29, p. 1.

Wang, S., 2005, JOM 57, p. 48.

Warren, G.W., Wadsworth, M.E., El-Raghy, S.M., 1982, Metall. Trans. B 13B, p. 571.

Watling, H.R., 2006, Hydrometallurgy 84, p. 81.

Wei, D., Osseo-Asare, K., 1997, J. Electrochem. Soc. 144, p. 546.

Wei, D., Osseo-Asare, K., 1996, J. Electrochem. Soc., 143, p. 3192.

Winkel, L., Alxneit, I., Sturzenegger, M., 2007, Minerals Eng. 20, p. 1179.

Yacobi, B.G., 2004, Semiconductor materials, an introduction to basic principles, Kluwer Academic Publishers, NY, chapters 1-4.

Yin, Q., Kelsall, G.H., Vaughan, D.J., England, K.E.R., 1995, Geochim. et Cosmochim. Acta 59, p. 1091.

Yin, Q., Vaughan, D.J., England, K.E.R., Kelsall, G.H., Brandon, N.P., 2000, J. Electrochem. Soc. 147, p. 2945.

Yin, M., Wu,C.K., Lou, Y., Burda, C., Koberstein, J.T., Zhu, Y., O'Brien, S., 2005, J. Am. Chem. Soc., 127, p. 9506.

Yu, X.R., Liu, F., Wang, Z.Y., Chen, Y., 1990, J. Electron Spectroscopy and Related Phenomena, 50, p. 159.